Publishing House ASV

begell house, inc. publishers

Scientific coordination is carried out by the Russian Academy of Architecture and Construction Sciences (RAACS)

Volume 21 • Issue 1 • 2025

ISSN 2588-0195 (Online)
ISSN 2587-9618 (Print) Continues ISSN 1524-5845

International Journal for

Computational Civil and Structural Engineering

Международный журнал по расчету гражданских и строительных конструкций

https://ijccse.iasv.ru/

DOI: 10.22337/2587-9618
GICID: 71.0000.1500.2830

PUBLISHER

ASV Publishing House
(ООО «Издательство АСВ»)
19/1,12, Yaroslavskoe Shosse, 120338, Moscow, Russia
Tel. +7(925)084-74-24; E-mail: iasv@iasv.ru; Интернет-сайт: http://iasv.ru/

ADVISORY EDITORIAL BOARD

TECHNICAL EDITOR

EDITORIAL TEAM

INVITED REVIEWERS

AIMS AND SCOPE

The aim of the Journal is to advance the research and practice in structural engineering through the application of computational methods. The Journal will publish original papers and educational articles of general value to the field that will bridge the gap between high-performance construction materials, large-scale engineering systems and advanced methods of analysis.

The scope of the Journal includes papers on computer methods in the areas of structural engineering, civil engineering materials and problems concerned with multiple physical processes interacting at multiple spatial and temporal scales. The Journal is intended to be of interest and use to researches and practitioners in academic, governmental and industrial communities.

ОБЩАЯ ИНФОРМАЦИЯ О ЖУРНАЛЕ

International Journal for Computational Civil and Structural Engineering

(Международный журнал по расчету гражданских и строительных конструкций)

Международный научный журнал "International Journal for Computational Civil and Structural Engineering (Международный журнал по расчету гражданских и строительных конструкций)" (IJCCSE) является ведущим научным периодическим изданием по направлению «Инженерные и технические науки», издаваемым, начиная с 1999 года (ISSN 2588-0195 (Online); ISSN 2587-9618 (Print) Continues ISSN 1524-5845). В журнале на высоком научно-техническом уровне рассматриваются проблемы численного и компьютерного моделирования в строительстве, актуальные вопросы разработки, исследования, развития, верификации, апробации и приложений численных, численно-аналитических методов, программно-алгоритмического обеспечения и выполнения автоматизированного проектирования, мониторинга и комплексного наукоемкого расчетно-теоретического и экспериментального обоснования напряженно-деформированного (и иного) состояния, прочности, устойчивости, надежности и безопасности ответственных объектов гражданского и промышленного строительства, энергетики, машиностроения, транспорта, биотехнологий и других высокотехнологичных отраслей.

В редакционный совет журнала входят известные российские и зарубежные деятели науки и техники (в том числе академики, члены-корреспонденты, иностранные члены, почетные члены и советники Российской академии архитектуры и строительных наук). Основной критерий отбора статей для публикации в журнале − их высокий научный уровень, соответствие которому определяется в ходе высококвалифицированного рецензирования и объективной экспертизы, поступающих в редакцию материалов.

Журнал входит в Перечень ВАК РФ ведущих рецензируемых научных изданий, в которых должны быть опубликованы основные научные результаты диссертаций на соискание ученой степени кандидата наук, на соискание ученой степени доктора наук по научным специальностям и соответствующим им отраслям науки:

- 1.1.8 – Механика деформируемого твердого тела (технические науки),
- 1.2.2 – Математическое моделирование численные методы и комплексы программ (технические науки),
- 2.1.1 – Строительные конструкции, здания и сооружения (технические науки),
- 2.1.2 – Основания и фундаменты, подземные сооружения (технические науки),
- 2.1.5 – Строительные материалы и изделия (технические науки),
- 05.23.07 – Гидротехническое строительство (технические науки),
- 2.1.9 – Строительная механика (технические науки)

В Российской Федерации журнал индексируется Российским индексом научного цитирования (РИНЦ).

Журнал входит в базу данных Russian Science Citation Index (RSCI), полностью интегрированную с платформой Web of Science. Журнал имеет международный статус и высылается в ведущие библиотеки и научные организации мира.

Издатели журнала – *Издательство Ассоциации строительных высших учебных заведений /АСВ/* (Россия, г. Москва) и до 2017 года *Издательский дом Begell House Inc*. (США, г. Нью-Йорк). Официальными партнерами издания является *Российская академия архитектуры и строительных наук* (РААСН), осуществляющая научное курирование издания, и *Научно-исследовательский центр СтаДиО* (ЗАО НИЦ СтаДиО).

Цели журнала – демонстрировать в публикациях российскому и международному профессиональному сообществу новейшие достижения науки в области вычислительных методов

решения фундаментальных и прикладных технических задач, прежде всего в области строительства.

Задачи журнала:

• предоставление российским и зарубежным ученым и специалистам возможности публиковать результаты своих исследований;

• привлечение внимания к наиболее актуальным, перспективным, прорывным и интересным направлениям развития и приложений численных и численно-аналитических методов решения фундаментальных и прикладных технических задач, совершенствования технологий математического, компьютерного моделирования, разработки и верификации реализующего программно-алгоритмического обеспечения;

• обеспечение обмена мнениями между исследователями из разных регионов и государств.

Тематика журнала. К рассмотрению и публикации в журнале принимаются аналитические материалы, научные статьи, обзоры, рецензии и отзывы на научные публикации по фундаментальным и прикладным вопросам технических наук, прежде всего в области строительства. В журнале также публикуются информационные материалы, освещающие научные мероприятия и передовые достижения Российской академии архитектуры и строительных наук, научно-образовательных и проектно-конструкторских организаций.

Тематика статей, принимаемых к публикации в журнале, соответствует его названию и охватывает направления научных исследований в области разработки, исследования и приложений численных и численно-аналитических методов, программного обеспечения, технологий компьютерного моделирования в решении прикладных задач в области строительства, а также соответствующие профильные специальности, представленные в диссертационных советах профильных образовательных организациях высшего образования.

Редакционная политика. Политика редакционной коллегии журнала базируется на современных юридических требованиях в отношении авторского права, законности, плагиата и клеветы, изложенных в законодательстве Российской Федерации, и этических принципах, поддерживаемых сообществом ведущих издателей научной периодики.

За публикацию статей плата с авторов не взымается. Публикация статей в журнале бесплатная. На платной основе в журнале могут быть опубликованы материалы рекламного характера, имеющие прямое отношение к тематике журнала.

Журнал предоставляет непосредственный открытый доступ к своему контенту, исходя из следующего принципа: свободный открытый доступ к результатам исследований способствует увеличению глобального обмена знаниями.

Индексирование. Публикации в журнале входят в системы расчетов индексов цитирования авторов и журналов. «Индекс цитирования» – числовой показатель, характеризующий значимость данной статьи и вычисляющийся на основе последующих публикаций, ссылающихся на данную работу.

Авторам. Прежде чем направить статью в редакцию журнала, авторам следует ознакомиться со всеми материалами, размещенными в разделах сайта журнала (интернет-сайт Российской академии архитектуры и строительных наук (http://raasn.ru); подраздел «Издания РААСН» или интернет-сайт Издательства АСВ (http://iasv.ru); подраздел «Журнал IJCCSE»): с основной информацией о журнале, его целями и задачами, составом редакционной коллегии и редакционного совета, редакционной политикой, порядком рецензирования направляемых в журнал статей, сведениями о соблюдении редакционной этики, о политике авторского права и лицензирования, о представлении журнала в информационных системах (индексировании), информацией о подписке на журнал, контактными данными и пр. Журнал работает по лицензии Creative Commons типа cc by-nc-sa (Attribution Non-Commercial Share Alike) – Лицензия «С указанием авторства – Некоммерческая – Копилефт».

Рецензирование. Все научные статьи, поступившие в редакцию журнала, проходят обязательное двойное слепое рецензирование (рецензент не знает авторов рукописи, авторы рукописи не знают рецензентов).

Заимствования и плагиат. Редакционная коллегия журнала при рассмотрении статьи проводит проверку материала с помощью системы «Антиплагиат». В случае обнаружения многочисленных заимствований редакция действует в соответствии с правилами COPE.

Подписка. Журнал зарегистрирован в Федеральном агентстве по средствам массовой информации и охраны культурного наследия Российской Федерации. Индекс в общероссийском каталоге РОСПЕЧАТЬ − 18076.

По вопросам подписки на международный научный журнал “International Journal for Computational Civil and Structural Engineering (Международный журнал по расчету гражданских и строительных конструкций)” обращайтесь в Агентство «Роспечать» (Официальный сайт в сети Интернет: http://www.rosp.ru/) или в издательство Ассоциации строительных вузов (АСВ) в соответствии со следующими контактными данными:

ООО «Издательство АСВ»

Юридический адрес: 129337, Россия, г. Москва, Ярославское ш., д. 26, офис 705;

Фактический адрес: 129337, Россия, г. Москва, Ярославское ш., д. 19, корп. 1, 5 этаж, офис 12 (ТЦ Соле Молл);

Телефоны: +7 (925) 084-74-24;

Интернет-сайт: www.iasv.ru. Адрес электронной почты: iasv@iasv.ru.

Контактная информация. По всем вопросам работы редакции, рецензирования, согласования правки текстов и публикации статей следует обращаться к главному редактору журнала академику РААСН *Сидорову Владимиру Николаевичу* (адреса электронной почты: sidorov.vladimir@gmail.com, sidorov@iasv.ru, iasv@iasv.ru, sidorov@raasn.ru) или к техническому редактору журнала советнику РААСН *Кайтукову Таймуразу Батразовичу* (адреса электронной почты: tkaytukov@gmail.com; kaytukov@raasn.ru). Кроме того, по указанным вопросам, а также по вопросам размещения в журнале рекламных материалов можно обращаться к генеральному директору ООО «Издательство АСВ» *Никитиной Надежде Сергеевне* (адреса электронной почты: iasv@iasv.ru, nsnikitina@mail.ru, ijccse@iasv.ru).

Журнал становится технологичнее. Издательство АСВ с сентября 2016 года является членом Международной ассоциации издателей научной литературы (Publishers International Linking Association (PILA)), осуществляющей свою деятельность на платформе CrossRef. Оригинальным статьям, публикуемым в журнале, будут присваиваться уникальные номера (индексы DOI – Digital Object Identifier), что значительно облегчит поиск метаданных и местонахождение полнотекстового произведения. DOI – это система определения научного контента в сети Интернет.

С октября 2016 года стал возможен прием статей на рассмотрение и рецензирование через онлайн систему приема статей Open Journal Systems на сайте журнала (электронная редакция): https://ijccse.iasv.ru.

Автор имеет возможность следить за продвижением статьи в редакции журнала в личном кабинете Open Journal Systems и получать соответствующие уведомления по электронной почте.

В феврале 2018 года журнал был зарегистрирован в Directory of open access journals (DOAJ) (это один из самых известных поисковых сервисов в мире, который предоставляет открытый доступ к материалам и индексирует не только заголовки журналов, но и научные статьи), в сентябре 2018 года включен в продукты EBSCO Publishing.

В ноябре 2020 года журнал начал индексироваться в международной базе Scopus.

International Journal for
Computational Civil and Structural Engineering
(Международный журнал по расчету гражданских и строительных конструкций)
Volume 21, Issue 1 ***2025***

Scientific coordination is carried out by the Russian Academy of Architecture and Construction Sciences (RAACS)

CONTENTS

International Journal for
Computational Civil and Structural Engineering
(Международный журнал по расчету гражданских и строительных конструкций)
Volume 21, Issue 1 ***2025***

Scientific coordination is carried out by the Russian Academy of Architecture and Construction Sciences (RAACS)

СОДЕРЖАНИЕ

International Journal for Computational Civil and Structural Engineering, 21(1) 14–27 (2025)

DOI:10.22337/2587-9618-2025-21-1-14-27

REFLECTION OF WAVES FROM HYDROTECHNICAL STRUCTURES IN DETERMINING THE PORT WATER WAVES

Izmail G. Kantarzhi [1], Alexander G. Gogin [2], Zhanna I. Nagornova [3]

[1] National Research Moscow State University of Civil Engineering (National Research University) (MSUCE), Moscow, RUSSIA

[2] JSC "KIS Istok", Moscow, RUSSIA

[3] National Research Moscow State University of Civil Engineering (National Research University) (MSUCE), Moscow, RUSSIA

Abstract: The article considers the influence of taking into account wave reflection and the discrepancy between the results of waves without reflection and with reflection in numerical modeling, compares the results of numerical modeling and the analytical method for determining dangerous directions of waves when servicing ships in the port. The reflectivity of hydraulic structures and the factors on which it depends are considered. Empirical formulas for obtaining the reflection coefficient for the designs of slope structures are presented. An expression for the reflection coefficient is used not only for smooth slopes, but also for permeable ones. The results are compared with the methodology given in normative SP 38.13330.2018. The stepwise behavior of the reflection coefficient is analyzed, depending on the gentleness of the wave and the slope laying.

Keywords: numerical modeling, analytical methods, reflection waves, reflection factor, critical parameter

ОТРАЖЕНИЕ ВОЛН ОТ ГИДРОТЕХНИЧЕСКИХ СООРУЖЕНИЙ ПРИ ОПРЕДЕЛЕНИИ РАСЧЕТНЫХ ВОЛН НА АКВАТОРИИ ПОРТА

Кантаржи И.Г. [1], Гогин А.Г. [2], Нагорнова Ж.И. [3]

[1] Национальный исследовательский Московский государственный строительный университет (НИУ МГСУ), город Москва, РОССИЯ

[2] АО «КИС Исток», Москва, РОССИЯ

[3] Национальный исследовательский Московский государственный строительный университет (НИУ МГСУ, город Москва, РОССИЯ

Аннотация: в статье рассматривается влияние учета отражения волн и расхождения результатов между волнами без отражения и с отражением при численном моделировании, сравниваются результаты численного моделирования и аналитического метода для определения опасных направлений волнений при обслуживании судов в порту. Рассматривается отражающая способность гидротехнических сооружений и факторы, от которых она зависит. Представлены эмпирические формулы для получения коэффициента отражения для конструкций откосных сооружений. Используются выражение для коэффициента отражения не только для гладких откосов, но и для проницаемых. Результаты сравниваются с методикой, приведенной в СП 38.13330.2018. Анализируется скачкообразный характер поведения коэффициента отражения, зависящий от пологости волны и заложения откоса.

Ключевые слова: численное моделирование, аналитические методы, отражение волн, коэффициент отражения, критический параметр

INTRODUCTION

An important aspect of port operation is ensuring safe interaction of vessels with berthing facilities [1]. The criteria for this safety are assessed by permissible wave heights, permissible wind speed and, in some cases, permissible current speed. As is known, ports can be protected and unprotected from waves. At the moment, there is

one regulatory document designed to determine the permissible wave parameters when servicing vessels for berths that are not sufficiently protected from waves.[1]There are also guidelines and recommendations that combine the ability to determine acceptable wave parameters for servicing ships and determine the port's security.[2,3], while the use of these documents does not exclude their use for unprotected ports. At first glance, in all three presented documents the methodology for determining safe conditions for interaction of vessels with berthing facilities during mooring, parking and cargo operations is quite similar, but upon closer examination, some differences are revealed. Further, it is considered how critical the existing differences in the methods are and how they can affect the final conclusion on the safety of mooring.

As an example, the conditions of the facility, hereinafter referred to as the Terminal (Fig. 1), which is located in the Kola Bay of the Barents Sea, are considered. For comparison, the calculation data obtained as a result of numerical modeling (the SWAN wind wave calculation model [2-3] and the COASTOX-CUR current and water level model) and the results of analytical calculation in accordance with the SP 38.13330 methodology were considered.[4], 2018 edition. Examples of combined modeling are presented in [4-9].

The assessment of safe conditions is carried out for piers No. 1, No. 2 and the port fleet pier; the design vessels with their characteristics are given in Table 1.

According to Figure 1, pier #1 corresponds to control points 5, 6 and 22, pier #2 – 7, 8, 40, 23 and 24 and the harbor fleet pier – 10. Control points 5, 6, 7, 8 and 40 are used to determine wave heights directly at the berth, and control points 22, 23 and 24 are located at a distance from the berth for approximately the width of the vessel. The wave parameters based on the results of the analytical calculation give values only near the object. For numerical modeling, the directions of the calculated storms include 5 rhumbs: N, NE, E, SE and S; for the analytical method, calculated storms of 4 rhumbs were tested: NE, E, SE and S.

Table 1. Parameters of design vessels

Parameter	Name of the vessel			
	SK-6000	SK-11700	Arc 8	Tugboat
Draught in cargo, m	13.5	15.0	14.00	6.0
Draft in ballast, m	8.2	9.0	11.45	
Maximum width, m	40.0	45.61	41.90	13.0
Total length, m	286.45	363.57	289.60	30.0
Displacement, thousand tons	105.81	178.29	124.20	0.645

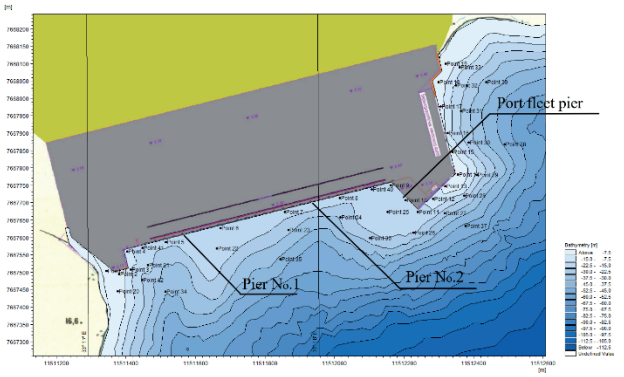

Figure 1. Bathymetry of the Terminal water area with indication of control points for issuing results

Further, based on the results of wave calculations, a table of dangerous wave directions is presented for servicing calculation vessels (for mooring

[1]R 31.3.07-01. Guidelines for calculating loads and impacts from waves, ships and ice on marine hydraulic structures: Supplement and clarification of SNiP 2.06.04 - 82*. Moscow, 2001.

[2]RD 31.33.10-87. Recommended Practice for Accounting for Hydrometeorological Conditions in the Design of Wharves with Insufficient Protection from Wave Action. Moscow, 1987.

[3]RD 31.33.03-88. Recommended Practice for the Determination of Permissible Wind and Wave Conditions for Design of Seaports. Moscow, 1989

[4]SP 38.13330.2018. Loads and impacts on hydraulic structures (wave, ice and from ships): Updated version of SNiP 2.06.04-82*. Moscow, 2018.

operations, parking of a moored vessel and performing cargo operations) at the Terminal.

Table 2 shows that there is practically no difference in the results when using different methods for determining safe waves, but taking into account wave reflection plays a significant role. When taking into account reflection, four directions of waves become dangerous, instead of one, S without taking into account reflection. It is also clear that the results diverge for two adjacent berths (along one berth wall). At the same time, approaching the corner of the cordon line (i.e., to the berth of the port fleet) the waves increase significantly, especially taking into account reflection.

Wave fields for the berthing area and on the approach to it for a storm with a recurrence rate of once per year for all dangerous directions based on the results of numerical modeling are shown in Table 3.

Table 2. Dangerous wave directions for servicing vessels at piers No. 1, No. 2 for design vessels and the port fleet pier for tugboat

	Waves without reflection, numerical modeling			Waves with reflection, numerical modeling			Analytical method	
All design vessels	Pier No. 1	Pier No. 2	Port fleet pier	Pier No. 1	Pier No. 2	Port fleet pier	Pier No. 1, No. 2	Port fleet pier
R 31.3.07-01	S	S	-	NE, E, SE, S	SE, S	S	E, SE, S	S
RD 31.33.10-87	S	S	S	NE, E, SE, S	SE, S	S	E, SE, S	S
RD 31.33.03-88	S	S	-	NE, E, SE, S	SE, S	S	E, SE, S	S

Table 3. Fields of significant wave heights during storms of the N, NE, E, SE and S direction with a probability of once a year with and without reflection

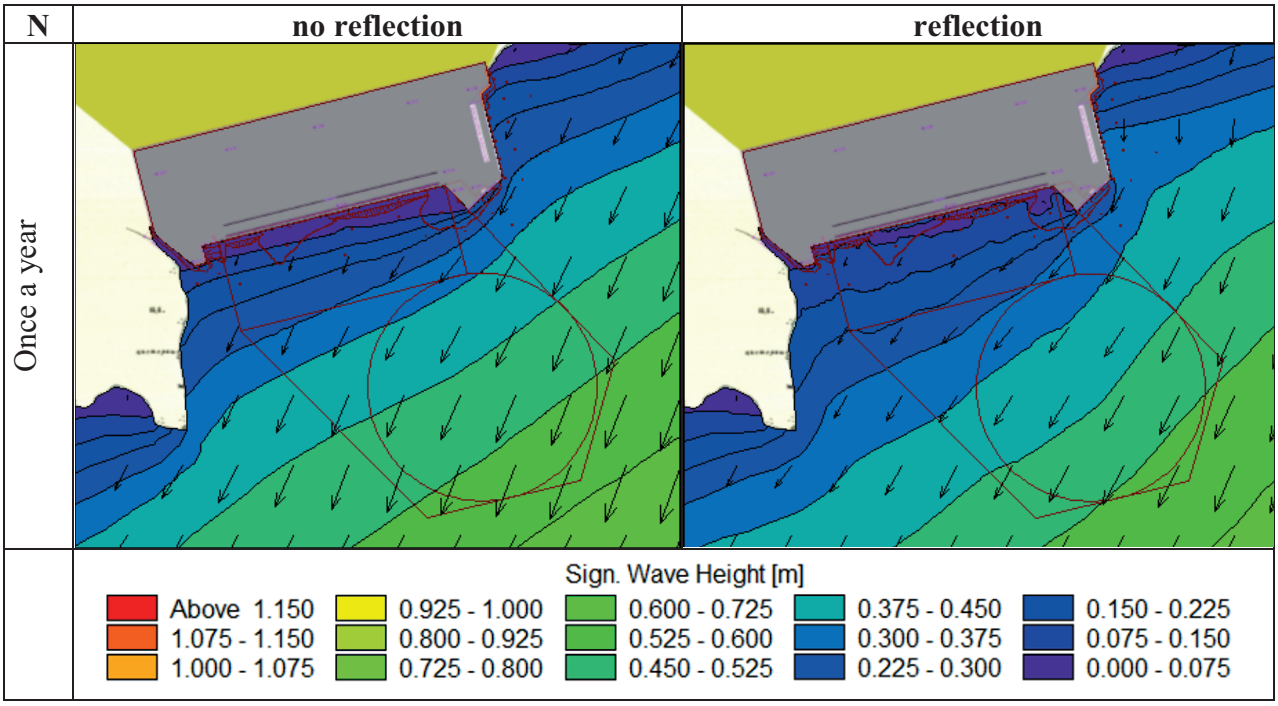

Continuation of table 3

	Wave parameters	p.5	p.6	p.22	p.7	p.8	p.40	p.23	p.24	p.10
		North direction of wave approach without reflection/ with reflection								
	$\bar{\lambda}$, м	0.10/0.10	0.10/0.10	0.70/0.80	0.10/0.10	0.10/0.10	0.10/0.10	0.60/0.60	0.30/0.30	0.10/0.10
	$\bar{T}$, с	0.30/0.30	0.30/0.30	0.70/0.80	0.20/0.20	0.30/0.30	0.30/0.30	0.60/0.60	0.40/0.40	0.30/0.30
	$\bar{h}$, м	0.01/0.01	0.01/0.01	0.04/0.04	0.01/0.01	0.01/0.01	0.01/0.01	0.04/0.05	0.02/0.03	0.02/0.01
	$h_{5\%}$, м	0.02/0.02	0.02/0.02	0.02/0.08	0.02/0.02	0.02/0.02	0.02/0.02	0.02/0.08	0.02/0.05	0.02/0.03
NE		**no reflection**				**reflection**				
Once a year		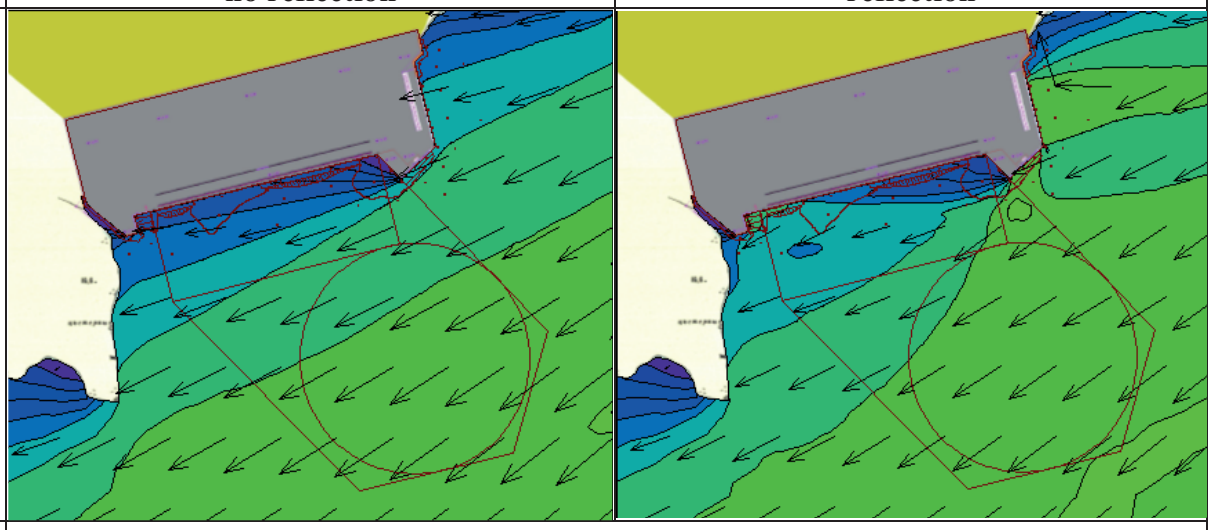								
		Sign. Wave Height [m] Above 1.150 · 1.075 - 1.150 · 1.000 - 1.075 · 0.925 - 1.000 · 0.800 - 0.925 · 0.725 - 0.800 · 0.600 - 0.725 · 0.525 - 0.600 · 0.450 - 0.525 · 0.375 - 0.450 · 0.300 - 0.375 · 0.225 - 0.300 · 0.150 - 0.225 · 0.075 - 0.150 · 0.000 - 0.075								
	Wave parameters	p.5	p.6	p.22	p.7	p.8	p.40	p.23	p.24	p.10
		North-east direction of wave approach without reflection/ with reflection								
	$\bar{\lambda}$, *m*	7.10/11.50	7.00/10.80	6.80/10.70	6.30/10.10	3.90/8.10	1.30/1.30	6.30/10.20	6.00/9.00	0.50/0.50
	$\bar{T}$, s	2.10/2.70	2.10/2.60	2.10/2.60	2.00/2.50	1.60/2.30	0.90/0.90	2.00/2.60	2.00/2.40	0.60/0.60
	$\bar{h}$, *m*	0.16/0.31	0.16/0.22	0.19/0.27	0.14/0.19	0.10/0.13	0.05/0.06	0.18/0.21	0.17/0.17	0.03/0.03
	$h_{5\%}$, *m*	0.29/0.54	0.29/0.40	0.29/0.48	0.29/0.34	0.29/0.24	0.29/0.10	0.29/0.37	0.29/0.30	0.29/0.06
E		**no reflection**				**reflection**				

Continuation of table 3

Once a year

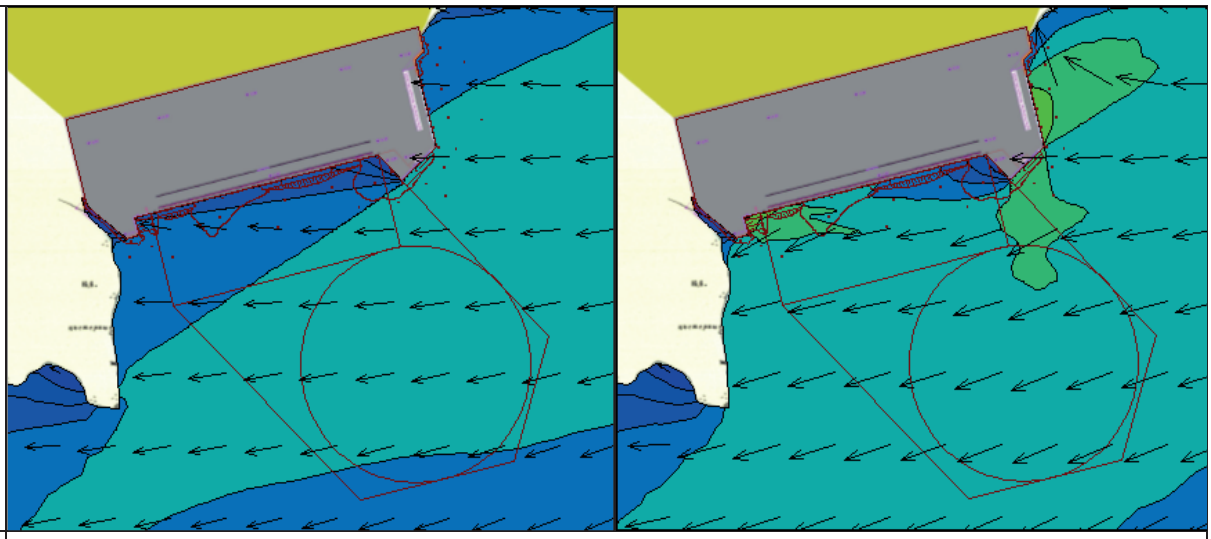

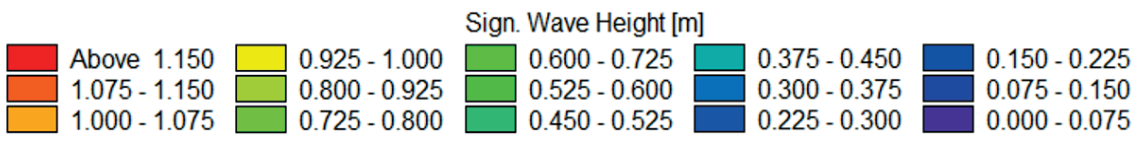

Параметры волн	p.5	p.6	p.22	p.7	p.8	p.40	p.23	p.24	p.10
	East direction of wave approach without reflection/ with reflection								
$\bar{\lambda}$, *m*	6.10/7.50	6.00/6.80	6.10/7.20	5.80/6.40	5.00/5.90	3.80/5.00	6.00/6.80	5.90/6.40	3.50/4.80
$\overline{T}$, s	2.00/2.20	2.00/2.10	2.00/2.00	1.90/2.00	1.80/1.90	1.60/1.80	2.00/2.10	2.00/2.20	1.50/1.80
$\bar{h}$, *m*	0.20/0.33	0.19/0.26	0.21/0.29	0.18/0.24	0.15/0.20	0.11/0.14	0.20/0.25	0.19/0.22	0.08/0.09
$h_{5\%}$, *m*	0.35/0.58	0.35/0.47	0.35/0.52	0.35/0.42	0.35/0.36	0.35/0.26	0.35/0.49	0.35/0.39	0.35/0.16

SE	**no reflection**	**reflection**

Once a year

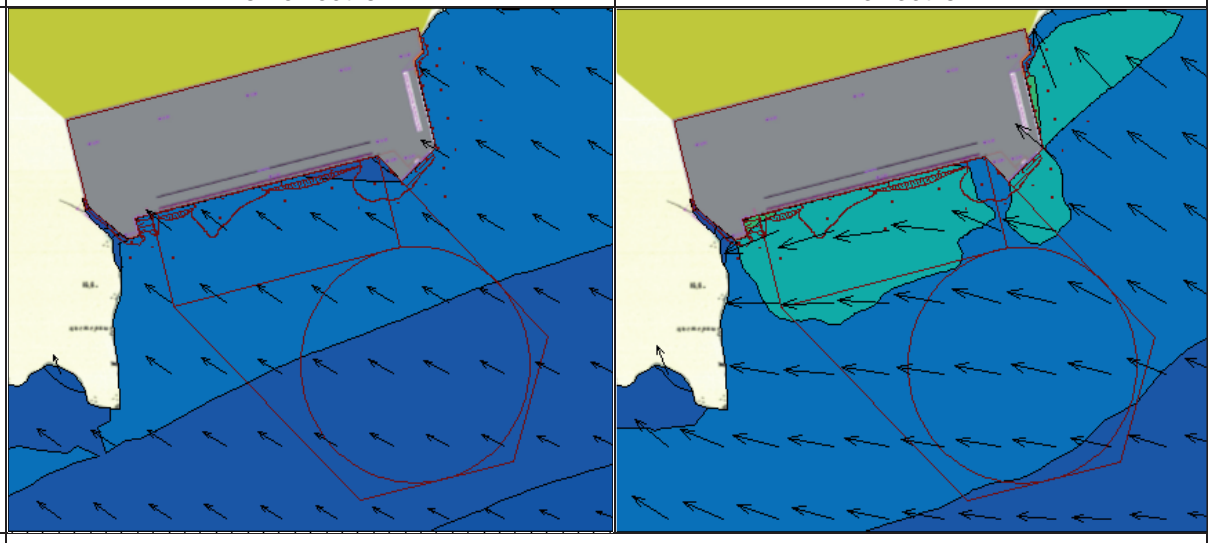

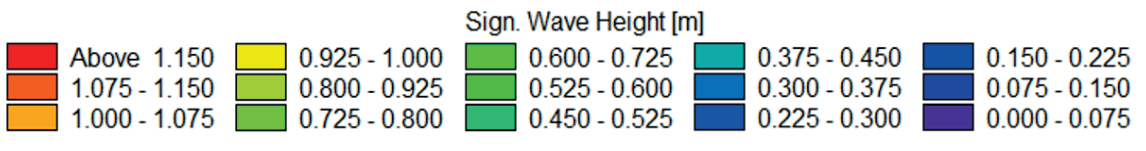

Continuation of table 3

	Wave parameters	p.5	p.6	p.22	p.7	p.8	p.40	p.23	p.24	p.10
		South-east direction of wave approach without reflection/ with reflection								
	$\bar{\lambda}$, *m*	5.40/5.80	5.40/5.50	5.50/5.60	5.30/5.30	5.00/5.10	4.50/4.80	5.40/5.40	5.30/5.20	4.40/4.80
	$\bar{T}$, s	1.90/1.90	1.90/1.90	1.90/1.90	1.80/1.80	1.80/1.80	1.70/1.70	1.90/1.90	1.80/1.80	1.70/1.80
	$\bar{h}$, *m*	0.21/0.29	0.21/0.27	0.21/0.27	0.21/0.26	0.19/0.25	0.17/0.25	0.21/0.27	0.21/0.26	0.15/0.20
	$h_{5\%}$, *m*	0.37/0.51	0.37/0.47	0.37/0.48	0.37/0.46	0.37/0.45	0.37/0.43	0.37/0.47	0.37/0.46	0.37/0.36

S	no reflection	reflection
Once a year	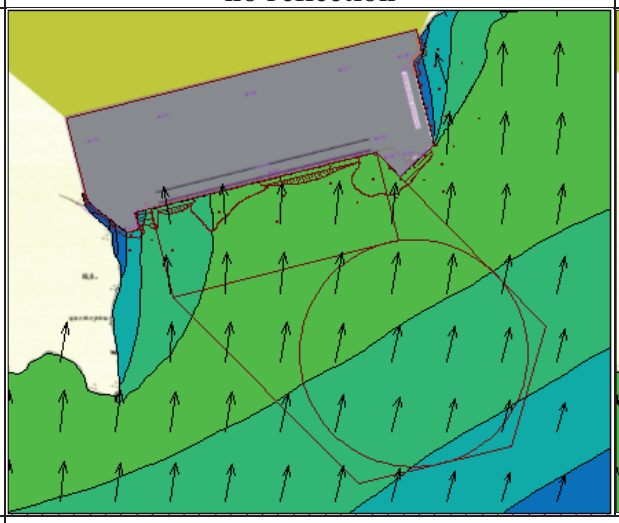	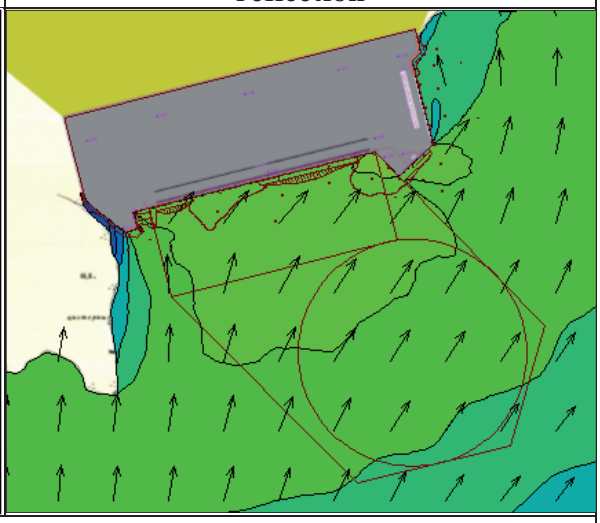

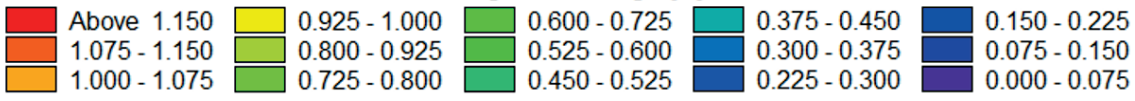

Wave parameters	p.5	p.6	p.22	p.7	p.8	p.40	p.23	p.24	p.10
	South direction of wave approach without reflection/ with reflection								
$\bar{\lambda}$, *m*	7.60/8.20	7.90/8.50	7.90/8.00	8.20/8.50	8.30/8.40	7.10/8.50	8.20/8.30	8.30/8.50	8.40/9.10
$\bar{T}$, s	2.20/2.30	2.20/2.30	2.20/2.30	2.30/2.30	2.30/2.30	2.10/2.30	2.30/2.30	2.30/2.30	2.30/2.40
$\bar{h}$, *m*	0.33/0.44	0.35/0.46	0.35/0.42	0.37/0.46	0.37/0.46	0.37/0.48	0.37/0.44	0.37/0.46	0.37/0.51
$h_{5\%}$, *m*	0.58/0.78	0.58/0.80	0.58/0.74	0.58/0.80	0.58/0.81	0.58/0.84	0.58/0.78	0.58/0.81	0.58/0.90

The largest discrepancy between the wave parameters calculated with reflection and without reflection is obtained for the NE direction, since in this direction the wave front is almost normal to the cordon line and the ship's side, while the port fleet pier is in the wave shadow for both scenarios, as is pier no. 2. And for waves in the N direction, the results with and without reflection are the same practically. For points located at a vessel's width from the berth, for berth no. 1 from the NE to the S direction, the differences in the heights of reflected waves of different strengths from waves without reflection decrease. For berth no. 2 from the NE to the S, the difference in the heights of reflected waves of different strengths from waves without reflection increases.

Thus, wave reflection plays an important role in the resulting wave heights, taking into account the configuration of port facilities relative to the direction of the waves. In turn, this can significantly affect the conclusions about the safe conditions for servicing ships in the port.

When wind waves interact with hydraulic structures, they undergo transformation – mainly

diffraction and reflection of waves, often multiple times. At the same time, underwater channels and natural bottom irregularities [10-11], as well as floating objects, which, in turn, act as sources of secondary waves due to their own oscillations [12], can also influence wind waves.

the wave climate in the port water area is formed by the interference of approaching, reflected and secondary generated waves.

The layout of sea ports assumes maximum protection of the inner water area from the impact of large wind waves. However, during a storm, the water area of any port may experience weakened but noticeable waves [13]. In this case, taking into account the reflection of waves from the port's hydraulic structures plays an important role in shaping the wave climate in the port water area. If the degree of reflection is underestimated, the wave load on the structures will be underestimated, and the danger of wave impact on ships sheltering in the port water area during a storm will be underestimated. In addition, incorrect consideration of wave reflection will also affect the unpredictable development of lithodynamic processes in the water area. Washout at berth and protective structures can lead to a loss of local stability of structures, as well as to excessive accumulation of sediments and the accompanying need for extraordinary dredging operations in the shipping waters of the port. If the degree of wave reflection from structures is unreasonably overestimated, there will be an overspending of funds and materials. In any case, incorrect consideration of wave reflection can have negative consequences for both the port's economy and its operational functionality.

METHODS

The reflectivity of hydraulic structures is usually characterized by the reflection coefficient, which is the ratio of the height of the reflected wave to the height of the approaching wave, that is:

$$k_{ref} = \frac{h_{ref}}{h} \quad (1)$$

The reflection coefficient depends on both the type and roughness of the reflecting surface and the parameters of the approaching waves, as well as on the angle between the front of the incoming waves and the axis of the reflecting surface. Determining the exact values of the reflection coefficient for a specific hydraulic structure design for different approach angles and wave parameters can only be done through physical experiments. Therefore, in engineering practice, they resort to a set of empirically obtained reflection coefficients collected in the scientific literature [14-16] and shown here in the figure below.

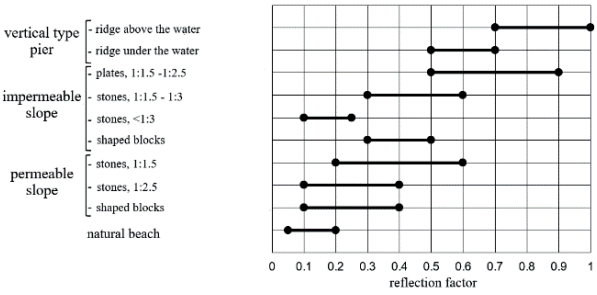

Figure 2. Approximate wave reflection factor of various structures

The choice of reflection coefficient values in the given ranges depends on the steepness of the suitable waves - the longer the waves, the greater the reflection coefficient. The upper limit of the ranges roughly corresponds to long-period swell waves.

In this case, if when calculating the parameters of wind waves in the port water area, the degree of wave reflection from berths with a vertical wall is intuitively clear and with sufficient accuracy and engineering reserve is specified by a reflection coefficient of 0.8-0.9. Then when considering alternative options for the design of a berth wall (for example, with a berth slope), as well as when it is necessary to take into account reflection from slope coastal protection structures, the assignment of a wave reflection coefficient becomes a non-trivial task.

Empirical formulas are known for obtaining the reflection coefficient for some designs of slope structures. They are based on the connection with

a critical parameter similar to the wave breaking parameter, which was obtained in [17-18] for a regular monochrome wave and the expression for which is written as follows:

$$\xi = \frac{\tan\alpha}{\sqrt{2\pi h/gT^2}}, \quad (2)$$

where h– wave height; T – wave period; α– slope angle.

The dependence of the reflection coefficient on the critical collapse parameter for a smooth slope (for example, reinforced with slabs), obtained in work [18], is written as follows:

$$k_{ref} = 0.1\xi^2 \quad (3)$$

It was later shown that this expression is valid only for small values of the critical parameter ξ.Therefore, it was further refined in the work [19] for large values of the critical parameter to the following form:

$$k_{ref} = \tanh(0.1\xi^2) \quad (4)$$

and also, in the approximation of irregular waves, with the breaking parameter determined by the significant wave height and the average period over the spectrum:

$$k_{ref} = \frac{a_1 \cdot \xi_m^2}{\xi_m^2 + b_1} \quad (5)$$

The authors of the work [19] first proposed to use the same expression to calculate the reflection coefficient not only for smooth slopes, but also for those with significant porosity. For this purpose, the following values of calibration coefficients were proposed:

Table 4. Values of calibration coefficients for slopes with significant porosity to formula (5)

Slope structure	a_1	b_1
Permeable, stones or shaped blocks	0.75	15
Impermeable, stone or shaped blocks	0.80	10
Plate slope	1.00	4.54

Later, based on newly obtained extensive experimental data on reflection coefficients, it was shown in [20] that this dependence with the proposed coefficients allows obtaining reliable results only for smooth slopes. In the same work, the authors proposed a new formula for smooth and porous slopes with a steepness from 1:1.5 to 1:4.0:

$$k_{ref} = \tanh(A \cdot \xi_m^B), \quad (6)$$

Where A and B are calibration coefficients that take the following values:

Table 5. Values of calibration coefficients for slopes with significant porosity to formula (6)

Slope structures	A	B
Permeable, stones	0.12	0.87
Permeable, shaped blocks (tetrapods, cubes)	0.10	0.87
Impermeable, stones or shaped blocks	0.14	0.90
Plate	0.16	1.43

Then this method of determining reflection coefficients was developed in terms of reflection from smooth slopes of mixed waves (mainly bimodal – wind waves together with swell waves) [21], in terms of using the capabilities of neural networks [22-23], and also received additional confirmation from natural data [24].

As can be seen from the figure below, the use of expression (4) allows us to approximate expression (3) in the region of small values of the critical parameter $\xi<2$, and in the region $\xi>2$ - to get the reflection coefficients that asymptotically tend to 1.0, i.e., total reflection. The graph shows the boundary solutions of expressions (5) and (6) - for a smooth impermeable slope and for a permeable porous slope. This allows us to estimate the minimum and maximum reflection coefficients from slope structures that can be obtained.

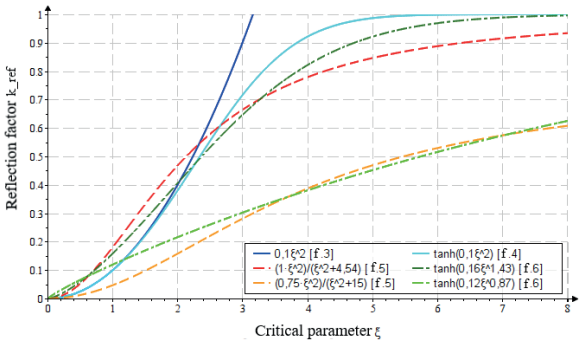

Figure 3. Dependence of the reflection coefficient on the critical parameter, obtained using expressions (3 – 6) for smooth and porous slopes

In domestic engineering practice, the method given in SP 38.13330 is used to determine the reflection coefficients of waves from slope structures. The expression for the reflection coefficient according to this method can be written as follows:

$$k_{ref} = k_r k_p k_{ref,i} \sqrt{\cos\theta_r \, e^{-0{,}08r/\lambda}}, \quad (7)$$

where k_r and k_p – coefficients of slope roughness and permeability, taking the following values:

Table 6. Values of the coefficient of slope roughness and permeability (SP 38.13330.2018 Table D.1)

Slope structure	Relative roughness, r/h (where *r* is the average size of the material fixing)	k_r	k_p
Concrete (reinforced concrete) plate	-	1	0.9
Gravel-pebble or stone covering, concrete (reinforced concrete) blocks	Less than 0.002	1	0.9
	0.005-0.01	0.95	0.85
	0.02	0.9	0.8
	0.05	0.8	0.7
	0,1	0.75	0.6
	More than 0.2	0.7	0.5

$k_{ref,i}$ – the coefficient depending on the flatness of the wave and the slope is taken from the following table:

Table 7. Values of the coefficient depending on the wave flatness and slope laying (SP 38.13330.2018 Table A.4)

Wave flatness, λ/h	Values $k_{ref,i}$ at slopes of the reflective surface *i*		
	1	0.5	0.25
10	0.5	0.02	0,0
15	0.8	0.15	0,0
20	1	0.5	0,0
30	1	0.7	0.05
40	1	0.9	0.18

The analysis of the coefficients proposed by the normative methodology shows that the reflection coefficient is a function of the steepness or flatness of the waves, the slope and the angle between the wave front and the axis of the reflecting structure. If we assume that the waves approach the structure normally, and the wavelength, according to the linear wave theory, is expressed through the period of the waves according to the dispersion relation (without taking into account the water depth):

$$\lambda = \frac{gT^2}{2\pi} \quad (8)$$

then it becomes possible to analytically link the value of the normative reflection coefficients and the critical parameter ξ.

For example, the figure below shows a comparison of the reflection coefficients that can be obtained using expressions (5) and (6), as well as using the normative methodology. As above, the boundary conditions of reflection from the slope are considered: from an impermeable smooth slope and from a permeable extremely porous slope. It should be noted that taking into account the characteristic size of the slope fastening material, r, gives the normative reflection coefficients in the region between the absolutely smooth and extremely porous slope.

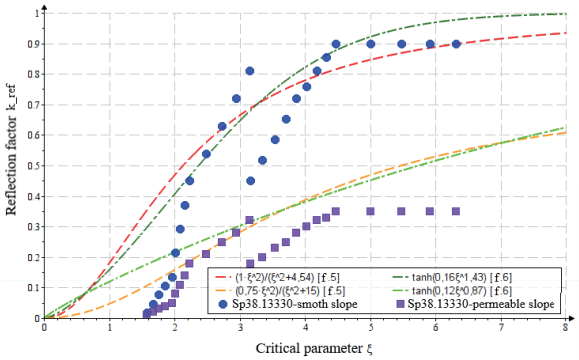

Figure 4. Comparison of reflection coefficients obtained using expressions (5) and (6) and using the normative methodology

According to the obtained results, there is a connection between the reflection coefficients and the critical parameter. A jump in the value of the normative reflection coefficients is noted in the interval $2 < \xi < 3.152$. In this case, the reflection coefficients in the interval $2 < \xi < 2.23$ are characterized by a sharp increase in the growth rate, while the reflection coefficients in the interval $2.23 < \xi < 3.15$ increase with moderate intensity. Note that a jump in the reflection coefficients is observed on both smooth and porous slopes.

RESULTS AND DISCUSSION

An analysis of the behavior of the standard reflection coefficients made it possible to determine that the abrupt nature of the behavior is manifested in the coefficient, which depends on the gentleness of the wave and the slope and is determined according to the table:

Table 8. Values of the reflection coefficient depending on the wave flatness and slope embedment

Wave flatness, λ/h	Values $k_{ref,i}$ at slopes of the reflective surface i		
	1	0.5	0.25
10	0.5	0.02	0,0
15	0.8	0.15	0,0
20	1	0.5	0,0
30	1	0.7	0.05
40	1	0.9	0.18

In this case, the area where the reflection coefficients jump is highlighted in color in Table 8. Bringing the normative coefficients to smooth growth relative to the critical parameter seems to be an important task today, since it allows us to obtain a more reasonable result. The assumption about the smoothness of their behavior relative to the critical parameter is associated with the functions of the dependence of the reflection coefficients on the critical parameter, obtained in the literature cited above and confirmed by extensive experimental data. In this regard, in this paper we propose to consider the updated wave reflection coefficients in the part of Table 8 highlighted by the color scheme. The updated parameters of the reflection coefficient, depending on the wave flatness and slope laying, are given in Table 9.

Table 9. Updated values of the reflection coefficient depending on the wave flatness and slope embedment

Wave flatness, λ/h	Values $k_{ref,i}$ at slopes of the reflective surface i		
	1	0.5	0.25
10	0.5	0.02	0,0
15	0.8	0.15	0,0
20	1	0.25	0,0
30	1	0.40	0.05
40	1	0.55	0.18

The position of the reflection coefficient values in relative dependence on the critical parameter is shown in Figure 5.

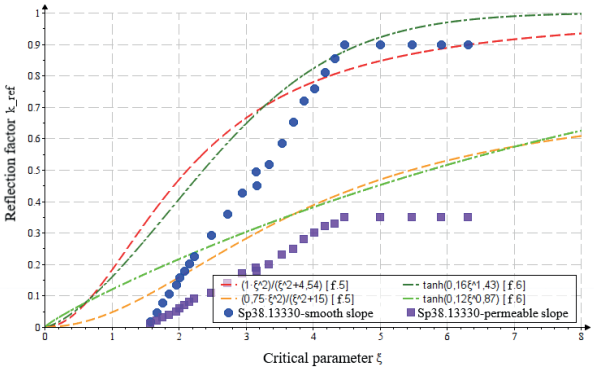

Figure 5. Comparison of reflection coefficients obtained using expressions (5) and (6) and using the normative methodology with adjusted coefficient values $k_{ref,i}$

The obtained distribution of reflection coefficients depending on the critical parameter is more consistent with modern ideas about the interaction of waves with slope hydraulic structures, which is confirmed by the comparison given above.

When analyzing the reflection of wind waves from a structure, it is also necessary to take into account the irregularity of wind waves. Thus, with total reflection, the height of a monochrome wave doubles at all nodes of the standing wave formed. Thus, the height of the waves at a distance from the reflecting structure will be 2h. At the same time, the significant wave height that characterizes irregular waves doubles only at the reflective surface, and in the water area in front of the structure (at a distance greater than one wavelength) it increases by 1.4 times.

This is important to take into account, for example, when calculating the wave protection of berths located opposite wave-reflecting structures.

CONCLUSION

It is shown that taking into account the reflection of waves from the berth under consideration can lead to a significant change in the conclusion about the safety of the conditions for mooring vessels at the berth. This applies both to the methods for determining the conditions of mooring according to normative documents and to the numerical modeling of waves at the berth.

The reflection coefficient from the surfaces of hydraulic structures depends on the steepness or flatness of the approaching waves, the slope, the roughness and permeability of the reflecting structure, and the angle between the wave front and the axis of the reflecting structure. Analysis of the normative methodology SP 38.13330 for determining the reflection coefficient, performed as a function of the reflection coefficient on the critical parameter ξ, showed a jump in values at a certain value of the critical parameter. A method is proposed to eliminate this problem and obtain corrected values of the reflection coefficients.

ACKNOWLEDGEMENTS

The research was founded by the National Research Moscow State University of Civil Engineering (grant for fundamental and applied scientific research, project No. 38-234/130).

REFERENCES

1. **A.S. Afremov, A.N. Kulikova, N.A. Smolina** (2011) *Obespechenie bezopasnosti stoyanki prishvartovannogo krupnotonnazhnogo sudna v usloviyax vetra i volneniya* [Ensuring the safety of moored large-tonnage vessel parking in conditions of wind and waves], Tr. Central Research Institute named after academician A. N. Krylov, No. 59, pp. 109-122.
2. **Holthuijsen L.H.** (2007) Waves in oceanic and coastal waters, Cambridge University Press. Cambridge
3. **Booij N, Haagsma IJ, Holthuijsen L, Kieftenburg A, Ris R,** van der Westhuysen A, Zijlema MSWAN Cycle III version 40.51. User manual. The Netherlands 4.
4. **H. Gerritsen, J. Sutherland, R. Deigaard, M. Sumer, C.J.E. Fortes, J.P. Sierra, U. Schmidtke** (2011) Composite modeling of interactions between beaches and structures. *Journal of Hydraulic Research*. no.2, pp.49 https://doi.org/10.1080/00221686.2011.589134
5. **H. Gerritsen, J. Sutherland, J. A Santos, S. Caires** (2011) Composite modeling, CRC Press, Users Guide to Physical Modeling and Experimentation: *Experience of the HYDRALAB*
6. **Kantarzhi I.G., Anshakov A.S.** (2021) Interactive numerical model of hydrometeorologic factors in Kola Bay, *E3S Web of Conferences 263*, 03016, https://doi.org/10.1051/e3sconf/2021263016

7. **Anshakov A.S., Kantarzhi I.G.** (2021) *Verifikaciya chislennogo gidrodinamicheskoj modeli Kol`skogo zaliva* [Verification of the numerical hydrodynamic model of the Kola bay] Vestnik MGSU [Monthly Journal on Construction and Architecture]; 16(4):473-485. doi: 10.22227/1997-0935.2021.4.473-485 (rus.).
8. **Kantarzhi I.G., Kuznetsov K.I.** (2014) *Naturny`e izmereniya volneniya pri opredelenii nagruzok na morskie gidrotexnicheskie sooruzheniya* [In-kind measurements of waves when determining loads on marine hydraulic structures] Engineering and construction journal. No. 4(48). P. 49–62.
9. **Kantarzhi I.G.** (2014) *Fizicheskoe i chislennoe modelirovanie voln u portovy`x gidrotexnicheskix sooruzhenij. Beregovaya zona – vzglyad v budushhee* [Physical and numerical modeling of waves near port hydraulic structures. Coastal zone – a look into the future] Proceedings of the XXV international coastal conference. Sochi: GEOS Publishing House, Vol. 2. pp. 128–131.
10. **Gritsuk I.I., Debolskiy V.K., Ponomarev N.K.** (2011) *Issledovanie gidravlicheskoj krupnosti chasticz graviya, prednaznachennogo dlya sozdaniya iskusstvennogo osnovaniya podvodny`x truboprovodov* [The investigation of gravel particles settling velocity to build up artificial submarine pipeline foundations], Privolzhsky Scientific Journal, No. 1, pp. 41-45.
11. **Kantarzhi I.G., Anshakov A.S.** (2018) *Vliyanie podkhodnogo kanala na volnovoy rezhim v akvatorii porta* [Influence of the approach navigation channel on wave regime in waterbody of port's area]. Stroitel'stvo: nauka i obrazovanie [Construction: Science and Education]. vol. 8, issue 1 (27), pp. 8. Available at: http://nso-journal.ru.
12. **Kantarzhi I.G., Gogin A.G.** (2020) *Modelirovanie vozdejstviya vetrovy`x voln na prichal s oshvartovanny`m sudnom* [Modeling of thw berth with a moored ship under wind waves loads] Hydrotechnical construction. No. 1. pp. 50-56.; doi:http://dx.doi.org/10.34831/EP.2020.1.53901
13. **Kantarzhi I.G., Mordvintsev K.P., Gogin A.G.** (2019) *Chislennoe issledovanie zashhishhennosti akvatorii porta* [Numerical study of wave penetration in port waters] Hydrotechnical construction, No. 5. pp. 45-52.
14. **Thompson E.F., Chen H.S., Hadley L.L.** (1996) Validation of numerical model for wind waves and swell in harbors, *Journal of Waterway, Port, Coastal, and Ocean Engineering.* vol. 122. No. 5. pp. 245-257.
15. **Goda Y.** (2010) Random seas and design of maritime structures. – World Scientific Publishing Company, vol. 33.
16. **Pratola L. et al.** (2021) Investigation on the reflection coefficient for seawalls protected by a rubble mound structure //*Journal of Marine science and Engineering.* vol. 9. No. 9. pp. 937.
17. **Irribarren C.R., Nogales C.** Protection des ports (1949)//*XVII, International Navigation Congress, Section II, Comm*. vol. 4. pp. 27-47.
18. **Battjes J.A.** (1974) Surf similarity //*Coastal Engineering 1974*. pp. 466-480.
19. **Seelig WN et al.** (1981) Estimation of wave reflection and energy dissipation coefficients for beaches, revetments, and breakwaters.
20. **Zanuttigh B., van der Meer J.W.** (2008) Wave reflection from coastal structures in design conditions, *Coastal engineering*. vol. 55. No. 10. pp. 771-779.
21. **Orimoloye S., Karunarathna H., Reeve D.E.** (2020) Reflection analysis of impermeable slopes under bimodal sea conditions //*Journal of Marine Science and Engineering*. vol. 8. No. 2. pp. 133.
22. **Formentin S.M., Zanuttigh B., van der Meer J.W.** (2017) A neural network tool for predicting wave reflection, overtopping and transmission // *Coastal Engineering*

Journal. vol. 59. No. 1. pp. 1750006-1-1750006-31.
23. **Díaz-Carrasco P. et al.** (2023) Simple and explicit neural network-derived formula to estimate wave reflection on mound breakwaters, *Coastal Engineering*. vol. 186. pp. 104404.
24. **Mahmoudof S.M., Eyhavand-Koohzadi A., Bagheri M.** (2021) Field study of wave reflection from permeable rubble mound breakwater of Chabahar Port, *Applied Ocean Research*. vol. 114. pp. 102786.

СПИСОК ЛИТЕРАТУРЫ

1. **А.Ш. Афремов, А.Н. Куликова, Н.А. Смолина,** Обеспечение безопасности стоянки пришвартованного крупнотоннажного судна в условиях ветра и волнения // Тр. ЦНИИ им. акад. А. Н. Крылова, 2011, № 59. 109-122 с.
2. **Holthuijsen L.H**. Waves in oceanic and coastal waters.2007, Cambridge University Press. Cambrige
3. **Booij N, Haagsma IJ, Holthuijsen L, Kieftenburg A, Ris R,** van der Westhuysen A, Zijlema M SWAN Cycle III version 40.51. User manual. The Netherlands 4.
4. **H. Gerritsen, J. Sutherland, R. Deigaard, M. Sumer, C.J.E.M. Fortes, J.P. Sierra, U. Schmidtke,** Composite modelling of interactions between beaches and structures. Journal of Hydraulic Research. 2011, no.2, 49 pages. https://doi.org/10.1080/00221686.2011.589134
5. **H. Gerritsen, J. Sutherland, J.A Santos, S. Caires,** Composite modelling, (CRC Press, Users Guide to Physical Modelling and Experimentation: Experience of the HYDRALAB, 2011)
6. **I. Kantarzhi and A. Anshakov,** Interactive numerical model of hydrometeorologic factors in Kola Bay, 2021, E3S Web of Conferences 263, 03016 https://doi.org/10.1051/e3sconf/2021263016
7. **Аншаков А.С., Кантаржи И.Г.** Верификация численного гидродинамической модели Кольского залива, Вестник МГСУ, 2021; no.16(4), pp.473-485. DOI: 10.22227/1997-0935.2021.4.473-485 с.
8. **Кантаржи И.Г., Кузнецов К.И.** Натурные измерения волнения при определении нагрузок на морские гидротехнические сооружения // Инженерно-строительный журнал. 2014, № 4(48). 49–62 с.
9. **Кантаржи И.Г**. Физическое и численное моделирование волн у портовых гидротехнических сооружений. Береговая зона – взгляд в будущее // Материалы XXV международной береговой конференции. Сочи: Изд-во ГЕОС, 2014. Т. 2. 128–131 с.
10. **Грицук И.И., Дебольский В.К., Пономарев Н.К.** Исследование гидравлической крупности частиц гравия, предназначенного для создания искусственного основания подводных трубопроводов //Приволжский научный журнал. – 2011, №. 1. 41-45 с.
11. **Кантаржи И.Г., Аншаков А.С.** Влияние подходного канала на волновой режим в акватории порта //Строительство: наука и образование. – 2018, №. 1, 8 с.
12. **Кантаржи И.Г., Гогин А.Г.** Моделирование воздействия ветровых волн на причал с ошвартованным судном //Гидротехническое строительство, 2020, №. 1, 50-56 с., DOI:http://dx.doi.org/10.34831/EP.2020.1.53901
13. **Кантаржи И.Г., Мордвинцев К.П., Гогин А.Г.** Численное исследование защищенности акватории порта //Гидротехническое строительство, 2019, №. 5, 45-52 с.
14. **Thompson E.F., Chen H.S., Hadley L.L.** (1996) Validation of numerical model for wind waves and swell in harbors // *Journal of Waterway, Port, Coastal, and Ocean Engineering.* vol. 122. No. 5. pp. 245-257.
15. **Goda Y.** (2010) Random seas and design of maritime structures. – World Scientific Publishing Company, vol. 33.

16. **Pratola L. et al.** (2021) Investigation on the reflection coefficient for seawalls protected by a rubble mound structure //*Journal of Marine science and Engineering.* vol. 9. No. 9. pp. 937.
17. **Irribarren CR, Nogales C.** Protection des ports (1949)//*XVII, International Navigation Congress, Section II, Comm*. vol. 4. pp. 27-47.
18. **Battjes JA** (1974) Surf similarity //*Coastal Engineering 1974*. pp. 466-480.
19. **Seelig WN et al.** (1981) Estimation of wave reflection and energy dissipation coefficients for beaches, revetments, and breakwaters.
20. **Zanuttigh B., van der Meer J.W.** (2008) Wave reflection from coastal structures in design conditions, *Coastal engineering*. vol. 55. No. 10. pp. 771-779.
21. **Orimoloye S., Karunarathna H., Reeve D.E**. (2020) Reflection analysis of impermeable slopes under bimodal sea conditions //*Journal of Marine Science and Engineering*. vol. 8. No. 2. pp. 133.
22. **Formentin SM, Zanuttigh B.,** van der Meer J.W. (2017) A neural network tool for predicting wave reflection, overtopping and transmission // *Coastal Engineering Journal*. vol. 59. No. 1. pp. 1750006-1-1750006-31.
23. **Díaz-Carrasco P. et al**. (2023) Simple and explicit neural network-derived formula to estimate wave reflection on mound breakwaters, *Coastal Engineering*. vol. 186. pp. 104404.
24. **Mahmoudof S.M., Eyhavand-Koohzadi A., Bagheri M.** (2021) Field study of wave reflection from permeable rubble mound breakwater of Chabahar Port, *Applied Ocean Research*. vol. 114. pp. 102786.

Izmail G. Kantrazhi – Dr. Sc., Professor, Professor of the Department of Hydraulics and Hydraulic Engineering, Department of Hydraulics and Hydraulic Engineering, Moscow State University of Civil Engineering (National Research University) (MSUCE), 12933, 26, Yaroslavskoe Shosse, Moscow, Russian Federation, kantardgi@yandex.ru.

Alexander G. Gogin - Ph.D., leading specialist, KIS Istok JSC, 115230, 46, Varshavskoe sh., Moscow, Russian Federation, alex.gogin@bk.ru.

Zhanna I. Nagornova – postgraduate student of the Department of Hydraulics and Hydraulic Engineering, Department of Hydraulics and Hydraulic Engineering, Moscow State University of Civil Engineering (National Research University) (MSUCE), 12933, 26, Yaroslavskoe Shosse, Moscow, Russian Federation, nagornova_zhanna10@mail.ru.

Измаил Григорьевич Кантаржи — доктор технических наук, профессор, профессор кафедры ГиГС, кафедра Гидравлики и гидротехнического строительства, Федеральное государственное бюджетное образовательное учреждение высшего образования «Национальный исследовательский Московский государственный строительный университет» (НИУ МГСУ), дом 26, Ярославское шоссе, город Москва, 129337, Российская Федерация, kantardgi@yandex.ru.

Александр Григорьевич Гогин – кандидат технических наук, ведущий специалист, АО «КИС Исток», 115230 дом 46, Варшавское шоссе, Москва, Российская Федерация, alex.gogin@bk.ru.

Жанна Ивановна Нагорнова — аспирант кафедры ГиГС, кафедра Гидравлики и гидротехнического строительства, Федеральное государственное бюджетное образовательное учреждение высшего образования «Национальный исследовательский Московский государственный строительный университет» (НИУ МГСУ), дом 26, Ярославское шоссе, город Москва, 129337, Российская Федерация, nagornova_zhanna10@mail.ru.

International Journal for Computational Civil and Structural Engineering, 21(1) 28–38 (2025)

DOI:10.22337/2587-9618-2025-21-1-28-38

THE CONCEPT OF REPRESENTATION OF GEOMETRIC SOLIDS IN BUILDING INFORMATION MODELING

Evgeniy V. Konopatskiy, Maxim V. Bezsolnov

Nizhny Novgorod State University of Architecture and Civil Engineering, Nizhny Novgorod, RUSSIA

Abstract. The problem of using the boundary model of geometric solids representation in BIM is formulated. A new concept of solid geometric modeling is presented, which allows to define geometric solids as a selected part of space, according to which geometric solids are represented by an organized set of points by analogy with other geometric objects. The mathematical apparatus “Point Calculus” is used for analytical description of geometric solids. Examples of modeling geometric solids in point calculus are given. The advantages of this approach are the possibility of representation of geometric information in BIM in compact vector form and realization of parallel calculations at the level of mathematical apparatus. The prospect of further research is the use of the proposed concept for the representation of various elements of building structures with the subsequent optimization of the representation of geometric objects in the IFC format. This will significantly reduce the volume required for the transfer of geometric information between the systems of information modeling and computer-aided design, increase their performance and radically solve the problem of interoperability of existing BIM software packages.

Keywords: BIM, geometric modeling, solid modeling, parametric modeling, parallel computing, BREP, IFC

КОНЦЕПЦИЯ ПРЕДСТАВЛЕНИЯ ГЕОМЕТРИЧЕСКИХ ТЕЛ В ТИМ

Е.В. Конопацкий, М.В. Безсольнов

Нижегородский государственный архитектурно-строительный университет, Нижний Новгород, РОССИЯ

Аннотация. Сформулирована проблема использования граничной модели представления геометрических тел в ТИМ. Представлена новая концепция твердотельного геометрического моделирования, которая позволяет определять геометрические тела в виде выделенной части пространства, в соответствии с которой геометрические тела по аналогии с другими геометрическими объектами представляются организованным множеством точек. Для аналитического описания геометрических тел используется математический аппарат «Точечное исчисление». Приведены примеры моделирования геометрических тел в точечном исчислении. Преимуществами такого подхода является возможность представления геометрической информации в ТИМ в компактной векторной форме и реализация параллельных вычислений на уровне математического аппарата. Перспективой дальнейших исследований является использование предложенной концепции для представления различных элементов строительных конструкций с последующей оптимизацией представления геометрических объектов в формате IFC. Это позволит в значительной мере сократить объём необходимый для передачи геометрической информации между системами информационного моделирования и автоматизированного проектирования, повысить их быстродействие и радикально решить проблему интероперабельности существующих ТИМ в строительной отрасли.

Ключевые слова: ТИМ, геометрическое моделирование, твердотельное моделирование, параметрическое моделирование, параллельные вычисления, BREP, IFC

INTRODUCTION

Modern society is rapidly entering the information age. One of the areas of active implementation of information systems is the construction industry. Being conservative by nature, the construction industry imposes special requirements to software products for information modeling of buildings and structures. Such models contain a huge number

of components, so in the process of working with them there is a need to operate huge amounts of information in real time. This necessity arises not only at the stage of creating a model of the object in the form of a full-fledged digital twin of capital construction objects, but also for its support at all stages of the life cycle. Existing domestic and foreign BIM are well suited for solving engineering problems with a limited number of construction objects and at this stage cannot provide the necessary performance to create a full-fledged digital twin at the level of neighborhood, district, city or region.

Another disadvantage is the lack of a single integrated software for construction and architecture, combining the capabilities of BIM and CAE. This leads to the need to import information models of capital construction objects into calculation complexes and is the source of the next problem associated with insufficient interoperability of domestic and foreign BIM and CAE. In addition, there are certain problems with the continuity of information models for different versions of the same software product, which significantly complicates digital support of construction objects at all stages of the life cycle, which, unlike software product versions, is counted in decades.

Many of the above-mentioned problems are related to the limited possibilities of representation of geometric information about the shape and position of objects in three-dimensional space or, in other words, the geometric core of BIM. At the moment there are several types of representation of geometric models, which include point, wireframe, boundary, structural and voxel models. The use of point and wireframe models is fraught with significant drawbacks. For example, the computational burden is high. Since the representation of even one geometric solid in the form of a point cloud can load a rather powerful computer. It is simply impossible to operate a set of them in real time. Therefore, the most widely used in BIM is the boundary model [1], which in foreign literature sources is represented by the abbreviation BREP (Boundary REPresentation) or B-rep [2-4]. If we use the CSG structural model, the result is still the representation of a geometric solid in the form of a closed shell [5-7].

Note that it is geometrically incorrect to call a closed shell a full-fledged solid model. This is just such a common convention, which is nevertheless widely used, including the popular data representation format IFC [8], which since 2019 is included in the National Standard of the Russian Federation [9]. All the more so that in computer-aided engineering (CAE) systems realized on the basis of the finite element method [10-12], it is often the volumetric finite elements that are used.

Ideologically the closest to the description of real geometric solids is the voxel model [13-15]. It provides representation of objects as a three-dimensional array of volumetric (cubic) elements. In essence, the voxel geometric model is a generalization of the pixel (raster) model for three-dimensional space and inherited all the disadvantages of raster models, which include:

– large amounts of information required to present voluminous data;
– significant memory overhead;
– a set of problems related to enlarging or reducing images.

In contrast to all of the above approaches, a fundamentally new concept of geometric solids definition was proposed in [16-18], which is devoid of the described disadvantages and can become an effective basis for the creation of high-performance BIM of the new generation.

1. METHODS

According to [19], a solid in geometric modeling is a connected set of points located on the inner side of one outer shell and several inner shells located inside the outer shell, together with the points of these shells. This definition is too complicated to understand and requires explanation of additional terms. But its meaning boils down to the fact that a solid is represented

as a closed shell. In English-language literature there is a different but similar in meaning definition of a solid in the form of a closed shell (B-Rep): “A solid is represented as a collection of connected surface elements, which define the boundary between interior and exterior points.”. The same approach is described in other works related to the representation of geometric solids in various information modeling and computer-aided design systems.

In contrast, in [16-18] a fundamentally new concept of defining geometric solids as a three-parameter set of points belonging to three-dimensional space was proposed, based on which the point equations of the set of prismatic, pyramidal, cylindrical, conical, spherical, elliptic and toroidal solids in the point calculus were derived.

What is the new concept based on? The simplest of geometric objects is a point. The point itself does not even have a size. It is a geometric analog of an infinitesimal value. However, using a set of points, it is possible to obtain geometric objects of any degree of complexity. As our organism consists of atoms, so any geometrical object of any space can be described by an organized set of points.

Let's consider examples and for this purpose first answer the question - what is the difference between a circle and a circle? In the first case it is a closed curve, in the second case it is an area inside a closed curve or, in other words, a selected part of the plane inside a circle. Generalizing to three-dimensional space, we get the definitions of sphere and ball. As in the plane case, the difference between these geometric objects is that a sphere is a closed shell, and a sphere is the set of all points of three-dimensional space bounded by a sphere, or, in other words, a selected part of three-dimensional space bounded by a sphere. As can be seen from the above examples, geometric solids and surfaces are completely different geometric objects that cannot be identified. Moreover, in [16-18] it is convincingly shown by examples that a surface is a two-parameter set of points, and a geometric solid in three-dimensional space is a three-parameter set. In both cases we are talking about variables or current parameters.

One of the possible realizations of the new concept is the use of multidimensional interpolation tools [20-22]. However, in the absence of the mathematical apparatus of point calculus, which allows any geometric object to be represented as an organized set of points, these works do not implement full-fledged solid models, but models based on parametric porous objects. Significantly better results are given by the geometric theory of multidimensional interpolation [23], already based on the use of the mathematical apparatus of “Point Calculus”, which is ideologically better suited for analytical representation of solid models of geometric solids.

There is an opinion that solid models cannot be described by an equation. If we consider only a set of equations in explicit form, this is indeed true. And this is due to the fact that one of the axes of the coordinate system is used as a function. Accordingly, the number of variables of an explicit equation is always one less than the dimensionality of the space in which the geometric object is defined. At the same time, the point calculus, which uses the apparatus of projection on the axes of the global coordinate system, allows to use all coordinate axes, the system of which defines the space of the required dimension. This makes it possible to obtain equations of geometrical solids by means of simple arithmetic operations on coordinates of points and functions from parameters. It is important that the number of parameters corresponds to the dimensionality of the space.

Let's consider an example. One of the most commonly used geometric objects in BIM is a parallelepiped. Parallelepiped is used to model walls, floors, roofs, window and door openings, etc. If you use the BREP boundary geometric model to specify the parallelepiped, then for its parameterization in general case it is necessary to define 6 planes. Each of these planes should be defined with the help of geometrical objects and conditions of their mutual position. In the general case there will be 54 such parameters: 3 points

for each of the 6 planes plus 3 coordinates to define each point. Of course, this is not the most optimal parameterization and the parameters can be less, but each of the parameters will have to be replaced by geometric conditions. And the programmatic implementation of each geometric condition is a computational burden on the CPU. When there are few modeled objects on the screen, this load actually remains unnoticeable. But when creating and supporting digital twins of capital construction objects with a large number of elements (for example, with a digital twin of a micro district or a city district) it will be at least uncomfortable to work with such a model. In order to provide more comfortable work, it is necessary to sacrifice the model detailing.

If we implement the proposed concept of solid modeling, in the most general case, only 12 parameters will be sufficient to unambiguously determine the shape and position of a parallelepiped. This was possible because the geometric conditions were described using simple point equations and represented in a compact vector form.

How was this realized in practice? First, a rather primitive geometrical scheme of the solid model of the parallelepiped was developed (Fig. 1).

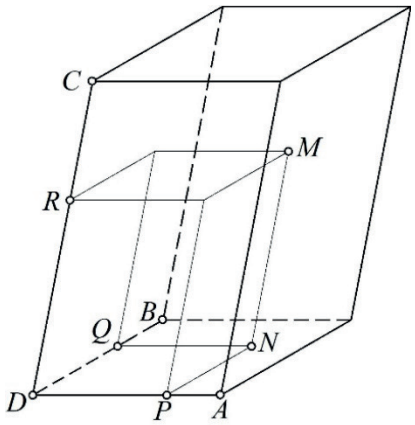

Figure 1. Geometric scheme for defining the solid model of a parallelepiped

To parameterize the solid model of the parallelepiped we will use simple relations of three points of lines DA, DB and DC on its sides (Fig. 1):

$$u = \frac{DP}{DA},\ v = \frac{DQ}{DB},\ w = \frac{DR}{DC}.$$

As a result, we have three point equations of straight lines:

$$P = (A - D)u + D,\ Q = (B - D)v + D,$$
$$R = (C - D)w + D.$$

To determine the current point M of the desired three-parameter set of points, we use the pointwise parallel transfer formula twice:

$$\begin{cases} N = P + Q - D \\ M = R + N - D \end{cases}$$
$$\Downarrow \qquad (1)$$
$$M = (A - D)u + (B - D)v + (C - D)w + D.$$

Equation (1) A, B, C, D – are contains the initial points, which not only form a local simplex of the three-dimensional space to determine the desired set of points, but also uniquely determine the position and dimensions of the parallelepiped in the global coordinate system. The parameters u, v, w in the proposed parameterization (Fig. 1) vary from 0 to 1, ensuring that the interior of the parallelepiped is filled with points.

Using the properties of the point calculus, we can represent equation (1) in another, more compact, form:

$$M = Au + Bv + Cw + D(1 - u - v - w).$$

These two forms of representation of geometric objects in the point calculus are completely identical and can always be derived one from the other. The choice of the form of representation of the point equation depends on the particular

problem and is determined solely by the convenience of use.

It should be noted that the points A, B, C, D, M in equation (1) are coordinate vectors. The number of coordinates depends on the dimensionality of space. Transitioning to the coordinate form for three-dimensional space, we obtain the following system of parametric equations:

$$\begin{cases} x_M = x_A u + x_B v + x_C w + x_D (1-u-v-w) \\ y_M = y_A u + y_B v + y_C w + y_D (1-u-v-w). \\ z_M = z_A u + z_B v + z_C w + z_D (1-u-v-w) \end{cases} \quad (2)$$

Thus, for unambiguous determination of all parameters of position and shape of the parallelepiped solid model in the global coordinate system, only 12 parameters were needed without exception.

Note that all equations of the system (2) are completely identical except for the coordinates of the points. If each of the equations of the system (2) is assigned a separate thread for computation, we will get the result 3 times faster. With this approach, the computational threads are completely balanced. They start and end at the same time, performing the same number of computational operations. This minimizes the downtime of a multi-core processor and optimizes its computational load.

Of course, this is not the only possible parameterization of the solid parallelepiped model. Besides, it should be noted that in equations (1) and (2) the parameters u, v, w change linearly. But the same parameters can also change nonlinearly. Then, by controlling the functions of the parameters, it is possible to construct a non-uniform distribution of points inside a geometric solid and thus model anisotropic geometric solids. Using this approach, it is possible to determine physical properties by means of geometrical solids with non-uniform distribution of points inside the geometrical solid.

The described solid parallelepiped model is a general case of representation of geometrical solids as a selected part of three-dimensional space. In other words, it is a generalization of the BREP boundary model, which can be obtained by fixing the boundary values of the parameters u, v, w:

$$u = 0 \Rightarrow BCD. \quad u = 1 \Rightarrow \alpha \in BCD.$$
$$v = 0 \Rightarrow ACD. \quad v = 1 \Rightarrow \beta \in ACD.$$
$$w = 0 \Rightarrow ABD. \quad w = 1 \Rightarrow \gamma \in ABD.$$

Similarly, we can obtain the frame geometric model by simultaneous fixation of two parameters, thus determining all 12 edges of the parallelepiped (Fig. 1). At simultaneous fixation of three parameters, we obtain all 8 nodal points of the parallelepiped, including initial points A, B, C, D. By changing the parameter values from 0 to 1, we can obtain a point geometric model in the form of a cloud of discrete points.

Note that the proposed concept is not limited to geometric solids of simple shape. The same concept can be used to model more complex geometric solids. For example, Figure 2 shows a visualization of a solid model of a channel surface, whose axis is a transcendental curve and whose constituent is a closed curve of the "sinusoid" type, whose axis is a circle.

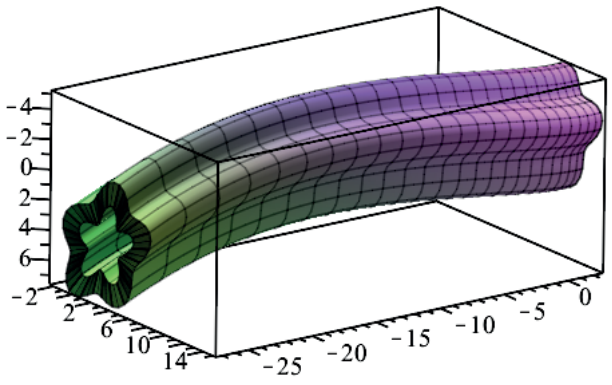

Figure 2. Visualization of the solid model of the channel surface

2. RESULTS AND DISCUSSION

Comparing the proposed solid modeling concept with existing approaches and methods, we highlight several aspects.

1. A distinctive feature of the proposed concept compared to existing methods is the representation of solid models in the form of an organized set of points, where the dimensionality of the space coincides with the number of current parameters.

2. Voxel geometric models are close in their ideology to full-fledged solid modeling. The proposed concept of modeling geometric solids as an organized set of points can be defined as a vector representation of voxel models. After all, if the size of a voxel is set to infinitesimal, it becomes a point, and we ideologically come to the description of geometric objects as an organized set of points, but at the same time we get rid of the above-described disadvantages of the voxel model. Thus, we will get a vector geometric model of solid, which is more preferable in BIM compared to the raster model because it provides a more convenient and compact approach to the use and storage of geometric information.

3. Another ideologically similar approach is the use of finite element methods, finite volumes, boundary elements, etc. In engineering mechanics, it is called analytical solid modeling [24]. It is more related to engineering calculations than to information modeling in construction. If the size of a volumetric element tends to an infinitesimal value (to a point), we will obtain a point solid model, which is close in its meaning to the proposed one, but the computational complexity of the finite element method will tend to infinity and remain unattainable for modern computing systems. At the same time, these same models are described by simple vector equations in point calculus and can be effectively used to calculate the stress-strain state of elements of building structures, buildings and structures. In addition, the proposed concept opens new possibilities for modeling thermal, sound, light, electric, magnetic and other fields.

4. In [25], equations in homogeneous coordinates similar to the system of equations (2) are given. It is noted that they describe the mapping of a linear tetrahedron. As an argument, a verification of the equation using the nodal points of the tetrahedron is given. In Figure 1, these are the points A, B, C, D. Note that if a nodal mesh is created to solve the problem and only the nodes of this mesh will be used in the calculation, then this statement is valid and gives the desired result. But if the parameters are variable, then we will get exactly the solid model of a parallelepiped. It is easy to check this if we substitute the values of the parameters $u=1,\ v=1,\ w=1$ for the system of equations (2). Then the obtained point will be outside the tetrahedron $ABCD$ and will form one of the vertices of the parallelepiped built on its basis.

5. As can be seen from equations (1) and (2) solid models of geometric solids in the point calculus are defined directly in the space in which they are located. This approach allows us to fully realize the new paradigm of three-dimensional design and eliminates the need to use transformation matrices, since all the necessary information about the shape and position of a geometric solid is contained in a rather compact form.

CONCLUSIONS

The proposed approach is very science-intensive and at the moment it has not been fully investigated. Since in fact the mathematical apparatus of vector representation of a new class of geometric objects, previously unexplored, is proposed. But already at this stage it is possible to highlight the advantages of the proposed approach and the prospects for its further use in information modeling of capital construction objects:

1. A new concept of solid modeling directly in three-dimensional space.

2. New methods for storing geometric-graphic information based on the use of compact point equations and computational algorithms based on them.
3. No need to use transformation matrices.
4. Realization of parallel calculations on data at the level of mathematical apparatus “Point Calculus”.
5. Realization of parallel computations on tasks due to the use of constructive algorithms of geometric modeling on projective and affine basis.
6. New methods for calculating the stress-strain state of solids based on functionally controlled anisotropy and alternative to the finite element method.
7. Replacing voxel models with vector models.

And this is by no means a complete list of the opportunities that the proposed concept opens up for BIM.

ACKNOWLEDGEMENTS

The study was supported by the Russia Science Foundation Grant No. 25-21-00003.

REFERENCE

1. **Kulakova I.V., Borzenko A.E.** Granichnoe predstavlenie modelej (metod B-REP v paketah SAPR) [Boundary representation of models (B-REP method in CAD packages)] // Informacionnye tekhnologii v konstruirovanii ES: Mezhvuzovskij sbornik nauchnyh trudov. Ryazan': IP Konyahin A.V. (Book Jet), 2023. pp. 139-143. (In Russian).
2. **Hu Z., Zhang J., Zhang X.** Construction collision detection for site entities based on 4-D space-time model // Qinghua Daxue Xuebao (Ziran Kexue Ban). 2010. Vol. 50, No. 6. pp. 820-825.
3. **Zou Q., Feng H.Yu.** A robust direct modeling method for quadric B-rep models based on geometry–topology inconsistency tracking // Engineering with Computers. 2022. Vol. 38, No. 4. pp. 3815-3830. DOI: 10.1007/s00366-021-01416-5.
4. **Teschemacher T., Bauer A. M., Oberbichler T., Breitenberger M., Rossi R., Wüchner R., Bletzinger K.U.** Realization of CAD-integrated shell simulation based on isogeometric B-Rep analysis // Advanced Modeling and Simulation in Engineering Sciences. 2018. Vol. 5, No. 1. pp. 1-54. DOI: 10.1186/s40323-018-0109-4.
5. **Luo Yu.T., Du H., Yan Yi.M.** MeshCNN-based BREP to CSG conversion algorithm for 3D CAD models and its application // Nuclear Science and Techniques. 2022. Vol. 33, No. 6. pp. 74. DOI: 10.1007/s41365-022-01063-5.
6. **Rossignac Ja.** {IBNC}: Integrated Boundary and Natural {CSG} for Polyhedra (Review, Simplifications, and Integration of Prior Art) // Computer-Aided Design. 2022. Vol. 150. pp. 103296. DOI: 10.1016/j.cad.2022.103296.
7. **Friedrich M., Illium S., Linnhoff-Popien C., Fayolle P.A.** CSG Tree Extraction from 3D Point Clouds and Meshes Using a Hybrid Approach // Communications in Computer and Information Science. 2022. Vol. 1474. pp. 53-79. DOI: 10.1007/978-3-030-94893-1_3.
8. IfcGeometricConstraintResource. URL: https://standards.buildingsmart.org/IFC/RELEASE/IFC4_3/HTML/ifcgeometricconstraintresource/content.html (date access: 18.07.2024).
9. National standard 10.0.02-2019/ISO 16739-1:2018 «System of standards for information modeling of buildings and structures». URL: https://docs.cntd.ru/document/1200164870 (date access: 03.03.2024). (In Russian).
10. **Fedorova N., Medyankin M., Moskovtseva V., Eniutina M., Quoc P.D.** Methodology for Modeling the Survivability of Multi-story Building Frames with Complex Stress Reinforced Concrete Elements // International Scientific Siberian

Transport Forum TransSiberia-2021. Vol. 2, Novosibirsk, May 11-14, 2021. – Novosibirsk: Springer Nature, 2022. pp. 1257-1266. DOI: 10.1007/978-3-030-96383-5_140.

11. **Klochkov Y.V., Vakhnina O.V., Sobolevskaya T.A., Nikolaev A.P., Fomin S.D., Klochkov M.Y.** A finite elemental algorithm for calculating the arbitrarily loaded shell using three-dimensional finite elements // ARPN Journal of Engineering and Applied Sciences. 2020. Vol. 15, No. 13. pp. 1472-1481.
12. **Buzalo N., Gontarenko I., Chernykhovskiy B., Alekseeva A.** Numerical Simulation of Steel Columns of Industrial Buildings with Local Mechanical Damage During Explotation // Lecture Notes in Civil Engineering. 2022. Vol. 182. pp. 349-356. DOI: 10.1007/978-3-030-85236-8_32.
13. **Tolok A.V., Tolok N.B.** Constructing the functional voxel model for terrain on the basis of bilinear interpolation of triangulated network // Advances in Intelligent Systems and Computing. 2020. Vol. 1226. pp. 340-347. DOI: 10.1007/978-3-030-51974-2_33.
14. **Cai H., Chen Y., Xu L., Zhang C., Elbaz K.** Intelligent building system for 3D construction of complex brick models // IEEE Access. 2020. Vol. 8. pp. 182506-182516. DOI: 10.1109/ACCESS.2020.3027807.
15. **Ridzuan N., Ujang U., Azri S., Mohamad Yusoff I., Choon T.L.** Voxelization techniques: data segmentation and data modelling for 3D building models // The International Archives of the Photogrammetry, Remote Sensing and Spatial Information Sciences. 2022. Vol. XLVIII-4/W3-2022. pp. 149-155. DOI: 10.5194/isprs-archives-xlviii-4-w3-2022-149-2022.
16. **Konopatskiy E.V., Bezditnyi A.A., Lagunova M.V., Naidysh A.V.** Principles of solid modelling in point calculus // Journal of Physics: Conference Series: 5, Omsk, 16–17 марта 2021 года. Omsk, 2021. pp. 012063. DOI: 10.1088/1742-6596/1901/1/012063.
17. **Konopatskiy E.V., Bezditnyi A.A.** Solid modeling of geometric objects in point calculus. Proceedings of the 31st International Conference on Computer Graphics and Vision (GraphiCon 2021). Nizhny Novgorod, Russia, September 27-30, 2021. Vol. 3027. pp. 666-672. DOI: 10.20948/graphicon-2021-3027-666-672.
18. **Konopatskiy E.V., Bezditnyi A.A.** The Problem of Visualizing Solid Models as a Three-Parameter Point Set // Scientific Visualization, 2022. Vol. 14. No. 2. pp. 49-61. DOI: 10.26583/sv.14.2.05.
19. **Golovanov N.N.** Geometricheskoe modelirovanie [Geometric modeling] // Moskva: KURS: INFRA-M, 2019. 400 p. (In Russian).
20. **Ausheev T.V., Bulychev R.N.** Modelirovanie parametricheskih racional'nyh tel s ispol'zovaniem obobshchennoj interpolyacii Bez'e [Modeling of parametric rational bodies using generalized bezier interpolation] // Vestnik Buryatskogo gosudarstvennogo universiteta. Matematika, informatika. 2018. № 1. C. 83-94. DOI: 10.18101/2304-5728-2018-1-83-94. (In Russian).
21. **Ayusheev T.V., Bulychev R.N., Rakshaeva O.D.** Postroenie trekhparametricheskih tel s vyrozhdennymi granichnymi poverhnostyami [Construction of three-parameter bodies with degenerate boundary surfaces] // Prikladnaya matematika i fundamental'naya informatika. 2019. Vol. 6, No. 4. pp. 4-17. DOI: 10.25206/2311-4908-2019-6-4-4-17. (In Russian).
22. **Ayusheev T.V., Damdinova T.Ts., Balzhinimaeva S.M.** Modelirovanie tel s ellipsoidnymi porami v vektorno-parametricheskom predstavlenii [Modeling of solids with ellipsoidal pores in vector-parametric representation] // Dinamika sistem, mekhanizmov i mashin. 2023. Vol.

11, No. 2. pp. 2-7. DOI: 10.25206/2310-9793-2023-11-2-2-7. (In Russian).
23. **Konopatskiy E.V., Bezditnyi A.A.** Geometric modeling of multifactor processes and phenomena by the multidimensional parabolic interpolation method // Journal of Physics: Conference Series: XIII International Scientific and Technical Conference "Applied Mechanics and Systems Dynamics", Omsk, 05–07 November 2019. Vol. 1441. Omsk: Institute of Physics Publishing, 2020. pp. 012063. DOI: 10.1088/1742-6596/1441/1/012063.
24. **Shchurova E.I.** Voxel and Finite Element Modeling of Twist Drill // Proceedings of the 5th International Conference on Industrial Engineering (ICIE 2019). Sochi, Russia, 25-29 March 2019. Springer International Publishing, Switzerland AG, 2020. pp. 181-190. DOI: 10.1007/978-3-030-22063-1_20.
25. Benergy P., Butterfield R. Metody granichnyh elementov v prikladnyh naukah [Boundary element methods in applied sciences]. Per. A.F. Zazovskogo i dr. // Moskva: Mir, 1984. 494 p. (In Russian).

СПИСОК ЛИТЕРАТУРЫ

1. **Кулакова И.В., Борзенко А.Е.** Граничное представление моделей (метод B-REP в пакетах САПР) // Информационные технологии в конструировании ЭС: Межвузовский сборник научных трудов. Рязань: ИП Коняхин А.В. (Book Jet), 2023. С. 139-143.
2. **Hu Z., Zhang J., Zhang X.** Construction collision detection for site entities based on 4-D space-time model // Qinghua Daxue Xuebao (Ziran Kexue Ban). 2010. Vol. 50, No. 6. pp. 820-825.
3. **Zou Q., Feng H.Yu.** A robust direct modeling method for quadric B-rep models based on geometry–topology inconsistency tracking // Engineering with Computers. 2022. Vol. 38, No. 4. pp. 3815-3830. DOI: 10.1007/s00366-021-01416-5.
4. **Teschemacher T., Bauer A. M., Oberbichler T., Breitenberger M., Rossi R., Wüchner R., Bletzinger K.U.** Realization of CAD-integrated shell simulation based on isogeometric B-Rep analysis // Advanced Modeling and Simulation in Engineering Sciences. 2018. Vol. 5, No. 1. pp. 1-54. DOI: 10.1186/s40323-018-0109-4.
5. **Luo Yu.T., Du H., Yan Yi.M.** MeshCNN-based BREP to CSG conversion algorithm for 3D CAD models and its application // Nuclear Science and Techniques. 2022. Vol. 33, No. 6. pp. 74. DOI: 10.1007/s41365-022-01063-5.
6. **Rossignac Ja.** {IBNC}: Integrated Boundary and Natural {CSG} for Polyhedra (Review, Simplifications, and Integration of Prior Art) // Computer-Aided Design. 2022. Vol. 150. pp. 103296. DOI: 10.1016/j.cad.2022.103296.
7. **Friedrich M., Illium S., Linnhoff-Popien C., Fayolle P.A.** CSG Tree Extraction from 3D Point Clouds and Meshes Using a Hybrid Approach // Communications in Computer and Information Science. 2022. Vol. 1474. pp. 53-79. DOI: 10.1007/978-3-030-94893-1_3.
8. IfcGeometricConstraintResource. URL: https://standards.buildingsmart.org/IFC/RELEASE/IFC4_3/HTML/ifcgeometricconstraintresource/content.html (дата обращения: 18.07.2024).
9. ГОСТ Р 10.0.02-2019/ИСО 16739-1:2018 «Система стандартов информационного моделирования зданий и сооружений». URL: https://docs.cntd.ru/document/1200164870 (дата обращения: 03.03.2024).
10. **Fedorova N., Medyankin M., Moskovtseva V., Eniutina M., Quoc P.D.** Methodology for Modeling the Survivability of Multi-story Building Frames with Complex Stress Reinforced Concrete Elements // International Scientific Siberian Transport Forum TransSiberia-2021. Vol. 2, Novosibirsk, May 11-14, 2021. –

Novosibirsk: Springer Nature, 2022. pp. 1257-1266. DOI: 10.1007/978-3-030-96383-5_140.

11. **Klochkov Y.V., Vakhnina O.V., Sobolevskaya T.A., Nikolaev A.P., Fomin S.D., Klochkov M.Y.** A finite elemental algorithm for calculating the arbitrarily loaded shell using three-dimensional finite elements // ARPN Journal of Engineering and Applied Sciences. 2020. Vol. 15, No. 13. pp. 1472-1481.
12. **Buzalo N., Gontarenko I., Chernykhovskiy B., Alekseeva A.** Numerical Simulation of Steel Columns of Industrial Buildings with Local Mechanical Damage During Explotation // Lecture Notes in Civil Engineering. 2022. Vol. 182. pp. 349-356. DOI: 10.1007/978-3-030-85236-8_32.
13. **Tolok A.V., Tolok N.B.** Constructing the functional voxel model for terrain on the basis of bilinear interpolation of triangulated network // Advances in Intelligent Systems and Computing. 2020. Vol. 1226. pp. 340-347. DOI: 10.1007/978-3-030-51974-2_33.
14. **Cai H., Chen Y., Xu L., Zhang C., Elbaz K.** Intelligent building system for 3D construction of complex brick models // IEEE Access. 2020. Vol. 8. pp. 182506-182516. DOI: 10.1109/ACCESS.2020.3027807.
15. **Ridzuan N., Ujang U., Azri S., Mohamad Yusoff I., Choon T.L.** Voxelization techniques: data segmentation and data modelling for 3D building models // The International Archives of the Photogrammetry, Remote Sensing and Spatial Information Sciences. 2022. Vol. XLVIII-4/W3-2022. pp. 149-155. DOI: 10.5194/isprs-archives-xlviii-4-w3-2022-149-2022.
16. **Konopatskiy E.V., Bezditnyi A.A., Lagunova M.V., Naidysh A.V.** Principles of solid modelling in point calculus // Journal of Physics: Conference Series: 5, Omsk, 16–17 марта 2021 года. Omsk, 2021. pp. 012063. DOI: 10.1088/1742-6596/1901/1/012063.
17. **Konopatskiy E.V., Bezditnyi A.A.** Solid modeling of geometric objects in point calculus. Proceedings of the 31st International Conference on Computer Graphics and Vision (GraphiCon 2021). Nizhny Novgorod, Russia, September 27-30, 2021. Vol. 3027. pp. 666-672. DOI: 10.20948/graphicon-2021-3027-666-672.
18. **Konopatskiy E.V., Bezditnyi A.A.** The Problem of Visualizing Solid Models as a Three-Parameter Point Set // Scientific Visualization, 2022. Vol. 14. No. 2. pp. 49-61. DOI: 10.26583/sv.14.2.05.
19. **Голованов Н.Н.** Геометрическое моделирование // М.: КУРС: ИНФРА-М, 2019. 400 с.
20. **Аюшеев Т.В., Булычев Р.Н.** Моделирование параметрических рациональных тел с использованием обобщенной интерполяции Безье // Вестник Бурятского государственного университета. Математика, информатика. 2018. № 1. С. 83-94. DOI: 10.18101/2304-5728-2018-1-83-94.
21. **Аюшеев Т.В., Булычев Р.Н., Ракшаева О.Д.** Построение трехпараметрических тел с вырожденными граничными поверхностями // Прикладная математика и фундаментальная информатика. 2019. Т. 6, № 4. С. 4-17. DOI: 10.25206/2311-4908-2019-6-4-4-17.
22. **Аюшеев Т.В., Дамдинова Т.Ц., Бальжинимаева С.М.** Моделирование тел с эллипсоидными порами в векторно-параметрическом представлении // Динамика систем, механизмов и машин. 2023. Т. 11, № 2. С. 2-7. DOI: 10.25206/2310-9793-2023-11-2-2-7.
23. **Konopatskiy E.V., Bezditnyi A.A.** Geometric modeling of multifactor processes and phenomena by the multidimensional parabolic interpolation method // Journal of Physics: Conference Series: XIII International Scientific and Technical Conference "Applied Mechanics

and Systems Dynamics", Omsk, 05–07 November 2019. Vol. 1441. Omsk: Institute of Physics Publishing, 2020. pp. 012063. DOI: 10.1088/1742-6596/1441/1/012063.

24. **Shchurova E.I.** Voxel and Finite Element Modeling of Twist Drill // Proceedings of the 5th International Conference on Industrial Engineering (ICIE 2019). Sochi, Russia, 25-29 March 2019. Springer International Publishing, Switzerland AG, 2020. pp. 181-190. DOI: 10.1007/978-3-030-22063-1_20.
25. **Бенерджи П., Баттерфилд Р.** Методы граничных элементов в прикладных науках. Пер. А.Ф. Зазовского и др. // М.: Мир, 1984. 494 с.

Evgeniy Viktorovich Konopatskiy – Doctor of Engineering, Docent, Director of the Institute of Information Technology, Head of the Department of Engineering Graphics and Information Modelling, Federal State Budgetary Educational Institution of Higher Education "Nizhny Novgorod State University of Architecture and Civil Engineering" (NNSAGU), 603000, Nizhny Novgorod, Ilyinskaya str., 65, e-mail: e.v.konopatskiy@mail.ru, +7(831)434-02-91.

Maxim Vladimirovich Bezsolnov – Postgraduate student of the Department of Engineering Graphics and Information Modeling, Federal State Budgetary Educational Institution of Higher Education "Nizhny Novgorod State University of Architecture and Civil Engineering" (NNSAGU), 603000, Nizhny Novgorod, Ilyinskaya str., 65, e-mail: bezsoff@yandex.ru, +7(831)434-02-91.

Евгений Викторович Конопацкий – д-р техн. наук, доцент, директор института информационных технологий, заведующий кафедрой инженерной графики и информационного моделирования, Федеральное государственное бюджетное образовательное учреждение высшего образования «Нижегородский государственный архитектурно-строительный университет» (ННГАСУ), 603000, г. Нижний Новгород, ул. Ильинская, д. 65, e-mail: e.v.konopatskiy@mail.ru, +7(831)434-02-91.

Максим Владимирович Безсольнов – аспирант кафедры инженерной графики и информационного моделирования, Федеральное государственное бюджетное образовательное учреждение высшего образования «Нижегородский государственный архитектурно-строительный университет» (ННГАСУ), 603000, г. Нижний Новгород, ул. Ильинская, д. 65, e-mail: e.v.konopatskiy@mail.ru, +7(831)434-02-91.

International Journal for Computational Civil and Structural Engineering, 21(1) 39–52 (2025)

DOI:10.22337/2587-9618-2025-21-1-39-52

DEFLECTION AND AXIAL FORCE IN GEOMETRICALLY NONLINEAR BEAM WITH PINNED SUPPORTS

Alexander P. Suvorov, Irina A. Makarova

National Research Moscow State University of Civil Engineering, Moscow, RUSSIA

Abstract: The problem of beam bending for large deflections is described in general. The nonlinear beam theory is considered for a simply-supported beam subjected to uniform load. The governing equations for displacements of this beam are derived. Numerical method for solving the governing equations is proposed. Convergence of the numerical method is studied. Numerical results are shown in the form of figures and formulas. These results suggest that the deflection predicted by the nonlinear theory at a specific point can be expressed solely as a function of the linear deflection at the same point. It is also shown how the axial force in the beam depends on the nonlinear deflection. Analytical expression for the axial force in the beam for small deflections is derived without solving the differential equation. For larger deflections, another representation for the axial force is obtained in terms of auxiliary functions that are defined only in terms of nonlinear and linear deflections. Comparison of the present results with the ABAQUS results is given. It is shown that the present theory can quite accurately predict the deflection and axial force in the beam for large deflections. However, the product of the axial force by the cosine of the slope angle at the support rather than the axial force itself will be a more accurate estimate of the horizontal support reaction.

Keywords: large deflection, axial force, nonlinear beam theory, finite difference method, convergence of iterative method, ABAQUS, nonlinear differential equations, principal of virtual work

ПРОГИБ И ОСЕВАЯ СИЛА В СВОБОДНО-ОПЕРТОЙ ГЕОМЕТРИЧЕСКИ-НЕЛИНЕЙНОЙ БАЛКЕ

А.П. Суворов, И.А. Макарова

Национальный исследовательский Московский государственный строительный университет, г. Москва, РОССИЯ

Аннотация: В общих чертах описана задача об изгибе балки при больших прогибах. Теория нелинейной балки рассматривается для свободно опертой балки, находящейся под действием равномерной нагрузки. Выведены определяющие уравнения для перемещений этой балки. Предложен численный метод решения определяющих уравнений. Исследована сходимость численного метода. Численные результаты представлены в виде рисунков и формул. Эти результаты позволяют предположить, что прогиб, предсказанный нелинейной теорией в конкретной точке, может быть выражен исключительно как функция линейного прогиба в той же точке. Также показано, как осевая сила в балке зависит от нелинейного прогиба. Аналитическое выражение для осевой силы в балке при малых прогибах получено без решения дифференциального уравнения. Для больших прогибов получено другое представление осевой силы через вспомогательные функции, которые зависят только от нелинейных или линейных прогибов. Приведено сравнение настоящих результатов с результатами по программе ABAQUS. Показано, что настоящая теория может довольно точно предсказать прогиб и осевую силу в балке при больших прогибах. Однако произведение осевой силы на косинус угла наклона на опоре, а не сама осевая сила, будет все же более точной оценкой горизонтальной реакции опоры.

Ключевые слова: большие прогибы, осевая сила, нелинейная теория балок, метод конечных разностей, сходимость итерационного метода, программа ABAQUS, нелинейные дифференциальные уравнения, принцип виртуальной работы

1. INTRODUCTION

In this paper we analyze a beam of length L subjected to the uniformly distributed load q. The beam is simply supported at its ends and also constrained from the axial movement at the supports. When dealing with thin metal sheets, we often have the situation when the thickness of the sheet t is small compared to the distance between the supports. In this case, it becomes important to take into account possible large deflections of the beam, which may be comparable with the thickness t and even larger than t. Denote the deflection of the beam by v.

The elementary beam theory allows us to account for these large displacements by incorporating axial strain of the beam into the equations. This strain is represented as the sum of the usual term $\frac{du}{dx}$ that is linearly dependent on the axial displacement u, and the term $\frac{1}{2}\left(\frac{dv}{dx}\right)^2$ that depends on the vertical displacement v nonlinearly. This approach is used in almost all previous investigations [1-11].

The axial strain naturally leads to the existence of the axial force N. For the theory in its simplest form, the axial force N is assumed constant along the length of the beam and it is also equal to the horizontal reaction at the supports. This assumption is very accurate only for sufficiently small displacements.

Timoshenko and Woinowsky-Krieger [1,2] derived exact solutions for beams with various supports. In particular, for a beam with pinned supports they obtained a nonlinear equation that can be solved for the axial force N

$$\left(\frac{Et^4}{qL^4}\right)^2 = \frac{135}{16}\frac{\tanh s}{s^9} + \frac{27}{16}\frac{\tanh^2 s}{s^8} - \frac{135}{16s^8} + \frac{9}{8s^6}$$

where

$$s^2 = \frac{3NL^2}{Et^3}.$$

Here E is the Young's modulus.

For faster calculations various approximate expressions were also proposed [1,3]. If we set

$$\alpha = \frac{384}{5}\frac{1}{\pi^2}\frac{N}{qL}\frac{t}{L}\left(\frac{v_{lin}(L/2)}{t}\right),$$

then the axial force N (and subsequently, the horizontal reaction) can be found as a root of the cubic equation

$$\frac{1}{3}\alpha(1+\alpha)^2 = \left(\frac{v_{lin}(L/2)}{t}\right)^2,$$

where v_{lin} is the known displacement predicted by the linear theory, evaluated here at the center of the beam, $x = L/2$.

For larger displacements, more accurate formula for calculation of the horizontal support reaction R_x is desired. It can be obtained by using the fact that the axial force will vary along the length of the beam and the support reaction is equal only to the axial force at the center of the beam.

In this paper, we will obtain certain estimates for the axial force that are very simple and don't require solutions of any nonlinear equations. The exact solution of the differential equation is also not required. In addition, we will obtain a simple upper bound for the axial force.

In our governing equations, we still assume that the axial force N is constant along the length (to simplify the equations), but after finding N, the deflection v, the beam's slope v' at the support, we will be able to estimate the horizontal support reaction more accurately by evaluating the product of the axial force and the cosine of the slope angle at the support, i.e., $R_x = N\cos v'$. By comparing R_x with ABAQUS software calculations, we have obtained a good match for the horizontal support reaction both for smaller and larger deflections. The value of the axial force N slightly overestimates the actual value of the horizontal support reaction if the displacements become large enough.

2. METHODS

2.1 Governing equations

Consider a simply-supported beam of length L subjected to the uniformly distributed load q. The x-axis is directed along the beam and $0 \le x \le L$ (Fig. 1). Let the vertical displacement or deflection of beam's cross-section be denoted by $v = v(x)$. Assume that the height of the cross-section of the beam is equal to t, the width is 1. Then the flexural stiffness of the beam EI can be found as

$$EI = E\frac{t^3}{12},$$

where E is the modulus of elasticity, the stiffness in tension or compression is

$$EA = Et.$$

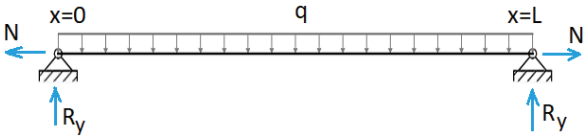

Figure 1. Beam geometry, applied loads and support reactions

If N is the internal axial force (assumed constant along the length of the beam), and M_T is the internal bending moment caused by the applied load, the differential equation for the beam's deflection v can be written as

$$EIv'' - Nv = M_T.$$

For uniformly distributed load and for simply-supported beam the bending moment is given by

$$M_T = \frac{q}{2}x(L - x).$$

Due to the supports the boundary conditions for the function v are

$$v(0) = v(L) = 0.$$

Obviously, for the simply supported beam the second derivative of v at the support points is also equal to zero, as the bending moment is equal to zero at the supports

$$v''(0) = v''(L) = 0.$$

Let $u(x)$ be the axial displacement, i.e., the displacement along the x-axis of the axis of the beam. It is known from the non-linear strain theory that the longitudinal strain for the points lying on the axis of the beam can be found as

$$\varepsilon_x = u' + \frac{1}{2}(v')^2.$$

Therefore, the axial force is determined from

$$N = EA\left(u' + \frac{1}{2}(v')^2\right),$$

where EA is the stiffness of the beam in tension or compression, A is the cross-sectional area. From the equilibrium in the direction of the x-axis, the axial force must be constant, i.e., $\frac{dN}{dx} = 0$, and therefore, the second differential equation for the function u can be written as

$$\frac{d}{dx}\left(EA\left(u' + \frac{1}{2}(v')^2\right)\right) = 0.$$

Since the axial stiffness is constant, this differential equation can be put in another form

$$u'' + v'v'' = 0,$$

where we have used the fact that

$$\frac{d}{dx}\left(\frac{1}{2}(v')^2\right) = v'v''.$$

Boundary conditions for the function $u(x)$ are given by

$$u(0)=u(L)=0.$$

We note that these differential equations can be derived from principal of virtual work. Let $\delta\left(u'+\frac{1}{2}(v')^2\right)$ be the virtual axial strain, and $\delta v''$ be the virtual curvature. Then the internal virtual work can be represented as

$$\int_a^b EIv''\delta v''dx + \int_a^b EA\left(u'+\frac{1}{2}(v')^2\right)\delta\left(u'+\frac{1}{2}(v')^2\right)dx$$

and the external virtual work is

$$\int_a^b q\delta v dx.$$

Equating these works leads to the final form of the equation

$$\int_a^b EIv''\delta v''dx + \int_a^b EA\left(u'+\frac{1}{2}(v')^2\right)\delta\left(u'+\frac{1}{2}(v')^2\right)dx = \int_a^b q\delta v dx.$$

Of course, the virtual displacements must satisfy

$$\delta v(0)=\delta v(L)=0,$$
$$\delta u(0)=\delta u(L)=0.$$

When integrating the expression for the axial force N along the length of the beam, we obtain

$$NL=\frac{EA}{2}\int (v')^2 dx$$

since the axial force is constant and

$$\int u'dx = 0.$$

Therefore, the differential equation for the deflection can also be written as

$$EIv''(x)-v\frac{EA}{2L}\int (v')^2 dx=\frac{q}{2}x(L-x).$$

2.2 Numerical solution

Numerical solutions of two-point boundary value problems by finite difference method have been discussed in [12-15]. Let us describe numerical algorithm for solving the present problem. To solve the given problem numerically, one can proceed with the algorithm that consists of the following steps:

1. Assume first that the axial force N is equal to zero.
2. Solve equation for the deflection v. The right-hand side of this equation is the moment caused by transverse loads, namely, $\frac{q}{2}x(L-x)$.
3. Find the first and second derivatives of the deflection v denoted by v' and v''.
4. Solve equation for the axial displacement u. The right-hand side of the equation becomes equal to $-v'v''$.
5. Find the first derivative of u denoted by u'.
6. With the knowledge of the displacements u and v, find the new estimate for the axial force as

$$N_{new}=EA\left(u'+\frac{1}{2}(v')^2\right).$$

This force should be independent of x coordinate, and it does not matter at which point this quantity is evaluated.

7. Check for convergence if N_{new} is sufficiently close to N. If not, set $N=N_{new}$ (update the axial force) and go to step 2.

Although this algorithm seems to be harmless it actually diverges when the load q gets large enough and deflections grow. To remedy the situation, we propose using in step 7 a different way of updating the axial force, namely,

$$N \leftarrow \frac{N}{2} + \frac{N_{new}}{2}.$$

Thus, we take the average of the previous value of the axial force N and the new value of the force N_{new}. With this important correction, this algorithm works well even for large values of the load q, and it converges in a smaller number of iterations.

We use standard finite difference scheme to solve differential equations for the displacements v and u. We divide the beam length into $n-1$ small intervals, where n is the number of points chosen to be sufficiently large. The length of each interval $h = L/(n-1)$. Then, if we denote v_i and u_i as the displacements evaluated at point i, $1 \le i \le n$, the differential equations can be written in finite difference form as

$$EI\frac{v_{i-1} - 2v_i + v_{i+1}}{h^2} - Nv_i = M_{Ti}$$

$$\frac{u_{i-1} - 2u_i + u_{i+1}}{h^2} = -\frac{v_{i+1} - v_{i-1}}{2h}\frac{v_{i-1} - 2v_i + v_{i+1}}{h^2}.$$

In the first equation the axial force N is assumed constant, chosen as described in the algorithm presented above. To evaluate accurately the second and first derivatives at the boundary points $i = 1$ and $i = n$, we introduce ghost points with the coordinates $x = 0 - h$ and $x = L + h$. We give them numbers $i = 0$ and $i = n + 1$, respectively. Then, the system of linear equations for finding v_i or u_i will comprise of $n + 2$ equations because there are now $n + 2$ points. The first equation in this system of equations will correspond to the finite difference equations evaluated for the left support with $i = 1$, i.e.,

$$EI\frac{v_0 - 2v_1 + v_2}{h^2} - Nv_1 = M_{T1}$$

$$\frac{u_0 - 2u_1 + u_2}{h^2} = -\frac{v_2 - v_0}{2h}\frac{v_0 - 2v_1 + v_2}{h^2}.$$

Similar expressions can be formed for the last equation in the system of linear equations. They are the finite difference equations evaluated at right support point with $i = n$.

2.3 Axial force for small displacements

Let us consider the limit of small vertical displacements and obtain estimate for the horizontal support reaction N in this case. In the limit of small deflections, the deflection predicted by the nonlinear theory is approximately equal to the displacement predicted by the linear theory. In the linear theory, the vertical displacement is given by

$$EIv(x) = \frac{q}{2}\left(\frac{x^3 L}{6} - \frac{x^4}{12}\right) - \frac{qL^3}{24}x$$

and the slope can be found as

$$EIv'(x) = \frac{q}{2}\left(\frac{x^2 L}{2} - \frac{x^3}{3}\right) - \frac{qL^3}{24}.$$

The axial force can now be evaluated from the relationship

$$N = \frac{EA}{2L}\int (v')^2 dx.$$

After substitution of the derivative of the linear displacement into this equation and subsequent evaluation of the integral, the axial force can be found as

$$N = \frac{EA}{8}\frac{17}{5040}\left(\frac{qL^3}{EI}\right)^2.$$

Now consider a beam with a cross-section of height t, and the unit width. The area of this

cross-section $A = t$ and the moment of inertia $I = t^3/12$. In this case, the axial force becomes

$$N = \frac{17}{280}\frac{1}{E}q^2\frac{L^6}{t^5}.$$

and thus the axial force depends on the applied loading quadratically.
It is also known that the deflection v at the center of the beam can be found as

$$\frac{v(L/2)}{t} = \frac{5}{32}\frac{qL^4}{Et^4}.$$

Using this expression, the above formula for the axial force can be transformed to

$$\frac{N}{qL/2} = \frac{136}{175}\frac{v(L/2)}{t}\frac{L}{t} = 0.777\frac{v(L/2)}{t}\frac{L}{t}.$$

This is our estimate for the axial force in the case of small deflections. This formula gives the ratio of the horizontal support reaction force to the vertical support reaction force.

2.4 Representations using dimensional theory
Let us obtain representations for the axial force and displacements using dimensional theory. Again consider a beam with a cross-section of thickness t and unit width. Introduce dimensionless (normalized) deflection as

$$w = \frac{v}{t}.$$

Denote the deflections predicted by the linear and nonlinear theories as w_{lin} and $w_{nl} = w$. It is well known that in the linear theory the dimensionless deflection w at the center is given by

$$w_{lin} = \frac{5}{32}\frac{qL^4}{Et^4}.$$

By analyzing numerical results (presented below) we can discover that the nonlinear vertical displacement at a particular point of the beam can be expressed solely in terms of linear vertical displacement evaluated at the same point. Let the function that relates nonlinear and linear displacements be denoted as g. Then

$$w_{nl} = g(w_{lin}).$$

This function is, of course, varies from point to point of the beam, but it is remarkable that in this relationship there is no dependence on L/t. Let us prove this fact. Recall that our differential equation for the deflection has this form

$$EIv''(x) - v\frac{EA}{2L}\int (v')^2 dx = \frac{q}{2}x(L-x).$$

Let us write this equation in dimensionless form. We introduce dimensionless coordinate x_1 as $x_1 = x/L$. Then, again using definitions for the area and the moment of inertia, we can derive

$$\frac{d^2w}{dx_1^2} - 6w\int\left(\frac{dw}{dx_1}\right)^2 dx_1 = 6\frac{qL^4}{Et^4}x_1(1-x_1).$$

Therefore,

$$p = \frac{qL^4}{Et^4} = \frac{32}{5}w_{lin}$$

is a dimensionless parameter that the deflection will depend on. But this parameter can be related to the displacement w_{lin} predicted by the linear theory. Therefore, we proved that upon fixing a point on the beam with the normalized coordinate x_1, the nonlinear deflection will depend only on the linear deflection at the same point.
The axial force can also be written in terms of dimensionless deflection w as follows

$$N = \frac{Et}{2}\frac{t^2}{L^2}\int\left(\frac{dw}{dx_1}\right)^2 dx_1.$$

But Young's modulus can be expressed in terms of linear displacement at the center

$$E = \frac{5}{32}\frac{qL^4}{w_{lin}t^4}.$$

Substituting this result into the equation for the axial force we obtain

$$N = \frac{5}{32}\frac{qL}{2}\frac{L}{t}\frac{1}{w_{lin}}\int\left(\frac{dw}{dx_1}\right)^2 dx_1.$$

Thus, the axial force N admits the following representation

$$N = \frac{qL}{2}\frac{L}{t}f\left(w_{nl}\right).$$

Here f is some function of nonlinear displacement, the shape of which will be established below, and $qL/2$ is the vertical reaction force R_y. This representation for the axial force was obtained by using dimensional analysis on the equation for the deflection $v(x)$. It follows that for a fixed value of nonlinear vertical displacement, the ratio of the axial force to the vertical support reaction force $qL/2$ will depend only on L/t, and therefore, will be twice larger for the beam with $L/t = 20$ compared to the beam with $L/t = 10$. Remember, however, that the nonlinear displacement will also depend on L/t in some nonlinear fashion.

Another important observation can be made from the fact that the nonlinear deflection can be expressed solely as a function of the linear deflection. The loading q can be found in terms of the linear deflection at the center as follows

$$q = \frac{32}{5}E\left(\frac{t}{L}\right)^4 w_{lin}.$$

For the same loading q and for the same geometry of the beam, the nonlinear deflection can be found. Using the connection between the linear and nonlinear displacements, this nonlinear deflection is therefore related to the magnitude of the loading by

$$q = \frac{32}{5}E\left(\frac{t}{L}\right)^4 g^{-1}\left(w_{nl}\right).$$

Thus, for the nonlinear theory, similar to the linear theory, the loading will also vary as $(t/L)^4$ for a fixed nonlinear deflection. This tells us, for example, that to produce the same nonlinear (normalized) deflection in the beam that is twice longer it is required to apply the loading that is 16 times smaller.

Let us obtain representation for the axial displacement in terms of vertical displacement. Since the first part of the axial force is given by

$$N_1 = EA\frac{du}{dx}$$

we can obtain, using the representation for the axial force, that

$$\frac{du}{dx} = \frac{q}{2E}\left(\frac{L}{t}\right)^2 f\left(w_{nl}\right).$$

Thus, using our representation for the loading q, we obtain

$$\frac{du}{dx} = \frac{16}{5}\left(\frac{t}{L}\right)^2 f\left(w_{nl}\right)g^{-1}\left(w_{nl}\right).$$

Introduce the dimensionless axial displacement and coordinate x as follows

$$u_1 = \frac{u}{t}, \qquad x_1 = \frac{x}{L}.$$

It is easy to show that

$$\frac{du_1}{dx_1} = \frac{16}{5}\left(\frac{t}{L}\right)f\left(w_{nl}\right)g^{-1}\left(w_{nl}\right).$$

or

$$du_1 = dx_1 \frac{16}{5}\left(\frac{t}{L}\right) f(w_{nl}) g^{-1}(w_{nl}).$$

Therefore, for the same increment in the coordinate dx_1 starting from the support (take, for example, quarter of the beam length) and for a fixed value of nonlinear deflection, the increment in the axial displacement will depend only on t/L, and therefore, the dimensionless axial displacement will be twice larger for the beam with $L/t = 10$ compared to the beam with $L/t = 20$. This result will be illustrated below.

3. RESULTS AND DISCUSSION

Consider a simply-supported beam of length L subjected to the uniformly distributed load q. The height of the cross-section of the beam is denoted by t (thickness), while the width of the cross-section is assumed equal to 1.
Introduce dimensionless (normalized) deflections as

$$w = \frac{v}{t}.$$

Denote the deflections predicted by the linear and nonlinear theories as w_{lin} and w_{nl}. In the linear theory the dimensionless deflection w at the center can be found as

$$w_{lin} = \frac{5}{32}\frac{qL^4}{Et^4}.$$

In what follows we investigate beams with two different geometries with L/t equal to 10 and 20. The beams are subjected to the same load q. On the following plots the results for the shorter beam with $L/t = 10$ are shown with solid lines. For the longer beam with $L/t = 20$ the results are shown with dashed lines. The size of the markers correspond (approximately) to the magnitude of the applied load q applied – the marker with the larger size corresponds to the larger magnitude of the load.
Figure 2 shows how the nonlinear displacement (normalized with respect to the thickness of the beam) depends on the linear displacement (also normalized).

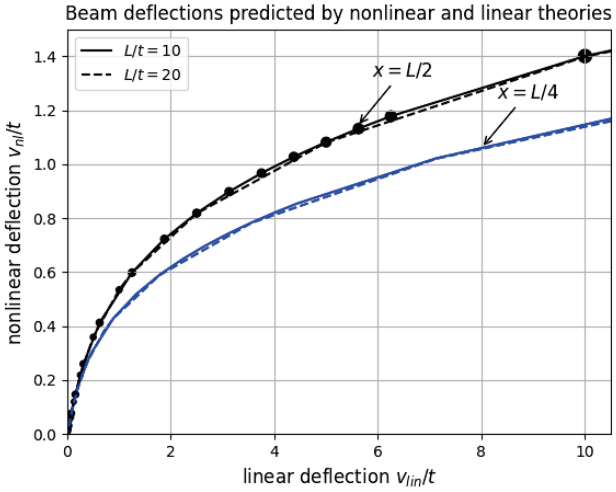

Figure 2. Dependence of the nonlinear displacement at the center of the beam on the linear displacement

The displacement is evaluated at the center of the beam, and thus it is maximum, and at a quarter of the total length of the beam. It is clear that the results for the two beam geometries overlap and thus the function that relates nonlinear and linear displacements at a specific point is independent of L/t, i.e.,

$$w_{nl} = g(w_{lin}).$$

We see clearly that the nonlinear displacements are significantly lower than the linear displacements. For example, for the linear displacement equal to 1, the nonlinear displacement is about 0.52; for the linear displacement equal to 4, the nonlinear one is only 1.
Figure 3 is central in our presentation. This figure shows by how much the horizontal support reaction N is smaller or larger than the vertical support reaction $qL/2$. Let us call the ratio of

the horizontal support reaction to the vertical reaction as the support reactions ratio. The figure shows how this ratio depends on the value of the normalized nonlinear displacement (at the center of the beam) for two geometries of the beam with $L/t=10$ and $L/t=20$. Size of the circles in the figure corresponds approximately to the magnitude of the applied load q.

Initially, of course, when the displacements are very small and the load is small, the horizontal support reaction is smaller than the vertical support reaction. It was shown in the previous section that for small loads the support reactions ratio can be well fitted with the function $0.777L/t(v/t)$ where v/t is normalized deflection at the center (linear or nonlinear deflections are about the same). It is seen from the graph that this approximation can be used with good accuracy when the deflection v/t is smaller than 0.2.

The point where the support reactions ratio becomes exactly equal to 1 depends on the ratio L/t: for more flexible beams with larger L/t it happens earlier, at smaller loads and at smaller displacements. After this point the horizontal support reaction quickly becomes larger than the vertical support reaction. It is interesting to observe that the point where the support reactions ratio reaches maximum does not depend on L/t: it happens when the nonlinear deflection at the center is about 0.59. For this value of nonlinear displacement the support reactions ratio can be evaluated approximately as $0.22L/t$. Therefore, the maximum of the support reactions ratio for $L/t=20$ is twice larger than for $L/t=10$.

In addition, the figure shows the ratio of R_x, defined as $N\cos(v'(0))$, to the vertical support reaction. It is seen that R_x is about the same as N except for very large displacements when it becomes somewhat smaller than N. This implies that the angle of slope of the deflected shape of the beam $v'(0)$ remains small even for large displacements.

We note that both the horizontal support reaction and vertical support reaction always grow with the increase of the load and the nonlinear displacement, but this figure shows that the rate of growth of the horizontal support reaction always changes during the loading. Indeed, for very large displacements the support reactions ratio decreases and again reaches the value of 1 and lower. Let us predict the support reactions ratio for large deflections from the elementary theory of flexible cables. Neglecting bending moment at the center we can obtain from the equilibrium of the half of the beam that this ratio is equal to $L/(4t)1/(v_{nl}/t)$, where v_{nl}/t is normalized nonlinear displacement at the center. Thus, this formula shows that the support reactions ratio for cables will eventually approach zero with the growth of nonlinear displacement, and thus also with the growth of vertical support reaction $qL/2$. This approximation for the support reactions ratio can be used with the good accuracy when v_{nl}/t is larger than 2.

But to use this graph for prediction of the axial force N or support reactions ratio, we must also remember that for different L/t ratios, the nonlinear displacement v_{nl}/t will also be different.

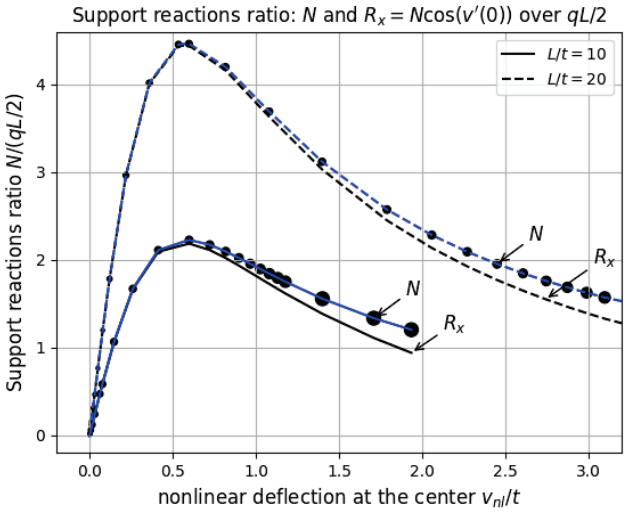

Figure 3. Ratio of the horizontal reaction force to the vertical reaction force as a function of the nonlinear displacement for two geometries with L/t equal to 10 and 20.

Figure 4 shows how f depends on the nonlinear displacement evaluated at the center of the beam. The function f is obtained by dividing the axial force N by $qL/2$ and L/t, i.e.,

$$f(w_{nl}) = \frac{N}{\frac{qL}{2}\frac{L}{t}}.$$

The results shown in Figure 4 do not depend on L/t, as expected.

We see that the maximum value of the function f is about 0.22. This maximum is achieved when the nonlinear displacement is 0.59.

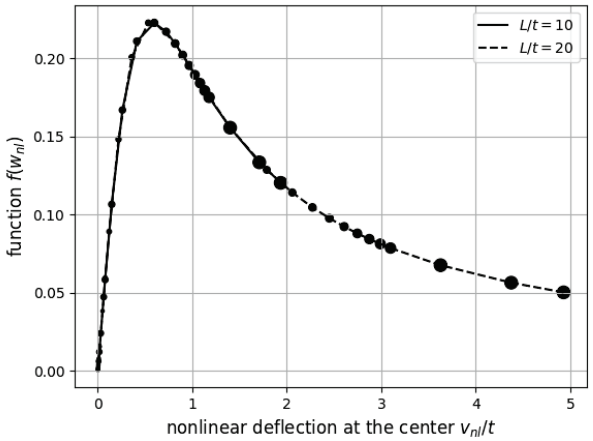

Figure 4. Dependence of the function f on the nonlinear displacement at the center of the beam

Using this maximum value, we can always obtain an upper bound for the axial force N,

$$N_u = 0.22\frac{qL}{2}\frac{L}{t},$$

although it will not be accurate if the nonlinear deflection is very different from 0.59.

The function f can also be expressed in terms of the linear displacement since we know from Figure 2 how the nonlinear deflection depends on the linear one. This dependence $f(w_{lin})$ is shown in Figure 5. To avoid skewed graph, we plot logarithm of the linear displacement on the horizontal axis of the graph instead of the linear displacement. We clearly see that the maximum of the function f is equal to about 0.22 and it is achieved when the normalized linear displacement is equal to about 1 ($\log_{10} 1 = 0$). Instead of using Figure 5 to find the value of the function f for a given linear deflection, one could use another option for determining the value f. Namely, find first the nonlinear displacement from Figure 2, and then determine the value of the function f from Figure 4.

Figure 6 shows maximum horizontal displacement (normalized with respect to thickness) versus vertical displacement for two beam geometries with L/t equal to 10 and 20.

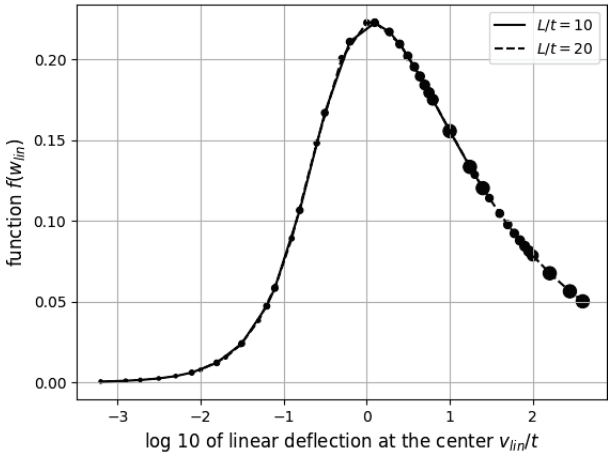

Figure 5. Dependence of the function f on the logarithm of the linear displacement at the center of the beam

The vertical displacement is evaluated at the center of the beam, but the maximum of the horizontal displacement occurs at $x = 3/4L$ and $x = 1/4L$. It is seen that the horizontal displacement is much smaller than the vertical displacement. Also, for the same value of the vertical displacement, the horizontal displacement for the beam with $L/t = 10$ is twice larger than that for the beam with $L/t = 20$. Since the horizontal displacement is maximum at $x = 3/4L$ and $x = 1/4L$. it follows that the horizontal dis-

placement has extremums exactly at these points. This fact, however, requires a strict proof.

Comparison of the numerical results obtained using the present technique with the ABAQUS software results is presented in Figure 7.

On the top figure we plot dependence of R_x, computed as product $N\cos v'(L)$, on the vertical reaction force $R_y = qL/2$. On the bottom figure we plot the axial force N, computed using the present method, versus the vertical reaction force. On both figures we compare these quantities with the horizontal reaction force computed in ABAQUS program $R_x(aba)$.

For convenience, we show absolute (not normalized) quantities for some specific choice of geometrical and physical parameters. But as before, solid line corresponds to $L/t = 10$, and dashed line corresponds to $L/t = 20$.

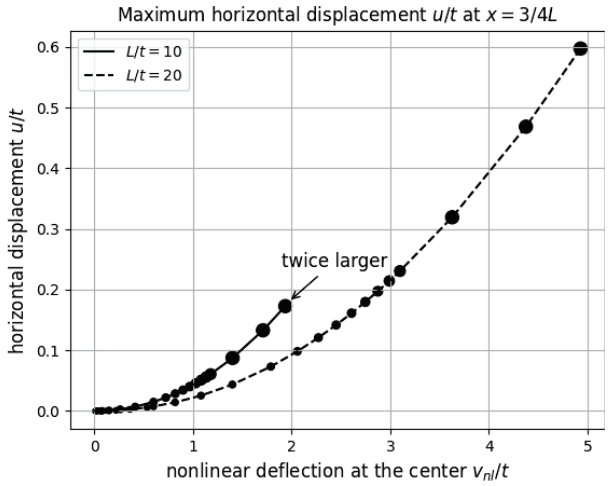

Figure 6. Maximum horizontal displacement versus maximum vertical displacement

The horizontal reaction force computed via ABAQUS $R_x(aba)$ is shown with circles for $L/t = 10$ and diamonds for $L/t = 20$. A good match is observed between the results on the top figure, but on the bottom figure we see some discrepancy between the results for larger values of the load q. Thus, the axial force multiplied by the cosine of the slope angle at the support $N\cos v'(L)$ is a better estimate for the horizontal reaction force than simply N.

Note that this graph shows that the horizontal support reaction always increases with increasing load q although the rate at which the horizontal support reaction grows diminishes.

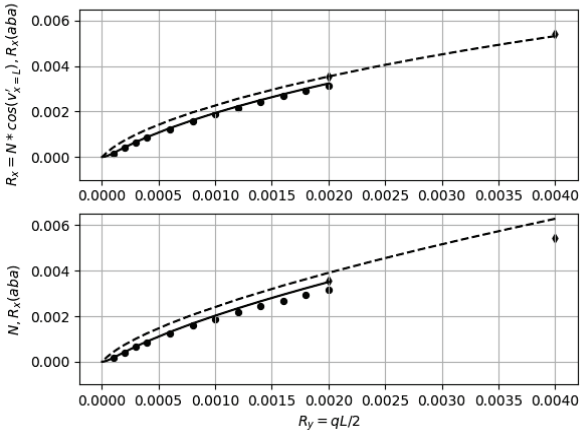

Figure 7. Comparison of R_x and the axial force N, computed using the present method (lines), with the horizontal reaction obtained in ABAQUS (dots). ABAQUS results are shown with markers – circles for $L/t = 10$ and diamonds for $L/t = 20$.

4. CONCLUSIONS

In this paper we have considered a well-known problem of determining deflection and horizontal support reaction for the simply-supported beam constrained from axial movement at the supports and subjected to the uniformly distributed load along the length. The axial strain of the beam included not only the usual term $\frac{du}{dx}$ linearly dependent on the axial displacement u, but also the term $\frac{1}{2}\left(\frac{dv}{dx}\right)^2$ depending on the vertical displacement v nonlinearly.

We have presented numerical procedure for solving the governing system of equations for

the displacements u and v. This procedure is iterative in which on each step the axial force N is updated. In order to ensure convergence of this scheme, we have come up with the rule for updating the axial force N, namely, the value of the axial force for the next iteration is taken as the average of the axial force used at the current iteration and the predicted value of the axial force also evaluated at the current iteration. With this update, the iterative scheme was convergent even for large loads and displacements. Convergence was achieved within a small number of iterations.

We have shown on the plots that the nonlinear deflection can be represented as a function of the linear deflection only. Also we have presented the graph for the function f that enables us to evaluate the axial force according to

$$N = \frac{qL}{2}\frac{L}{t}f.$$

The function f can be represented as the function of the nonlinear displacement or as the function of the linear displacement. The maximum of the function f is equal to 0.22, and this allows us to obtain an upper bound on the axial force N for any magnitude of the load q:

$$N \le 0.22\frac{qL}{2}\frac{L}{t}.$$

The maximum of the function f is achieved when the normalized nonlinear displacement is equal to about 0.59, and the normalized linear displacement is equal to about 1.

We have also obtained an expression for the axial force in the limit of small displacements and it was shown that for small displacements the axial force depends on the loading quadratically. The support reactions ratio was shown to be a linear function of the vertical displacement. These approximations work well when the normalized deflection at the center does not exceed 0.2. We have also established that when the normalized deflection exceeds 2, the bending moment can be neglected in the beam and the cable approximation can be used to predict the axial force.

By comparing our results with more accurate ABAQUS finite element results, we have observed a very good match for the axial force N. However, the horizontal support reaction can be more accurately predicted by using the formula

$$R_x = N\cos v'(0) = N\cos v'(L).$$

This formula becomes more accurate for larger displacements and our calculations allow us to obtain R_x by using this formula since the beam's slope v' is available at each point.

REFERENCES

1. **Timoshenko S., Woinowsky-Krieger S.** Theory of plates and shells. Mcgraw-Hill Book Company, 1959, 594 p.
2. **Woinowsky-Krieger, S.** The effect of an axial force on the vibration of hinged bars, J. Appl. Mech., 1950, 17, pp. 35–36.
3. **Gibshman E.E.** Proektirovanie metallicheskikh mostov [Steel bridge design]. Moscow, Transport, 1969, 416 p. (in Russian)
4. **Belenya E.I., Baldin V.A., Vedenikov G.S.** Metallicheskie kontstruktsii [Steel structures]. Moscow, Stroyizdat, 1986, 560 p. (in Russian)
5. **Loc V. Tran, Jarkko Niiranen**. A geometrically nonlinear Euler-Bernoulli beam model within strain gradient elasticity with isogeometric analysis and lattice structure applications, Mathematics and Mechanics of Complex Systems, 2020, vol. 8, no. 4.
6. **Paavani D., Aswathy M., Arun C.O., Praveen Krishna I.R.** Analysis of geometrically nonlinear Euler-Bernoulli beam using EFGM, IOP Conf. Series:

Materials Science and Engineering, 2020, 936, 012050.
7. **Worden K., Tomlinson G.R.** Nonlinearity in Structural Dynamics (Detection, Identification and Modelling), Institute of Physics Publishing, Bristol and Philadelphia, 2001.
8. **Lukash P.A**. Osnovy nelineinoy stroitel'noi mekhaniki [Foundations of Nonlinear Structural Mechanics]. Moscow, Stroyizdat, 1978, 204 p. (in Russian)
9. **Reddy J.N.** An Introduction to Nonlinear Finite Element Analysis. Oxford Univeristy Press, 2010.
10. **Jain S., Tiso P., Haller G**. Exact nonlinear model reduction for a von Karman beam: Slow-fast decomposition and spectral submanifolds, Journal of Sound and Vibration, 2018, vol. 423, pp. 195-211.
11. **Mehrpouya M.A., Salehi R., Wong P.J.Y.** A Fast and Accurate Numerical Method for Solving Nonlinear Fourth-Order Boundary Value Problems in the Beam Theory. Axioms, 2024, 13, 757.
12. **Kiusalaas J.** Numerical Methods in Engineering with Python 3. Cambridge University Press, 2013.
13. **Hoffman J.D.** Numerical Methods for Engineers and Scientists. McGraw-Hill, Inc., New York, 1992
14. **LeVeque R.J.** Finite Difference Methods for Ordinary and Partial Differential Equations. Society for Industrial and Applied Mathematics, Philadelphia, 2007.
15. **Butler J.S.** Numerical Methods for Differential Equations with Python. https://johnsbutler.netlify.app.

СПИСОК ЛИТЕРАТУРЫ

1. **Timoshenko S., Woinowsky-Krieger S.** Theory of plates and shells. Mcgraw-Hill Book Company, 1959, 594 p.
2. **Woinowsky-Krieger, S.** The effect of an axial force on the vibration of hinged bars, J. Appl. Mech., 1950, 17, pp. 35–36.
3. **Гибшман Е.Е.** Проектирование металлических мостов. – М.: Транспорт, 1969. – 416 с.
4. **Беленя Е.И., Балдин В.А., Ведеников Г.С.** Металлические конструкции. – М.: Стройиздат, 1986. – 560 с.
5. **Loc V. Tran, Jarkko Niiranen.** A geometrically nonlinear Euler-Bernoulli beam model within strain gradient elasticity with isogeometric analysis and lattice structure applications, Mathematics and Mechanics of Complex Systems, 2020, vol. 8, no. 4.
6. **Paavani D., Aswathy M., Arun C.O., Praveen Krishna I.R.** Analysis of geometrically nonlinear Euler-Bernoulli beam using EFGM, IOP Conf. Series: Materials Science and Engineering, 2020, 936, 012050.
7. **Worden K., Tomlinson G.R.** Nonlinearity in Structural Dynamics (Detection, Identification and Modelling), Institute of Physics Publishing, Bristol and Philadelphia, 2001.
8. **Лукаш П.А.** Основы нелинейной строительной механики. – М.: Стройиздат, 1978. – 204 с.
9. **Reddy J.N.** An Introduction to Nonlinear Finite Element Analysis. Oxford Univeristy Press, 2010.
10. **Jain S., Tiso P., Haller G.** Exact nonlinear model reduction for a von Karman beam: Slow-fast decomposition and spectral submanifolds, Journal of Sound and Vibration, 2018, vol. 423, pp. 195-211.
11. **Mehrpouya M.A., Salehi R., Wong P.J.Y.** A Fast and Accurate Numerical Method for Solving Nonlinear Fourth-Order Boundary Value Problems in the Beam Theory. Axioms, 2024, 13, 757.
12. **Kiusalaas J.** Numerical Methods in Engineering with Python 3. Cambridge University Press, 2013.
13. **Hoffman J.D.** Numerical Methods for Engineers and Scientists. McGraw-Hill, Inc., New York, 1992

14. **LeVeque R.J.** Finite Difference Methods for Ordinary and Partial Differential Equations. Society for Industrial and Applied Mathematics, Philadelphia, 2007.

15. **Butler J.S.** Numerical Methods for Differential Equations with Python. https://johnsbutler.netlify.app.

Alexander P. Suvorov — Ph.D. of Engineering Sciences, Associate Professor, Department of Computer Science and Applied Mathematics; Moscow State University of Civil Engineering (National Research University) (MGSU); 26 Yaroslavskoe shosse, Moscow, 129337, Russian Federation; ORCID: 0000-0001-7377-5817, e-mail: suvorovap@mgsu.ru;

Irina A. Makarova — Ph.D. of Engineering Sciences, Associate Professor, Department of Computer Science and Applied Mathematics; Moscow State University of Civil Engineering (National Research University) (MGSU); 26 Yaroslavskoe shosse, Moscow, 129337, Russian Federation; e-mail: makarovai@mgsu.ru.

Суворов Александр Павлович, доцент, кандидат технических наук, кафедра информатики и прикладной математики Национального исследовательского Московского государственного строительного университета; Ярославское шоссе 26, Москва, 129337, Россия; ORCID: 0000-0001-7377-5817, e-mail: suvorovap@mgsu.ru;

Макарова Ирина Анатольевна, доцент, кандидат технических наук, кафедра информатики и прикладной математики Национального исследовательского Московского государственного строительного университета; Ярославское шоссе 26, Москва, 129337, Россия; e-mail: makarovai@mgsu.ru.

International Journal for Computational Civil and Structural Engineering, 21(1) 53–68 (2025)

DOI:10.22337/2587-9618-2025-21-1-53-68

STRESS-STRAIN STATE OF CRANE SECONDARY TRUSSES WITH HORIZONTAL BENDING

Yulia D. Markina, Boris B. Lampsi

Nizhny Novgorod State University of Architecture and Civil Engineering, Nizhny Novgorod, RUSSIA

Abstract: Crane secondary trusses perform the functions of crane and secondary structures. The lower chord of the truss is designed to resist torsion, vertical and horizontal bending forces. The aim of the study was to investigate the stress–strain state of the truss under horizontal bending conditions. The influence of geometric parameters on the horizontal flexibility and internal forces within the beam during horizontal bending was analyzed. Various techniques were employed to determine horizontal displacements, internal forces, and stresses in the beam due to the one-sided location of the crane and the braking of the crane trolley. Contributions from horizontal bending stresses to the overall stress state of the chord were demonstrated. Factors affecting the accuracy of calculations for horizontal bending were identified. The validity of the research findings was confirmed by comparing numerical calculation results with those from a field survey. The differences between the stress-strain states of the truss chord and the equivalent beam have been analyzed. It has been justified that a more accurate method for the preliminary calculation of the riding chord for horizontal bending needs to be developed. For verification calculations of the crane secondary truss, a spatial finite element shell calculation scheme should be used in specialized software systems. The stiffness of the truss chord during horizontal bending greatly exceeds that of the crane beam. When checking crane structures for deflections in the horizontal plane, deflections should be determined based on the braking forces from the trolley of a single crane acting across the path, as per the requirements of SP 20.13330.2016. When torsion occurs, the ride chord of the crane secondary truss undergoes a horizontal bending, therefore, when checking for horizontal maximum deflections, it is necessary to also take into account asymmetric vertical loads due to the one-sided arrangement of the crane.

Keywords: crane structures, crane secondary truss, stiffness of nodes, braking load, horizontal bending, torsion, malleability

НАПРЯЖЕННО-ДЕФОРМИРОВАННОЕ СОСТОЯНИЕ ПОДКРАНОВО-ПОДСТРОПИЛЬНЫХ ФЕРМ ПРИ ГОРИЗОНТАЛЬНОМ ИЗГИБЕ

Ю.Д. Маркина, Б.Б. Лампси

Нижегородский государственный архитектурно-строительный университет, г. Нижний Новгород, РОССИЯ

Аннотация: Подкраново-подстропильные фермы выполняют функции подкрановых и подстропильных ферм. Ездовой нижний пояс фермы предназначен для работы на кручение, вертикальный и горизонтальный изгиб. Цель работы – изучение напряженно-деформированного состояния фермы при горизонтальном изгибе. Проанализировано влияние геометрических параметров ферм на горизонтальную податливость и внутренние усилия в её ездовом поясе при горизонтальном изгибе. Различными методами определены горизонтальные перемещения, внутренние усилия и напряжения в поясе от нагрузок, вызванных односторонним расположением крана и торможением крановой тележки. Показан вклад напряжений от горизонтального изгиба в общее напряженное состояние пояса. Приведены факторы, оказывающие влияние на точность расчёта при горизонтальном изгибе. Достоверность результатов исследования подтверждается сопоставимостью результатов численного расчета с результатами натурного обследования. Проанализированы отличий напряженно-деформированного состояния пояса фермы от напряженно-деформированного состояния эквивалентной балки. Обоснована необходимость разработки более точного метода предварительного расчёта ездового пояса на горизонтальный изгиб. Для поверочного расчёта подкраново-подстропильной фермы в специализированных программных комплексах следует использовать пространственную расчётную схему из оболочечных конечных элементов. Жесткость пояса фермы при горизонтальном изгибе значительно превышает жесткость подкрановой балки. В соответствии с СП

20.13330.2016 при проверке подкрановых конструкций по деформациям в горизонтальной плоскости, прогиб следует определять от сил торможения тележки одного крана, направленных поперек пути. При кручении ездовой пояс подкраново-подстропильной фермы испытывает горизонтальный изгиб, поэтому при его проверке по горизонтальным предельным прогибам в расчёте также необходимо учитывать несимметричные вертикальные нагрузки от одностороннего расположения кран.

Ключевые слова: подкрановые конструкции, подкраново-подстропильная ферма, жесткость узлов, тормозная нагрузка, горизонтальный изгиб, кручение, податливость

INTRODUCTION

Crane secondary trusses (CST) are unique large-span structures that combine the functions of crane and secondary trusses [1]. The riding lower chord is designed not only to work on vertical bending, but also on torsion caused by the one-sided arrangement of the crane [2, 3], as well as on horizontal bending caused by braking the crane trolley [4]. The riding chord is a prismatic folded system, which was studied on the basis of the theory of thin-walled rods by V.Z. Vlasov and A.A. Umansky [5-7] by B.B. Lampsi, E.A. Beilin and others [8, 9]. The stress-strain state (SSS) of thin-walled beams of a closed profile and methods of its analysis are considered in [10-15]. According to the recommendations [16], with horizontal bending and torsion, the forces in the CST riding chord should be determined both in a single-span beam, with a span and a section corresponding to an equivalent chord. The inclusion of lattice elements in the operation of the CST for horizontal bending is not taken into account. The disadvantages of the calculation method used are noted in [17-21]. The purpose of this research are to identify the differences between the SSS of the truss chord and the SSS of an equivalent beam, to analyze the contribution of stresses from horizontal bending to the overall stress state of the chord and to consider factors affecting the accuracy of calculating the horizontal bending rate. To achieve the set goals, the following tasks were solved:

1) Study of the influence of the geometric parameters of the CST on the horizontal compliance and internal forces in its lower riding chord under horizontal load;

2) Determination by various methods of internal forces and stresses in the CST chord from an asymmetric vertical load caused by the one-sided position of the crane and a horizontal load caused by the braking of the crane. Analysis of the results obtained;

3) Determination of the maximum horizontal movements of the riding chord when the crane is positioned one-way and the trolley is braking. Calculation of the CST for the second group of limit states for horizontal limit deflections in accordance with SP 16.13330.2017 and SP 20.13330.2016.

METHODS

The first stage of the research is to analyze the influence of the geometric parameters of CST on the horizontal compliance and internal forces within its lower riding chord during horizontal bending. Four types of CST with different geometric characteristics are considered:

- Three-panel CST No. 1 with a span of 36 meters and a height of 6.5 meters;
- Three-panel CST No. 2 with a span of 36 meters and a height of 15.44 meters;
- Four-panel CST No. 3 with a span of 48 meters and a height of 13 meters;
- A three-panel experimental model CST No. 4 with a span of 9 meters and a height of 3.3 meters [17].

The change in the stiffness ratio of the lower chord and the entire CST, as well as the ratio of the height of the prefab to its span, is considered [22].

To obtain statistical data in order to assess the impact of the geometric characteristics of the CST on the horizontal flexibility of the chord, we constructed 52 flat computational schemes. To analyze the influence of the height-to-span ratio of the CST, we sequentially changed the

height of each of the four CST's in six stages, so that the ratio of CST height to span length was consistently reduced from 0.5 to 0.1. To analyze the effect of stiffness ratio for each CST, we also sequentially changed the stiffness of lattice elements in six stages. In each case, we determined bending moment in horizontal plane, torque, malleability of junction between lattice and lower chord, and stiffness of lattice [23] using formula (1):

$$\mathrm{C} = \frac{1}{\delta_{CST}} - \frac{1}{\delta_b} \left[\frac{kN}{m}\right]; \quad (1)$$

where δ_{CST} – liability of the CST, determined by the formula:

$$\delta_{CST} = \frac{f_{CST}}{F} \left[\frac{m}{kN}\right]; \quad (2)$$

where f_{CST} – deflection of the CST at the point where force *F* is applied.
δ_b – compliance of an equivalent beam with a section corresponding to the CST driving chord, determined by the formula:

$$\delta_b = \frac{f_b}{F} \left[\frac{m}{kN}\right]; \quad (3)$$

where f_b – deflection of an equivalent beam at the point of application of force *F*.
The decrease in maximum displacements in the driving chord of the CTS relative to the equivalent beam is determined by the formula:

$$\Delta\delta = \left(1 - \frac{\delta_{CST}}{\delta_b}\right) \cdot 100\ [\%]; \quad (4)$$

The decrease in the ratio of span and height of the CST is determined by the formula:

$$\Delta\frac{h}{l} = \left(1 - \frac{h}{l}\right) \cdot 100\ [\%]; \quad (5)$$

where h – height of CST, m;
l – CST span, m.

The relative increase in lattice stiffness is determined by the formula:

$$\Delta C = \left(1 - \frac{\mathrm{C}_1}{\mathrm{C}_i}\right) \cdot 100\ [\%]; \quad (6)$$

where C_1 – lattice stiffness of the first (highest) CST from a number of studied;
C_i – stiffness of the elastic supports of the investigated CST.
The ratio of the stiffness of the lattice and the riding chord from the CST plane is defined as the ratio of the shear stiffness of the lattice section to the bending stiffness of the section of the riding chord. A concentrated force *F* = 100 *kN* is applied to the node in question from the CST plane.
The second stage of the study is to determine displacements, internal forces and stresses caused by the unilateral location of the crane and braking of the crane trolley. The object of research is CST No. 3, with an uncut lower chord. The calculation is performed using the following calculation schemes (CS):
- CS No. 1 – equivalent beam according to the recommendations [16];
- CS No. 2 – single-span flat rod CST considering misalignment of nodes [24] and rigid connections at supports [25];
- CS No. 3 – single-span CST flat rod considering alignment of nodes and supports;
- CS No. 4 – continuous flat CST core;
- CS No. 5 – uncut spatial CST using shell finite elements (Fig. 1).

Loading was carried out by a single crane with a lifting capacity of 450 tons. The weight of the cargo is 396 tons. Two of the most dangerous positions of the crane are considered [26, 27] – in the middle of the span and on the support. The value of the horizontal load from braking of the trolley is determined by [28] in accordance with SP 20.13330.2016. For CS No. 1-4, equivalent stresses were calculated analytically according to SP 16.13330.2017, the geometric characteristics of the section of the riding chord were determined by [28].

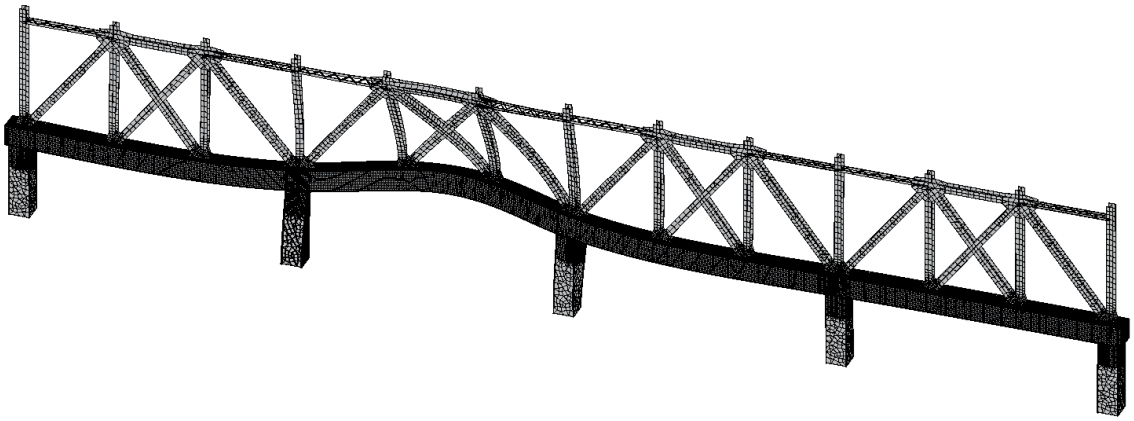

Figure 1. Deformations of CS No. 5 under horizontal load from crane braking in the middle of the span

The horizontal movements of the CST driving chord were calculated and the calculation was performed for the second group of limit states in accordance with SP 16.13330.2017 and SP 20.13330.2016.

In accordance with the appendix. D SP 20.13330.2016 horizontal maximum deflection of crane track beams for a group of crane operating modes 7K-8K:

$$f_u = \frac{l}{2000}\ ; \qquad (7)$$

where l – calculated span of the structural element.

The deflection is determined from the braking forces of the trolley of one crane directed across the track, at the mark of the head of the crane rails.

RESULTS AND DISCUSSION

The results of the study of the influence of the geometric parameters of the CST on the horizontal compliance and internal forces in its lower riding chord are shown in Fig. 2 and 3.

When changing the ratio of height and span of the CST, the ratio of horizontal movements in the riding chord and the equivalent beam does not exceed 8.5%. When the stiffness ratio changes, the ratio of horizontal movements in the riding chord and the equivalent beam does not exceed 12.7%.

With an increase in the height and span ratio of the CST, horizontal compliance increases and the rigidity of the lattice decreases from the CST plane. The ratio of maximum movement in the CST riding chord and equivalent beam also decreases. When the stiffness of the grating and CST driving chord increase, the horizontal compliance decreases and the stiffness of the grating increases from the CST plane in a linearly proportional manner.

The graphs of percentage increase in lattice stiffness for all CSTs coincide when considering the dependence on percentage ratio of height, span, and stiffness. This confirms the reliability of the numerical experiment results.

Considering the calculation of the lower beam for horizontal bending of lattice elements leads to a reduction in the bending moment from the CST plane. When designing the core of the entire CST structure, the bending moments in the horizontal plane are at most 11% less than when calculated according to the equivalent girder beam design scheme. At the same time, using the beam design scheme does not allow us to obtain the torque values that occur in the drive chord during horizontal bending. As the ratio of CST height and span increases, the bending moment from the CST plane decreases. As the stiffness ratio of the grating and drive chord of the CST increases, so do the torque and bending moments from the CST plane.

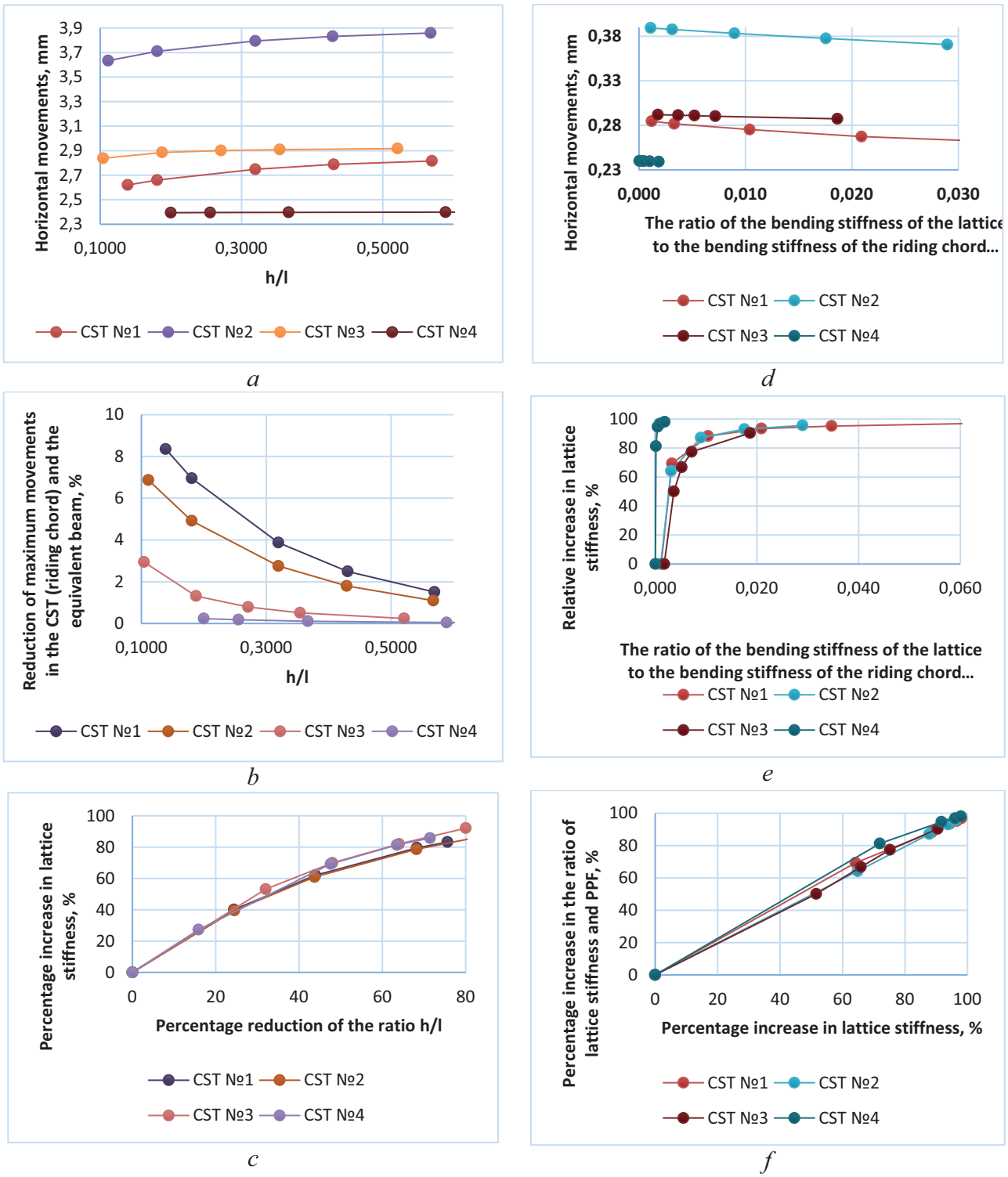

Figure 2. Effect of geometric parameters of CST on horizontal compliance of riding chord: a) effect of ratio of height and span on horizontal compliance; b) reduction in maximum horizontal movement in CST riding chord compared to equivalent beam; c) effect of ratio of height and span on rigidity of lattice; d) effect of stiffness of CST elements on horizontal pliability; e) effect of CST element stiffness on lattice stiffness; f) effect of CST element stiffness on lattice stiffness

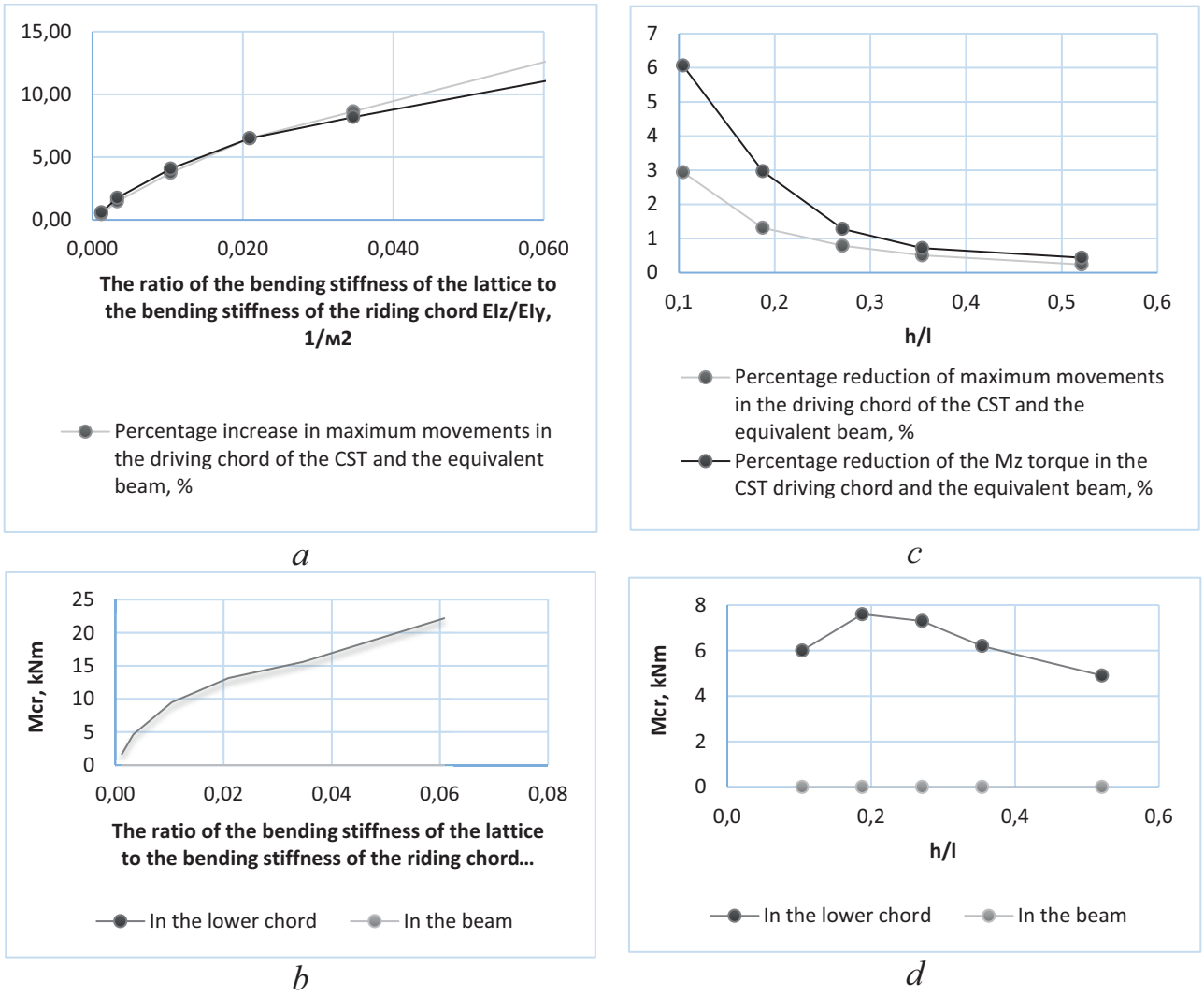

Figure 3. Effect of geometric parameters of CST on internal forces and movements of riding chord: a) effect of stiffness ratio on horizontal movement and horizontal plane moment of CST No. 1 riding chord; b) effect of stiffness ratio on torque of CST No. 1; c) effect of height and span ratio on horizontal movement and horizontal plane moment for CST No. 2; d) effect of height and span ratio on torque for CST No.2

The operation of the riding chord under a horizontal load caused by crane braking is more challenging than under an asymmetric vertical load resulting from a one-sided arrangement of the crane [29, 30]. With an asymmetric vertical load, the operating scheme of the CST can be divided into vertical bending and twisting of the riding chord, along with bending and twisting of lattice elements. Under a horizontal load, bending of the chord away from the CST plane occurs along with its twisting, and twisting is accompanied by horizontal bending. Simultaneously, both linear and angular displacements have opposing signs when dividing the effect into components, reducing the bending moment of the chord relative to the plane of the CST compared to the bending moment in the horizontal plane of an equivalent beam.

The results of the analysis of displacements, internal forces, and stresses caused by an asymmetric vertical load due to the one-sided positioning of the crane, as well as a horizontal load resulting from the braking of the crane, are presented in Table 1 and Fig. 4 and 5.

Due to braking with a one-way crane, the maximum torque in the driving chord increased by

16%, the bending moment from the CST plane increased by 39%, the transverse force increased by 35%, and the maximum horizontal movement increased by 43%. The maximum horizontal movement determined by CS No. 1, according to the recommendations [16], is more than three times higher than the movement determined by spatial CS No. 5. The maximum horizontal movements determined by the flat rod CS No. 1-4 are at least 1.6 times higher than the movement determined by the spatial CS No. 5 of the shell elements. The forces and stresses determined by CS No. 1 for the beam differ significantly from the results of numerical calculations for the riding chord as part of CST.

Table 1. Forces and movements of the CST driving chord

No. CS	Horiz. mov., mm	N_{max} in the outermost panels, t	N in the middle panel, t	$N_{k,max}$ in the outermost panels, tm	M_k in the middle panel, tm	$M_{y,max}$ in the middle panel, tm	$M_{z,max}$ in the middle panel, tm	$Q_{y,max}$ in the outermost panels, t	$Q_{z,max}$ in the middle panel, t
The load from the crane on one side and the braking									
1	26,8	0	0	-1563	-768	8198,0	344,3	26,3	-315,1
2	13,2	29,2	-55,5	420,9	7,53	1048,9	286,3	51,2	-311
3	58,3	43,0	-82,5	371,4	8,39	901,0	744,6	50,0	-311
4	14,9	314,6	207,8*	400,9	14,88	1047,4*	391,9	54,1	-309
5	8,5	-	-	-	-	-	-	-	-
Crane load on one side without braking									
4	14,3	314,6	207,8	333,3	12,44	1047,4	238,3	34,9	-309
Breaking load									
1	26,8	-	-	-	-	-	344,3	26,3	-
2	5,3	-	-	24,1	-	-	111,9	24,2	-
3	19,9	-	-	40,6	-	-	253,1	22,0	-
4	5,7	-	-	41,1	-	-	153,6	24,7	-
5	3,5	-	-	-	-	-	-	-	-
Note: forces with * were used to plot the stresses of CS No. 1-4									

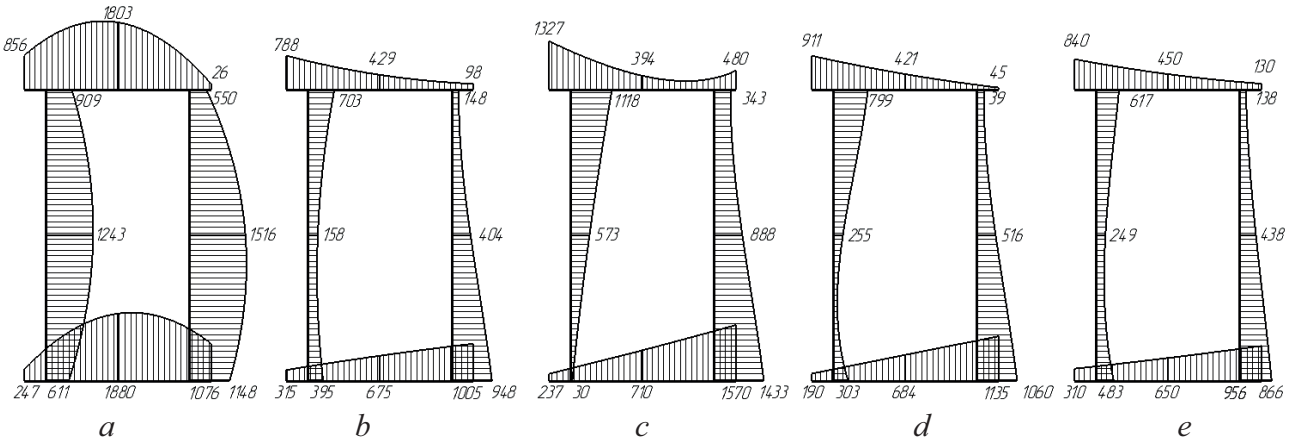

Figure 4. Diagrams of equivalent stresses [kgf/cm^2] of the driving chord in the middle of the span, obtained by analytical calculation: a – according to CS No. 1; b – according to CS No. 2; c – according to CS No. 3; d – according to CS No. 4; numerical calculation; d – according to CS No. 5. The load from the crane on one side and the braking of the trolley

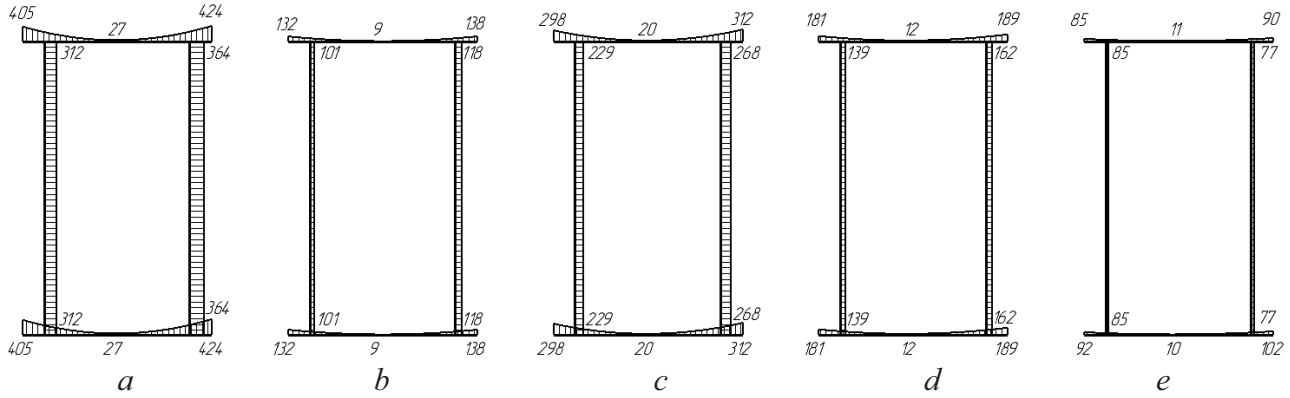

Figure 5. Diagrams of equivalent stresses [kgf/cm^2] of the driving chord in the middle of the span, obtained by analytical calculation: a – according to CS No. 1; b – according to CS No. 2; c – according to CS No. 3; d – according to CS No. 4; numerical calculation; d – according to CS No. 5. Braking load of the crane trolley

From a one-way crane load with braking, the torque according to CS No. 1 was four times higher than according to CS No. 2, and the bending moment from the CST plane was almost eight times higher. When braking without considering the vertical load from the crane, the bending moment on the CST plane, according to CS No. 1, is three times greater than according to CS No. 2. When switching from rigid connections on the supports, according to CS No. 2, to articulated ones, according to CS No. 3, under braking loads, the maximum torque increases by a factor of 1.7, the bending moment in the horizontal plane increases by a factor of 2.3, and the horizontal movement increases almost fourfold.

In the split CST according to CS No. 2, relatively uncut according to CS No. 4, under braking load, the torque is 1.7 times lower, the bending moment in the horizontal plane is 1.4 times lower. At the same time, the first typical single-span CSTs have a minimum zero survivability [31, 32]. Later CSTs [33, 34], to ensure the smoothness of the axis of the riding chord during deformations and increase its rigidity, are made continuous [35].

Due to braking with a one-way crane, the maximum torque in the driving chord increased by 16%, the bending moment from the CST plane increased by 39%, the transverse force increased by 35%, and the maximum horizontal movement increased by 43%. The maximum horizontal movement determined by CS No. 1, according to the recommendations [16], is more than three times higher than the movement determined by spatial CS No. 5. The maximum horizontal movements determined by the flat rod CS No. 1-4 are at least 1.6 times higher than the movement determined by the spatial CS No. 5 of the shell elements. The forces and stresses determined by CS No. 1 for the beam differ significantly from the results of numerical calculations for the riding chord as part of CST.

From a one-way crane load with braking, the torque according to CS No. 1 was four times higher than according to CS No. 2, and the bending moment from the CST plane was almost eight times higher. When braking without considering the vertical load from the crane, the bending moment on the CST plane, according to CS No. 1, is three times greater than according to CS No. 2. When switching from rigid connections on the supports, according to CS No. 2, to articulated ones, according to CS No. 3, under braking loads, the maximum torque increases by a factor of 1.7, the bending moment in the horizontal plane increases by a factor of 2.3, and the horizontal movement increases almost fourfold.

In the split CST according to CS No. 2, relatively uncut according to CS No. 4, under braking load, the torque is 1.7 times lower, the bending moment in the horizontal plane is 1.4 times lower. At the same time, the first typical single-

span CSTs have a minimum zero survivability [31, 32]. Later CSTs [33, 34], to ensure the smoothness of the axis of the riding chord during deformations and increase its rigidity, are made continuous [35].

The deflection from the braking forces of the trolley of one crane, directed across the path, is 3.5 mm (Table 1). Checking for the second group of limit states along the horizontal limit deflection is performed with a large margin:

$$f_b = 3{,}5\ mm < f_u = \frac{36000}{2000} = 18\ mm.$$

For an equivalent beam at a given load, the maximum horizontal displacement is 26.8 mm (Table 1), the rigidity condition is not met. The stiffness of the CST chord for horizontal bending is 7.7 times higher than the stiffness of the beam.

Since the CST riding chord undergoes horizontal bending during torsion [30], the horizontal deflection limit should include a component of horizontal displacement caused by an asymmetric vertical load due to the one-sided location of the crane. The maximum horizontal displacement resulting from the combined effects of the loads caused by the single-sided position of the crane and the braking of the crane trolley is 8.5 mm (Table 1). The contribution to the overall horizontal movement from the asymmetric vertical load component is 1.4 times greater than that from braking, and should not be ignored when checking for stiffness.

$$f_{b+c} = 8{,}5\ mm < f_u = \frac{36000}{2000} = 18\ mm.$$

The check is in progress. Taking into account the component of the asymmetric vertical load, the stiffness of the chord is more than 3 times higher than the stiffness of the equivalent beam.

As part of the author's supervision, specialists from TSNIIproektstalkonstruction and Chelyabproektstalkonstruction carried out an inspection of the converter shop of the Magnitogorsk Metallurgical Combine [36-39], commissioned in 1990, which uses longitudinal CSTs. A series of full-scale tests was carried out with the measurement of SSS in the most frequently damaged nodes of CST No. 3 using the strain gauge method. In [29, 30], the results of numerical calculation of CS No. 5 are compared with the results of a field survey. They have a relatively small discrepancy, presumably caused by the influence of welding stresses and the accumulation of crack-like defects in the near-seam zones [40, 41].

CONCLUSIONS

1. The CS of the beam [16] does not display the operation of the CST riding chord for horizontal bending. The horizontal displacements determined by the CS of the beam greatly exceed the displacements determined by the spatial CS of the shell finite elements. The forces and stresses determined by the CS of the beam differ significantly from the results of numerical calculations of the riding chord as part of the CST. The use of a CS beam does not allow to obtain the values of the torque that occurs in the driving chord during horizontal bending. It is necessary to develop a more accurate method of preliminary calculation of the CST driving chord for horizontal bending.

2. With horizontal bending of the riding chord caused by braking of the crane trolley, flat rod CS give a significant error in determining displacements and stresses (analytically calculated from internal forces) relative to the spatial CS. For the verification calculation of the CST, it is recommended to use spatial CS from shell finite elements. The entire frame or part of the structure should be included in the CS [42].

3. Verification of the second group of limit states is carried out in accordance with SP 20.13330.2016, which does not distinguish CST from other crane structures. It is recommended to determine the deflection from the braking forces of the trolley of one crane directed across the path. During torsion, the CST riding chord experiences horizontal bending, the contribution to the total horizontal movement of the component from the asymmetric vertical load caused by the one-sided

arrangement of the crane may exceed the contribution from the horizontal load caused by the braking of the trolley. When checking the CST for the second group of limit states for horizontal limit deflections, it is necessary to take into account not only the horizontal forces from braking the crane trolley, but also the asymmetric vertical loads from its one-sided location. The rigidity of the CST riding chord for horizontal bending significantly exceeds the rigidity of the crane beam.

ACKNOWLEDGEMENTS

The article was prepared with the financial support of the «Foundation of the Future» grant, which is carried out within the framework of the NNGASU development program, implemented under the academic leadership program «Priority 2030», in the aspect of the development of the university's research policy.
The authors express their gratitude to the anonymous reviewers, whose critical assessment of the submitted materials contributed to improving the quality of the article.

REFERENCES

1. **El`nov N.A. Kochetova E.A.** Analiz primeneniya sistem tipa «podkranovo-podstropil`ny`e fermy`» v bol`sheproletny`x cexax odnoe`tazhny`x promy`shlenny`x zdanij [Analysis of the application of systems such as «crane secondary trusses» in large-span workshops of single-storey industrial buildings]. *Trudy` nauchnogo kongressa 14-go rossijskogo arxitekturno-stroitel`nogo foruma* [Proceedings of the scientific congress of the 14th Russian architectural and construction forum]. 2016, pp. 143–146. (In Russian)
2. **Mentrasti L**. Torsion of closed cross-section thin-walled beams: the influence of shearing strain. Thin-Walled Structures. 1987, vol. 5, No.4, pp. 277–305.
3. **Mentrasti L.** Distortion (and torsion) of rectangular thin-walled beams. Thin-Walled Structures. 1990, vol. 10, No. 3, pp. 175–193.
4. **Rykaluk K.** Fatigue hazards in welded plate crane runway girders-locations, causes and calculations. K. Rykaluk, K. Marcinczak, S. Rowicski. Archives of Civil and Mechanical Engineering. 2018, No. 18, pp. 69-82.
5. **Umanskij A.A.** Kruchenie i izgib tonkostenny`x aviakonstrukcij [Torsion and bending of thin-walled aircraft structures]. M.: *Oboronizdat*, 1939, 112 p. (In Russian)
6. **Vlasov V.Z.** Stroitel`naya mexanika tonkostenny`x prostranstvenny`x system [Structural mechanics of thin-walled spatial systems]. M.: *Gostexizdat*, 1950, 695 p. (In Russian)
7. **Vlasov V.Z.** Izbranny`e trudy` [Selected works]. vol. 2 Tonkostenny`e uprugie sterzhni. Principy` postroeniya obshhej texnicheskoj teorii obolochek [Thin-walled elastic rods. Principles of construction of the general technical theory of shells]. M.: *Izd-vo AN USSR* [Publishing house AN USSR]. 1963, 328 p. (In Russian)
8. **Lampsi B.B**. Metallicheskie tonkostenny`e nesushhie konstrukcii pri lokal`ny`x nagruzkax [Thin-walled metal load-bearing structures under local loads]. M.: *Strojizdat*, 1979, 270 p. (In Russian)
9. **Bejlin E.A**. Variant edinoj teorii krucheniya tonkostenny`x sterzhnej otkry`togo, zamknutogo i chastichno zamknutogo profilej [A variant of the unified theory of torsion of thin-walled rods of open, closed and partially closed profiles]. *Issledovaniya po mexanike stroitel`ny`x konstrukcij i materialov. Mezhvuzovskij tematicheskij sbornik trudov* [Research on the mechanics of building structures and materials. Interuniversity thematic collection of works]. 1991, pp. 57-74. (In Russian)
10. **Musat S.D., Epureanu B.I.** Study of warping torsion of thin-walled beams with closed cross-section using macro-elements. Communications in Numerical Methods in Engineering. 1996, vol. 12, pp. 873–884.

11. **Srinivasan V., Purushothaman T., Chatterjee S.** Stress analysis of thin-walled circular and rectangular tubes subjected to torsion. International Journal of Mechanical Engineering and Technology. 2017, vol. 8, No. 8, pp. 1580–1587.
12. **Doostfatemeh A., Hematiyan M., Arghavan S**. Closed-form approximate formulas for torsional analysis of hollow tubes with straight and circular edges. Journal of Mechanics. 2009, vol. 25, No. 4, pp. 401–409.
13. **Omidvari A., Hematiyan M.** Approximate closed-form formulae for buckling analysis of rectangular tubes under torsion. International Journal of Engineering. 2015, vol. 28, No. 8, pp. 1226–1232.
14. **Chiskis A., Parnes R**. On torsion of closed thin-wall members with arbitrary stress-strain laws: a general criterion for cross-sections exhibiting no warping. Journal of Applied Mechanics. 2000, vol. 67, pp. 460–464.
15. **Li L-Y., Easterbrook D.** Free torsion of thin-walled structural members of open and closed-sections. Applied Mathematics and Mechanics. 2014, vol. 35, No. 1, pp. 25–32.
16. Rukovodstvo po proektirovaniyu stal`ny`x podkranovy`x konstrukcij [Guide to the design of steel crane structures]. M.: *CzNIIProektstal`konstrukciya.* 1976, 112 p. (In Russian)
17. **Lampsi B.B.** Ocenka vliyaniya osobennostej konstrukcii i nagruzki na napryazhennoe sostoyanie i prochnost` ezdovy`x poyasov sistem tipa podkranovo-podstropil`ny`x ferm: dis. kand. texn. nauk: 05.23.01, 01.02.03 [Assessment of the influence of design features and load on the stress state and strength of the riding chords of systems such as crane secondary trusses: thesis of candidate of technical sciences: 05.23.01, 01.02.03]. Lampsi Boris Borisovich. – Gor`kij: *Gor`kovskij ordena trudovogo krasnogo znameni inzhenerno-stroitel`ny`j institut im. V.P. Chkalova* [Gorky Order of the Red Banner of Labor V.P. Chkalov Institute of Civil Engineering]. 1983, 220 p. (In Russian)
18. **Tusnina O.A.** Opy`t zameny` nizhnego poyasa naxodyashhejsya pod nagruzkoj podkranovo-podstropil`noj fermy` [The experience of replacing the lower chord of a crane secondary truss under load. O.A. Tusnina, V.F. Takki, I.F. Egorov. *Promy`shlennoe i grazhdanskoe stroitel`stvo* [Industrial and civil engineering]. 2023, No. 4, pp. 21-28, doi: 10.33622/0869-7019.2023.04.21-28. (In Russian)
19. **Markina Yu.D.** Osobennosti raboty` podkranovo-podstropil`noj fermy` na gorizontal`ny`j izgib i kruchenie [Features of the crane secondary truss operation for horizontal bending and torsion]. Yu.D. Markina. *Arxitekturno-stroitel`ny`j i dorozhno-transportny`j kompleksy`: problemy`, perspektivy`, innovacii: sbornik materialov VIII Mezhdunarodnoj nauchno-prakticheskoj konferencii* [Architectural, construction and road transport complex: problems, prospects, innovations: collection of materials of the VIII International scientific and practical conference], Omsk, 23–24 noyabrya 2023 goda. Omsk, Izdatel`stvo SibADI. 2023, p. 669-672. (In Russian)
20. **Markina Yu.D.** Osobennosti staticheskogo raschyota podkranovo-podstropil`noj fermy` [Features of the static calculation of the crane secondary truss]. Yu.D. Markina. *Mexanika kompozicionny`x materialov i konstrukcij, slozhny`x i geterogenny`x sred: sbornik trudov 13oj Vserossijskoj nauchnoj konferencii s mezhdunarodny`m uchastiem im. I.F. Obrazczova i Yu.G. Yanovskogo* [Mechanics of composite materials and structures, complex and heterogeneous media: proceedings of the 13th All-Russian scientific conference with international participation named after I.F. Obraztsov and Yu.G. Yanovsky], Moskva, 14–16 noyabrya 2023 goda. Moskva: IPRIM RAN, Izdatel`stvo Obshhestvo s ogranichennoj otvetstvennost`yu "Sam Poligrafist" [Publishing house limited liability company "Sam Polygraphist"]. 2023, p. 113-120. (In Russian)

21. **Eryomin K.I.** Napryazhenno - deformirovannoe sostoyanie uzlov podkranovo-podstropil`ny`x ferm [Stress-strain state of crane secondary trusses]. K.I. Eremin, S.N. Shul`ga. *Promy`shlennoe i grazhdanskoe stroitel`stvo* [Industrial and civil engineering]. 2012, No. 4, pp. 52-54. (In Russian)
22. **Lampsi B.B.** Zhestkost` uzlov podkranovo-podstropil`noj fermy` v eyo ploskosti [Stiffness of the crane secondary truss nodes in its plane]. B.B. Lampsi, Yu.D. Markina. *Stroitel`naya mexanika i konstrukcii* [Construction mechanics and structures]. 2023, No. 4 (39), pp. 51–63. DOI 10.36622/VSTU.2023.39.4.006. (In Russian)
23. **Lampsi B.B.** Vliyanie vy`soty` podkranovo-podstropil`noj fermy` (PPF) na podatlivost` ezdovogo poyasa [The effect of the height of the crane secondary truss (CST) on the pliability of the riding chord]. B.B. Lampsi, Yu.D. Markina, P.A. Xazov. *Privolzhskij nauchny`j zhurnal* [Volga Scientific Journal]. 2023, No. 1 (65), pp. 28-34. (In Russian)
24. **Markina Yu.D.** Verification and refinement of the methodology for calculating the stiffness of crane secondary truss joints in its plane. Yu.D. Markina. *Privolzhskij nauchny`j zhurnal* [Volga Scientific Journal]. 2024, No. 1 (69), pp. 11-21.
25. Vliyanie zhestkosti e`lementov reshetki na podatlivost` ezdovogo poyasa podkranovo-podstropil`noj fermy` (PPF) [The effect of the rigidity of the lattice elements on the pliability of the crane secondary truss (CST) riding chord]. B.B. Lampsi, P.A. Xazov, Yu.D. Markina, D.M. Brikkel`. *Privolzhskij nauchny`j zhurnal* [Volga Scientific Journal]. 2022, No. 2 (62), pp. 29-36. (In Russian)
26. **Eremin K.I.** Predotvrashhenie razrushenij stroitel`ny`x metallicheskix konstrukcij: monografiya [Prevention of destruction of building metal structures: monograph]. K. I. Eremin. *M-vo obrazovaniya Ros. Federacii, Magnitog. gos. texn. un-t im. G. I. Nosova* [Ministry of Education of the Russian Federation, Magnitogorsk State Technical University named after G. I. Nosov]. Magnitogorsk: MGTU im. G.I. Nosova. 2004, 235 p. (In Russian)
27. **Goriczkij V.M.** O sostoyanii podkranovy`x konstrukcij korpusa konverternogo proizvodstva OAO «Severstal`» [About the condition of crane structures of the converter housing manufactured by JSC Severstal]. V.M. Goriczkij, V.N. Artyuxov, E.A. Shherbakov, G.R. Shnejderov. *Promy`shlennoe i grazhdanskoe stroitel`stvo* [Industrial and civil engineering]. 2001, No. 6, pp. 31-34. (In Russian)
28. **Lampsi B.B.** Podkranovo-podstropil`ny`e fermy`. Osobennosti konstrukcii, raboty` i raschyota: monografiya [Crane secondary trusses. Design, operation and calculation features: monograph]. B.B. Lampsi, Yu.D. Markina. Nizhnij Novgorod: *Nizhegorodskij gosudarstvenny`j arxitekturno-stroitel`ny`j universitet* [Nizhny Novgorod State University of Architecture and Civil Engineering]. 2024, 169 p. (In Russian)
29. **Markina Yu.D.** Kruchenie nizhnego poyasa podkranovo-podstropil`noj fermy`[Torsion of the lower chord of the crane secondary truss]. Yu.D. Markina. *Vestnik BGTU im. V.G. Shuxova* [Proceedings of the Belgorod State Technological University named after V.G. Shukhov]. 2023, No. 11, pp. 27–36. DOI: 10.34031/2071-7318-2023-8-11-27-36. (In Russian)
30. **Markina Yu.D**. Napryazhennoe sostoyanie nizhnego poyasa podkranovo-podstropil`noj fermy` pri stesnennom kruchenii [The stressed state of the lower chord of the crane secondary truss with constrained torsion]. Yu.D. Markina. *Vestnik grazhdanskix inzhenerov* [Proceedings of civil engineers]. 2024, No. 7 (102), pp. 36-43. (In Russian)
31. **Nezhdanov K.K.** Preimushhestva ispol`zovaniya nerazrezny`x podkranovy`x konstrukcij [Advantages of using continuous crane structures]. K.K.

Nezhdanov, I.N. Gor`kin. *Vestnik PGUAS: stroitel`stvo, nauka i obrazovanie* [Proceedings of the Penza State University of Architecture and Construction: construction, science and education]. 2018, No. 1 (6), pp. 9-16. (In Russian)

32. **Nezhdanov K.K.** Rezul`taty` ispy`tanij nerazrezny`x podkranovy`x konstrukcij [Test results of continuous crane structures]. K.K. Nezhdanov, I.N. Gor`kin, D.X. Kurtkezov. *Regional`naya arxitektura i stroitel`stvo* [Regional architecture and construction]. 2020, No. 3 (44), pp. 78-83. (In Russian)
33. **Nikitina E.A.** Opredelenie ostatochnogo resursa podkranovo-podstropil`noj fermy` s uchetom nakopleniya povrezhdenij v real`ny`x usloviyax e`kspluatacii [Determination of the remaining life of the crane secondary truss, taking into account the accumulation of damage in real operating conditions]. E.A. Nikitina, P.A. Xazov, D.M. Brikkel`. *Privolzhskij nauchny`j zhurnal* [Volga Scientific Journal]. 2018, No. 1, pp. 9-14. (In Russian)
34. **Romanov M.V.** Napryazhyonno-deformirovannoe sostoyanie oporny`x chastej podkranovo-podstropil`ny`x ferm: dis. kand. texn. nauk: 05.23.01 [Stress-strain state of the supporting parts of crane secondary trusses: thesis of candidate of technical sciences: 05.23.01]. Romanov Mixail Viktorovich. Magnitogorsk. 2002, 166 p. (In Russian)
35. **Shul`ga S.N.** Metodika ocenki zhivuchesti i opredelenie ostatochnogo resursa podkranovo-podstropil`ny`x ferm s treshhinopodobny`mi defektami [The methodology for assessing survivability and determining the residual life of crane secondary trusses with crack-like defects]. S.N. Shul`ga. *Nauka i bezopasnost`* [Science and Security]. 2014, No. 4(13), pp. 1–33. (In Russian)
36. **Shul`ga S.N.** Ostatochny`j resurs podkranovo-podstropil`ny`x ferm s nerazrezny`m nizhnim poyasom na stadii rosta ustalostnoj treshhiny`: dis. kand. texn. nauk: 05.23.01 [Residual resource of crane secondary trusses with an uncut lower chord at the stage of fatigue crack growth: thesis of candidate of technical sciences: 05.23.01]. Shul`ga Stepan Nikolaevich. M., 2015, 133 p. (In Russian)
37. **Eremin K.I.** Osobennosti e`kspluatacii metallicheskix konstrukcij promy`shlenny`x zdanij: monografiya [Features of operation of metal structures of industrial buildings: monograph]. K.I. Eremin, A.N. Shuvalov, G.A. Pavlova, S.A. Matveyushkin, M.V. Nashhekin, E.L. Alekseeva; pod red. K.I. Eremina. *M-vo obrazovaniya i nauki Ross. Federacii, FGBOU VPO Mosk. gos. str. un-t* [Ministry of Education and Science of the Russian Federation, Moscow State University of Civil Engineering]. Moskva: Izdatel`stvo MISI – MGSU [MISI – MGSU Publishing House]. 2012, 248 p. (In Russian)
38. **Eremin K.I.** Modelirovanie razvitiya ustalostny`x povrezhdenij v podkranovo-podstropil`ny`x fermax [Modeling the development of fatigue damage in crane secondary trusses]. K.I. Eremin, S.N. Shul`ga. *Vestnik MGSU* [Proceedings of the Moscow State University of Civil Engineering].2014, No. 5, pp. 30-38. (In Russian)
39. **Eryomin K.P.** Zakonomernost` povrezhdenij podkranovo-podstropil`ny`x ferm pa stadii e`kspluatacii [The pattern of damage to crane secondary trusses at the stage of operation]. K.I. Eremin, S.N. Shul`ga. *Promy`shlennoe i grazhdanskoe stroitel`stvo* [Industrial and civil engineering]. 2013, No. 4, pp. 34-36. (In Russian)
40. **Eremin K.I.** Vliyanie e`kscentrisiteta na napryazhenno-deformirovannoe sostoyanie verxnej zony` stenok podkranovo-podstropil`ny`x ferm [The effect of eccentricity on the stress-strain state of the upper zone of the walls of crane secondary trusses]. K.I. Eremin, S.N. Shul`ga. *Nauka i*

bezopasnost` [Science and security]. 2015, No. 5(18), pp. 49–52. (In Russian)
41. **Eremin K.I.** Scenarii progressiruyushhego obrusheniya nerazrezny`x podkranovo-podstropil`ny`x ferm s nakoplenny`mi ustalostny`mi povrezhdeniyami [Scenarios of progressive collapse of continuous crane secondary trusses with accumulated fatigue damage]. K.I. Eremin, S.N. Shul`ga. *Promy`shlennoe i grazhdanskoe stroitel`stvo* [Industrial and civil engineering]. 2014, No. 5, pp. 46 -49. (In Russian)
42. **Tusnina O.A.** Finite element analysis of crane secondary truss. O.A. Tusnina. Magazine of Civil Engineering. 2018, No. 1(77), pp. 68-89. doi: 10.18720/MCE.77.7.

СПИСОК ЛИТЕРАТУРЫ

1. **Ельнов Н.А. Кочетова Е.А.** Анализ применения систем типа «подкраново-подстропильные фермы» в большепролетных цехах одноэтажных промышленных зданий // Труды научного конгресса 14-го российского архитектурно-строительного форума. 2016. С. 143–146.
2. **Mentrasti L.** Torsion of closed cross-section thin-walled beams: the influence of shearing strain // Thin-Walled Structures. 1987. Vol. 5. No. 4. Pp. 277–305.
3. **Mentrasti L.** Distortion (and torsion) of rectangular thin-walled beams // Thin-Walled Structures. 1990. Vol. 10. No. 3. Pp. 175–193.
4. **Rykaluk K**. Fatigue hazards in welded plate crane runway girders-locations, causes and calculations / K. Rykaluk, K. Marcinczak, S. Rowicski // Archives of Civil and Mechanical Engineering. 2018. No. 18. Pp. 69-82.
5. **Уманский А.А.** Кручение и изгиб тонкостенных авиаконструкций. М.: Оборониздат, 1939. 112 с.
6. **Власов В.З.** Строительная механика тонкостенных пространственных систем. М.: Гостехиздат, 1950. 695 с.
7. **Власов В.З.** Избранные труды. Т. 2 Тонкостенные упругие стержни. Принципы построения общей технической теории оболочек. М.: Изд-во АН СССР, 1963. 328 с.
8. **Лампси Б.Б.** Металлические тонкостенные несущие конструкции при локальных нарузках. М.: Стройиздат, 1979. 270 с.
9. **Бейлин Е.А.** Вариант единой теории кручения тонкостенных стержней открытого, замкнутого и частично замкнутого профилей // Исследования по механике строительных конструкций и материалов. Межвузовский тематический сборник трудов. 1991. С. 57-74.
10. **Musat S.D., Epureanu B.I.** Study of warping torsion of thin-walled beams with closed cross-section using macro-elements // Communications in Numerical Methods in Engineering. 1996. Vol. 12. Pp. 873–884.
11. **Srinivasan V., Purushothaman T., Chatterjee S.** Stress analysis of thin-walled circular and rectangular tubes subjected to torsion // International Journal of Mechanical Engineering and Technology. 2017. Vol. 8. No. 8. Pp. 1580–1587.
12. **Doostfatemeh A., Hematiyan M., Arghavan S.** Closed-form approximate formulas for torsional analysis of hollow tubes with straight and circular edges // Journal of Mechanics. 2009. Vol. 25. No. 4. Pp. 401–409.
13. **Omidvari A., Hematiyan M.** Approximate closed-form formulae for buckling analysis of rectangular tubes under torsion // International Journal of Engineering. 2015. Vol. 28. No. 8. Pp. 1226–1232.
14. **Chiskis A., Parnes R.** On torsion of closed thin-wall members with arbitrary stress-strain laws: a general criterion for cross-sections exhibiting no warping // Journal of Applied Mechanics. 2000. Vol. 67. Pp. 460–464.
15. **Li L-Y., Easterbrook D.** Free torsion of thin-walled structural members of open and

closed-sections // Applied Mathematics and Mechanics. 2014. Vol. 35. No. 1. Pp. 25–32.
16. Руководство по проектированию стальных подкрановых конструкций. М.: ЦНИИПроектстальконструкция, 1976. 112 с.
17. **Лампси Б.Б.** Оценка влияния особенностей конструкции и нагрузки на напряженное состояние и прочность ездовых поясов систем типа подкраново-подстропильных ферм: дис. ... канд. техн. наук: 05.23.01, 01.02.03. Горький, 1983. 220 с.
18. **Туснина О.А., Такки В.Ф., Егоров И.Ф.** Опыт замены нижнего пояса находящейся под нагрузкой подкраново-подстропильной фермы // Промышленное и гражданское строительство. 2023. № 4. С. 21-28. doi: 10.33622/0869-7019.2023.04.21-28.
19. **Маркина Ю.Д.** Особенности работы подкраново-подстропильной фермы на горизонтальный изгиб и кручение // Архитектурно-строительный и дорожно-транспортный комплексы: проблемы, перспективы, инновации: сборник материалов VIII Международной научно-практической конференции. 2023. С. 669-672.
20. **Маркина Ю.Д.** Особенности статического расчёта подкраново-подстропильной фермы // Механика композиционных материалов и конструкций, сложных и гетерогенных сред: сборник трудов 13ой Всероссийской научной конференции с международным участием им. И.Ф. Образцова и Ю.Г. Яновского. 2023. С. 113-120.
21. **Ерёмин К.И., Шульга С.Н**. Напряженно-деформированное состояние узлов подкраново-подстропильных ферм // Промышленное и гражданское строительство. 2012. №4. С. 52-54.
22. **Лампси Б.Б., Маркина Ю.Д.** Жесткость узлов подкраново-подстропильной фермы в её плоскости // Строительная механика и конструкции. 2023. № 4 (39). С. 51–63. DOI 10.36622/VSTU.2023.39.4.006
23. **Лампси Б.Б., Маркина Ю.Д., Хазов П.А.** Влияние высоты подкраново-подстропильной фермы (ППФ) на податливость ездового пояса // Приволжский научный журнал. 2023. № 1 (65). С. 28-34.
24. **Markina Yu.D.** Verification and refinement of the methodology for calculating the stiffness of crane secondary truss joints in its plane // Приволжский научный журнал. 2024. № 1 (69). С. 11-21.
25. Влияние жесткости элементов решетки на податливость ездового пояса подкраново-подстропильной фермы (ППФ) / Б.Б. Лампси [и др.] // Приволжский научный журнал. 2022. № 2 (62). С. 29-36
26. **Еремин К.И.** Предотвращение разрушений строительных металлических конструкций: монография. Магнитогорск : МГТУ им. Г. И. Носова, 2004. 235 с.
27. О состоянии подкрановых конструкций корпуса конвертерного производства ОАО «Северсталь» / В.М. Горицкий [и др.] // Промышленное и гражданское строительство. 2001. №6. С. 31-34.
28. **Лампси Б.Б., Маркина Ю.Д.** Подкраново-подстропильные фермы. Особенности конструкции, работы и расчёта: монография. Нижний Новгород: ННГАСУ, 2024. 169 с.
29. **Маркина Ю.Д.** Кручение нижнего пояса подкраново-подстропильной фермы // Вестник БГТУ им. В.Г. Шухов. 2023. № 11. С. 27–36. DOI: 10.34031/2071-7318-2023-8-11-27-36
30. **Маркина Ю.Д.** Напряженное состояние нижнего пояса подкраново-подстропильной фермы при стесненном кручении // Вестник гражданских инженеров. 2024. № 7 (102). С. 36-43.
31. **Нежданов К.К., Горькин И.Н.** Преимущества использования неразрезных подкрановых конструкций

// Вестник ПГУАС: строительство, наука и образование. 2018. № 1 (6). С. 9-16
32. **Нежданов К.К., Горькин И.Н., Курткезов Д.Х.** Результаты испытаний неразрезных подкрановых конструкций // Региональная архитектура и строительство. 2020. № 3 (44). С. 78-83.
33. **Никитина Е.А., Хазов П.А., Бриккель Д.М.** Определение остаточного ресурса подкраново-подстропильной фермы с учетом накопления повреждений в реальных условиях эксплуатации // Приволжский научный журнал. 2018. №1 С. 9-14.
34. **Романов М.В.** Напряжённо-деформированное состояние опорных частей подкраново-подстропильных ферм: дис. ... канд. техн. наук: 05.23.01. Магнитогорск, 2002. 166 с.
35. **Шульга С.Н.** Методика оценки живучести и определение остаточного ресурса подкраново-подстропильных ферм с трещиноподобными дефектами // Наука и безопасность. 2014. № 4(13). С. 1–33.
36. **Шульга С.Н.** Остаточный ресурс подкраново-подстропильных ферм с неразрезным нижним поясом на стадии роста усталостной трещины: дис. ... канд. техн. наук: 05.23.01. М., 2015. 133 с
37. Особенности эксплуатации металлических конструкций промышленных зданий: монография / К.И. Еремин[и др.]. М.: МГСУ, 2012. 248 с.
38. **Еремин К.И., Шульга С.Н.** Моделирование развития усталостных повреждений в подкраново-подстропильных фермах // Вестник МГСУ. 2014. №5 С. 30-38.
39. **Ерёмин К.П., Шульга С.Н.** Закономерность повреждений подкраново-подстропильных ферм па стадии эксплуатации // Промышленное и гражданское строительство. 2013. №4. С. 34-36.
40. **Еремин К.И., Шульга С.Н.** Влияние эксцентриситета на напряженно-деформированное состояние верхней зоны стенок подкраново-подстропильных ферм // Наука и безопасность. 2015. № 5(18). С. 49–52.
41. **Еремин К.И., Шульга С.Н.** Сценарии прогрессирующего обрушения неразрезных подкраново-подстропильных ферм с накопленными усталостными повреждениями // Промышленное и гражданское строительство. 2014. №5. С. 46 -49.
42. **Tusnina O.A.** Finite element analysis of crane secondary truss // Magazine of Civil Engineering. 2018. No. 1(77). Pp. 68-89. doi: 10.18720/MCE.77.7

Yulia Dmitrievna Markina — senior lecturer of the chair of theory of structures and technical mechanics, Nizhny Novgorod State University of Architecture and Civil Engineering (NNGASU), Russia, 603950, Nizhny Novgorod, Ilyinskaya str., 65. poluektoff@bk.ru.

Boris Borisovich Lampsi — candidate of technical sciences, associate professor, head of the chair of theory of structures and technical mechanics, Nizhny Novgorod State University of Architecture and Civil Engineering (NNGASU), Russia, 603950, Nizhny Novgorod, Ilyinskaya str., 65. lampsi@yandex.ru.

Юлия Дмитриевна Маркина — ст. преп. кафедры теории сооружений и технической механики, ФГБОУ ВО «Нижегородский государственный архитектурно-строительный университет» (ННГАСУ), Россия, 603950, г. Н. Новгород, ул. Ильинская, д. 65. poluektoff@bk.ru.

Борис Борисович Лампси — канд. техн. наук, доц., зав. кафедрой теории сооружений и технической механики, ФГБОУ ВО «Нижегородский государственный архитектурно-строительный университет» (ННГАСУ), Россия, 603950, г. Н. Новгород, ул. Ильинская, д. 65. lampsi@yandex.ru.

International Journal for Computational Civil and Structural Engineering, 21(1) 69–78 (2025)

DOI:10.22337/2587-9618-2025-21-1-69-78

HYDRAULIC ENGINEERING CONCRETE BASED ON A COMPOSITE BINDER USING DISPERSED PERLITE AND A COLLOIDAL ADDITIVE

Larisa A. Urkhanova [1], Andrey A. Ivanov [2], Solbon A. Lkhasaranov [2]

[1] National Research Moscow State University of Civil Engineering, Moscow, RUSSIA
[2] East Siberian State University of Technology and Management, Ulan-Ude, RUSSIA

Abstract: Concreting of massive hydraulic structures is accompanied by the phenomenon of exothermic heating of structures caused by the process of cement hydration. Under natural conditions, the heat released in massive concrete is slowly removed from the structure. Often, a significant temperature difference occurs between the central part of the massif and its surface. If the critical value of the temperature difference is reached, temperature cracks occur, violating the monolithicity of the structures.

In order to solve the problem of crack formation, the article considers the possibility of obtaining hydraulic concrete using a composite binder based on finely dispersed aluminosilicate rocks - perlites, a colloidal additive in the form of silicic acid sol and a superplasticizer.

To obtain a composite binder, aluminosilicate materials - perlite rocks with different degrees of crystallinity were ground in a laboratory vibratory grinder to the required specific surface. To obtain a colloidal additive - silicic acid sol, the method of hydrolysis of soluble salts was used in the work, in particular sodium fluorosilicate Na_2SiF_6 without removing sodium cations Na^+. The crack resistance index of hydraulic concrete Ktr was determined indirectly by the ratio of the tensile strength of concrete under bending to the compressive strength - Rben/Rcom. The grade of concrete water resistance was assessed by an express method for determining the water resistance of concrete by its air permeability.

It has been established that the most rational compositions are composite binders containing 10-20% glassy perlite, with a specific surface area of 600 m^2/kg, a colloidal additive in the form of silicic acid sol in an amount of 0.4% of the cement weight and the Polyplast superplasticizer, which provides an increase in the compressive strength of hydrated stone after 28 days by 33% and an increase in bending strength by 40-45% compared to the control composition. At the same time, the crack resistance index of hydraulic concrete Ktr using finely dispersed perlite, silicic acid sol and the Polyplast polycarbide superplasticizer increases by 21% compared to the control concrete composition, the concrete grade for water resistance is W16, which is 60% higher than the water resistance grade of the control concrete composition.

Keywords: hydraulic concrete, plasticizing additive, silica sol, glassy perlite, crystallized perlite, degree of dispersion, specific surface, water resistance, crack resistance, compressive strength

ГИДРОТЕХНИЧЕСКИЙ БЕТОН НА ОСНОВЕ КОМПОЗИЦИОННОГО ВЯЖУЩЕГО С ПРИМЕНЕНИЕМ ДИСПЕРСНОГО ПЕРЛИТА И КОЛЛОИДНОЙ ДОБАВКИ

Л.А. Урханова [1], А.А. Иванов [2], С.А. Лхасаранов [2]

[1] Национальный исследовательский Московский государственный строительный университет, г. Москва, РОССИЯ
[2] Восточно-Сибирский государственный университет технологий и управления, г. Улан-Удэ, РОССИЯ

Аннотация: Бетонирование массивных гидротехнических сооружений сопровождается явлением экзотермического разогрева конструкций, вызванного процессом гидратации цемента. В естественных условиях выделяемое в массивном бетоне тепло медленно отводится из конструкции. Часто между центральной частью массива и его поверхностью возникает значительный температурный перепад. В случае достижения критической величины температурного перепада возникают температурные трещины, нарушающие монолитность конструкций.

В статье для решения вопроса трещинообразования рассмотрена возможность получения гидротехнического бетона с использованием композиционного вяжущего на основе тонкодисперсных алюмосиликатных пород - перлитов, коллоидной добавки в виде золя кремниевой кислоты и суперпластификатора.

Для получения композиционного вяжущего алюмосиликатные материалы - перлитовые породы с разной степенью кристалличности измельчали в лабораторном виброистирателе до необходимой удельной поверхности. Для получения коллоидной добавки - золя кремниевой кислоты в работе применяли способ гидролиза растворимых солей, в частности кремнефтористого натрия Na_2SiF_6 без удаления катионов натрия Na^+. Показатель трещиностойкости гидротехнического бетона $K_{тр}$ определялся косвенно по отношению прочности бетона на растяжение при изгибе к прочности при сжатии - $R_{изг}/R_{сж}$. Марка по водонепроницаемости бетона оценивалась экспресс-методом определения водонепроницаемости бетона по его воздухопроницаемости.
Установлено, что наиболее рациональными являются составы композиционных вяжущих с содержанием 10-20% стекловидного перлита, с удельной поверхностью 600 м^2/кг, коллоидной добавки в виде золя кремниевой кислоты в количестве 0,4% от массы цемента и суперпластификатором Полипласт, обеспечивающим прирост прочности на сжатие гидратного камня через 28 суток на 33% и прирост прочности на изгиб - на 40-45% по сравнению с контрольным составом. При этом показатель трещиностойкости гидротехнического бетона $K_{тр}$ с использованием тонкодисперсного перлита, золя кремниевой кислоты и поликарбрксилатного суперпластификатора «Полипласт» увеличивается 21% по сравнению с контрольным составом бетона, марка бетона по водонепроницаемости составляет W16, что больше марки по водонепроницаемости контрольного состава бетона на 60%.

Ключевые слова: гидротехнический бетон, пластифицирующая добавка, золь кремниевой кислоты, стекловидный перлит, закристаллизованный перлит, степень дисперсности, удельная поверхность, водонепроницаемость, трещиностойкость, прочность при сжатии

INTRODUCTION

Currently, due to the development of hydraulic engineering construction in the Siberian and Far Eastern regions of Russia, there is a need for concrete for hydraulic engineering structures. According to GOST 26633-2015, it is recommended to use sulfate-resistant and pozzolanic cements as a binder for the production of hydraulic engineering concrete. However, the use of such cements leads to a significant increase in the cost of hydraulic engineering concrete, since these types of Portland cement are much more expensive than ordinary Portland cement and the production volume of such cements is limited [1].

Concretes for hydraulic engineering structures must meet increased durability requirements imposed on them under operating conditions at the boundary of air and water environments. Under such conditions, cracking in hydraulic engineering concrete is most dangerous. As a result of cement hydration, heat is released, which initially causes compressive stresses in hydraulic engineering structures. Then, as a result of a decrease in temperature, concrete shrinkage occurs and tensile stresses appear. At the moment when tensile stresses exceed the tensile strength of concrete, cracks are formed [2-4].

Improvement of the characteristics of hydraulic concrete can be achieved by introducing active mineral additives into Portland cement, which eliminate the negative impact of a high temperature gradient during cement hydration by modifying the structure of the cement stone, increasing water resistance, increasing corrosion resistance, reducing overall porosity, increasing the physical and mechanical and operational properties of hydraulic concrete [5-7]. In addition, the formation of the physical and mechanical characteristics of concrete is interconnected with the formation of new complex hydrate compounds with improved characteristics and a certain crystallization structure, which also affects the physical and mechanical properties of concrete. There are works on the use of microsilica in combination with surfactants, which, in accordance with their chemical nature, have a positive effect on improving the properties of artificial stone, but the effectiveness of their action as a result of limited reaction activity does not ensure the creation of concrete of a new level of properties [8].

In the presented work, perlite rocks subjected to mechanochemical activation in energy-intensive devices, an ultrafine silica additive and a superplasticizer based on polycarboxylate were used to obtain hydraulic concrete. An ultrafine silica

additive in the form of a sol and an active mineral additive subjected to mechanical activation will contribute to improving the microstructure of cement stone due to water reduction of the cement system, the formation of a dense packing of particles of a dispersed composite binder and hydration interaction of Portland cement with silica-containing additives [9], improving the physical and mechanical properties of concrete with their use.

MATERIALS AND METHODS

To improve the properties and increase the crack resistance of hydraulic concrete based on finely dispersed, colloidal additives and surfactants, Portland cement CEM I 42.5 N GOST 31108-2020 OOO Timlyuycement was used as a binder. Finely ground glassy and crystallized perlite from the Mukhor-Talinskoye deposit (Republic of Buryatia) were used as active mineral additives depending on the composition. The chemical compositions of glassy and crystallized perlite are given in Table 1.

Table 1. Chemical composition of glassy and crystallized perlite, mass.%

Material	SiO_2	Al_2O_3	Fe_2O_3	FeO	CaO	MgO	TiO_2	SO_3	K_2O	Na_2O	R_2O	p.p.p.
Perlite vitreous	68,40	13,75	0,50	0,06	0,50	0,30	0,15	0,10	3,91	3,37	-	5,97
Crystallized perlite	73,13	11,7	1,08	1,71	0,55	0,30	-	-	-	-	6,4	7,65

Perlites were pre-crushed in a laboratory vibratory grinder VI-4x350 to a specific surface of 550 - 600 m^2/kg. A superplasticizer based on modified polycarboxylates (OOO "Polyplast-Sibir") was used as a surfactant, introduced into the cement with mixing water in an amount of 0.2% of the cement weight. The basis of the superplasticizer "Polyplast" are polycarboxylate esters. To obtain a silicic acid sol - a colloidal additive, a method of hydrolysis of soluble salts was used in the work, in particular sodium fluorosilicate Na_2SiF_6 without removing sodium cations Na^+. The optimal concentration of the sol is 0.75%. Hydrolysis of sodium fluorosilicate occurs according to the following reaction:

$$Na_2SiF_6 + 4H_2O \rightarrow 2NaF + 4HF + H_4SiO_4, \quad (1)$$

The resulting silicic acid sol in the form of an aqueous solution has a density of 1.018 g/cm^3, the value of the hydrogen index pH = 4.5-4.8, was introduced into the composition of concrete with mixing water with an optimal concentration of 0.4% of the cement weight.

The superplasticizer "Polyplast PK type S" based on modified polycarboxylates (OOO "Polyplast-Sibir") was used as a surfactant, introduced into the composition of cement with mixing water. The basis of the superplasticizer "Polyplast" are polycarboxylate esters.

The binder was prepared by thoroughly mixing Portland cement and finely dispersed glassy and crystallized perlite, crushed to a specific surface of 550-600 m^2/kg.

Concrete mix using composite binder with workability grade P3 (cone slump 12 cm) was prepared by mixing in a laboratory concrete mixer for 1 min pre-dosed components - Portland cement, finely dispersed perlite, sand with fineness modulus Mkr. = 2.1, crushed stone of fraction 10-20 mm and water containing dosed silica-containing component - silicic acid sol and superplasticizer Polyplast. From concrete mix of equal mobility, cube samples measuring 100x100x100 mm were molded, which were tested according to standard methods. For each type of test, samples were made in accordance with the requirements of GOST 10181-2014 "Concrete mixes. Test methods", GOST 10180-2012 "Concretes. Methods for Determining Strength Using Control Samples", GOST 12730.5-2018 "Concrete. Methods for Determining Water Resistance", GOST 24452-2023 "Concrete. Methods for Determining Prism Strength, Elastic Modulus, and Poisson's Ratio". The crack resistance index of hydraulic concrete Ktr was determined indirectly by the ratio of concrete tensile strength under bending to compressive strength - Rben/Rcom.

RESULTS AND DISCUSSION

All the components under study in rational quantities provide improvement of physical and mechanical properties of hydraulic concrete (Table 2).

Table 2. Effect of dispersed perlite, specific surface area of 600 m^2/kg and silica sol on physical and mechanical properties of hydraulic concrete

Name	Compressive strength, in MPa, after hardening for			Bending strength, in MPa, after hardening for		Ktr (Rben /Rcom)
	3 days	7 days	28 days	7 days	28 days	
Control composition	24,6	34,8	38,7	4,1	7,1	0,18
PC+ 10% Vitreous perlite+ Polyplast	25,4	36,3	39,9	4,3	7,3	0,18
PC+ 20% Vitreous perlite+ Polyplast	25,6	37,4	40,7	4,5	6,9	0,17
PC+ Sol $_6$+ Polyplast	30,8	37,4	40,9	5,6	9,1	0,22
PC+ 10% Vitreous perlite+ + Sol + Polyplast	33,1	39,0	48,6	6,9	10,6	0,22
PC+ 20% Vitreous perlite + Sol + Polyplast	35,2	42,4	53,4	7,8	10,9	0,20
PC+ 10% Crystallized perlite + Sol + Polyplast	32,6	38,5	41,1	4,0	6,9	0,16
PC+ 20% Crystallized perlite + Sol + Polyplast	33,2	40,0	42,9	4,4	7,6	0,17

Introduction of finely ground perlite into the concrete composition leads to an increase in the water-binding ratio by 7-13%. The use of the polycarboxylate superplasticizer Polyplast in an optimal amount of 0.2% of the binder weight not only reduces water consumption by 9-16%, thereby compensating for the loss of strength of hydrated stone associated with a decrease in the amount of cement in the composition, but also changes the structure of hardened concrete.

Colloidal additive in combination with finely ground perlite and plasticizer has a positive effect on increasing the strength of concrete. The maximum values of compressive strength were shown by the compositions with the addition of vitreous perlite and silicic acid sol: PC + 20% vitreous perlite + sol in the amount of 0.4% of the cement mass + Polyplast - 53.4 MPa, which is 33% higher than the strength of the control composition, respectively.

The use of polycarboxylate polymer in combination with fine and ultrafine silica-containing additives, to the greatest extent, starting from an early age, increases the tensile strength of concrete in bending. The maximum values of concrete tensile strength in bending at the age of 28 days were shown by concrete compositions: PC + 10% vitreous perlite + sol in the amount of 0.4% of the cement mass - 10.6 MPa; PC + 20% vitreous perlite + sol in the amount of 0.4% of the cement mass – 10.9 MPa, which is on average 40-45% greater than the flexural strength of the control concrete composition.

The increase in strength is the result of the influence of perlite on the structure and chemical and mineralogical composition of hydraulic concrete on a composite binder. A significant role is played by the chemical factor of perlite action, which is expressed in a change in the balance between the hydrated phases in the composition of cement stone towards an increase in the volume of stronger and more stable low-base calcium hydrosilicates (CHS) with the formation of dense conglomerate structures [9, 10]. The amorphous phase of silica, contained in large volumes in vitreous perlite, leads to an increase in compressive strength due to the replacement of the mechanically weak phase of calcium hydroxide with a stronger hydrosilicate phase [11].

The presence of a glassy phase (60-80%) in the perlite composition causes an increase in the

strength of composite cement compared to the use of crystallized perlite of equal chemical composition, which is associated with an increase in the content of the amorphous phase in aluminosilicate rocks, their further amorphization during fine grinding in energy-intensive grinders [12]. Amorphous silica in perlite binds free calcium hydroxide formed during cement hydration, with the formation of an additional amount of low-basic calcium hydrosilicates.

In addition, as studies have shown, the morphology of the particles of the original crushed materials of natural and artificial origin changes depending on the grinding method [13]. In an energy-intensive grinder, which includes a rod vibratory grinder, during the grinding of glassy perlite, more rounded grains of the material are formed with a small amount of roughness on the surface, as a result of which the particles fit more tightly to each other with an increase in the contact surface, which indicates the efficiency of grinding the raw material in the rod vibratory grinder. When grinding crystallized perlite, grains of a flat, elongated shape are formed with the formation of a less dense packing of mixtures using it.

A colloidal additive, represented by a silicic acid sol, turns into a gel, compacting the microstructure of the hardening system, and also enhances the hydration activity of silicate-containing minerals of Portland cement and interacts with hydrolytic lime, thereby ensuring the formation of tobermorite-like calcium hydrosilicates, which in turn reinforce the hardening system, providing increased bending strength [14].

The crack resistance index of hydraulic concrete Ktr, indirectly estimated by the ratio Rben/Rcom, using finely dispersed perlite and silica sol is 0.22, which exceeds the crack resistance index of concrete without additives by 21%.

The results of the physical and mechanical properties of concrete confirm the resistance of concrete based on a composite binder, with colloidal and plasticizing additives to crack formation. To increase the durability and crack resistance of hydraulic concrete, studies were carried out to determine the deformation properties of concrete (Table 3).

Table 3. Deformative properties of hydraulic concrete based on composite binder

Compound	Prism strength, MPa		Modulus of elasticity Eb, MPa × 10^3		Poisson's ratio	
	3 days	28 days	3 days	28 days	3 days	28 days
PC	19,8	34,6	22974	32362	0,18	0,216
PC + 20% vitreous perlite + Polyplast	23,4	40,2	24084	35680	0,18	0,202
PC + Sol + Polyplast	25,6	39,6	23742	34493	0,17	0,191
PC + 20% vitreous pearl + Sol + Polyplast	30,1	46,3	26247	37345	0,17	0,199

The prismatic strength of hydraulic concrete on the optimal compositions with the combined use of finely dispersed perlite, silica sol and superplasticizer Polyplast in relation to the compressive strength is 17%, while on the control samples this ratio is 9%, which confirms the increased resistance of concrete to cracking. The increase in the prismatic strength of hydraulic concrete is mainly due to the high cubic strength of the presented concrete compositions compared to the control sample.

The modulus of elasticity of the hydraulic concrete compositions using finely dispersed perlite + superplasticizer Polyplast and the composition of silica sol + superplasticizer Polyplast increased on average by 3-5% in 3 days and by 7-10% in 28 days compared to the control composition. The composition with the combined use of vitreous perlite, silica sol and the superplasticizer Polyplast increases the modulus of elasticity compared to the control composition at 3 days by 14%, at 28 days - by 15%, respectively.

The increase in the modulus of elasticity of hydraulic concrete based on a composite binder occurs due to the compaction of the structure due to the interaction of perlite, sol and superplasticizer with cement hydration products and the formation of additional bonds in the form of calcium hydrosilicates. Also, the increase in the modulus of elasticity is associated with a lower water-cement ratio, at which porosity decreases, which causes an increase in the modulus of elasticity [15, 16].

The Poisson ratio at the age of 3 days for the composition with vitreous perlite remained unchanged compared to the control composition. The Poisson ratio for the compositions with silica sol + Polyplast and the composition with vitreous perlite + sol + Polyplast decreased by 5% compared to the control composition. At the age of 28 days, the Poisson's ratio for the compositions: vitreous perlite + Polyplast; sol + Polyplast; vitreous perlite + sol + Polyplast decreased by 6, 11 and 8%, respectively.

The decrease in the Poisson's ratio of modified concrete can be explained by the fact that when introducing a polycarboxylate superplasticizer and silicic acid sol, due to the modification of the concrete structure, a greater number of structural elements are formed in the hydrated shells of the grains, and, consequently, the sliding surface of the particles increases, which leads to a more intensive reduction in transverse deformations and a decrease in the Poisson's ratio [17, 18].

To ensure the durability of hydraulic concrete, it is important to ensure a high value of water resistance. The concrete grade by water resistance, estimated by the express method of determining the water resistance of concrete by its air permeability, for the compositions of hydraulic concrete using finely dispersed perlite + superplasticizer Polyplast and the composition of silica sol + superplasticizer Polyplast is W12 and W14, which exceeds the water resistance of concrete without additives by 20 and 40%, respectively (Table 4). The composition with the combined use of glassy perlite, silica sol and superplasticizer Polyplast increases the concrete grade by water resistance by 60% compared to the control composition - up to W16.

The increase in water resistance can be explained by the fact that during the polycondensation process, which takes place at all stages of the sol-gel process, microgel structures are formed containing molecules of different molecular weights (from monomer to polymers) [19-21]. Polycondensation in the volume of particles leads to their compaction. At the gelation stage, this reaction helps to strengthen the coagulation contacts between particles [22]. In turn, the gelation products fill the micropores of the concrete structure with sol particles and the products of its interaction, thereby creating a dense structure [23-25]. The introduction of perlite into the composition of concrete leads to the formation of low-basic calcium hydrosilicates, which in turn also increase water resistance.

Table 4. Concrete grade by water resistance

Compound	Time of pressure drop in the chamber of the VV-2 device, s	Concrete grade by water resistance
PC	186 сек.	W10
PC + 20% vitreous perlite + Polyplast	294 сек.	W12
PC + Sol + Polyplast	391 сек.	W14
PC + 20% vitreous perlite + Sol + Polyplast	573 сек.	W16

CONCLUSIONS

It is possible to obtain durable concrete for hydraulic structures with high initial strength, increased water resistance and crack resistance by using highly effective plasticizers, active mineral additives of natural origin, subjected to mechanical activation in order to obtain finely dispersed additives, and ultra-dispersed additives obtained using sol-gel technologies.

Thus, it can be concluded that the additive for hydraulic concrete using vitreous perlite, silicic acid sol and superplasticizer based on polycarboxylate polymers is effective, the use of which promotes the formation of low-basic calcium hydrosilicates, the formation of a denser microstructure of cement stone, while improving the strength properties of modified cement stone in concrete, which, in our opinion, can increase the thermal crack resistance of hydraulic concrete.

REFERENCES

1. **Grigoriev V.G., Kozlova V.K., Andryushina E.E., Shkrobko E.V., Likhosherstov A.A.** (2012) Composite Portland cements for

hydraulic engineering construction // Polzunovsky Vestnik. no. 1-2. pp. 62-64. URL:https://cyberleninka.ru/article/n/kompozitsionnye-portlandtsementy-dlya-gidrotehnicheskogo-stroitelstva.

2. **Ivanov A.A., Urkhanova L.A., Lkhasaranov S.A., Khardaev P.K.** (2023) Study of the influence of finely dispersed additives on the properties of composite binders for hydraulic concrete // Vestnik of VSGUTU. no. 2 (89). pp. 80-88. DOI: 10.53980/24131997_2023_2_80
3. **Li Q., Liang G., Hu Y., Zuo Z.** (2014) Numerical analysis on temperature rise of a concrete arch dam after sealing based on measured data // Mathematical Problems in Engineering. no 6, pp. 1-10. DOI:10.1155/2014/602818
4. **Aniskina N.A, Chong Chyk Nguyen.** (2020) The problem of temperature cracking in concrete gravity dams // Bulletin of MGSU. no. 3. pp. 380-398. DOI: 10.22227/1997-0935.2020.3.380-398
5. **Yerramala A., Ganesh Babu K.** (2011) Transport properties of high-volume fly ash roller compacted concrete // Cement and Concrete Composites. no. 33, issue. 10. pp. 1057–1062. DOI:10.1016/j.cemconcomp.2011.07.010
6. **Dolen T.P., Ibáñez-de-Aldecoa R., Eharz J.L., Dunstan M.R.H.** (2003) Successful large RCC dams – what are the common features? // Proceedings of the fourth international symposium on roller compacted concrete (RCC) dams. no. 2. pp. 127–137. DOI:10.34031/2071-7318-2020-5-8-8-17
7. **Larsen O.A., Aleksandrova O.V., Narut V.V., Polozov A.A., Bakhrakh A.M.** (2020) Study of the properties of active mineral additives for use in hydraulic engineering // Bulletin of BSTU named after V.G. Shukhov. no. 8. pp. 8-14. DOI: 10.34031/2071-7318-2020-5-8-8-17
8. **Kasatkin S.P.** (2023) Highly efficient concrete modified with a complex chemical additive containing nanodispersions of silicon hydrodioxide: dissertation for the degree of Candidate of Technical Sciences. – St. Petersburg. 138 p. URL: https://pstu.ru/files/2/file/Dissertaciya._Kasatkin_S.P._02.07.2023.pdf
9. **Urkhanova, L.A., Ivanov A.A., Lhasaranov S.A.** (2024) Composite cement with dispersed perlite and colloidal additive for hydraulic concrete // Cement and its application. no. 1-2024. DOI: 10.61907/CIA.2024.87.76.001
10. **Bazhenov Yu.M., Alimov L.A., Voronin V.V.** (2013) Structure and properties of concrete with nanomodifiers based on technogenic waste. Moscow: MISI-MGSU. 201 p. URL: https://mgsu.ru/resources/izdatelskaya-deyatelnost/izdaniya/monografii/1725/?ysclid=m09bb4v43i945506938
11. **Shane D., Mark T., Cheeseman C.R.** (2010) Comparison of test methods to assess pozzolanic activity // Cement and Concrete Composites. no. 32 (2). pp. 121–127. DOI:10.1016/j.cemconcomp.2009.10.008
12. **Urkhanova L.A., Tsydypova A.T.** (2018) Effect of silica sol on the physical and mechanical properties of polystyrene concrete // Construction materials. no. 1–2. pp. 45–51. DOI: https://doi.org/10.31659/0585-430X-2018-756-1-2-45-51
13. **Zhernovoy F.E., Miroshnikov E.V.** (2018) Comprehensive assessment of factors for increasing the strength of cement stone by adding ultrafine perlite // Bulletin of the V.G. Shukhov BSTU. no. 2. pp. 55–60. URL: https://cyberleninka.ru/article/n/kompleksnaya-otsenka-faktorov-povysheniya-prochnosti-tsementnogo-kamnya-dobavkami-ultradispersnogo-perlita
14. **Lesovik V.S., Zhernovoy F.E., Glagolev E.S.** (2009) Use of natural perlite in the composition of mixed cements // Construction materials. no. 6. pp. 84–87. URL: https://elibrary.ru/kuucdt?ysclid=m09bh8i6g321380846
15. **Aniskin N.A., Nguyen T.C., Hoang Q.L.** (2018) Influence of size and construction schedule of massive concrete structures on its temperature regime // MATEC Web of Con-

ferences. vol. 251. p. 02014. DOI: 10.1051/matecconf/201825102014
16. **Hai T.H., Thuc L.V.** (2017) The effect of splitting concrete placement on controlling thermal cracking in mass concrete // Journal of Science and Technology in Civil Engineering. vol. 11. issue 6. pp. 22–28. URL: http://stce.nuce.edu.vn/index.php/en/article/view/932
17. **Hang X., Shi R., Dai H., Liu Q., Zhang X.** (2019) Simulation and research on temperature field of taishan roller compacted concrete gravity dam // IOP Conference Series: Earth and Environmental Science. vol. 237. p. 032117. DOI: 10.1088/1755-1315/237/3/032117
18. **Lkhasaranov S.A., Urkhanova L.A., Ivanov A.A., Smirnyagina N.N.** (2024) Study of phase composition of composite binders for hydraulic concrete // Bulletin of VSGUTU. no. 2 (93). DOI 10.53980/24131997_2024_2_112
19. **Dem'yanenko O.V., Kopanitsa N.O., Sarkisov Y.S.** (2020) Study of the properties of cement stone with a complex additive // Bulletin of TSUACE. vol. 22, no. 4. pp. 147–156. DOI: 10.31675/1607-1859-2020-22-4-147-156
20. **Zelenkevich D.S., Yagubkin A.N., Bozylev V.V.** (2013) Use of polymer-mineral additives to improve the water resistance and frost resistance of concrete // Bulletin of Polotsk State University. Series F. Construction. Applied Sciences. no. 16. URL: https://cyberleninka.ru/article/n/ispolzovanie-polimerno-mineralnyh-dobavok-dlya-povysheniya-vodonepronitsaemosti-i-morozostoykosti-betona
21. **Bayburin A.Kh., Kocharina E.N., Kocharin N.V., Kiyanets A.V., Lebed A.R.** (2022) Influence of chemical additives on the properties of concrete // IVD. no. 6 (90). URL: https://cyberleninka.ru/article/n/vliyanie-himicheskih-dobavok-na-svoystva-betona.
22. **Izotov B.S., Seliverstova O.V., Krasnova T.A.** (2010) Influence of polyacrylate-based hyperplasticizer on the strength, density and water resistance of concrete // Izvestiya KazGASU. no. 1 (13). URL: https://cyberleninka.ru/article/n/vliyanie-giperplastifikatora-na-osnove-poliakrilatov-na-prochnost-plotnost-i-vodonepronitsaemost-betona.
23. **Nguyen T.C., Huynh T.P., Tang V.L.** (2019) Prevention of crack formation in mass concrete at early age by cooling pipe system // Asian Journal of Civil Engineering. vol. 20. issue 8. pp. 1101–1107. DOI: 10.1007/s42107-019-00175-5
24. **Solovieva V.Y., Stepanova I.V., Kasatkina A.V.** (2010) New generation protective coatings for transport building structures // Transport of the Russian Federation. Journal of Science, Practice, Economics. no. 2 (27). URL: https://cyberleninka.ru/article/n/zaschitnye-pokrytiya-novogo-pokoleniya-dlya-transportnyh-stroitelnyh-konstruktsiy
25. **Nguyen T.C., Luu X.B.** (2019) Reducing temperature difference in mass concrete by surface insulation // Magazine of Civil Engineering. vol. 4 (88). pp. 70–79. DOI: 10.18720/MCE.88.

СПИСОК ЛИТЕРАТУРЫ

1. **Григорьев В.Г., Козлова В.К., Андрюшина Е.Е., Шкробко Е.В., Лихошерстов А.А.** (2012) Композиционные портландцементы для гидротехнического строительства // Ползуновский вестник. №1-2. С. 62-64. URL: https://cyberleninka.ru/article/n/kompozitsionnye-portlandtsementy-dlya-gidrotehnicheskogo-stroitelstva.
2. **Иванов А.А., Урханова Л.А., Лхасаранов С.А., Хардаев П.К.** (2023) Исследование влияния тонкодисперсных добавок на свойства композиционных вяжущих для гидротехнического бетона // Вестник ВСГУТУ. № 2(89). С. 80-88. DOI: 10.53980/24131997_2023_2_80

3. **Li Q., Liang G., Hu Y., Zuo Z.** (2014) Numerical analysis on temperature rise of a concrete arch dam after sealing based on measured data // Mathematical Problems in Engineering, no. 6, pp. 1-10. DOI:10.1155/2014/602818
4. **Анискин Н.А, Чонг Чык Нгуен.** (2020) Проблема температурного трещинообразования в бетонных гравитационных плотинах // Вестник МГСУ, №3. – С. 380-398. DOI: 10.22227/1997-0935.2020.3.380-398
5. **Yerramala A., Ganesh Babu K.** (2011) Transport properties of high-volume fly ash roller compacted concrete // Cement and Concrete Composites. № 33, issue. 10. pp. 1057–1062. DOI:10.1016/j.cemconcomp.2011.07.010
6. **Dolen T.P., Ibáñez-de-Aldecoa R., Eharz J.L., Dunstan M.R.H**. (2003) Successful large RCC dams – what are the common features? // Proceedings of the fourth international symposium on roller compacted concrete (RCC) no. 2. pp. 127–137. DOI:10.34031/2071-7318-2020-5-8-8-17
7. **Ларсен О.А., Александрова О.В., Наруть В.В., Полозов А.А., Бахрах А.М.** (2020) Исследование свойств активных минеральных добавок для применения в гидротехническом строительстве // Вестник БГТУ имени В. Г. Шухова. №8. С. 8-14. DOI: 10.34031/2071-7318-2020-5-8-8-17.
8. **Касаткин С.П.** (2023) Высокоэффективный бетон, модифицированный комплексной химической добавкой, содержащей нанодисперсии гидродиоксида кремния: диссертация на соискание уч. степени канд. техн. наук. – Санкт-Петербург, – 138 с. URL: https://pstu.ru/files/2/file/Dissertaciya._Kasatkin_S.P._02.07.2023.pdf
9. **Урханова, Л.А., Иванов А.А., Лхасаранов С.А.** (2024) Композиционный цемент с дисперсным перлитом и коллоидной добавкой для гидротехнического бетона // Цемент и его применение. № 1-2024. DOI: 10.61907/CIA.2024.87.76.001
10. **Баженов Ю.М., Алимов Л.А., Воронин В.В.** (2013) Структура и свойства бетонов с наномодификаторами на основе техногенных отходов. М.: МИСИ-МГСУ. 201 с. URL: https://mgsu.ru/resources/izdatelskaya-deyatelnost/izdaniya/monografii/1725/?ysclid=m09bb4v43i945506938
11. **Shane D., Mark T., Cheeseman C.R.** (2010) Comparison of test methods to assess pozzolanic activity // Cement and Concrete Composites. № 32 (2). pp. 121–127. DOI:10.1016/j.cemconcomp.2009.10.008
12. **Урханова Л.А., Цыдыпова А.Ц.** (2018) Влияние золя кремнекислоты на физико-механические свойства полистиролбетона //Строительные материалы. №1-2. С.45-51. DOI: https://doi.org/10.31659/0585-430X-2018-756-1-2-45-51
13. **Жерновой Ф.Е., Мирошников Е.В.** (2009) Комплексная оценка факторов повышения прочности цементного камня добавками ультрадисперсного перлита // Вестник БГТУ имени В. Г. Шухова. №2. С. 55-60. URL: https://cyberleninka.ru/article/n/kompleksnaya-otsenka-faktorov-povysheniya-prochnosti-tsementnogo-kamnya-dobavkami-ultradispersnogo-perlita
14. **Лесовик В.С., Жерновой Ф.Е., Глаголев Е.С.** (2009) Использование природного перлита в составе смешанных цементов // Строительные материалы. № 6. С. 84-87. URL: https://elibrary.ru/kuucdt?ysclid=m09bh8i6g321380846
15. **Aniskin N.A., Nguyen T.C., Hoang Q.L.** (2018) Influence of size and construction schedule of massive concrete structures on its temperature regime // MATEC Web of Conferences. vol. 251. p. 02014. DOI: 10.1051/matecconf/201825102014
16. **Hai T.H., Thuc L.V.** (2017) The effect of splitting concrete placement on controlling thermal cracking in mass concrete // Journal of Science and Technology in Civil Engineering. vol. 11. issue 6. pp. 22–28. URL: http://stce.nuce.edu.vn/index.php/en/article/view/932
17. **Hang X., Shi R., Dai H., Liu Q., Zhang X.** (2019) Simulation and research on tempera-

ture field of taishan roller compacted concrete gravity dam // IOP Conference Series: Earth and Environmental Science. vol. 237. p. 032117. DOI: 10.1088/1755-1315/237/3/032117

18. **Лхасаранов С.А., Урханова Л.А., Иванов А.А., Смирнягина Н.Н.** (2024) Исследование фазового состава композиционных вяжущих для гидротехнического бетона // Вестник ВСГУТУ. №2 (93). DOI 10.53980/24131997_2024_2_112
19. **Демьяненко О.В., Копаница Н.О., Саркисов Ю.С.** (2020) Исследование свойств цементного камня с комплексной добавкой // Вестник ТГАСУ. – Т. 22, № 4. – С. 147–156. DOI: 10.31675/1607-1859-2020-22-4-147-156
20. **Зеленкевич Д.С., Ягубкин А.Н., Бозылев В.В.** (2013) Использование полимерно-минеральных добавок для повышения водонепроницаемости и морозостойкости бетона // Вестник Полоцкого государственного университета. Серия F. Строительство. Прикладные науки. №16. URL: https://cyberleninka.ru/article/n/ispolzovanie-polimerno-mineralnyh-dobavok-dlya-povysheniya-vodonepronitsaemosti-i-morozostoykosti-betona
21. **Байбурин А.Х., Кочарина Е.Н., Кочарин Н.В., Киянец А.В., Лебедь А.Р.** (2022) Влияние химических добавок на свойства бетона // ИВД. №6 (90). URL: https://cyberleninka.ru/article/n/vliyanie-himicheskih-dobavok-na-svoystva-betona.
22. **Изотов В.С., Селиверстова О.В., Краснова Т.А.** (2010) Влияние гиперпластификатора на основе полиакрилатов на прочность, плотность и водонепроницаемость бетона // Известия КазГАСУ. №1 (13). URL: https://cyberleninka.ru/article/n/vliyanie- giper-plastifikatora-na-osnove-poliakrilatov-na-prochnost-plotnost-i-vodonepronitsaemost-betona.
23. **Nguyen T.C., Huynh T.P., Tang V.L.** (2019) Prevention of crack formation in mass concrete at early age by cooling pipe system // Asian Journal of Civil Engineering. vol. 20. issue 8. pp. 1101–1107. DOI: 10.1007/s42107-019-00175-5
24. **Соловьева В.Я., Степанова И.В., Касаткина А.В.** (2010) Защитные покрытия нового поколения для транспортных строительных конструкций // Транспорт Российской Федерации. Журнал о науке, практике, экономике. №2 (27). URL: https://cyberleninka.ru/article/n/zaschitnye-pokrytiya-novogo-pokoleniya-dlya-transportnyh-stroitelnyh-konstruktsiy
25. **Nguyen T.C., Luu X.B.** (2019) Reducing temperature difference in mass concrete by surface insulation // Magazine of Civil Engineering. vol. 4 (88). pp. 70–79. DOI: 10.18720/MCE.88.

Larisa Alekseevna Urkhanova - Doctor of Technical Sciences, Professor of the Department of Urban Development, National Research Moscow State University of Civil Engineering (NRU MGSU), 129337, Moscow, Yaroslavskoe shosse, 26, urkhanova@mail.ru

Andrey Andreevich Ivanov - Postgraduate Student, Department of Construction Materials, Highways and Woodworking, East Siberian State University of Technology and Management (VSGUTU), 670013, Ulan-Ude, Klyuchevskaya St., 40B, Bldg. 1, vadim290607@gmail.com

Solbon Aleksandrovich Lkhasaranov - Candidate of Technical Sciences, Associate Professor, Head of the Department of Construction Materials, Highways and Woodworking, East Siberian State University of Technology and Management (VSGUTU), 670013, Ulan-Ude, Klyuchevskaya, 40B, building 1, solbon230187@mail.ru

Лариса Алексеевна Урханова — доктор технических наук, профессор кафедры «Градостроительство», Национальный исследовательский Московский государственный строительный университет (НИУ МГСУ), 129337, г. Москва, Ярославское шоссе, д. 26, urkhanova@mail.ru

Андрей Андреевич Иванов – аспирант кафедры «Строительные материалы, автомобильные дороги и деревообработка», Восточно-Сибирский государственный университет технологий и управления (ВСГУТУ), 670013, г.Улан-Удэ, ул. Ключевская, д.40В, строение 1, vadim290607@gmail.com

Солбон Александрович Лхасаранов – кандидат технических наук, доцент, заведующий кафедрой «Строительные материалы, автомобильные дороги и деревообработка», Восточно-Сибирский государственный университет технологий и управления» (ВСГУТУ), 670013, г.Улан-Удэ, ул. Ключевская, д.40В, строение 1, solbon230187@mail.ru

International Journal for Computational Civil and Structural Engineering, 21(1) 79–92 (2025)

DOI:10.22337/2587-9618-2025-21-1-79-92

VARIATION OF PORE WATER PRESSURE IN OVER-CONSOLIDATED CLAY UNDER CYCLIC LOADING: EXPERIMENTAL INVESTIGATION

Ngoc-Thang Nguyen [1], Guo-Wei LI [2]

[1] Civil and Industrial Construction Division, Faculty of Civil Engineering, Thuyloi University, Hanoi, VIETNAM
[2] Key Laboratory of Ministry of Education for Geotechnique and Embankment Engineering, Hohai University, Nanjing, CHINA

Abstract: Under cyclic loading, the cyclical effect of external load during loading time will result in multiple rearrangement of soil particles, and thus causing the particles to arrange more closely together than un static loading. As the soil volume decreases with increase in the number of loading cycles, the accumulated excess pore water pressure dissipates through draining of the soil. This study presented results of prediction the behavior of clay in partially drained cyclic plane test. The results from cyclic triaxial test on a highly plastic marine clay were formulated to predict the time dependent variations of excess pore pressure and axial strains during partially drain cyclic loading. The study further revealed that when saturated clay is exposed to cyclic loading, the reduction in effective stress due to the generation of excess pore water pressure leads to a decrease in soil strength. Over the long term, the accumulation of pore water pressure in saturated clay is influenced by various factors, including the magnitude of the applied load, its frequency, and the intrinsic properties of the soil.

Keywords: Soft Clay, Consolidation, Cyclic Loading, Excess Pore Water Pressure

ИЗМЕНЕНИЕ ДАВЛЕНИЯ ПОРОВОЙ ВОДЫ В ПЕРЕУПЛОТНЕННОЙ ГЛИНЕ ПРИ ЦИКЛИЧЕСКОМ НАГРУЖЕНИИ: ЭКСПЕРИМЕНТАЛЬНОЕ ИССЛЕДОВАНИЕ

Нгок-Тханг Нгуен[1], Гуо-Вей Ли [2]

[1] Отделение гражданского и промышленного строительства, факультет гражданского строительства, Университет Тхуйлой, г. Ханой, ВЬЕТНАМ
[2] Главная лаборатория Министерства образования по геотехнике и строительству береговых сооружений, Университет Хохай, г. Нанкин, КИТАЙ

Аннотация: При циклическом нагружении циклическое воздействие внешней нагрузки в течение времени нагружения приводит к многократной перегруппировке частиц грунта, в результате чего частицы располагаются более плотно друг к другу, чем при статическом нагружении. Поскольку объем грунта уменьшается с увеличением количества циклов нагружения, накопленное избыточное давление поровой воды рассеивается за счет дренирования грунта. В данном исследовании представлены результаты прогнозирования поведения глины в частично дренированном циклическом плоском испытании. Результаты циклических трехосных испытаний высокопластичной морской глины были использованы для прогнозирования зависящих от времени изменений избыточного порового давления и осевых деформаций при циклическом нагружении с частичным дренированием. Исследование показало, что, когда насыщенная глина подвергается циклическому нагружению, снижение эффективного напряжения из-за создания избыточного давления поровой воды приводит к снижению прочности грунта. В долгосрочной перспективе на накопление давления поровой воды в насыщенной глине влияют различные факторы, включая величину приложенной нагрузки, ее частоту и собственные свойства грунта.

Ключевые слова: Мягкая глина, консолидация, циклическое нагружение, избыточное давление поровой воды

1. INTRODUCTION

The classic theory of consolidation was developed by Terzaghi (1943) [1]. This is still today the foundation of one-dimensional (1-D) consolidation theory. This theory, developed for the prediction of long term settlement of soil, uses the rate of seepage of pore water under the action of external load to determine the deformation of a layer of saturated soil. Conventional consolidation analysis based on Terzaghi's one-dimensional theory overlooks the non-linear characteristics of soil. Davis and Raymond (1965) [2] introduced a non-linear theory of soil consolidation. Wilson et al. (1974) [3], through theoretical analysis, noted that consolidation under cyclic loading progresses more slowly than under an equivalent sustained load, making it impossible to achieve 100% consolidation with cyclic loading. Baligh et al. (1978) [4] proposed a straightforward method for predicting the behavior of an inelastic clay layer initially in a normally consolidated state and subjected to cyclic loading. Favaretti et al. (1995) [5] developed a simplified solution to predict consolidation under cyclic loading for non-dimensional time intervals.

When the load is first applied the total stress increases but, as shown above for 1-D conditions, there can be no instantaneous change in vertical effective stress, implying that the pore-pressure must increase by exactly the same amount as the increase in total stress. Subsequently, there will be flow from regions of higher excess pore pressure to regions of lower excess pore-pressure, and the excess pore pressures will dissipate leading to change in effective stress and the soil will deform (consolidate) with time [6-8].

When soft clay soils are exposed to time-dependent cyclic loading, excess pore water pressure gradually builds up. After a certain number of cycles, this pore water pressure begins to dissipate, leading to progressive deformation over time often significantly greater than that caused by static loading. Common examples of cyclic loads include earthquakes, ocean waves, high-intensity traffic, seasonal fluctuations in groundwater levels, and changing fuel levels in oil tanks. Long-term cyclic loads, can sometimes induce consolidation of the underlying soil.

Yin et. al (1989) [9, 10] reported a case study on settlement of a road in "Jie Pu highway, in Guangdong province, China", built on a low bank road embankment on typical soft alluvial clay. It settled substantially after opening to traffic, which was nearly 2m over a length of 1700m. Xie et al. (2006) [11] reported a case study on long term settlement of break water constructed at the port of Tianjin in China due to static and wave-induced cyclic loads.

Chen et al. (2005) [12] predicted that pore water pressure increases during loading and decreases during unloading under low frequency cyclic loading with different boundary conditions.

Guo-Wei Li and Hu [13-15] studied the effect of dynamic cyclic loading and surcharge preloading method on the settlement of low embankments and showed that the settlement increases with increasing amplitude of cyclic load and the effectiveness of surcharge preloading depends on the difference between the magnitude of surcharge and amplitude of the cyclic load. This study presents selected results of the effects of the frequency on the post-construction settlement of low embankments subjected to cyclic loading and showed that under drained condition the variation of pore water pressure is compatible with the axial creep strain of soft clay in the over-consolidated state. The measured pore water pressure values can be used to assess the long-term settlement of the soft ground after construction.

When a clay sample is suddenly loaded in the oedometer test its void ratio or compression decreases with time. The consolidation process is traditionally divided into primary and secondary consolidation phases. During the primary consolidation phase settlement is controlled by the dissipation of excess pore pressures and Darcy's law. Whereas during secondary consolidation the rate of settlement is controlled by soil viscosity, Leroueil (1996)

[16]. However, settlement requires a hydraulic gradient, i.e. excess pore pressure exists at that stage. Secondary consolidation or creep is characterized by the slope of the consolidation/compression curve.

Soft soil is widely distributed over coastal and riverside regions, where the embankment loads are sensitive for differential settlement. In a marine environment, cyclic loading forms a significant proportion of the loading and this decides the safety of many structures founded on the ocean bed. By and large, marine structures subjected to cyclic loading are offshore petroleum production platforms, offshore pipelines, storm surge barriers and harbor structures [17]. The foundations of these structures truly transmit the cyclic loads to the soil below in one form or another. Rail track subgrade is very important for railway stability and therefore the behaviour of soft soil subgrade under cyclic loading is of paramount significance in railway engineering. Most of rail tracks travel through coastal areas comprising of soft soils and highly compressible marine deposits. Load cycles from moving trains rapidly generate high excess pore pressures. In the absence of good drainage conditions, cyclic pore pressure will dramatically reduce the effective load bearing capacity of the soft formation [18].

Zhu et al. 2005 [19] presented a study on the deformation behavior of a saturated soft clay under cyclic loading. Considering the intrinsic anisotropy of the soil, a soil specimen was initially restored to the in-situ stress state under K_0 consolidation in a triaxial cell, and the specimen was then sheared in the same triaxial cell under axial cyclic loading and tested under a drained or undrained creep condition. The test results show that the increase of excess pore water pressure initially lagged behind that of stress. The stable excess pore pressure was about 50% of the stress amplitude for an drained specimen. However the residual excess pore water pressure was approximately 20% of stress amplitude for a drained specimen.

When a pressure is applied to a saturated soil and drainage is allowed, the gradient of the excess pore pressure causes flow of water out of the soil, Prediction the dissipation of pore water pressure is important to understanding the behaviour of soils under cyclic loading and also for estimation of their effective stresses. In the proposed paper, an analytical solution for one-dimensional consolidation of soft cohesive soil under cyclic loading has been developed based on the formulations given by Thang.,.N.N. (2023) [20] and a hyperbolic relationship for generation of pore water pressure under drained condition. The model successfully explained the generation and dissipation of pore water pressure during consolidation under cyclic loading.

2. MODEL OF CYCLIC TRAFFIC LOAD

2.1 Numerical Model of Traffic Load Form

A method for analyzing the behavior of clay under long-term cyclic loading has been proposed by Hyodo and Yasuhara, in which Terzaghi's consolidation equation is proposed for calculating the settlement of low embankment subjected to the traffic load [21, 22]. Hyodo and Yasuhara used a 10-ton truck moving at different speeds of 0km/h, 10km/h, 20km/h, 30km/h, and 35km/h to simulate vehicular load and investigated the vertical stresses acting on top of a subgrade and at different depths of a low embankment. On the subgrade, the vertical stress waveform at some points, shown in Fig. 1, described as sine curve.

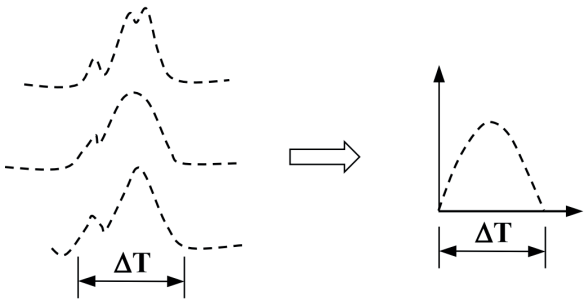

Figure 1. Vertical pressure waveform [21]

Based on the multi-layer elastic theory, Ling and Shoji [23, 24] conducted research on the residual deformation of saturated clay subgrade under vehicular load, analyzing the impact of vehicle speed and loading time without considering the influence of inertia and viscosity on the loading time. Different vehicle speeds of 40km/h, 60km/h, 80km/h, and 100km/h were used to establish an asphalt pavement structure. The loading time at any point on top of the subgrade is 0.7205s, 0.4805s, 0.3605s and 0.2885s, respectively. The relationship between vehicle speed and loading time is shown in Figure 2.

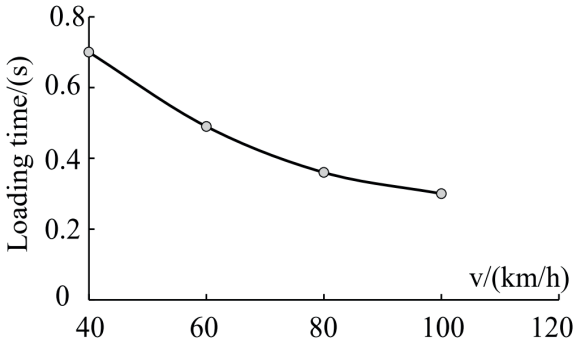

Figure 2. Vehicle speed - Loading time [23, 24]

As shown in Figure 3, the triangular waveform load simulates the vertical stress distribution on top of the subgrade for a typical pavement structure, with a correlation coefficient greater than 0.9. Therefore, the waveform load can be used to simulate the effect of traffic loads on top of the subgrade. In this Figure, the dotted line represents the surface of the subgrade at any point; the solid line is the vertical stress distribution caused by traffic load that affects the surface of the subgrade; the dashed line is the triangular waveform load simulating variation of vertical stresses.

XIE et al. (2006) [26] presented the variations of excess pore water pressure with dimensionless depth z/H, in case of trapezoidal cyclic loading. They presented a nonlinear analytical solution for the 1-D consolidation of soft soil under cyclic loading. A soil stratum with thickness H, vertical permeability coefficient k_υ, volume compressibility coefficient m_υ, and consolidation coefficient C_υ is shown in Fig. 4.

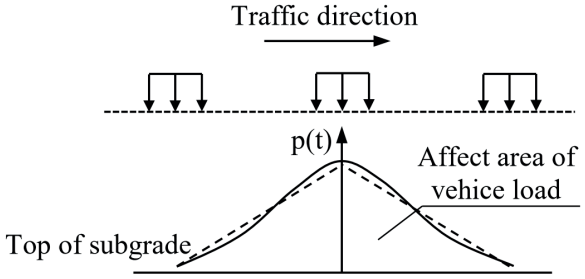

Figure 3. Vertical stress distribution on top of subgrade under vehicular load [25]

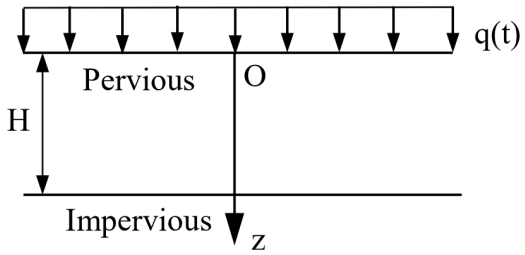

Figure 4. Model of clay layer under cyclic loading [26]

It shown that the greater the value of z/H, the greater the excess pore water pressure, indicating that the effective stress σ' and excess pore water pressure u vary with depth. In this state the pore water pressures and the effective stresses have final or equilibrium values; this is a steady state condition under cyclic loading.

2.2 Cyclic Loading Test Model

Based on the results of previous experimental studies and combining the actual conditions of the vehicular traffic flow and loading characteristics of laboratory equipment, a continuous half-sinusoidal dynamic load waveform is chosen for this study. This takes into consideration a non-continuous load distribution and thus accounts for the distance between vehicles.

The dynamic load waveform is illustrated in Figure 5, where T_1, t_0 are the continuous and interrupted duration of traffic load, respectively.

T_1 is the period of time that the dynamic load acted on the soft ground in one cycle. In this model, traffic loads are simulated as a half-sine wave cyclic load. For each test group, the cyclic load frequency, *f*, is constant in order to minimize the differences between the various types of vehicular traffic and their speeds and also to reduce the impact of varying distances between vehicles. P is the sum of vehicle weight and overburden pressure of the embankment; σ_{dmax} is the amplitude of traffic load. The same values of σ_{dmax} are used for a group test, irrespective of the impact of varying sizes of the vehicles.

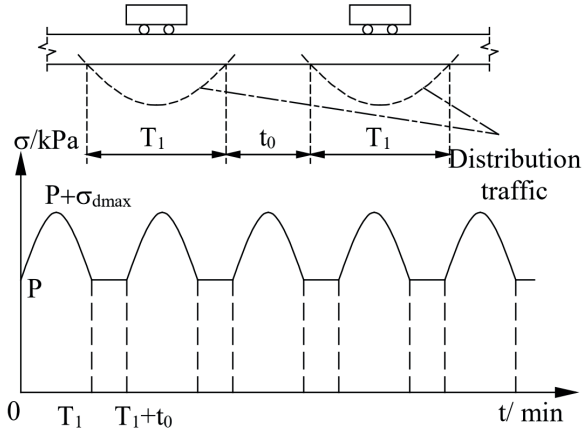

Figure 5. Simulation of the effect of traffic loading

Fujiwara et al. 1990 [27] conducted experimental study on the shear characteristics of clays with respect to cyclic stress-strain history and its corresponding pore pressures. The results of the study clarified the effect of load frequency, effective confining pressure, cyclic stress level and over-consolidation ratio on the excess pore pressure during cyclic loading.

Nash (2001) [28] also explained the physical process of consolidation under cyclic loading. When the load is applied for the first application, the entire load is carried by the water in the pores as excess pore pressure; the gradient of the excess pore pressure causes drainage and part of the load is transferred to the soil structure with an increase in the effective stress. When the load is removed, stress is reduced, the soil tries to rebound; these negative pore pressures cause water to flow into the soil, which causes a reduction in effective stress. When loaded again, a part of the load is carried by the residaal effective stress and the rest is carried by the water as excess pore pressure.

3. LABORATORY STUDIES

3.1. Sample and specimen

Soil samples were taken from a soft clay deposit located beneath the embankment. The test was conducted on a group of specimens; that had 2 cm and 30 cm2 height and cross-sectional area, respectively. The main physico-mechanical properties determined from the samples according to standard procedures are shown in Table 1.

Table 1. Physico-mechanical properties of soil samples

Physico-mechanical properties		Value
Density ρ (g/cm^3)		1.595
Water Content ω (%)		61.61
Specific Gravity G_s		2.70
Void Ratio e		1.736
Liquid Limit w_l (%)		57
Plastic Limit w_p (%)		32
Plasticity Index I_p		25
Liquidity Index I_L		1.178
Degree of Saturation S_r (%)		98.9
Compression Factor $\alpha_{0.1\text{-}0.2}$ (MPa^{-1})		1.372
Compression Modulus E_s (MPa)		1.356
Coefficient of consolidation	C_{v100}	0.391
	C_{v200}	0.487

C_{v100} $(10^{-3}cm^2/s)$ and C_{v200} $10^{-3}cm^2/s$: correspond with the pre-consolidation stresses of 100kPa and 200kPa, respectively.

A series of creep tests were carried out by using the plane strain creep apparatus for both normally and over-consolidated clay. In the initial loading step, the specimens were consolidated under a sustained load (σ_x - σ_z) of (25 - 25) kPa for 24 hours in order to eliminate the differences of various soil specimens, such

as the differences in the initial pre-compression, the physical properties and the non-uniform dispersion of the clay particles. In the next steps, the specimens were subjected to vertical consolidation stresses, σ_z values of 75, 100, 150 kPa for cyclic loading tests. The loading scheme of cyclic test scheme is summarized in Table 2.

3.2. Test procedure

A test equipment for creep under plain strain condition due to Li et al., [29- 31], Yuzhou et al., [32] and Thang., N. N [33, 34] was developed as illustrated principle sketch of the apparatus in Figure 6a. The test was developed based on the principle of conventional triaxial testing, featuring both the loading system of the former and air pressure controlling system of the latter. A data acquisition system, is connected to the computer shown in Figure 6b.

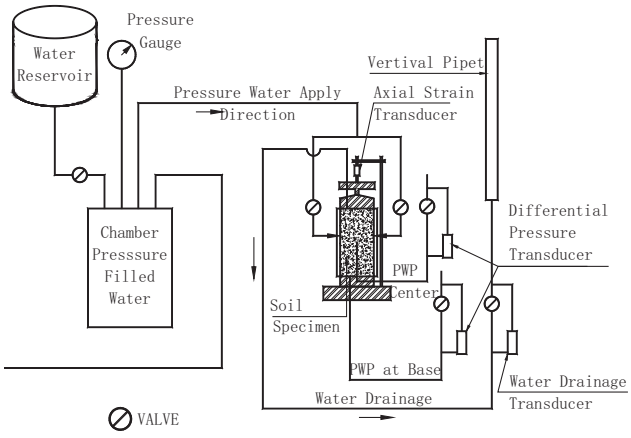

(a) Sketch of the apparatus

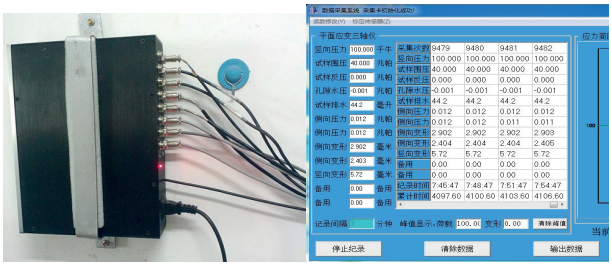

(b) Data acquisition system

Figure 6. Principle schematic sketch of cyclic test [29]

Table 2. Loading scheme of cyclic tests

N°	State	Static Loading		Cyclic Loading	
		σ_x/ kPa	σ_z/ kPa	σ_d/ kPa	f/ Hz
N°-1	Normal consolidation	25	25	-	-
		37.5	75	20	0.05
		50	100	20	0.05
		75	150	20	0.05
		25	25	-	-
N°-2	Over consolidation	37.5	75	20	0.05
		50	100	20	0.05
		75	150	20	0.05

4. TEST RESULTS AND ANALYSIS

4.1. Excess Pore Water Pressure

Figure 7 shows the excess pore water pressure histories for both normally and over-consolidated soil specimens under cyclic loading for plane strain tests scheme shown in Table 3 with cyclic load amplitude of 20 kPa and frequency of 0.05Hz. The excess pore pressure due to effect of cyclic loading developed and increased rapidly to reach the peak value and then dissipated gradually to the stable equilibrium value in creep deformation process. The results are similar to that of static load condition in [34].

Table 3 provides a summary of the average excess pore pressure values observed in cyclic loading tests. The results indicate that as the level of cyclic loading increases, the peak values of excess pore pressure, u_{max}, decrease in both normally consolidated and over-consolidated states. Moreover, the values of u_{max} for over-consolidated state are much smaller in comparison with those in normally consolidated state at the same value of external load. The results also show that u_{max} decrease with increasing external load under cyclic loading.

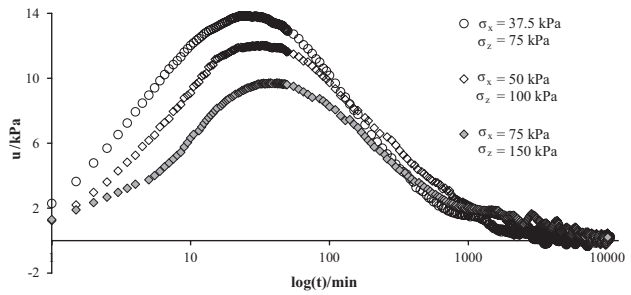

(a) Normal consolidation

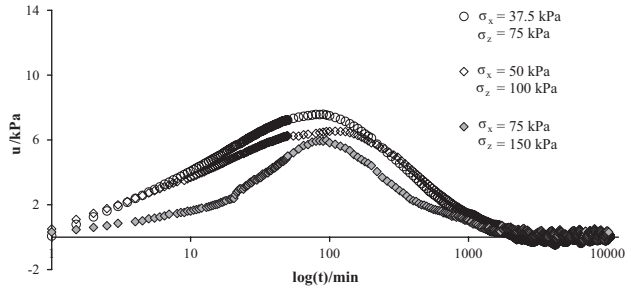

(b) Over consolidation

Figure 7. Variation of excess pore water pressure due to cyclic load

Table 3. Summary of excess pore water pressure generation in plane strain tests under cyclic loading condition

Consoi dation state / Stress (σ_x, σ_z)/kPa	Normally Consolidation		Over Consolidation	
	Peak PWP/ kPa	Peak Time /mins	Peak PWP/ kPa	Peak Time/ mins
37.5, 75 (σ_d = 20)	14.4	25	7.6	90
50, 100 (σ_d = 20)	11.2	35	6.5	110
75, 150 (σ_d = 20)	9.7	38	5.9	95

Note: PWP = Pore water pressure, σ_d = 20kPa, f = 0.05Hz

Actually, the generation and dissipation of excess pore water pressure depend on the pores spaces and contact interaction between the soil particles. Immediately after the load application, deformation occurs throughout the soil skeleton which produces the excess pore pressure while sliding at some of the grain contacts produces non-recoverable strains. As a result of sliding at contacts which have failed, permanent deformation occurs.

Since the pore water is resisting the particle rearrangement, the pore water pressure is added above the static value and immediately the increase in total stress takes place to reach a maximum value. Due to the water draining out during loading, however, soil particle rearrangement and pore pressure starts to decrease again. Thus, in the end of the loading process, excess pore pressure dissipates to a stable equilibrium value, corresponding with the soil particles being in a state of high stability and the void ratio of soil sample decreases significantly.

Figure 8(a-c) show the excess pore pressure histories of over-consolidation samples for a time period of 10 minutes at different times corresponding to the various loading stages, (σ_x, σ_z), of (37.5, 75), (50, 100) and (75, 150) kPa.

The curves show that the distribution of excess pore pressure with elapsed time during the beginning of loading duration, in which the deformation in rapidly incresing status, has cyclical form with difference frequency and amplitude for different loading stages. The amplitude of pore pressure increased with decreasing magnitude of loading, while the frequency increased with increasing magnitude of external loading.

The pore water pressure in a saturated soft cohesive soil may increase with the number of cyclic loadings. At the initial loading stage, pore water pressure is generated and varied under the effect of cyclic load with the cyclical variation. In the short period of time, the changing of pore water pressure in sine form in which the amplitude and frequency are similar to that of the cyclic load, as shown in Fig 9a and Fig 9b for normally and over consolidated, respectively.

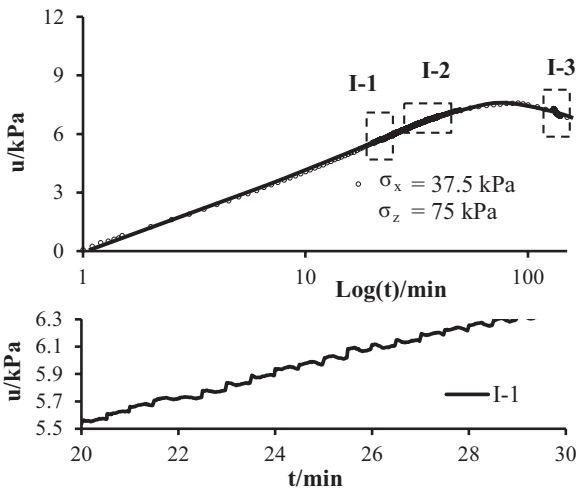

(a) (σ_x, σ_z) = (37.5, 75) kPa

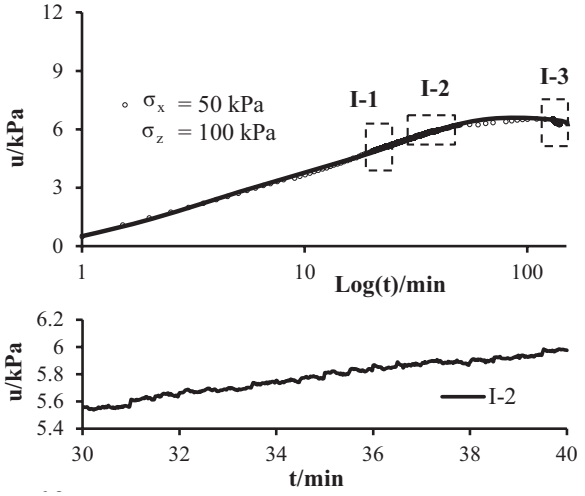

(b) (σ_x, σ_z) = (50, 100) kPa

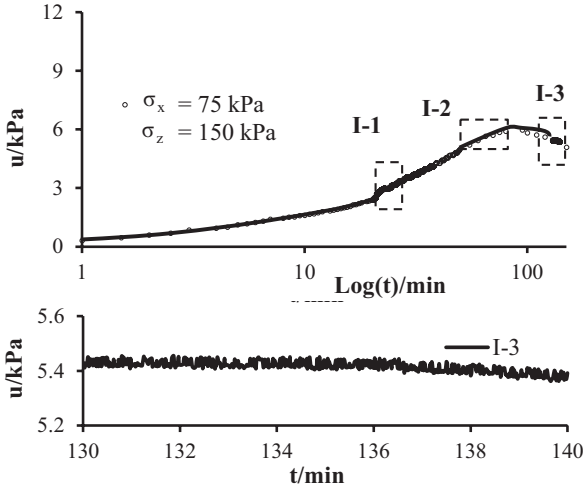

(c) (σ_x, σ_z) = (75, 150) kPa

Figure 8. Variation of excess pore water pressure in shortly time due to cyclic load for over-consolidation samples

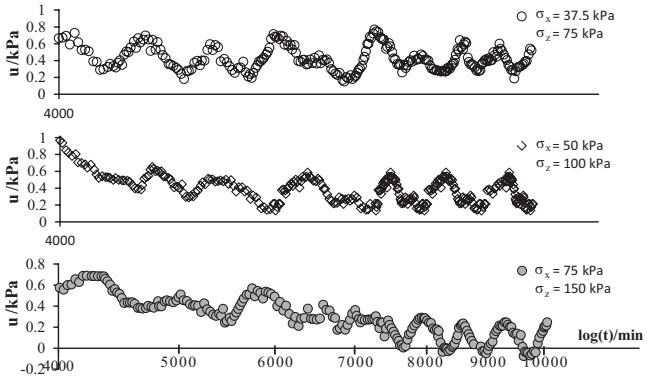

(a) Normally consolidated

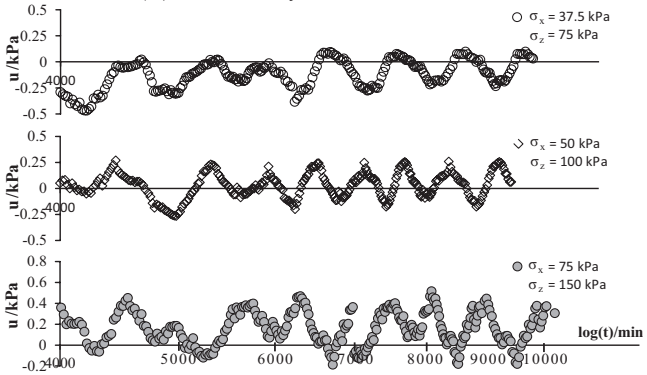

(b) Over consolidated

Figure 9. Variation of excess pore water pressure due to cyclic loading in creep deformation stage

Figure 9 illustrates the variation of pore pressure versus logarithm of elapsed time, for the started time of t = 4000 minutes and shows that the variation of pore pressure corresponding to the different load levels in the cyclical variation. In this stage, the soil exhibit a tendency for volume reduction when cyclically loaded. In the next stage of loading process when the time is long enough, however, the accumulated pore water pressure decreases by drainage as well as the rate of variation of volumetric strain decreases with increase in number of loading cycles. The values of volumetric strain tend to the constant values, the pore water pressure is approaching a stable equilibrium value approximate of the zero and the volume of the water drained out is almost the constancy. The distribution of pore water pressure in the creep process are illustrated in Figure 9, in which the creep deformation of soil consist of volumetric and axial creep strain at the relatively stable values.

4.2. Stabilization State of Soft Clay

The influence of cyclic loads on the generation and dissipation of pore water pressure in the loading stages are different. In the initial phase of each loading step, pore water pressure varies similar to the variation of cyclic load as analysed above. However, after reaching the maximum value, the pore water was discharged out, it decrease and tends to the stable value of zero when the time is long enough. The Table 4 recored the different values of T_s based on the plane strain creep test results, in which T_s are named as the duration time from the initial applying load to the time when variation of the PWP is almost independent with the cyclic load. Results in Table 4 indicate that the influence of cyclic load to cyclical variation of the pore water pressure is different from the current loading level and consolidation state of soil; the higher in (σ_x, σ_z) values, the bigger in values of T_s. It reflects that in case of the higher current loading level, the longer in effect of cyclic loading on the variation of pore water pressure. They also show that the values of T_s is become smaller when soil changed from normally to over consolidated state at the same external loading level.

Table 4. T_s for the pore water pressure in stabilization state under cyclic loading

Duration time	Consolidation state	Current loading (σ_x, σ_z) /kPa		
		(37.5, 75)	(50, 100)	(150, 300)
T_s/ min	Normally	4200	6000	7500
	Over	3800	5500	6000

The minimum value, u_{min}, the maximum value u_{max}, the changed value, Δu, and periodic time, T, of the pore water pressure during creep period are summarized in the Table 5. These resutls indicate that the distribution of pore pressure during creep deformation is independent of loading stages.

Table 5. Excess pore pressure under cyclic loading

Current loading (σ_x, σ_z) /kPa	Consolidation state	u_{min} /Kpa	u_{max} /kPa	Δu /kPa	T /min
37.5, 75	Norm	0.151	0.698	0.547	820
	Over	-0.218	0.095	0.313	950
50, 100	Norm	0.133	0.534	0.401	760
	Over	-0.123	0.181	0.304	930
75, 150	Norm	-0.176	0.286	0.462	670
	Over	-0.182	0.423	0.605	890

Note: u_{min}, u_{max} and Δu = The minimum, maximum and average value of Pore water pressure (kPa), respectively; T = periodic time (min).

Under plane strain conditions with sufficiently long loading duration, changes in pore water pressure are minimal, and it dissipates to a stable equilibrium value close to zero. During the creep deformation stage, the variation in pore water pressure is unaffected by cyclic loading on soft clay. Therefore, calculating long-term soil settlement under cyclic loading can effectively use methods designed for static loading conditions, simplifying the calculations while yielding similar results.

5. CONCLUSION

The results for cyclic loading tests show that the excess pore pressure develops and increases rapidly to reach the peak values as soon as the external loads was applied on the sample, and then decreases gradually to a stable value of zero during creep deformation stage of soil specimen. The peak excess pore pressure in both normally and overconsolidation state increase with increasing magnitude of external loading. However, the rate of distribution of excess pore pressure is much slower when soil samples changed from the normally to over-consolidated state.

On the other hand, due to effect of cyclic loading, the variation of pore water pressure

corresponding to the different load levels in both normally and over-consolidated state has cyclical variation. The amplitude of pore pressure increased with decreasing magnitude of loading, while their frequency increased with increasing magnitude of external loading.

When the loading time is long enough, the variation of pore water pressure is relatively small. Pore water pressure dissipated to a stable equiblirium value of approximately zero. The variation of pore water pressure is independent of the effect of cyclic loading on the soft clay during the creep deformation stage. Therefore, in calculating the long-term settlement of soil in case of cyclic loading can deal with the method applied for static loading condition in order to be simply calculation and the results are similar.

Subsequent dissipation of the permanent excess pore water pressure results in both axial and volumetric strain. This results in increase in the interaction forces of the soil skeleton, and thus making the structure of soil particle highly stable. Thus in the next loading step, the maximum value of pore pressure does not exceed the value reached in the previous loading step.

REFERENCES

1. **Terzaghi, K.,** Theoretical Soil Mechanics. *John Wiley and Sons Inc*. New York, 1943.
2. **Davis, E.H. and Raymond, G. P.** (1965). A nonlinear theory of consolidation. *Georechnique,* 15(2), 161-173.
3. **Wilson, N. E. and Elgohary, M. M.** (1974). Consolidation of soils under cyclic loading. *Canadian Geotechnical Journal,* 11(3), 420-423.
4. **Baligh, M.M. and Levadoux, J. N.** (1978). Consolidation theory for cyclic loading. *Journal Geotechnical Engineering Div, Proc. ASCE,* 104(GT4), 415-431.
5. **Fevaretti, M. and Soranzo, M.** (1995). A simplified consolidation theory in cyclic loading conditions. *In proceedings of international symposium on compression and consolidation of the clayey soils, Japan*, 405-409.
6. **Crawford, C. B.** (1964). Interpretation of consolidation tests, J. Soil Mech. *Found. Div., ASCE,* Vol. 90, Issue 5, pp. 108-124.
7. **Bjerrum, L.** (1967). Engineering geology of Norwegian normally consolidated marine clays as related to settlements of buildings. *Geotechnique,* Vol. 17, Issue 2, pp. 81-118.
8. **Gholamreza, M. and Anoushiravan, R.** (1974). Theory of Consolidation for Clays. *Journal of the Geotechnical Engineering Division, ASCE,* Vol. 90, Issue 8, pp. 87-102.
9. **Yin, J. H. and Graham, J.** (1989a). Viscous-elastic-plastic modeling of one-dimensional time dependent behavior of clays. *Canadian Geotechnical Journal,* Vol. 26, pp. 199-209.
10. **Yin, J. H. and Graham, J.** (1989b). General elastic viscous plastic constitutive relationships for 1-D straining in clays. Proc. of 3rd International Symposium on Numerical Models in Geomechanics. *Niagara Falls, Canada*, pp. 108-117.
11. **Xie, K., Tian, Q. Dong, Y.** (2006). Nonlinear analytical solution for one-dimensional consolidation of soft soil under cyclic loading. *Journal of Zhejiang university science,* 7(8), 1658-1364.
12. **Chen R.P, Zhou W. H., Wang H. Z. and Chen Y. M.** (2005). One dimensional nonlinear consolidation of multi-layered soil by quadrature method. *Computers and Geotechnics,* 32, 358-369.
13. **Guo-Wei L., Thang N. N., and Andrew C. A.**, Settlement Prediction of Surcharge Preloaded Low Embankment on Soft Ground Subjected to Cyclic Loading. *Marine Georesources & Geotechnology,* Vol. 34, Issue 6, 2016, pp.154-161.
14. **Li G. W., Li X., Ruan Y. S., Hou Y. Z., and Yin J. H.,** Creep model of over-consolidated soft clay under plane strain. *Chinese Journal of Rock Mechanics and*

Engineering, Vol. 35, Issue 11, 2016, pp.2307–2315.

15. **Hu Y. Y., Yang P., and Yu Q. Z.,** Time effect of secondary consolidation coefficient of over-consolidated soil. *China Journal of Highway and Transport,* Vol. 29, Issue 9, 2016, pp. 29–37.
16. **Leroueil, S.,** Compressibility of Clays: Fundamental and Practical Aspects. *ASCE Journal of Geotechnical Engineering,* 1996. 122(7): p. 534-543.
17. **Yin, J. H. and Graham, J.** (1994). Equivalent times and one-dimensional elastic visco-plastic molding of time-dependent stress-strain behavior of clays. *Canadian Geotechnical Journal,* Vol. 31, pp. 42-52.
18. **Yin, J. H. and Graham, J.** (1996). Elastic visco-plastic modeling of one-dimensional consolidation. *Geotechnique,* Vol. 46, Issue 3, pp. 515-527.
19. **ZHU Deng-feng, H.H.-w., YIN Jian-hua,** Cyclic creep behavior of saturated soft clay. *Chinese Journal of Geotechnical Engineering,* 2005. 27(9): p. 1060-1064.
20. **Nguyen Ngoc Thang.** (2023). Creep behaviour of saturated clay subjected to cyclic loading in plain strain condition. *Journal of Science and Technology in Civil Engineering, HUCE,* Vol. 17, Issue. 2, pp. 35–46.
21. **Hyodo M., and Yasuhara K.**, Analytical procedure for evaluating pore-water pressure and deformation of saturated clay ground subjected to traffic loads. *Proceedings of the sixth international conference on numerical methods in geomechanics, Innsbruck, Austria,* Vol. 1, Issue 3, 1988, pp. 653-658.
22. **Yasuhara K., Hirao K. and Kato S.,** Cyclic induced settlement in soft clay. *8th European Conf, SMFE,* Vol. 1, 1991, pp. 887- 890.
23. **Hyodo M., and Yasuhara K.,** Analytical procedure for evaluating pore-water pressure and deformation of saturated clay ground subjected to traffic loads. *Proceedings of the sixth international conference on numerical methods in geomechanics, Innsbruck, Austria,* Vol. 1, Issue 3, 1988, pp. 653-658.
24. **Yasuhara K., Hirao K. and Kato S.,** Cyclic induced settlement in soft clay. *8th European Conf, SMFE,* Vol. 1, 1991, pp. 887- 890.
25. **Ling J. M., Wang W., and Wu H. B.,** On Residual Deformation of Saturated Clay Subgrade under Vehicle Load. *Journal of TongJi University*, Vol. 3, Issue 11, 2002, pp. 1315- 1320.
26. **XIE, K.H., WANG, K., CHEN, G., and HU,** A., One-dimensional consolidation of over consolidated soil under time-dependent loading. *Frontiers of Architecture and Civil Engineering in China*, 2008. 2(1): p. 67-72.
27. **Fujiwara, H. and S, Ue.** (1990). Effect of preloading on post-construction consolidation settlement of soft clay subjected to repeated loading. *Soil and Foundations,* Vol. 30, pp. 76-86.
28. **Nash, D.** (2001). Modeling the effects of surcharge to reduce long term settlement of reclamations over soft clays: *A numerical case study. Soil and foundations,* Vol. 41, Issue 5, pp. 1-13.
29. **Li, G., Li, X., Ruan, Y., Hou, Y., Yin, J. et al.,** Creep model of over-consolidated soft clay under plane strain. *Chinese Journal of Rock Mechanics and Engineering*, Vol. 35, Issue 11, 2016, pp. 2307–2315.
30. **Li, G. W., Zhou, Y., Ruan, Y. S., Huang, K., Yin, J.**, Plane strain tests on creep characteristics of over-consolidated clay. *Chinese Journal of Geotechnical Engineering*, Vol. 36, Issue 6, 2014, pp. 1028–1035.
31. **Li, G., Huang, K., Ruan, Y., Li, X., Yin, J.**, The effect of principal stress ratio on creep behaviour of over-consolidated clay under plane strain conditions. *Chinese Journal of Rock Mechanics and*

Engineering, Vol. 34, Issue 12, 2015, pp. 2550–2558.
32. **Yuzhou H., Yang Z., Boyi Z., and Guowei L.,** Experiments of creep rate for over-consolidated clay under plain strain condition and a simple correlation. *All Earth*, Vol.33, Issue 1, 2021, pp. 88-97.
33. **Thang N. N.**, Experimental investigation of creep behaviour of saturated soft clay subjected static loading. *International Journal of GEOMATE*, Vol.25, Issue 108, 2023, pp. 81-88.
34. **Nguyen, N. T.,** Experimental investigation of creep behaviour of saturated soft clay subjected static loading. *International Journal of GEOMATE*, Vol. 25, Issue 108, 2023, pp. 81–88.

СПИСОК ЛИТЕРАТУРЫ

1. **Terzaghi, K.,** Theoretical Soil Mechanics. John Wiley and Sons Inc. New York, 1943.
2. **Davis, E.H. and Raymond, G. P.** (1965). A nonlinear theory of consolidation. Georechnique, 15(2), 161-173.
3. **Wilson, N. E. and Elgohary, M. M.** (1974). Consolidation of soils under cyclic loading. Canadian Geotechnical Journal, 11(3), 420-423.
4. **Baligh, M.M. and Levadoux, J. N.** (1978). Consolidation theory for cyclic loading. Journal Geotechnical Engineering Div, Proc. ASCE, 104(GT4), 415-431.
5. **Fevaretti, M. and Soranzo, M.** (1995). A simplified consolidation theory in cyclic loading conditions. In proceedings of international symposium on compression and consolidation of the clayey soils, Japan, 405-409.
6. **Crawford, C.B**. (1964). Interpretation of consolidation tests, J. Soil Mech. Found. Div., ASCE, Vol. 90, Issue 5, pp. 108-124.
7. **Bjerrum, L**. (1967). Engineering geology of Norwegian normally consolidated marine clays as related to settlements of buildings. Geotechnique, Vol. 17, Issue 2, pp. 81-118.
8. **Gholamreza, M. and Anoushiravan, R.** (1974). Theory of Consolidation for Clays. Journal of the Geotechnical Engineering Division, ASCE, Vol. 90, Issue 8, pp. 87-102.
9. **Yin, J. H. and Graham, J.** (1989a). Viscous-elastic-plastic modeling of one-dimensional time dependent behavior of clays. Canadian Geotechnical Journal, Vol. 26, pp. 199-209.
10. **Yin, J. H. and Graham, J**. (1989b). General elastic viscous plastic constitutive relationships for 1-D straining in clays. Proc. of 3rd International Symposium on Numerical Models in Geomechanics. Niagara Falls, Canada, pp. 108-117.
11. **Xie, K., Tian, Q. Dong, Y.** (2006). Nonlinear analytical solution for one-dimensional consolidation of soft soil under cyclic loading. Journal of Zhejiang university science, 7(8), 1658-1364.
12. **Chen R.P, Zhou W.H., Wang H.Z. and Chen Y.M.** (2005). One dimensional nonlinear consolidation of multi-layered soil by quadrature method. Computers and Geotechnics, 32, 358-369.
13. **Guo-Wei L., Thang N.N., and Andrew C.A.,** Settlement Prediction of Surcharge Preloaded Low Embankment on Soft Ground Subjected to Cyclic Loading. Marine Georesources & Geotechnology, Vol. 34, Issue 6, 2016, pp.154-161.
14. **Li G.W., Li X., Ruan Y.S., Hou Y.Z., and Yin J.H.,** Creep model of over-consolidated soft clay under plane strain. Chinese Journal of Rock Mechanics and Engineering, Vol. 35, Issue 11, 2016, pp.2307–2315.
15. **Hu Y.Y., Yang P., and Yu Q.Z.,** Time effect of secondary consolidation coefficient of over-consolidated soil. China Journal of Highway and Transport, Vol. 29, Issue 9, 2016, pp. 29–37.
16. **Leroueil, S.,** Compressibility of Clays: Fundamental and Practical Aspects. ASCE

Journal of Geotechnical Engineering, 1996. 122(7): p. 534-543.
17. **Yin, J. H. and Graham, J.** (1994). Equivalent times and one-dimensional elastic visco-plastic molding of time-dependent stress-strain behavior of clays. Canadian Geotechnical Journal, Vol. 31, pp. 42-52.
18. **Yin, J. H. and Graham, J.** (1996). Elastic visco-plastic modeling of one-dimensional consolidation. Geotechnique, Vol. 46, Issue 3, pp. 515-527.
19. **ZHU Deng-feng, H.H.-w., YIN Jian-hua**, Cyclic creep behavior of saturated soft clay. Chinese Journal of Geotechnical Engineering, 2005. 27(9): p. 1060-1064.
20. **Nguyen Ngoc Thang.** (2023). Creep behaviour of saturated clay subjected to cyclic loading in plain strain condition. Journal of Science and Technology in Civil Engineering, HUCE, Vol. 17, Issue. 2, pp. 35–46.
21. **Hyodo M., and Yasuhara K.,** Analytical procedure for evaluating pore-water pressure and deformation of saturated clay ground subjected to traffic loads. Proceedings of the sixth international conference on numerical methods in geomechanics, Innsbruck, Austria, Vol. 1, Issue 3, 1988, pp. 653-658.
22. **Yasuhara K., Hirao K. and Kato S.,** Cyclic induced settlement in soft clay. 8th European Conf, SMFE, Vol. 1, 1991, pp. 887- 890.
23. **Hyodo M., and Yasuhara K.,** Analytical procedure for evaluating pore-water pressure and deformation of saturated clay ground subjected to traffic loads. Proceedings of the sixth international conference on numerical methods in geomechanics, Innsbruck, Austria, Vol. 1, Issue 3, 1988, pp. 653-658.
24. **Yasuhara K., Hirao K. and Kato S.,** Cyclic induced settlement in soft clay. 8th European Conf, SMFE, Vol. 1, 1991, pp. 887- 890.
25. **Ling J. M., Wang W., and Wu H. B.,** On Residual Deformation of Saturated Clay Subgrade under Vehicle Load. Journal of TongJi University, Vol. 3, Issue 11, 2002, pp. 1315- 1320.
26. **XIE, K.H., WANG, K., CHEN, G., and HU, A.,** One-dimensional consolidation of over consolidated soil under time-dependent loading. Frontiers of Architecture and Civil Engineering in China, 2008. 2(1): p. 67-72.
27. **Fujiwara, H. and S, Ue.** (1990). Effect of preloading on post-construction consolidation settlement of soft clay subjected to repeated loading. Soil and Foundations, Vol. 30, pp. 76-86.
28. **Nash, D.** (2001). Modeling the effects of surcharge to reduce long term settlement of reclamations over soft clays: A numerical case study. Soil and foundations, Vol. 41, Issue 5, pp. 1-13.
29. **Li, G., Li, X., Ruan, Y., Hou, Y., Yin, J. et al.**, Creep model of over-consolidated soft clay under plane strain. Chinese Journal of Rock Mechanics and Engineering, Vol. 35, Issue 11, 2016, pp. 2307–2315.
30. **Li, G. W., Zhou, Y., Ruan, Y. S., Huang, K., Yin, J.,** Plane strain tests on creep characteristics of over-consolidated clay. Chinese Journal of Geotechnical Engineering, Vol. 36, Issue 6, 2014, pp. 1028–1035.
31. **Li, G., Huang, K., Ruan, Y., Li, X., Yin, J.,** The effect of principal stress ratio on creep behaviour of over-consolidated clay under plane strain conditions. Chinese Journal of Rock Mechanics and Engineering, Vol. 34, Issue 12, 2015, pp. 2550–2558.
32. **Yuzhou H., Yang Z., Boyi Z., and Guowei L.,** Experiments of creep rate for over-consolidated clay under plain strain condition and a simple correlation. All Earth, Vol.33, Issue 1, 2021, pp. 88-97.
33. **Thang N. N.,** Experimental investigation of creep behaviour of saturated soft clay

subjected static loading. International Journal of GEOMATE, Vol.25, Issue 108, 2023, pp. 81-88.
34. **Nguyen, N. T**., Experimental investigation of creep behaviour of saturated soft clay subjected static loading. International Journal of GEOMATE, Vol. 25, Issue 108, 2023, pp. 81–88.

Dr. Ngoc-Thang Nguyen, Civil and Industrial Construction Division, Faculty of Civil Engineering, Thuyloi University, 175 Tay Son, Dong Da, Hanoi-100000, VIETNAM. Email: thangnn@tlu.edu.vn

Д-р Нгок-Тханг Нгуен, отделение гражданского и промышленного строительства, факультет гражданского строительства, Университет Тхуйлой, 175 Тай Сон, Донг Да, Ханой, 100000, Вьетнам. E-mail: thangnn@tlu.edu.vn

International Journal for Computational Civil and Structural Engineering, 21(1) 93–104 (2025)

DOI:10.22337/2587-9618-2025-21-1-93-104

FEATURES OF MODELING THE OPERATION OF REINFORCED CONCRETE STRUCTURES USING INCONSISTENT FINITE ELEMENT MODELS

Ivan V. Nesterov, Ksenia K. Pantyukhova, Elizabeth A. Sheiko

Russian University of Transport (MIIT), Moscow, RUSSIA

Abstract: This article is devoted to the development of inconsistent finite element models of reinforcing rods for strength analysis of reinforced concrete structures. Currently, reinforcement in the calculations of reinforced concrete structures is taken into account using various methods. The authors pay special attention to the embedded finite element model. The article discusses mathematical models and technology for the output of stiffness matrices of reinforcing rods embedded in finite elements of various configurations. Using the derived finite elements, a number of comparative test calculations of reinforced concrete beams were carried out. Numerical solutions on inconsistent FE grids were compared with the results obtained on a consistent finite element grid.

Keywords: finite element method, reinforced concrete structures, consistent finite element model, inconsistent finite element model, reinforcement, discrete model, simplex element, plate element

ОСОБЕННОСТИ МОДЕЛИРОВАНИЯ РАБОТЫ ЖЕЛЕЗОБЕТОННЫХ КОНСТРУКЦИЙ С ИСПОЛЬЗОВАНИЕМ НЕСОГЛАСОВАННЫХ КОНЕЧНО-ЭЛЕМЕНТНЫХ МОДЕЛЕЙ

И.В. Нестеров, К.К. Пантюхова, Е.А. Шейко

Российский университет транспорта (МИИТ), г. Москва, РОССИЯ

Аннотация: Данная статья посвящена разработке несогласованных конечно-элементных моделей арматурных стержней для прочностного анализа железобетонных конструкций. В настоящее время арматура в расчётах железобетонных конструкциях учитывается с помощью разных методов. Особое внимание авторы уделят встроенной конечно-элементной модели. В статье рассматриваются математические модели и технология вывода матриц жесткости арматурных стержней, встроенных в конечные элементы различной конфигурации. С использованием выведенных конечных элементов был проведен ряд сравнительных тестовых расчетов железобетонных балок. Численные решения на несогласованных сетках КЭ сравнивались с результатами, полученными на согласованных сетках конечных элементов.

Ключевые слова: метод конечных элементов, железобетонные конструкции, согласованная конечно-элементная модель, несогласованная конечно-элементная модель, арматура, дискретная модель, симплекс-элемент, пластинчатый элемент

INTRODUCTION

Currently, reinforced concrete structures are widely used in the construction industry. Reinforced concrete is a complex composite material for strength analysis. Therefore, when calculating this class of structures, it is necessary to take into account such factors as creep, shrinkage, nonlinear deformations from the acting load, etc. One of the main problems that arise when calculating reinforced concrete structures is modeling the interaction of the reinforcement frame and concrete.

There are different methods for calculating reinforced concrete structures. The finite element method (FEM) is the most common among designers for studying the stress-strain state of a structure [1]. The finite element method is implemented in many software packages used for strength analysis of engineering structures. It is worth highlighting the most popular of them: Midas, Abaqus, ANSYS, Sofistik, Scad, etc.

The joint work of reinforcement and concrete in finite element models is taken into account in different ways. The most common, simple and affordable method is to recalculate the given physical characteristics of concrete, taking into account the percentage of reinforcement according to standard SNiP methods. Calculation recommendations are specified in SP 63.13330.2018 "Concrete and reinforced concrete structures" [2], as well as in the methodological guide for the calculation of reinforced concrete elements "Methodological recommendations for the use of SP 35.13330.2011" [3]. This method of accounting for fittings is convenient for standard (simple) cross-sections. In a complex section, when reduced to an equivalent one, the stress distribution may differ significantly from the real picture of the stress-strain state. The most accurate method is to create a discrete model based on consistent finite element grids (FE). In this simulation, the nodes of the reinforcing rods coincide with the nodes of the concrete component (Fig. 1).

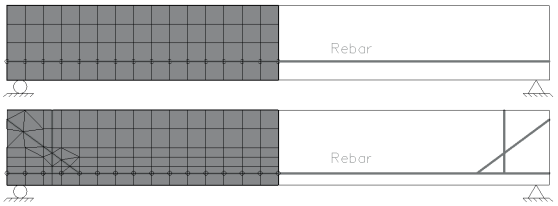

Figure 1. Discrete model on matched FE grids

However, the process of creating such a design scheme is very laborious. The reinforcement frame can consist of different types of rods having different positions, lengths, etc. For example, there may be horizontal, vertical, and inclined rods in one design scheme. During the design process, the configuration (parameters) of the beams and reinforcement frame often change. Accordingly, each time you will have to redo the calculation scheme. Therefore, it is impractical to use a consistent finite element model for such tasks. Basically, this model is applicable for simple reinforcement frames, or for test calculations.

Methods that do not require consistency of the grid nodes, the concrete component, and the reinforcement frame are more convenient for calculation. One of these is a discrete model using scalable contour lines [4]. With this method, the initial model is discretized. The finite elements through which the reinforcement passes are divided into subdomains in the form of polyhedra (Fig. 2).

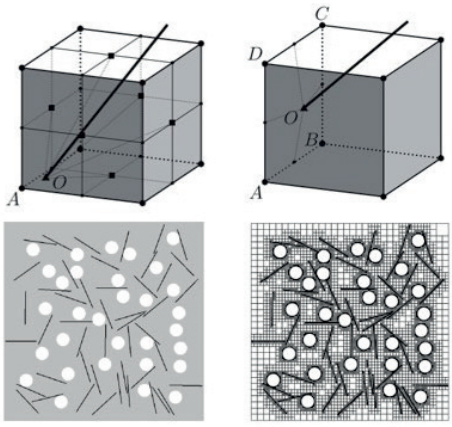

Figure 2. Discrete model using scalable contour lines [4]

There is also a distributed FE model, which also does not require the consistency of FE nodes [5]. In this method, the reinforcement is modeled as thin plates that are “stretched” onto the plates of the concrete component through which the rod passes. An anisotropic plate is obtained. This technology is implemented in the Abaqus and Ansys software packages. Currently, embedded finite element models are being intensively developed [6,7], which make it possible to accurately take into account the influence of reinforcement in the design scheme of reinforced concrete structures, without worrying about matching the grid nodes of the concrete

component and the reinforcement frame. This approach is convenient for software users, but for software developers there are difficulties associated with the need to create an additional library of finite elements and make adjustments to the architecture of the software package. This model is most fully implemented in the Midas software package. In domestic strength analysis systems, the embedded model is insufficiently developed and requires a full-fledged software implementation.

A GENERAL ALGORITHM FOR THE FORMATION OF FINITE ELEMENT STIFFNESS MATRICES FOR AN EMBEDDED FE MODEL OF REINFORCED CONCRETE

The theoretical basis of the integrated reinforcement accounting model is the hypothesis of the compatibility of concrete and reinforcement deformations, as a result of which nodal reactions are added to the nodal reactions of the plate element from single displacements according to degrees of freedom from deformation of the reinforcing rod in the contour of the plate, but not from single displacements of the rod nodes, but from single displacements of the plate nodes through which it passes (3). This additive is calculated using the integral over the length of the embedded rod.

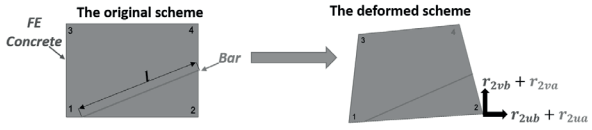

Figure 3. Deformation of a plate finite element with an integrated reinforcing rod

Thus, based on the hypothesis of joint deformations of concrete and reinforcement, the field of displacement of the reinforcing rod is actually a cross-section of the field of displacement of the plate. Based on this, the reaction matrix of a plate element with an integrated reinforcing rod can be obtained by the formula (1).

$$r = \int_V \sigma^T \varepsilon \, dV + \int_l \sigma^T \varepsilon \, dl = \int_V B^T D B \, dV + \\ + F \int_l B_a^T E B_a \, dl, \qquad (1)$$

Where B - is the deformation matrix of the plate element (concrete),

D - is the matrix of Hooke's law [8],

B_a - reinforcement deformation matrix,

F_a - is the cross-sectional area of the reinforcement.

Using this approach, several finite elements were derived: a triangular simplex element, a 4-node plate FE, a 9-node plate FE, and a bending plate.

OUTPUT OF THE STIFFNESS MATRIX OF A TRIANGULAR SIMPLEX ELEMENT WITH AN INTEGRATED REINFORCING ROD

Using the above algorithm, we obtain a stiffness matrix for a triangular simplex element with an integrated reinforcing rod. For a triangular finite element, the basic functions are the equations of the plane, respectively, the displacement field is a function of two variables (2).

$$\vec{z}(x) = \begin{bmatrix} n_1(xy) & 0 & n_2(xy) & 0 \\ 0 & n_1(xy) & 0 & n_2(xy) \\ n_3(xy) & 0 & & \\ 0 & n_3(xy) & & \end{bmatrix} \vec{Z} \qquad (2)$$

In order to obtain the displacement field (3) for the embedded reinforcing rod in the triangle, it is necessary to switch to the local coordinate system of the rod.

$$\vec{z}(x) = \begin{bmatrix} nl_1(x) & 0 & nl_2(x) & 0 \\ 0 & nl_1(x) & 0 & nl_2(x) \\ nl_3(x) & 0 & & \\ 0 & nl_3(x) & & \end{bmatrix} \vec{Z} \qquad (3)$$

This makes it possible to obtain the displacement field of the embedded rod by a set of functions of one variable, which are sections of functions of the triangle shape (4) (Fig.4).

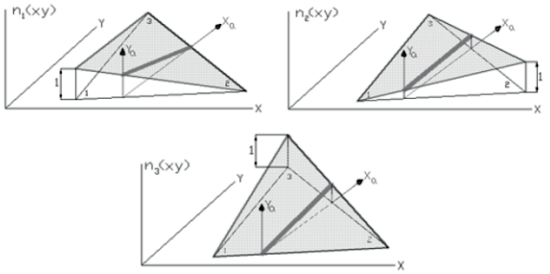

Figure 4. Basic functions of an embedded reinforcing bar in a triangle

$$nl_1(x) = \frac{(-a_1 \cdot xx - c_1)}{b_1},$$
$$nl_2(x) = \frac{(-a_2 \cdot xx - c_2)}{b_2},$$
$$nl_3(x) = \frac{(-a_3 \cdot xx - c_3)}{b_3}, \quad (4)$$

Where a_1, a_2, a_3, b_1, b_2, b_3, c_1, c_2, c_3, xx - parameters of the direct line

The embedded reinforcing rod in the plate element has its own tilt angle relative to the global coordinate system (Fig.5), therefore, the stiffness matrix of the embedded element must be multiplied by the rotation matrix (5).

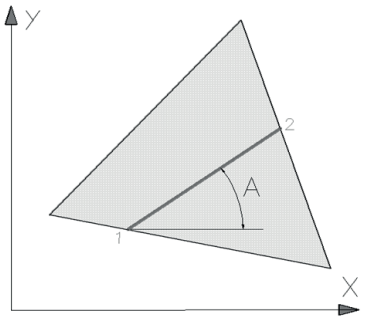

Figure 5. Tilt angle of the embedded rod

$$C = \begin{bmatrix} CA & 0 & 0 \\ 0 & CA & 0 \\ 0 & 0 & CA \end{bmatrix}, CA = \begin{bmatrix} cosA & sinA \\ -sinA & cosA \end{bmatrix} \quad (5)$$

The final stiffness matrix of a triangular simplex element with an integrated reinforcing rod is obtained by summing the stiffness matrix of a triangular plate element and the reinforcement matrix (6).

$$r = \frac{\delta}{F_{\text{тр}}} B^T DB + C^T [FlB_a^T E_a B_a] C, \quad (6)$$

Where B - is the deformation matrix of the plate element (concrete),

B_a - is the deformation matrix of the reinforcement,

C - is the matrix of transition to the local coordinate system of the rod (5),

D - is the matrix of Hooke's law [8],

F - is the cross-sectional area of the reinforcement.

OUTPUT OF THE STIFFNESS MATRIX OF A FLAT QUADRILATERAL WITH AN INTEGRATED REINFORCING ROD

In a similar way, a stiffness matrix was obtained for a four-node plane FE with an embedded reinforcing rod. The basic functions of a flat quadrilateral are linear surfaces, so the displacement field is also a function of two variables (7).

$$\vec{z}(x) = \left[\begin{array}{cc|cc} n_1(xy) & 0 & n_2(xy) & 0 \\ 0 & n_1(xy) & 0 & n_2(xy) \\ \hline n_3(xy) & 0 & n_4(xy) & 0 \\ 0 & n_3(xy) & 0 & n_4(xy) \end{array}\right] \vec{z} \quad (7)$$

To obtain the stiffness matrix based on the embedded rod, it is necessary to switch to the local coordinate system of the rod. Thus, the displacement field of the embedded reinforcing rod (8) becomes a function of one variable.

$$\vec{z}(x) = \left[\begin{array}{cc|cc|cc} nl_1(x) & 0 & nl_2(xy) & 0 & nl_3(x) & 0 \\ 0 & 0 & 0 & 0 & 0 & 0 \\ \hline & & nl_4(x) & 0 & & \\ & & 0 & 0 & & \end{array}\right] \vec{z} \quad (8)$$

The basic functions for an embedded reinforcing bar in a flat quadrilateral are shown below (Fig.6) (9):

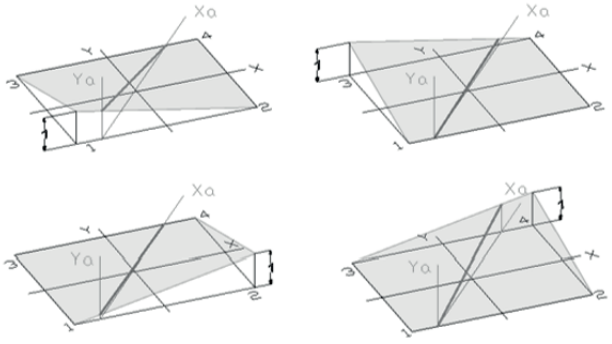

Figure 6. Basic functions of an embedded reinforcing bar in a flat quadrilateral

$$nl_1(x) = \left(\frac{1}{2} - \frac{cosAdl + x1}{a}\right)\left(\frac{1}{2} - \frac{sinAdl + y1}{b}\right),$$
$$nl_2(x) = \left(\frac{1}{2} + \frac{cosAdl + x1}{a}\right)\left(\frac{1}{2} - \frac{sinAdl + y1}{b}\right),$$
$$nl_3(x) = \left(\frac{1}{2} - \frac{cosAdl + x1}{a}\right)\left(\frac{1}{2} + \frac{sinAdl + y1}{b}\right),$$
$$nl_4(x) = \left(\frac{1}{2} + \frac{cosAdl + x1}{a}\right)\left(\frac{1}{2} + \frac{sinAdl + y1}{b}\right), \quad (9)$$

Where dl - is the parameter of the line,

a, b - are the dimensions of the sides of a flat quadrangle,

$x1$, $y1$ - is the initial coordinate of the reinforcing bar.

The reinforcing bar embedded in the rectangle relative to the global coordinate system is rotated by an angle A (Fig.7).

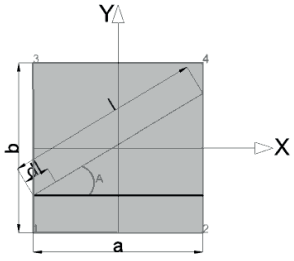

Figure 7. Angle of inclination of the embedded rod

The stiffness matrix of the rod must be multiplied by the cosine matrix consisting of diagonal blocks (10).

$$C = \begin{bmatrix} CA & 0 & 0 & 0 \\ 0 & CA & 0 & 0 \\ 0 & 0 & CA & 0 \\ 0 & 0 & 0 & CA \end{bmatrix}, CA = \begin{bmatrix} cosA & sinA \\ -sinA & cosA \end{bmatrix} \quad (10)$$

The final stiffness matrix of the plate four-node FE, taking into account the reinforcement, is obtained by summing the local stiffness matrix of the plate element (concrete component) and the matrix of the embedded reinforcing rod according to the formula (11).

$$r = \delta \int_{-\frac{a}{2}}^{\frac{a}{2}} \int_{-\frac{b}{2}}^{\frac{b}{2}} B^T D B \, dx \, dy + C^T \left[F_a \int_0^l B_a^T E B_a \, dx_a \right] C, \quad (11)$$

Where B - is the deformation matrix of the plate element (concrete),

B_a - is reinforcement deformation matrix,

C - is the matrix of transition to the local coordinate system of the rod (10),

D - is the matrix of Hooke's law [8],

F_a - is the cross-sectional area of the reinforcement.

OUTPUT OF THE STIFFNESS MATRIX OF A FLAT 9-NODE QUADRILATERAL WITH AN INTEGRATED REINFORCING ROD

The stiffness matrix of a flat 9-node quadrilateral with an integrated reinforcing rod is derived according to the principle of triangular and four-node finite elements. In this case, only the basic functions are second-order surfaces. Accordingly, the displacement field for a 9-node element is a dependence of two variables (12).

$$\vec{z}(x) = \begin{bmatrix} n_1(xy) & 0 \\ 0 & n_1(xy) \end{bmatrix} | \dots | \begin{bmatrix} n_9(xy) & 0 \\ 0 & n_9(xy) \end{bmatrix} \vec{z} \quad (12)$$

To obtain the stiffness matrix of a 9-node plate core with an integrated reinforcing rod, it is necessary to switch to the local coordinate system of the rod. For a reinforcing bar, the displacement field is a cross-section of the shape functions of a 9-node finite element and is a function of one variable (13).

$$\vec{z}(x) = \begin{bmatrix} nl_1(x) & 0 \\ 0 & 0 \end{bmatrix} | \ldots | \begin{bmatrix} nl_9(x) & 0 \\ 0 & 0 \end{bmatrix} \vec{z} \quad (13)$$

The basic functions for an integrated reinforcing rod in a flat 9-node plate FE are shown below (Fig.8) (14):

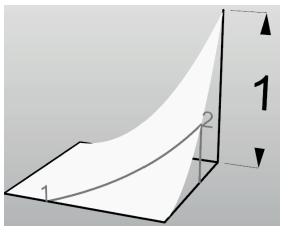

Figure 8. Example of the basic function of an embedded reinforcing bar in a 9-node quadrilateral

$$nl_1(x) = \left(-\frac{4(cosAdl + x1)^2}{a^2} + 1\right) \left(-\frac{4(sinAdl + y1)^2}{b^2} + 1\right),$$

$$nl_2(x) = \left(\frac{2(cosAdl + x1)^2}{a^2} - \frac{cosAdl + x1}{a}\right) \left(\frac{2(sinAdl + y1)^2}{b^2} - \frac{sinAdl + y1}{b}\right),$$

$$nl_3(x) = \left(\frac{2(cosAdl + x1)^2}{a^2} + \frac{cosAdl + x1}{a}\right) \left(\frac{2(sinAdl + y1)^2}{b^2} - \frac{sinAdl + y1}{b}\right),$$

$$nl_4(x) = \left(\frac{2(cosAdl + x1)^2}{a^2} - \frac{cosAdl + x1}{a}\right) \left(\frac{2(sinAdl + y1)^2}{b^2} + \frac{sinAdl + y1}{b}\right),$$

$$nl_5(x) = \left(\frac{2(cosAdl + x1)^2}{a^2} + \frac{cosAdl + x1}{a}\right) \left(\frac{2(sinAdl + y1)^2}{b^2} + \frac{sinAdl + y1}{b}\right),$$

$$nl_6(x) = \left(-\frac{4(cosAdl + x1)^2}{a^2} + 1\right) \left(\frac{2(sinAdl + y1)^2}{b^2} - \frac{sinAdl + y1}{b}\right),$$

$$nl_7(x) = \left(\frac{2(cosAdl + x1)^2}{a^2} + \frac{cosAdl + x1}{a}\right) \left(-\frac{4(sinAdl + y1)^2}{b^2} + 1\right),$$

$$nl_8(x) = \left(-\frac{4(cosAdl + x1)^2}{a^2} + 1\right) \left(\frac{2(sinAdl + y1)^2}{b^2} + \frac{sinAdl + y1}{b}\right),$$

$$nl_9(x) = \left(\frac{2(cosAdl + x1)^2}{a^2} - \frac{cosAdl + x1}{a}\right) \left(-\frac{4(sinAdl + y1)^2}{b^2} + 1\right), \quad (14)$$

Where dl - is the parameter of a straight line that takes any real values,

$a,\ b$ - are the dimensions of the sides of a flat quadrangle,

$x1,\ y1$ - is the initial coordinate of the reinforcing bar.

Also, as with the previous elements, the embedded rod has an angle of inclination A (Fig.9), therefore it is multiplied by the cosine matrix (15).

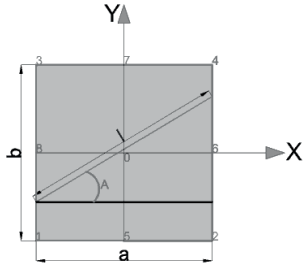

Figure 9. Angle of inclination of the embedded rod

$$C = \left[\begin{pmatrix} CA & \cdots & 0 \\ \vdots & \ddots & \vdots \\ 0 & \cdots & CA \end{pmatrix}\right], CA = \begin{bmatrix} cosA & sinA \\ -sinA & cosA \end{bmatrix} \quad (15)$$

The final stiffness matrix of the plate 9-node FE, taking into account the reinforcement, is obtained

by summing the local stiffness matrix of the plate element and the matrix of the embedded reinforcing rod according to the formula (16).

$$r = \delta \int_{-\frac{a}{2}}^{\frac{a}{2}} \int_{-\frac{b}{2}}^{\frac{b}{2}} B^T D B \, dx \, dy + C^T \left[F_a \int_0^l B_a^T E B_a \, dx_a \right] C, \qquad (16)$$

OUTPUT OF THE STIFFNESS MATRIX OF A BENDING QUADRILATERAL WITH AN INTEGRATED REINFORCING ROD

The output of the stiffness matrix of a bending quadrilateral with an integrated reinforcing rod differs from the previous elements. In this element, the basic functions are second-order surfaces. The displacement field is obtained from the following relation (16):

$$z(xy) = \begin{bmatrix} w(xy) \\ \dfrac{\partial w(xy)}{\partial y} \\ -\dfrac{\partial w(xy)}{\partial x} \end{bmatrix} = L(xy)\vec{\alpha} \qquad (16)$$

The reinforcement in the bending quadrangular element is modeled using rigid links [9]. The matrix of rigid insertion (15):

$$V = \begin{bmatrix} V_{\text{н}} & 0 \\ 0 & V_{\text{к}} \end{bmatrix}, V_{\text{н}} = \begin{bmatrix} 1 & 0 & 0 \\ e_{\text{н}} & 1 & 0 \\ 0 & 0 & 1 \end{bmatrix}, \quad V_{\text{к}} = \begin{bmatrix} 1 & 0 & 0 \\ e_{\text{к}} & 1 & 0 \\ 0 & 0 & 1 \end{bmatrix}, \qquad (15)$$

Where V- the matrix of rigid insertion,

$e_{\text{н}}$, $e_{\text{к}}$ - height of the rigid insert.

For the reinforcing rod, the stiffness matrix of the rod embedded in a flat quadrilateral is used. This matrix is then multiplied by a matrix of rigid inserts on both sides (15). The final stiffness matrix of a bending quadrilateral with an integrated reinforcing bar is obtained by adding the stiffness matrix of the bending plate and the stiffness matrix of the reinforcing bar, taking into account the rigid inserts (16).

$$r = \frac{\delta^3}{12} (L^{-1})^T \iint B^T D B \, dx \, dy L^{-1} + V^T C^T \left[F_a \int_0^l B_a^T E_a B_a \, dx_a \right] C V \qquad (16)$$

TESTING OF FINITE ELEMENTS WITH INTEGRATED REINFORCEMENT ROD

For strength calculations of reinforced concrete structures based on the embedded FE model, the authors developed a C++ program that includes a library with the finite elements described above. Test calculations of beams with reinforcing rods were performed. A beam with the following geometric characteristics was accepted for calculation: height - 14, length - 102.5, thickness -11.5. All dimensions are indicated in cm. A four-point loading scheme was used for calculations (Fig. 10). The physical characteristics of concrete and reinforcement are indicated in the calculation scheme (Fig. 10).

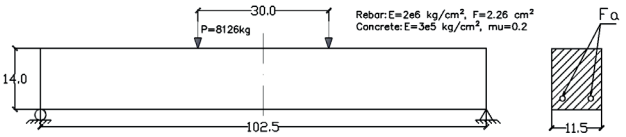

Figure 10. Calculation scheme

The comparison of the results obtained on the inconsistent meshes of the FE (the left part of the beam) was performed with the model on the consistent meshes of the FE (the right part of the beam). The model based on matched grids is calculated in the KATRAN software package.

Test-1

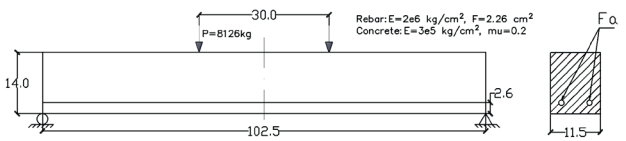

Figure 11. Calculation scheme

The first test calculations were performed on grids with triangular finite elements. The first calculation was performed on a relatively coarse mesh with a single reinforcing rod (Fig. 12). The results are shown in Table 1.

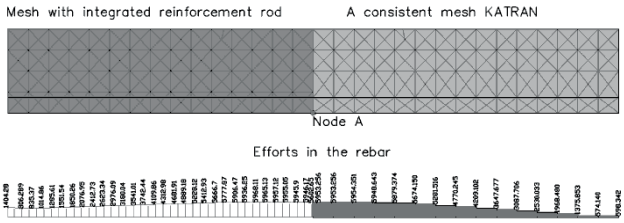

Figure 12. Finite element model and reinforcement forces on a sparse grid

In the second test calculation, the grid was thickened by 2 times (Fig. 13). The position of the reinforcing rod in the design scheme remains the same. The results are shown in the table 2.

Table 1

Criteria	Inconsistent model	A consistent model	Error rate, %
Displacement at node A (middle of the beam), cm	0.378035	0.3794	0.36
Effort, kg	5602.65	5953.26	5.89

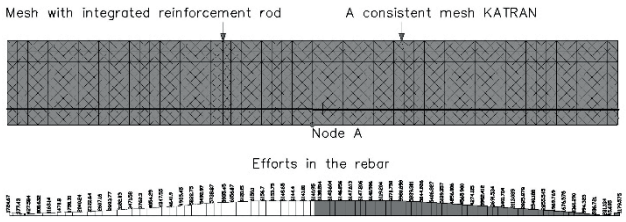

Figure 13. A finite element model and reinforcement forces on a dense grid

Table 2

Criteria	Inconsistent model	A consistent model	Error rate, %
Displacement at node A (middle of the beam), cm	0.394302	0.39465	0.088
Effort, kg	6140.95	6138.514	0.0397

Test-2

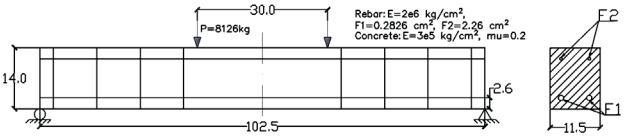

Figure 14. Calculation scheme

In the next test, a reinforcement frame with horizontal and vertical rods was added to the design scheme (Fig. 14). The results are shown in Table 3. (Fig. 15)

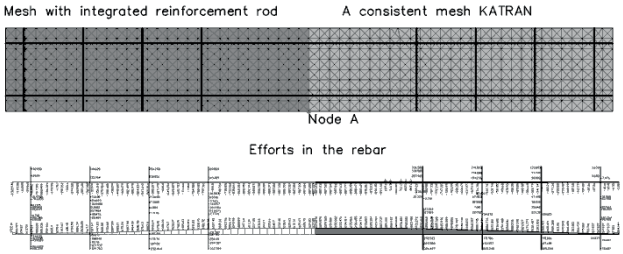

Figure 15. A finite element model with a reinforcing frame

Table 3

Criteria	Inconsistent model	A consistent model	Error rate, %
Displacement at node A (middle of the beam), cm	0.389066	0.38933	0.0678
Efforts in the upper bar, kg	887.339	887.23	0.0123
Efforts in the lower bar, kg	6127.89	6125.876	0.0329
Efforts in vertical bar, kg	339.589	330.588	2.7

Test-3

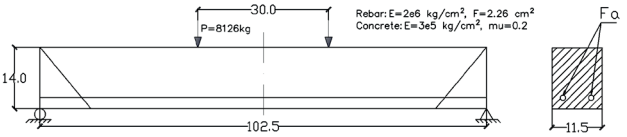

Figure 16. Calculation scheme

A four-cornered flat plate element with an integrated reinforcing rod.
Testing was performed for a beam with the same geometry as in the previous calculation (Fig. 16). But inclined reinforcing rods were added to the design scheme. The results are shown in table 4. (Fig. 17)

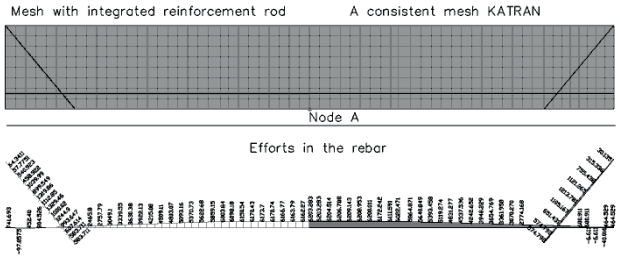

Figure 17. A finite element model with an inclined bar

Table 4

Criteria	Inconsistent model	A consistent model	Error rate, %
Displacement at node A (middle of the beam), cm	0.395492	0.39983	1.08
Efforts in the lower bar, kg	6162.27	6203.283	0.66
Efforts in the inclined rod, kg	583.711	574.792	1.5

Test-4
A beam with a reinforcing frame was also calculated. The calculation scheme is fully consistent (Fig. 14). The results are shown in Table 5 (Fig.18).

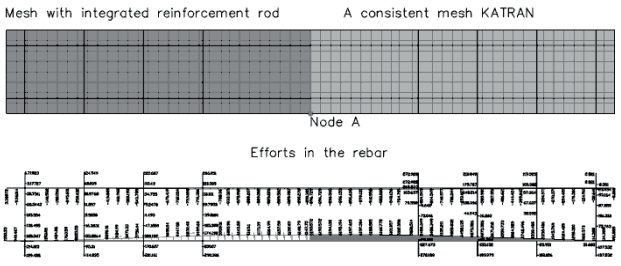

Figure 18. A finite element model with a reinforcing frame

Table 5

Criteria	Inconsistent model	A consistent model	Error rate, %
Displacement at node A (middle of the beam), cm	0.390491	0.39429	0.96
Efforts in the upper bar, kg	890.381	896.729	0.71
Efforts in the lower bar, kg	6147.75	6193.572	0.74
Efforts in vertical bar, kg	266.051	272.928	2.5

Test-5
A flat 9-node quadrilateral with a embedded reinforcing rod.
Based on this type of FE, a beam with a reinforcing frame was calculated (Fig. 14). The calculation results are shown in Table 6 (Fig. 19).

Table 6

Criteria	Inconsistent model	A consistent model	Error rate, %
Displacement at node A (middle of the beam), cm	0.39667	0.39429	0.6
Efforts in the upper bar, kg	896.003	896.729	0.081
Efforts in the lower bar, kg	6189.72	6193.572	0.062
Efforts in vertical bar, kg	240.527	272.928	11.87

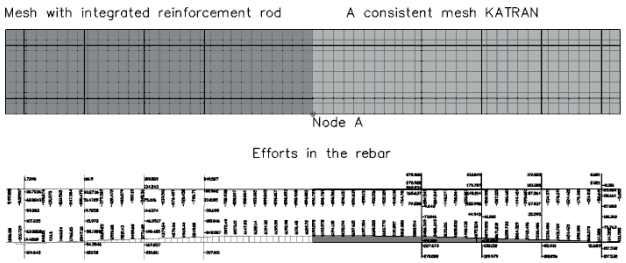

Figure 19. Finite element model with reinforcement frame

Test-6

A bending quadrilateral with a embedded reinforcing rod.

To test the bending plate with an integrated reinforcing bar, a spatial model with a T-shaped cross-section was created. The section parameters are shown in the figure (Fig. 20). The length of the beam is 500 cm. Reinforcement rods are located in the upper and lower parts of the beam. The physical characteristics of the materials have not changed.

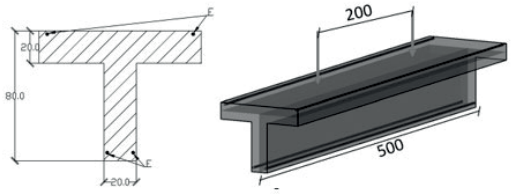

Figure 20. Cross-section profile of the T-beam

To verify the results, a calculation was performed with a model on a consistent grid (Fig.21), where rigid inserts are an element of great rigidity, with which the reinforcement rod is connected to the plate model (Fig. 22, the right part of the beam).

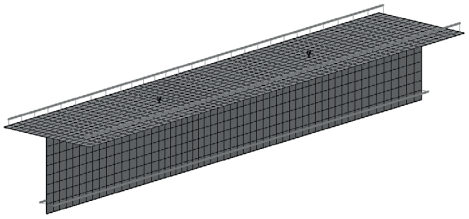

Figure 21. A finite element model with an armature frame on mismatched gridsax

The calculation results are shown in Table 7 (Fig. 22).

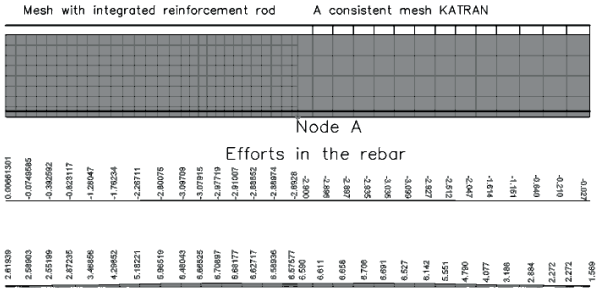

Figure 22. A finite element model with a reinforcing frame

Table 7

Criteria	Inconsistent model	A consistent model	Error rate, %
Displacement at node A (middle of the beam), cm	9.37E-04	9.54E-04	1.8
Efforts in the upper bar, kg	2.8928	2.9	0.24
Efforts in the lower bar, kg	6.57577	6.59	0.22

CONCLUSION

The method of constructing finite element models of reinforced concrete structures using embedded rod finite elements based on the hypothesis of compatibility of the deformation field of reinforcement and concrete has been improved.

The stiffness matrices of flat and flexural plate finite elements with the inclusion of reinforcing rods inconsistent with the nodes of the main grid of the FE were verified and tested.

A software package has been developed that implements finite element models of reinforced concrete structures with integrated reinforcement.

Based on a series of test calculations, a comparative analysis of coordinated and uncoordinated FE models of reinforced concrete structures was carried out, which showed high accuracy of finite element models with integrated reinforcing rods.

REFERENCES

1. **Gallagher R.**, Finite element method. Fundamentals: Translated from English– Moscow: Mir, 1984– 428 p.
2. SP 63.13330.2018. A set of rules. Concrete and reinforced concrete structures. (2019). Moscow: Standartinform.

3. Methodological recommendations for the application of SP 35.13330.2011. (2017). Moscow: Standartinform
4. **Zhang J., Eisenträger J., Duczek S., Song C**. Discrete modeling of fiber reinforced composites using the scaled boundary finite element method//Composite Structures. 2019. Vol.235. Pp.1-37
5. **Fialko S.Y.** Four-node finite element for modeling the behavior of thin-walled reinforced concrete structures // Magazine of Civil Engineering, No.5,2014, 27-36 p.
6. **Klovanich S.F.,** Finite element method in nonlinear problems of engineering mechanics: IPO LLC Zaporizhia", 2009, 400 p.
7. **Jendele L., Cˇervenka J**. On the solution of multi-point constraints – application to FE analysis of reinforced concrete structures // Computers&Structures. 2009. Vol.87. Pp. 970-980.
8. **Darkov A.V., Shaposhnikov N.N.,** Construction mechanics: Textbook.for builds. spec of universities. - M.: Higher School, 1986. – 607 p.
9. **Smirnov A.F., Alexandrov A.V., Lashchenikov B.Y., Shaposhnikov N.N.,** Construction mechanics: Textbook for universities, Moscow: Stroyizdat, 1981– 512 p.

СПИСОК ЛИТЕРАТУРЫ

1. **Галлагер Р.**, Метод конечных элементов. Основы: Пер. с англ. – М.: Мир, 1984. – 428 с.
2. СП 63.13330.2018. Свод правил. Бетонные и железобетонные конструкции. (2019). М.: Стандартинформ
3. Методическое пособие. Методические рекомендации по применению СП 35.13330.2011. (2017). М.: Стандартинформ
4. **Zhang J., Eisenträger J., Duczek S., Song C**. Discrete modeling of fiber reinforced composites using the scaled boundary finite element method//Composite Structures. 2019. Vol.235. Pp.1-37
5. **Фиалко С.Ю**. Четырехузловой конечный элемент для моделирования поведения тонкостенных железобетонных конструкций // Magazine of Civil Engineering, No.5, 2014, 27-36 с.
6. **Клованич С.Ф**., Метод конечных элементов в нелинейных задачах инженерной механики: ООО "ИПО" Запорожье", 2009, 400 с.
7. **Jendele L., Cˇervenka J**. On the solution of multi-point constraints – application to FE analysis of reinforced concrete structures // Computers&Structures. 2009. Vol.87. Pp. 970-980.
8. **Дарков А.В., Шапошников Н.Н.**, Строительная механика: Учеб.для строи. спец вузов. - М.: Высш. Шк., 1986. – 607 с.
9. **Смирнов А.Ф., Александров А.В., Лащеников Б.Я., Шапошников Н.Н.**, Строительная механика: Учеб. для вузов - М.: Стройиздат, 1981. – 512 с.

Ivan V. Nesterov, Associate Professor, Ph.D, Associate Professor of «Computer Aided Design» Department, Institute of Railway Track, Construction and Structures, Russian University of Transport (MIIT), 127994, GSP-4, Moscow, Obraztsova str., 9, building 9, e-mail: saprforever@gmail.com

Ksenia K. Pantyukhova, Master's Student at the Russian University of Transport (MIIT), specialist of the Center for Integrated Projects of Management of New Projects and Technologies of the Russian University of Transport (MIIT), a leading engineer of the design department of LLC «Intermost», 127994, GSP-4, Moscow, Obraztsova str., 9, building 9, e-mail: ksushap13.03.2001@mail.ru

Elizabeth A. Sheiko, Assistant of «Computer Aided Design» Department, Institute of Railway Track, Construction and Structures, Russian University of Transport (MIIT), 127994, GSP-4, Moscow, Obraztsova str., 9, building 9, e-mail: elizabet-250997@mail.ru

Нестеров Иван Владимирович, доцент, кандидат технических наук, доцент кафедры «Системы автоматизированного проектирования» Института пути, строительства и сооружений Российского университета транспорта (МИИТа), 127994, ГСП-4, Москва, ул. Образцова, д.9, стр. 9, e-mail: saprforever@gmail.com

Пантюхова Ксения Константиновна, магистрант Российского университета транспорта (МИИТа), специалист Центра комплексных проектов Управления новых проектов и технологий Российского университета транспорта (МИИТа), ведущий инженер отдела проектирования ООО «Интермост», 127994, ГСП-4, Москва, ул. Образцова, д.9, стр. 9, e-mail: ksushap13.03.2001@mail.ru

Шейко Елизавета Алексеевна, ассистент кафедры «Системы автоматизированного проектирования» Института пути, строительства и сооружений Российского университета транспорта (МИИТа), 127994, ГСП-4, Москва, ул. Образцова, д.9, стр. 9, e-mail: elizabet-250997@mail.ru

International Journal for Computational Civil and Structural Engineering, 21(1) 105–120 (2025)

DOI:10.22337/2587-9618-2025-21-1-105-120

NEW MAGNETIC LINEAR SENSOR FOR CRACK MONITORING IN STRUCTURES

Sergej I. Evtushenko, ***Maksim M. Zheleznov, Mikhail A. Kuchumov, Liubov A. Adamtsevich***

National Research Moscow State University of Civil Engineering, Moscow, RUSSIA

Abstract: Due to the recent deployment of new sensing technologies and monitoring devices aiming to control technical condition of structures and its safety, the problem of optimization of data acquisition process and economic expediency during Structural Health Monitoring has arisen. This article presents the design and implementation of a new linear displacement sensor prototype with advanced functionality capable to measure three significant parameters affecting the condition of concrete and brick structures: cracks width, environmental temperature and humidity. The measuring method is based on the efficient principle of converting input values using Hall effect, which is rarely found in structural monitoring. The sensor prototype also includes a hardware set for immediate processing and transmitting data, which ensures efficient remote monitoring. As a result of the work, research and analysis of methods and principles for measuring linear displacements were carried out, selection and justification of the choice of hardware components of the sensor were performed, electronic circuit and functional diagrams were developed. Furthermore, work was done on modeling the structural elements of the sensor and their final production was executed. According to the results of tests of the sensor prototype, numerical characteristics were obtained, its performance was confirmed and, eventually, the ways of further improvement are proposed.

Keywords: Structural Health Monitoring, magnetic sensor, linear sensor, cracks

НОВЫЙ МАГНИТНЫЙ ЛИНЕЙНЫЙ ДАТЧИК ДЛЯ КОНТРОЛЯ ТРЕЩИН В КОНСТРУКЦИЯХ

С.И. Евтушенко, ***М.М. Железнов, М.А. Кучумов, Л.А. Адамцевич***

Национальный исследовательский Московский государственный строительный университет, г. Москва, РОССИЯ

Аннотация: В связи с недавним внедрением новых сенсорных технологий и устройств мониторинга, направленных на контроль технического состояния конструкций и их безопасности, возникла проблема оптимизации процесса сбора данных и вопрос экономической целесообразности при проведении мониторинга состояния конструкций. В статье представлена разработка и реализация нового прототипа датчика линейных перемещений с расширенным функционалом, способного измерять три значимых параметра, влияющих на состояние бетонных и кирпичных конструкций: ширину трещин, температуру и влажность окружающей среды. Метод измерения основан на эффективном принципе преобразования входных величин с использованием эффекта Холла, что редко встречается в мониторинге конструкций. В состав прототипа датчика также входит аппаратный комплекс для немедленной обработки и передачи данных, что обеспечивает эффективный удаленный мониторинг. В результате работы были проведены исследования и анализ методов и принципов измерения линейных перемещений, выполнен выбор и обоснование выбора аппаратных компонентов датчика, разработаны электронные принципиальные и функциональные схемы. Кроме того, была проведена работа по моделированию конструктивных элементов датчика и осуществлено их конечное изготовление. По результатам испытаний прототипа датчика получены числовые характеристики, подтверждена его работоспособность и, в итоге, предложены пути дальнейшего совершенствования.

Ключевые слова: Мониторинг состояния конструкций, магнитный датчик, линейный датчик, трещины

1. INTRODUCTION

Currently, most methods of surveying and assessing the technical condition of building structures involve the use of portable technical means and a relatively simple instrumental base with limited functionality. Although highly reliable, these monitoring methods have a significant drawback, namely that they can only be performed during a scheduled survey, repair or reconstruction. In addition, the monitoring methods used today can be very labor-intensive, costly, and thus ineffective when performing tasks at technically complex facilities, which include, for example, seaports, bridges, tunnels, as well as unique facilities for which technical regulations have not been established. Most facilities have individual space-planning and design solutions, and the types of materials used in the structures. Building structures are operated in various conditions and are not always located in easily accessible places (monitoring unique buildings, surveying chimneys, hydraulic structures, bridges and overpasses). [1] The authors are confident that in order to solve such complex engineering problems dictated by the dynamic development of the construction industry, it is necessary to improve the currently used measurement base and introduce new measurement tools that could provide the most accurate results and increase the quantity and quality of information obtained both for applied (for example, within the framework of geotechnical monitoring) and experimental purposes.

2. LITERATURE REVIEW

Detecting cracks in bridge structures is inherently challenging due to the size, complexity, and varied materials of bridges. According to Bao et al. [2], visual inspections, the most traditional method, are often inadequate because they are subjective, labor-intensive, and prone to human error. Advanced methods, such as ultrasonic testing or thermography, provide more precise detection but face limitations regarding accessibility, especially in hard-to-reach areas of large bridges [3]. Even when cracks are detected, interpreting the data to assess the severity and progression of damage presents another challenge. As noted by Johnson et al. [4], SHM systems generate vast amounts of data, which can overwhelm engineers and lead to delays in decision-making. Additionally, integrating data from different sensors and monitoring systems to provide a comprehensive understanding of bridge health remains a complex task, often requiring advanced algorithms. Environmental and operational conditions greatly affect crack monitoring efforts. Temperature fluctuations, humidity, and vibration from traffic can all influence the readings of crack monitoring sensors, leading to false positives or negatives. According to Kim et al. [5], bridges in regions with extreme weather conditions present unique challenges, as sensors must be resilient to harsh environments while maintaining accuracy.

It is worth noting the importance of a correct and comprehensive assessment of historical buildings. Given the availability of constant, reliable information about both the state of the elements and environmental conditions, it becomes possible to simulate realistic damage scenarios that may occur in the future [6] and prevent structural anomalies. This approach is the key to expanding knowledge of old structures. However, currently used conservative methods for aged buildings have a number of limitations and may be unreliable. For example, they often underestimate the load carrying capacity, which may result in uneconomical or unnecessary mitigation measures being taken to maintain old structures [7]. Therefor the use of more sophisticated methods is needed for old structures maintenance to avoid moving towards its discontinuation and losing benefits of their functioning.

While significant advancements have been made in crack monitoring technologies for bridge SHM, several challenges remain. These

include the limitations of detection technologies, difficulties in data interpretation, environmental influences, and the high costs associated with current monitoring systems. Addressing these challenges requires continued research and innovation, particularly in improving sensor durability, and developing cost-effective monitoring solutions. Recent studies have explored those advancements in wireless sensor networks offer promising avenues for more cost-effective and efficient monitoring solutions [8].

Among the various aspects of Structural Health Monitoring (SHM) discussed in this work, the authors focus on measuring linear displacements that could indicate potential issues, such as crack detection, monitoring expansion joints, and observing changes in the geometric alignment of structural junctions. One promising solution to these challenges involves recent advancements in electromagnetism. Many studies have explored new, advanced sensors for position, displacement, and crack monitoring based on magnetic effects [9-12]. However, the use of magnetic sensors has traditionally been more prevalent in mechanical engineering and the automotive industry. There has been limited research on their application in SHM systems, and their use in current practice remains minimal.

In order to analyse the current state of scientific research in the target area, statistics were collected on the number of publications presented in the international Scopus database in the main areas: "Linear sensor"; "Linear position sensor"; "Linear potentiometer"; "Linear converter"; "Displacement sensor"; "Photogrammetry"; "Crack monitoring".

The highest number of publications is displayed for the keyword "Linear sensor ". So, in the period from 2011 to 2021, 69,336 publications were published, which is of considerable interest to scientists in this field. Figure 1 represents growth dynamics of the number of publications by keywords.

At the same time, within the framework of the presented study, the authors decided to take a sample for further research, compiled according to the two keywords "Linear sensor" and "Crack monitoring". A total of 205 document search results for the specified keywords are displayed. The distribution of publications by years is shown in Figure 2.

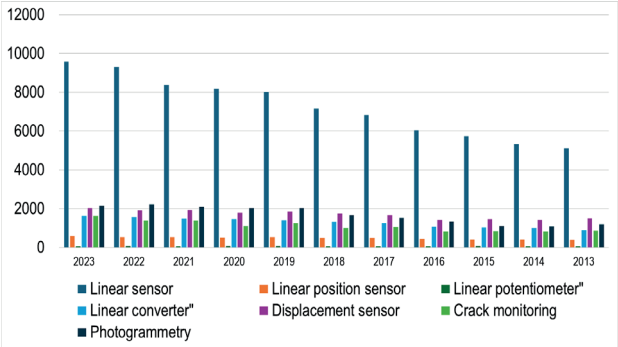

Figure 1. Growth dynamics of publications by keywords: "Linear sensor"; "Linear position sensor"; "Linear potentiometer"; "Linear converter"; "Displacement sensor"; "Photogrammetry"; "Crack monitoring" presented in the international Scopus database in the period from 2013 to 2023

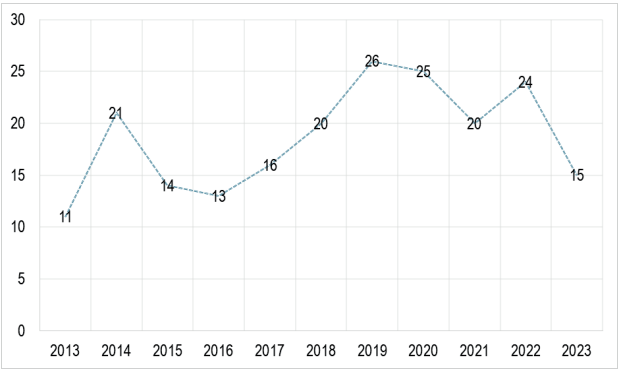

Figure 2. Distribution of publications by years by keywords "Linear sensor" and "Crack monitoring"

The distribution of publications by country is shown in Figure 3 (the first 15 countries), and Figure 4 shows the distribution of publications by branches of knowledge.

As can be seen from Figure 3a, the leaders in the area under consideration are authors from the China (69 publications), the second place is occupied by authors from United States (33

publications), the three leaders are closed by authors from the UK (16 publications). At the same time, the largest number of publications relates to the field of knowledge "Engineering" (39,1%). Thus, considerable attention is paid to the issues of using the sensor in monitoring building structures.

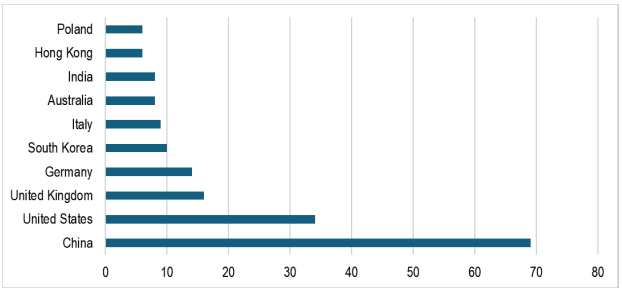

Figure 3. Statistics on the publications of the sample by country

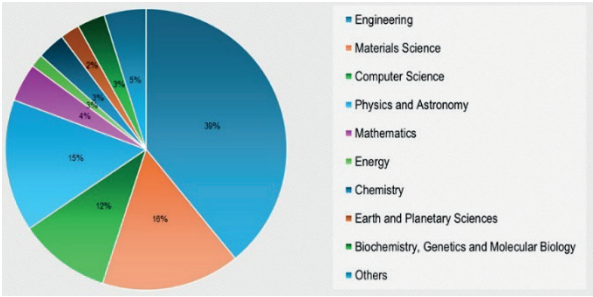

Figure 4. Statistics on the publications of the sample by branches of knowledge

A brief description of the most cited publications from the sample is presented in Table 1.

Table 1. Summary of the most cited publications in the sample

title	year	abstract	citates
[13]	2017	The article addresses the issue of the minimum number of sensors required and their placement for structural health monitoring using the example of an Italian monumental bell tower, which was monitored for over nine months. The correlations between natural frequencies and environmental parameters are examined in detail, and the predictive capabilities of linear statistical regression models based on the use of multiple continuous environmental monitoring sensors are assessed.	186
[14]	2014	Engineering structures are subject to fatigue damage during their service life, which entails early detection and continuous monitoring of fatigue damage from its inception to growth. A hybrid approach for fatigue damage characterization was developed using two types of damage indicators constructed based on linear and nonlinear characteristics of acoustoultrasonic waves. The results showed that nonlinear characteristics of acoustoultrasonic waves outperform their linear counterparts in terms of detectability.	168
[15]	2014	This article presents predictive modeling of nonlinear propagation of guided waves for structural health monitoring using both finite element method and analytical approach. In the study, the nonlinearity of guided waves is generated by interaction with a nonlinear breathing crack.	129
[16]	2015	By means of numerical simulation and subsequent experimental verification, two damage indices are comparatively constructed based on the linear and nonlinear time characteristics of Lamb waves, which are used to localize the fatigue damage near the rivet hole of the aluminum plate.	109
[17]	2016	The renewable energy industry is constantly improving and developing all over the world, wind energy seems to be the most in demand, which leads to the need to ensure a high level of reliability, availability, maintainability and safety of wind turbines. This article is devoted to the issue of ensuring the reliability of wind turbines through the use of a new fault location approach for acoustic emission techniques in wind turbines	85

title	year	abstract	citates
[18]	2015	This article proposes a method to obtain crack initiation, location and width data in concrete structures subjected to bending and equipped with an optical backscatter reflectometer system.	78
[19]	2017	The objective of this review is to demonstrate how acoustic emission (AE) location in loaded polymer composites can be used to gain a deeper understanding of damage onset and growth and associated failure events and sequences.	73
[20]	2019	This article investigates the possibility of using new microwave sensors for crack detection in reinforced concrete structures.	71
[21]	2018	Glass fiber reinforced polymers have attracted increasing attention in recent years, but this material has low elastic modulus, and linear elastic properties compared with steel bars, which leads to different bond characteristics between bars and concrete. In this article, an active sensing approach based on piezoelectric ceramics is proposed and developed to detect the bond failure between glass fiber reinforced polymer bars and concrete structures.	71
[22]	2019	There is a need to develop a structural health monitoring method to evaluate micro-sized fatigue cracks in metallic structures, since cracks are considered as precursors to structural failure. However, traditional linear ultrasound-based technology is insensitive to cracks when they are barely visible in metallic environments. In this paper, we present a nonlinear ultrasonic technology based on crack-wave interaction to study fatigue crack growth.	62
[23]	2014	“Sensor sheets” based on large-area electronics consist of a dense array of single strain sensors. They are an effective and affordable structural health monitoring tool that can detect and continuously monitor crack growth in structures. This paper presents a study of the quantitative relationship between crack width and strain, the latter measured by a single sensor that will be part of the sensor sheet.	62
[24]	2016	This research work assessed the feasibility of using telecommunication single-mode optical fiber (SMF) as a distributed fiber-optic strain and crack sensor in concrete pavement monitoring	56
[25]	2022	Flexible pressure sensors with high sensitivity over a wide pressure range are in great demand, but they are difficult to fabricate to meet the practical application requirements in daily activities and more significantly in some extreme conditions. This work demonstrates a thin, lightweight, and high-performance pressure sensor based on flexible porous phenyl silicone/functionalized carbon nanotube film.	54
[26]	2020	Marine structures are subject to fatigue damage due to fluctuating environmental and operational forces. This article compares the use of mode shapes from a finite element model with that of extended experimental mode shapes. Modal expansion is applied to a scaled offshore platform in a laboratory to evaluate the deformation response using finite element mode shapes and extended experimental mode shapes using different expansion methods. Based on this study, the expansion of experimental mode shapes has the potential to reduce errors in stress/strain estimation. However, the expansion is a fitting process and thus contains case-dependent fitting error. In this research work, finite element mode shapes outperform some mode shape expansion methods due to these fitting errors.	51
[27]	2018	This article presents a study of the features of nonlinear scattering of guided waves from fatigue cracks initiated in rivet holes, considering the state of a rough contact surface.	50

3. MATERIALS AND METHODS

Within this work the authors set the following tasks, solution of which would make it possible to achieve the necessary technical requirements for the sensor:
1. Finding the principle of input signal conversion, the choice of a measuring element.
2. Determination of the set of hardware components, electronic circuit schemes and its primary prototyping;
3. Selection of the required technical characteristics of electronic components;
4. Justification of the set of hardware selected.

3.1. The development of a methodology for input signals conversion

When choosing a method for measuring linear displacements, the following methods were considered:

1. Mechanical-electrical (using microrheostat);
2. Mechanical-optical (using optical encoder);
3. Mechanical-magnetic (using a combination of Hall sensor and permanent magnet).

The third method was chosen as most preferred, because it outperformed the others in all key metrics: simplicity, cost, reliability. Common disadvantages of rheostat sensors are the presence of sliding contact and, consequently, contact resistance, abrasion and possible oxidation of contact surfaces, the possibility of their contamination, the creation of electrical noise. The main drawbacks to optical encoders are its mechanical fragility, and poor reliability in dust-polluted environments. Apart from that, high rate of linearity and the durability to the vibrations, created by the other operating devices, make magnetic sensors preferable [28].
As a magnetic field recorder, a Hall sensor was chosen, analogous to 100G, bipolar, in an SS41 design with the following characteristics:

- output signal, digital;
- sensing type, dipolar;
- turn-on induction, 1000, Gauss;
- switch-off induction, -1000, Gauss;
- temperature range, -40…150 oC;
- weight, 0.09 g.

As it was planned by the authors the magnet and Hall sensor are fixed to the movable sensor parts located on both sides of the crack in building structure. Depending on the distance between the Hall sensor and the magnet, the Hall sensor generates an output voltage level corresponding to the magnetic induction of the current relative position of the measuring pair.
Another task was to find the suitable shape of the magnet. The fact is that the shape of the magnet determines the location of its magnetic lines, the uniformity of distribution and collinearity of which, as well as the linearity of the change in the vector angle of the magnetic flux, directly affect the accuracy of measurements and the complexity of sensor calibration. Within the framework of this work, toroidal and rectangular magnets were considered, their physical properties were determined by measuring the analog signal received from the output of the Hall sensor when interacting with magnets in various positions (see Figures 5).

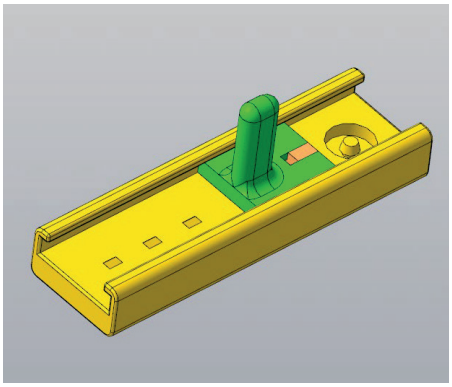

Figure 5. Model of the layout for preliminary tests

Based on the results of initial prototyping and analysis of the received signal, a rectangular magnet with an axial direction of magnetization was chosen as the source of the magnetic field, which made it possible to achieve a measurement range of 20 mm, with the following characteristics:

- Length, 20 mm;
- Width, 10 mm;
- Thickness, 2 mm;
- Weight, 3 g;
- Magnetization: axial;
- Max. temperature 80 Co;
- Degaussing time, 1% per 10 years.

Later, the problem arose of placing a magnet in the Measuring Part (MP) of the linear sensor prototype, which was solved at the stage of design development.

3.2. The development of an electronic control board

The main issues existed on this stage of work were:

1. Formation of requirements to the Electronic Control Board (ECB) and its general technical capabilities;
2. Determination of the list of components necessary to solve the tasks set for the ECB;
3. Design of the housing that should meet the specifics of working environment, determining the locations of the key components of the board, soldering points for connectors;
4. Computer modelling of the ECB;
5. Production of a printed circuit board and soldering of the ECB components;
6. Software and constructive debugging of the ECB components;
7. Finalization of the ECB.

As part of the development, three stages of step-by-step refinement of the ECB took place. The model of the current design is shown in Figure 6.

The electronic control board of the linear sensor prototype is a dielectric printed circuit board included a number of electronic components and measuring unit connected by electronic measuring circuit. The main function of the ECB is to receive, process and transmit a signal generated by the transducer (Hall sensor) with information about the linear displacement of the object under study. The main electronic components of the ECB:

- POA (programmable operational amplifier) with built-in analog-to-digital signal converter PGA280;
- STM32F373CCT6 microcontroller;
- transceiver RS-485 ADM2687EBRIZ;
- LDO voltage regulator LD117AS33TR;
- power supply unit: POWERLINE ICR18650 2200 mAh accumulator;
- GSM-module SIM800;
- temperature and humidity sensor DHT22;
- reference voltage source REF2033AIDDC;
- DC/DC converter EM 0515V;
- quartz resonator HC-49S;
- a set of resistors, capacitors, diodes;
- connecting parts: screw terminal blocks, PLD-40 connectors.

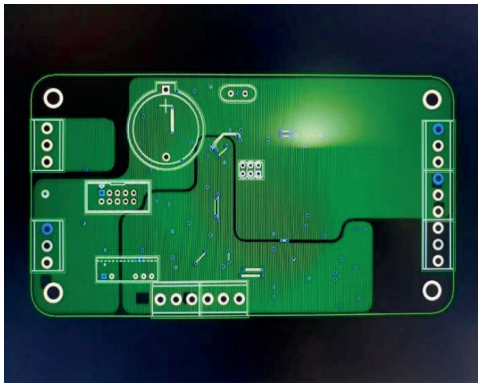

Figure 6. Model of the Electronic Control Board

An analog signal from Hall sensor is supplied to the operational amplifier PGA280. Further, the signal amplified to a certain level is converted into a digital representation using the built-in ADC, and then processed by the microcontroller.

Amplifiers are used to amplify weak DC signals. After analyzing ready-made solutions in the semiconductor market, we settled on the Texas Instruments PGA280 programmable operational amplifier. It is characterized by:

- wide input supply range, ±15.5…±18 V;
- switchable gain, 128V/V…1/8 V/V;
- low bias level (3 μV) at gain level, 128 V/V;
- absence of zero drift over a long period of observation;
- small temperature drift 0.5 ppm/°C.

Also, POA (programmable operational amplifier) has a 16-fold margin for the accuracy of the measured signal, low drift, near-zero errors.

The bit depth of an ADC is the bit depth of its output signal, that is, the number of bits in the value at the ADC output. For example, a 16-bit PGA280 ADC can output 216 = 65536 values (from 0 to 65536 if we are talking about positive numbers). Thus, we can determine the further accuracy of the linear sensor prototype, which the selected ADC can provide. This can be done using the following formula:

$$X = \frac{D}{2^P}, \quad (2)$$

where P is the ADC capacity, bit; D – range of measurement of linear displacements, mm; X is the accuracy of measuring linear displacements (discreteness), mm.

$$X = \frac{20}{2^{16}} = 0{,}0003 \text{ mm}. \quad (3)$$

Since the measuring range of linear displacement is 20 mm, under ideal conditions, the hardware of the prototype sensor can measure linear displacement with an accuracy of 0.0003 mm.

The STM32 microcontroller is a popular and highly demanded platform that allows you to create professional solutions for automation in a wide variety of areas, based on STMicroelectronics microcontrollers with an ARM processor, various modules and peripherals. The processor frequency is 76 MHz, which is enough to calculate and transfer data almost instantly and provide a reading time of less than 1 second.

Protection of wires and connections is a fundamental task to ensure durability of the SHM system and data quality [29]. Therefore, it is more preferred to utilize wireless communication interface. In linear sensor it is provided by the presence of the SIM800 module in the ECB. This module is in no way inferior to a conventional cell phone in terms of functional characteristics, and with its help you can send SMS messages, make or receive phone calls, connect to the Internet via GPRS, TCP / IP without distance limitation.

Environmental factors have a significant impact on the parameters of structures, especially concrete [30]. Thus it is also possible to integrate a temperature and humidity sensor into the ECB, for example, DHT22 with the following confirmed technical characteristics:

- humidity measurement range, 0…100%;
- temperature measurement range, -40…+80 C.

3.3. The development of a functional scheme of work and design

The functional diagram of the linear sensor prototype consists of two distinct structural components: the Measuring Part (MP), which includes a Hall sensor, and the Electronic Control Board (ECB) housed in a sealed casing. The MP produces an output signal in response to an input action within the system and sends this signal to the analogue input of the ECB. The analogue signal, which carries information about the linear movement, is then processed, and the resulting data is transmitted over a wireless communication channel.

The linear sensor comprises a Measuring Part (MP) made up of two grooved rails that move linearly in relation to each other. One rail has a Hall sensor mounted on it, while the other features a magnet placed directly beneath the sensor, separated by an air gap of less than 1 mm. The rails are connected by a hinge, which enables them to adjust their position in two planes at the same time, parallel to the object's surface.

The second structural element of the sensor is the housing, installed in close proximity to the MP, with the necessary set of connectors and pressure seals, in which the ECB is located, connected to the Hall sensor by a wired interface. The standard G258C 160x80x55mm enclosure (option with transparent top cover), meeting the IP54 standard, provides protection

of internal electronic components from environmental influences.
The results of designing the MP of the linear sensor prototype for its further production by the FDM printing method (3D printing with PETG polymer) are shown in Figures 7, 8.

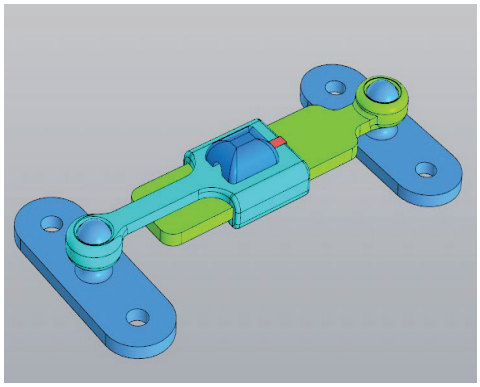

Figure 7. Model of the sensor's MP (zero position)

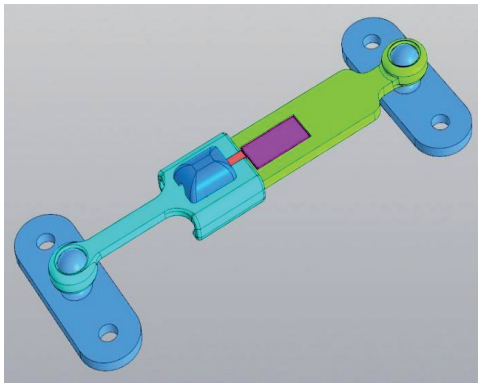

Figure 8. Model of the sensor's MP (extreme positions)

3.4. Production of the linear sensor prototype
The production of a linear displacement sensor prototype took place in three stages:
1. Soldering and mounting of ECB electronic components;
2. Refinement of a typical housing by installing additional connectors, spacers, brackets and installing an ECB inside the housing;
3. Production of the MP by 3D printing and subsequent refinement.
A general view of the finished ECB with mounted elements is shown in Figure 9.

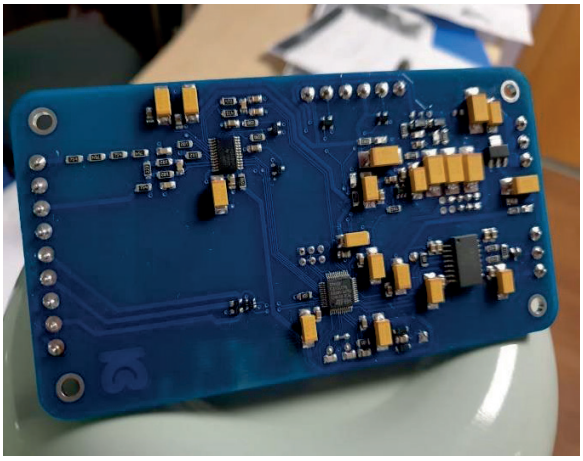

Figure 9. General view of the ECB

It should be mentioned that in addition to the components placed on the board, the circuit involves a separate modem board designed specifically for embedded solutions - SIM800. To locate the modem board inside the case, special bracket was made (see Figure 10). It solves several problems, including convenient location of the modem board (for connecting an external antenna, changing a SIM card), noise immunity of the radio part due to the removal of the board from the rest ECB components.

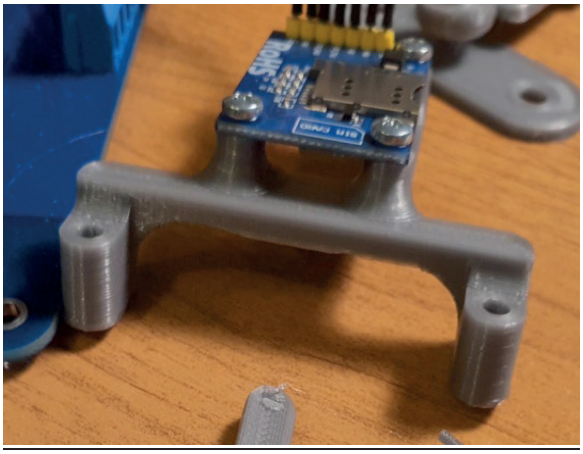

Figure 10. GSM module board bracket and board spacers

Figure 11 shows the attachment of the SIM800 GSM module board to the inner surface of the sensor housing.

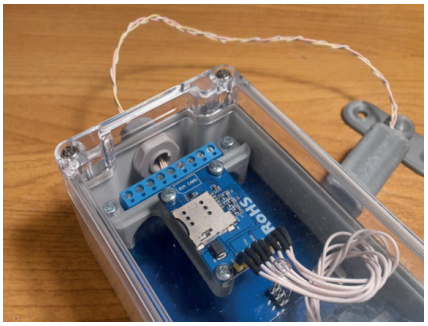

Figure 11. Mounting unit for the SIM800 GSM module board

The manufacturing of sensor's MP was carried out using the FDM printing method (3D printing with PETG polymer).

The finished MP of the sensor is shown in Figure 12.

Summing up the stages of design development and manufacturing of a linear displacement sensor prototype, it became possible to determine the main functional and design characteristics:

1. Execution IP54, due to the selected housing and the organization of the input of cable connections through pressure seals of the appropriate calibre;
2. Possibility to connect to the power supply as from an external source using the appropriate connector or use the built-in battery;
3. Ability to connect two analogue sensors for simultaneous measurement of linear displacements in two planes;

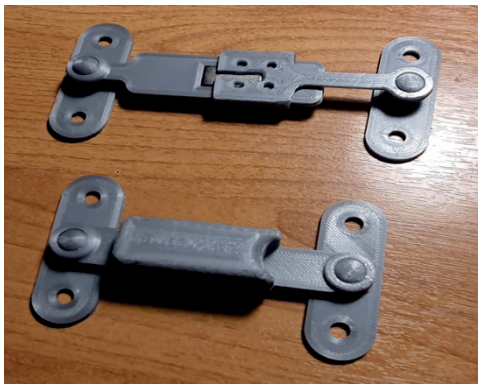

Figure 12. The final version of the Measuring Part

A general view of the linear sensor prototype is shown in Figure 13.

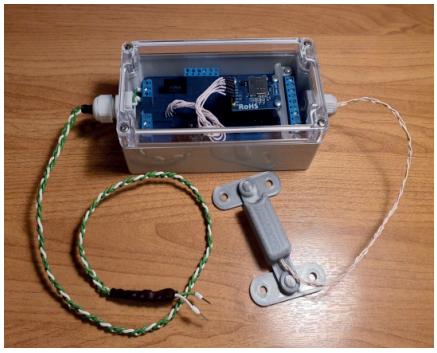

Figure 13. General view of the linear sensor prototype

3.5. Laboratory test

Laboratory test of the linear sensor prototype were carried out in order to validate the correctness of the technical solutions adopted, as well as to obtain reliable information about the characteristics of the prototype.

Testing of the linear displacement sensor prototype consisted in studying the amplitude and time characteristics of the electrical signal received from the sensor by connecting an oscilloscope.

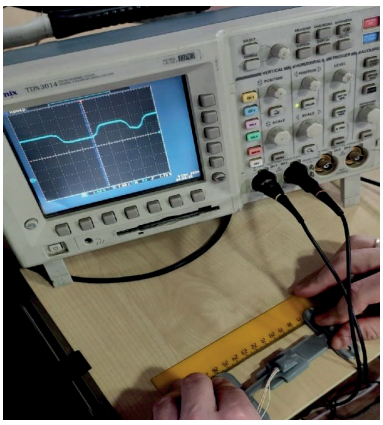

Figure 14. Obtaining an electrical signal from a sensor prototype

4. Results and Discussion

Based on the results of sensor prototype development and testing, the following technical characteristics were achieved:

- measuring range of linear displacements, 0…20 mm (±10 mm in each direction from the zero position);
- accuracy of measurement of linear displacements, 0.0003 mm;

- measuring base of linear displacements, 110 mm;
- overall dimensions, 160x80x55 mm;
-weight, 350 g.

Experimental results validate the accuracy of the linear displacement sensing with a competitive behaviour. Given that under ideal conditions sensor provides high measurement accuracy, further research needed to determine the sensitivity to electromagnetic interference and signal contamination [31], which is typical for magnetic sensor, and degree of its influence on measurements accuracy in the field conditions needs to be found.

It is also worth noting that data processing, reduction and storage are fundamental SHM issues, in particular having a large number of sensors installed on the monitored structure. The availability of procedures able to reduce then transmission data volumes is a key aspect for reliability and sustainability of SHM systems. The proposed solution where the sensor also acts as a data logger combines two subsystems of the SHM system at once – sensing and data aqusation and transmitting. It may mitigate the necessary data analyses capacity of the system, deployment costs and enhance reliability and resources optimization, which is crucial for the modern SHM systems [32].

CONCLUSION

When investigating the causes of negative processes occurring in the load-bearing structures of buildings and facilities at the stress-strain state, as well as the dynamics of their development, it is crucial to comprehensively measure not only the parameters of visible defects, such as cracks, but also to simultaneously record changes in the parameters of the soil foundation under external dynamic loads. Only in this way can the observer obtain comprehensive information about the current state of the technical object and the natural environment, which together form a geotechnical system whose components are constantly in close interdependence. For this purpose, the authors propose to add to a load cell [33] determining the stress state of the soil to the measurement system to expand the amount of data received during SHM.

REFERENCES

1. **Evtushenko S.I., Kuchumov M.A.** Linear displacement sensor for use in monitoring systems for engineering structures of civil infrastructure facilities. Actual problems of computer modeling of structures and constructions: Abstracts of reports of the VIIIth international symposium / FSBEI HE "Tambov State Technical University". - Tambov, 2023.–379-381
2. **Bao, X., Li, Z., Wang, Z.** (2019). Challenges in Crack Detection for Bridge Structures: A Review, Journal of Bridge Engineering, 24(3), 112-125.
3. **Gao, Y., Liu, F., & Yang, H.** (2018). Advanced Non-Destructive Testing Methods for Crack Detection in Bridges, Structural Health Monitoring, 15(5), 421-438.
4. **Johnson, M., Kim, J., Singh, A.** (2020). Data Management and Interpretation in Bridge Health Monitoring Systems, Computers and Structures, 89(2), 102-114.
5. **Kim, S., Park, D., & Lee, H.** (2018). Impact of Environmental Factors on Crack Monitoring in Bridges, Journal of Civil Engineering and Management, 14(6), 353-366.
6. **Cabboi A, Gentile C, Saisi A.** (2017) From continuous vibration monitoring to FEM-based damage assessment: Application on a stone-masonry tower, Construction Buildings Materials, 156, 2017 - pp. 252-265
7. **Orban Z.** (2004) Assessment, reliability and maintenance of masonry arch railway bridges in Europe, ARCH´04 P. Roca and E. Oñate (Eds) CIMNE, Barcelona, p. 5-8
8. **Huang, Z., Fang, X., Guo, S**. (2019). Wireless Sensor Networks in Bridge

Monitoring: A Review, Sensors, 19(15), 3342.
9. **Vega R.C., Cubas G., Sandoval-Chileño M.A., Castañeda Briones L.A**. (2022) Position Measurements Using Magnetic Sensors for a Shape Memory Alloy Linear Actuator, Sensors,22(19), 7460; https://doi.org/10.3390/s22197460
10. **Yan L., Zhang H., Ye P.** (2017) Mover Position Detection for PMTLM Based on Linear Hall Sensors through EKF Processing, Sensors,17(4), 782; https://doi.org/10.3390/s17040782
11. **Zhang J., Shi Y., Huang Y.** (2022) A Displacement Sensing Method Based on Permanent Magnet and Magnetic Flux Measurement, Sensors, 22(12), 4326; https://doi.org/10.3390/s22124326
12. **Gkantou, M., Muradov, M., Kamaris, G.S., Hashim H., Atherton, W., Kot P.** (2023) Novel electromagnetic sensors embedded in reinforced concrete beams for crack detection, Sensors (Switzerland) 19(23), 5175.
13. **Ubertini, F., Comanducci, G., Cavalagli, N., Laura Pisello, A., Luigi Materazzi, A., Cotana, F.** (2017) Environmental effects on natural frequencies of the San Pietro bell tower in Perugia, Italy, and their removal for structural performance assessment, Mechanical Systems and Signal Processing, vol. 82, pp. 307-322, 2017, doi: 10.1016/j.ymssp.2016.05.025
14. **Su, Z., Zhou, C., Hong, M., Cheng, L., Wang, Q., Qing, X.** (2014) Acousto-ultrasonics-based fatigue damage characterization: Linear versus nonlinear signal features, Mechanical Systems and Signal Processing, vol. 45, pp. 225-239, doi: 10.1016/j.ymssp.2013.10.017
15. **Shen, Y., Giurgiutiu, V.** (2014) Predictive modeling of nonlinear wave propagation for structural health monitoring with piezoelectric wafer active sensors, Journal of Intelligent Material Systems and Structures, vol. 25, pp. 506-520, 2014, doi: 10.1177/1045389X13500572
16. **Hong, M., Su, Z., Lu, Y., Sohn, H., Qing, X.** (2015) Locating fatigue damage using temporal signal features of nonlinear Lamb waves, Mechanical Systems and Signal Processing, vol. 60, pp. 182-197, doi: 10.1016/j.ymssp.2015.01.020
17. **Muñoz, C.Q.G., Márquez, F.P.G.** (2016) A new fault location approach for acoustic emission techniques in wind turbines, Energies, vol. 9, doi: 10.3390/en9010040
18. **Rodríguez, G., Casas, J.R., Villaba, S.** (2015) Cracking assessment in concrete structures by distributed optical fiber, Smart Materials and Structures, vol. 24, doi: 10.1088/0964-1726/24/3/035005
19. **Romhány, G., Czigány, T., Karger-Kocsis, J.** (2017) Failure Assessment and Evaluation of Damage Development and Crack Growth in Polymer Composites Via Localization of Acoustic Emission Events: A Review, Polymer Reviews, vol. 57, pp. 397-439, doi: 10.1080/15583724.2017.1309663
20. **Gkantou, M., Muradov, M., Kamaris, G.S., Hashim, K., Atherton, W., Kot, P.** (2019) Novel electromagnetic sensors embedded in reinforced concrete beams for crack detection, Sensors (Switzerland), vol. 19, doi: 10.3390/s19235175
21. **Xu, K., Ren, C., Deng, Q., Jin, Q., Chen, X.** (2018) Real-time monitoring of bond slip between GFRP bar and concrete structure using piezoceramic transducer-enabled active sensing, Sensors (Switzerland), vol. 18, doi: 10.3390/s18082653
22. **Wang, R., Wu, Q., Yu, F., Okabe, Y., Xiong, K.** (2019) Nonlinear ultrasonic detection for evaluating fatigue crack in metal plate, Structural Health Monitoring, vol. 18, pp. 869-881, doi: 10.1177/1475921718784451
23. **Tung, S.-T., Yao, Y., Glisic, B.** (2014) Sensing sheet: The sensitivity of thin-film full-bridge strain sensors for crack detection and characterization, Measurement Science

and Technology, vol. 25, doi: 10.1088/0957-0233/25/7/075602
24. **Bao, Y., Tang, F., Chen, Y., Meng, W., Huang, Y., Chen, G**. (2016) Concrete pavement monitoring with PPP-BOTDA distributed strain and crack sensors, Smart Structures and Systems, vol. 18, pp. 405-423 doi: 10.12989/sss.2016.18.3.405
25. **Hou, Y., Wang, L., Sun, R., Zhang, Y., Gu, M., Zhu, Y., Tong, Y., Liu, X., Wang, Z., Xia, J., Hu, Y., Wei, L., Yang, C., Chen, M**. (2022) Crack-Across-Pore Enabled High-Performance Flexible Pressure Sensors for Deep Neural Network Enhanced Sensing and Human Action Recognition, ACS Nano, vol. 16, pp. 8358-8369, doi: 10.1021/acsnano.2c02609
26. **Tarpø, M., Nabuco, B., Georgakis, C., Brincker, R**. (2020) Expansion of experimental mode shape from operational modal analysis and virtual sensing for fatigue analysis using the modal expansion method, International Journal of Fatigue, vol. 130, doi: 10.1016/j.ijfatigue.2019.105280
27. **Shen, Y., Wang, J., Xu, W**. (2018) Nonlinear features of guided wave scattering from rivet hole nucleated fatigue cracks considering the rough contact surface condition, Smart Materials and Structures, vol. 27, doi: 10.1088/1361-665X/aadd2d
28. **Papoutsidakis M., Drosos C., Chatzopoulos A.** (2018) Position Sensors – A Brief Guide of Use of the Most Common Types / International Journal of Computer Applications, p. 11.
29. **Rainieri, C.; Fabbrocino, G.; Cosenza, E.** (2008) Integrated systems for structural health monitoring: Worldwide applications and perspectives. In Proceedings of the 4th European Workshop on Structural Health Monitoring; Uhl, T., Ostachowicz, W., Holnicki-Szulc, J., Eds.; DEStech Publications, Inc.: Lancaster, PA, USA; p. 4
30. **Li Z., Jin Z. Shao S., Zhao T., Wang P.** (2019) Influence of Moisture Content on Electromagnetic Response of Concrete Studied Using a Homemade Apparatus, Sensors, 19(21), 4637; https://doi.org/10.3390/s19214637
31. **Leyang Yan, Hui Zhang, Peiqing Ye**.(2017) Mover Position Detection for PMTLM Based on Linear Hall Sensors through EKF Processing // Sensors 17(4), 782; https://doi.org/10.3390/s17040782 - p. 2.
32. **Nong S.-X., Yang D.-H., Yi T.-H.** (2021) Pareto-Based Bi-Objective Optimization Method of Sensor Placement in Structural Health Monitoring // Buildings 11(11), 549; https://doi.org/10.3390/buildings11110549
33. **Kuchumov M., Evtushenko S**.(2022) New Soil Stress Measurement Sensor Based on the Effect of Elastic Charging of Electrodes / Buildings 12(3), 327; https://doi.org/10.3390/buildings12030327

СПИСОК ЛИТЕРАТУРЫ

1. **Евтушенко С.И., Кучумов М.А.** Датчик линейных перемещений для использования в системах мониторинга инженерных конструкций объектов гражданской инфраструктуры//В книге: Актуальные проблемы компьютерного моделирования конструкций и сооружений. Тезисы докладов VIII-го международного симпозиума. 2023. С. 379-381.
2. **Bao, X., Li, Z., Wang, Z.** Challenges in Crack Detection for Bridge Structures: A Review// Journal of Bridge Engineering, 2019,24(3), pp.112-125.
3. **Gao, Y., Liu, F., & Yang, H.** Advanced Non-Destructive Testing Methods for Crack Detection in Bridges//Structural Health Monitoring, 2018, 15(5), pp.421-438.
4. **Johnson, M., Kim, J., & Singh, A**. Data Management and Interpretation in Bridge Health Monitoring Systems.// Computers and Structures, 2020, 89(2), pp.102-114.

5. **Kim, S., Park, D., & Lee, H.** Impact of Environmental Factors on Crack Monitoring in Bridges// Journal of Civil Engineering and Management, 2018, 14(6), pp.353-366.
6. **Cabboi A, Gentile C, Saisi A**. From continuous vibration monitoring to FEM-based damage assessment: Application on a stone-masonry tower // Construction Buildings Material, 2017, 156, pp. 252-265
7. **Orban Z.** Assessment, reliability and maintenance of masonry arch railway bridges in Europe / ARCH´04 P. Roca and E. Oñate (Eds) CIMNE, Barcelona, 2004, pp. 5-8
8. **Huang, Z., Fang, X., & Guo, S.** Wireless Sensor Networks in Bridge Monitoring: A Review// Sensors, 2019, 19(15), 3342.
9. **Vega R.C., Cubas G., Sandoval-Chileño M.A., Castañeda Briones L.A.** Position Measurements Using Magnetic Sensors for a Shape Memory Alloy Linear Actuator // Sensors, 2022, 22(19), 7460; https://doi.org/10.3390/s22197460
10. **Yan L., Zhang H., Ye P**. Mover Position Detection for PMTLM Based on Linear Hall Sensors through EKF Processing // Sensors, 2017, 17(4), 782; https://doi.org/10.3390/s17040782
11. **Zhang J., Shi Y., Huang Y.** A Displacement Sensing Method Based on Permanent Magnet and Magnetic Flux Measurement // Sensors, 2022, 22(12), 4326; https://doi.org/10.3390/s22124326
12. **Gkantou, M., Muradov, M., Kamaris, G.S., Hashim H., Atherton, W., Kot P.** Novel electromagnetic sensors embedded in reinforced concrete beams for crack detection // Sensors (Switzerland),2023, 19(23), 5175.
13. **Ubertini, F., Comanducci, G., Cavalagli, N., Laura Pisello, A., Luigi Materazzi, A., Cotana, F.,** Environmental effects on natural frequencies of the San Pietro bell tower in Perugia, Italy, and their removal for structural performance assessment // Mechanical Systems and Signal Processing,2017, vol. 82, pp. 307-322 doi: 10.1016/j.ymssp.2016.05.025
14. **Su, Z., Zhou, C., Hong, M., Cheng, L., Wang, Q., Qing, X**., Acousto-ultrasonics-based fatigue damage characterization: Linear versus nonlinear signal features//Mechanical Systems and Signal Processing, 2013, 45, pp. 225-239, 2014, doi: 10.1016/j.ymssp.2013.10.017
15. **Shen, Y., Giurgiutiu, V.,** Predictive modeling of nonlinear wave propagation for structural health monitoring with piezoelectric wafer active sensors// Journal of Intelligent Material Systems and Structures, 2014, 25, pp. 506-520, doi: 10.1177/1045389X13500572
16. **Hong, M., Su, Z., Lu, Y., Sohn, H., Qing, X.,** Locating fatigue damage using temporal signal features of nonlinear Lamb waves// Mechanical Systems and Signal Processing, 2015, 60, pp. 182-197 doi: 10.1016/j.ymssp.2015.01.020
17. **Muñoz, C.Q.G., Márquez, F.P.G.,** A new fault location approach for acoustic emission techniques in wind turbines//Energies,2016, 9, doi: 10.3390/en9010040
18. **Rodríguez, G., Casas, J.R., Villaba, S**., Cracking assessment in concrete structures by distributed optical fiber// Smart Materials and Structures, 2015, 24, doi: 10.1088/0964-1726/24/3/035005
19. **Romhány, G., Czigány, T., Karger-Kocsis, J.,** Failure Assessment and Evaluation of Damage Development and Crack Growth in Polymer Composites Via Localization of Acoustic Emission Events: A Review// Polymer Reviews, 2017, 57, pp. 397-439, doi: 10.1080/15583724.2017.1309663
20. **Gkantou, M., Muradov, M., Kamaris, G.S., Hashim, K., Atherton, W., Kot, P**., Novel electromagnetic sensors embedded in reinforced concrete beams for crack detection// Sensors (Switzerland), 2019, 19, doi: 10.3390/s19235175
21. **Xu, K., Ren, C., Deng, Q., Jin, Q., Chen, X**., Real-time monitoring of bond slip

between GFRP bar and concrete structure using piezoceramic transducer-enabled active sensing//Sensors (Switzerland),2018, 18, doi: 10.3390/s18082653

22. **Wang, R., Wu, Q., Yu, F., Okabe, Y., Xiong, K.,** Nonlinear ultrasonic detection for evaluating fatigue crack in metal plate// Structural Health Monitoring, 2019, 18, pp. 869-881, doi: 10.1177/1475921718784451
23. **Tung, S.-T., Yao, Y., Glisic, B**., Sensing sheet: The sensitivity of thin-film full-bridge strain sensors for crack detection and characterization//Measurement Science and Technology, 2014, 25, doi: 10.1088/0957-0233/25/7/075602
24. **Bao, Y., Tang, F., Chen, Y., Meng, W., Huang, Y., Chen, G**., Concrete pavement monitoring with PPP-BOTDA distributed strain and crack sensors// Smart Structures and Systems, 2016, 18, pp. 405-423, doi: 10.12989/sss.2016.18.3.405
25. **Hou, Y., Wang, L., Sun, R., Zhang, Y., Gu, M., Zhu, Y., Tong, Y., Liu, X., Wang, Z., Xia, J., Hu, Y., Wei, L., Yang, C., Chen, M.**, Crack-Across-Pore Enabled High-Performance Flexible Pressure Sensors for Deep Neural Network Enhanced Sensing and Human Action Recognition// ACS Nano, 2022, 16, pp. 8358-8369, doi: 10.1021/acsnano.2c02609
26. **Tarpø, M., Nabuco, B., Georgakis, C., Brincker, R.**, Expansion of experimental mode shape from operational modal analysis and virtual sensing for fatigue analysis using the modal expansion method// International Journal of Fatigue, 2020, 130, doi: 10.1016/j.ijfatigue.2019.105280
27. **Shen, Y., Wang, J., Xu, W.,** Nonlinear features of guided wave scattering from rivet hole nucleated fatigue cracks considering the rough contact surface condition// Smart Materials and Structures, 2018, 27, doi: 10.1088/1361-665X/aadd2d
28. **Papoutsidakis M., Drosos C., Chatzopoulos A**. Position Sensors – A Brief Guide of Use of the Most Common Types // International Journal of Computer Applications , 2018, p. 11.
29. **Rainieri, C.; Fabbrocino, G.; Cosenza, E**. Integrated systems for structural health monitoring: Worldwide applications and perspectives// In Proceedings of the 4th European Workshop on Structural Health Monitoring; Uhl, T., Ostachowicz, W., Holnicki-Szulc, J., Eds.; DEStech Publications, Inc.: Lancaster, PA, USA, 2008; p. 4
30. **Li Z., Jin Z. Shao S., Zhao T., Wang P.** Influence of Moisture Content on Electromagnetic Response of Concrete Studied Using a Homemade Apparatus/ / Sensors, 2019, 19(21), 4637; https://doi.org/10.3390/s19214637
31. **Leyang Yan, Hui Zhang, Peiqing Ye**. Mover Position Detection for PMTLM Based on Linear Hall Sensors through EKF Processing // Sensors, 2017, 17(4), 782; https://doi.org/10.3390/s17040782 - p. 2.
32. **Nong S.-X., Yang D.-H., Yi T.-H.** Pareto-Based Bi-Objective Optimization Method of Sensor Placement in Structural Health Monitoring // Buildings 2021, 11(11), 549; https://doi.org/10.3390/buildings11110549
33. **Kuchumov M., Evtushenko S.** New Soil Stress Measurement Sensor Based on the Effect of Elastic Charging of Electrodes / Buildings 2022, 12(3), 327; https://doi.org/10.3390/buildings12030327

Sergej I. Evtushenko Doctor of Technical Sciences, Professor, Professor of the department of Informational technology, systems and automatization in construction of the National Research Moscow State University of Civil Engineering; 129337, Russia, Moscow, Yaroslavskoe shosse, 26. E-mail: EvtushenkoSI@mgsu.ru.

Евтушенко Сергей Иванович, доктор технических наук, профессор, профессор кафедры Информационных систем, технологий и автоматизации в строительстве Национального исследовательского Московского государственного строительного университета, 129337, Москва, Ярославское ш., д.26; e-mail: EvtushenkoSI@mgsu.ru

Maksim M. Zheleznov Doctor of Technical Sciences, Associate Professor, Professor of the department of Informational technology, systems and automatization in construction of the National Research Moscow State University of Civil Engineering; 129337, Russia, Moscow, Yaroslavskoe shosse, 26. E-mail: ZheleznovMM@mgsu.ru.

Mikhail A. Kuchumov PhD student of the department of Informational technology, systems and automatization in construction of the National Research Moscow State University of Civil Engineering; 129337, Russia, Moscow, Yaroslavskoe shosse, 26. E-mail: mku4umoff@gmauil.com

Liubov A. Adamtsevich Candidate of Technical Sciences, Associate Professor, Associate Professor of the department of Informational technology, systems and automatization in construction of the National Research Moscow State University of Civil Engineering; 129337, Russia, Moscow, Yaroslavskoe shosse, 26. E-mail: AdamtsevichLA@mgsu.ru.

Железнов Максим Максимович, доктор технических наук, доцент, профессор кафедры Информационных систем, технологий и автоматизации в строительстве Национального исследовательского Московского государственного строительного университета, 129337, Москва, Ярославское ш., д.26; e-mail: ZheleznovMM@mgsu.ru

Кучумов Михаил Андреевич аспирант кафедры Информационных систем, технологий и автоматизации в строительстве Национального исследовательского Московского государственного строительного университета, 129337, Москва, Ярославское ш. ,д.26; e-mail: mku4umoff@gmauil.com

Адамцевич Любовь Андреевна, кандидат технических наук, доцент, доцент кафедры Информационных систем, технологий и автоматизации в строительстве Национального исследовательского Московского государственного строительного университета, 129337, Москва, Ярославское ш. ,д.26; e-mail: AdamtsevichLA@mgsu.ru ; ORCID: 0000-0002-5843-0076M

International Journal for Computational Civil and Structural Engineering, 21(1) 121–135 (2025)

DOI:10.22337/2587-9618-2025-21-1-121-135

APPLICATION OF THE STEEL-RUBBER VIBRATION ISOLATORS WITH PERFORATION FOR VIBRATION ISOLATION OF BUILDINGS

Vladimir L. Mondrus [1], Dmitry K. Sizov [2], Timofei M. Kvasnikov [1]

[1] National Research Moscow State University of Civil Engineering, Moscow, RUSSIA
[2] OOO "Vibroseismozastchita", Moscow, RUSSIA

Abstract: The article presents the derivation of a formula taking into account the coefficient of convexity under load, which takes into account the bulging of rubber along the edges of a steel-rubber vibration isolator. The article also provides a comparison for a vibration isolator with a hole and a vibration isolator without holes. It also presents a formula that allows taking into account the ambient temperature when calculating vibration isolators. Graphs of the dependence of the elastic modulus on temperature for a rubber-metal isolator with a hole are given.

Keywords: vibration isolation, vibration isolator with holes, steel-rubber vibration isolator, vibration isolator without holes, effects of vibration isolation systems on human health

ПРИМЕНЕНИЕ ПЕРФОРИРОВАННЫХ РЕЗИНОМЕТАЛЛИЧЕСКИХ ВИБРОИЗОЛЯТОРОВ ДЛЯ ВИБРОИЗОЛЯЦИИ ЗДАНИЙ

В.Л. Мондрус[1], Д.К. Сизов[2], Т.М. Квасников[1]

[1] Национальный исследовательский Московский государственный строительный университет, г. Москва, РОССИЯ
[2] ООО «Вибросейсмозащита», г. Москва, РОССИЯ

Аннотация: В статье представлен вывод формулы с учетом коэффициента коэффициентом выпуклости под нагрузкой, который учитывает выпучиваение резины по краям резинометалличекого виброизолятора. Также в статье приведено сравнение для виброизолятора с отверстием и виброизолятора без отверстий. Также представлена формула, которая позволяет учитывать температуру окружающей среды при расчете виброизоляторов. Приведены графики зависимости модуля упругости от температуры для резинометаллического изолятора с отверстием.

Ключевые слова: виброизоляция, виброизолятор с отверстиями, резинометаллический виброизолятор, виброизолятор без отверстий, воздействия систем виброизоляции на здоровье людей

1. INTRODUCTION

Transportation routes are the circulatory system of any state. It is impossible to imagine trade, production, and everything that our world is based on without transportation routes. But lately it is not the quantity of roads, and even not their quality, but the quality of human life provided by transportation routes that comes to the fore.

Urban rail transport is an important part of the urban transportation system and one of the strategic vectors of development of megalopolises due to its advantages such as high speed, energy efficiency, environmental friendliness, as well as safety and punctuality. At the same time, the vibrations caused by the movement of the train on the rails propagate through the ground and affect the buildings located near the rail lines.

These vibrations have a negative impact on the health of peoples.

Thus, it is critical to study the vibrations caused by both rail and subway traffic and their impact on human health and the urban environment.

At the same time, as the need for people to improve their quality of life continues to grow, there are increasing demands for protection from vibration induced by external factors.

Although vibration isolation measures applied directly to the railroad track can somewhat reduce the impact on the building, they are still insufficient for full-fledged vibration isolation of the structure.

One of the ways to damp the vibration impact arising due to the movement of rail transport is the use of rubber-metal vibration isolators installed in a reinforced concrete deck under the lload-bearing structures of buildings, or in the walls and columns at different levels. With the rapid development of the subway, the requirements for the stability of movement and comfort of high-speed trains are constantly increasing, as well as the requirements for the comfort of buildings located near shallow subway lines [1-4]. Therefore, it is necessary to accurately define the stiffness of rubber vibration isolators in order to effectively design and predict the structure of buildings. The operating conditions and load capacity of vibration isolators are constantly changing. The change of static stiffness of vibration isolators depending on temperature and load should be expressed by the appropriate formula, which will be of great importance in the authors' further studies on the analysis of dynamic properties [5-7]. The calculation of mechanical properties of rubber vibration isolators has always been the focus of research, but previous studies have focused mainly on dynamic stiffness. Most models consider different combinations of elements such as springs, isolators; and the main impact factors are frequency and amplitude [8-10]. Currently, there are some studies on the static stiffness of rubber vibration isolators under deformation conditions at room temperature. For rubber vibration isolators with different shapes, there are several theories and empirical formulas for calculation. Most of these formulas assume linear stiffness or consider a certain geometric nonlinear stiffness. In addition, the finite element method is widely used in the study of rubber behavior. This method can accurately simulate small static deformation in regard with experiments. These deformations are calculated using strain energy and tensor function [11, 12], but the parameters calculated by computer simulation still depend on the experimental data.

Ogden [13] has already pointed out that the procedure for modeling vibration isolators at different temperatures is a very difficult task, and Destrade [14] proposed mathematical equations to describe rubber vibration isolators based on commonly available data.

Cheremisinoff [15] studied the effect of humidity, temperature on the load carrying capacity of rubber isolators.

Dickens [16] examined the effect of temperature on the stiffness of insulators at temperatures ranging from 10°C to 60°C.

Hwang [17] conducted field experiments of isolators at temperatures ranging from 0°C to 28°C to validate his fractional derivative model for calculation of isolators.

The insulator developed by Hou [18] was tested in the extreme range from -70°C to 300°C and confirmed its intended characteristics.

Gajewski [19] presented the theory of finite element modeling for large deformations and analyzed the effectiveness of different models. In addition, Gajewski [20] proposed a method to estimate the magnitude of energy dissipation of elastic materials at large deformations. These results are important in the study of large deformations.

Cardon et al. [21] studied the relationship between rubber properties and temperature. They focused mainly on the shear modulus, and the temperature ranged from 20°C to 60°C. But at present there are very few studies on the behavior of rubber vibration isolator at low temperatures.

Stevenson [22] studied the relationship between low-temperature crystallization and the

strain modulus of rubber vibration isolator. The results showed that the strain modulus increases significantly with low-temperature crystallization. In addition, the relationship between low-temperature deformation and crystallization was also studied. Authors of the papers [23] and [24] analyzed and studied the performance of rubber insulators at low temperature. The results showed that low temperature has a significant effect on the properties of rubber.

Kari [25] proposed a nonlinear temperature model of rubber vibration isolator based on shape factor and investigated the effect of temperature on geometric parameters under load. To calculate the shape factor, they used the equivalent cylinder approximation in the equation to calculate the shape factor.

2. RESEARCH METHODS

For an ideal rubber material, the entropy of the molecular chain can be utilized to analyze the elasticity. In microscopic theory, the complex structure is simplified using some assumptions and the ideal structure is considered to facilitate calculation and analysis.

Let us summarize the static theory and derive the modulus of elasticity E. According to the theory of elasticity, the following equation is satisfied for the rubber layer:

$$E = \frac{\sigma}{\varepsilon} = \frac{3\rho RairT}{Mc}, \tag{1}$$

where E is the rubber modulus of elasticity; σ is the stress; ε is the strain; M_c is the mean molecular weight between cross-linked nodes; ρ is the rubber density; R_{air} is the Universal gas constant; T is the temperature.

Due to the complexity of the composition and inner structure of rubber materials, Mc is difficult to measure directly. However, Mc can be obtained from the modulus of elasticity at a certain temperature and small strain. This method can be used to derive an expression for Mc. The formula for Mc can be used to further derive the modulus of elasticity of rubber at different temperatures.

$$Mc = \frac{3\rho k\mathrm{RTk}}{Ek}, \qquad E = \frac{3\rho\mathrm{RT}}{Mc} = \frac{\rho\mathrm{TEk}}{\rho kTk}, \tag{2}$$

where T_k is the room temperature adopted as 25±2°C;

ρ_k is the rubber density at room temperature;

E_k is the modulus of elasticity at room temperature.

The density of rubber varies with temperature since its volume varies with temperature. The linear coefficient of thermal expansion of rubber is denoted as α. Since α is extremely small, the coefficient of volume expansion can be expressed as $(1 + \alpha)3 - 1 \approx 3\alpha$. Thus the density of rubber is as follows:

$$[1 + 3\alpha(T - Tk)]\rho = \rho k \quad for\ T > Tk,$$

$$\rho = [1 + 3\alpha(Tk - T)]\rho k \quad for\ T < Tk,$$

$$\rho = \rho k \quad for\ T = Tk, \tag{3}$$

In addition, the following formula can be derived:

$$\frac{\rho}{\rho k} = \frac{1}{[1 + 3\alpha(Tk - T)]} \quad for\ T > Tk,$$

$$\frac{\rho}{\rho k} = [1 + 3\alpha(Tk - T)] \quad for\ T < Tk, \tag{4}$$

$$\frac{\rho}{\rho k} = 1\ for\ T = Tk,$$

If one accepts $\Delta\mathrm{T} = T - Tc \quad for\ T < Tc$, and multiply the numerator and denominator by $1 + 3\alpha\Delta\mathrm{T}$, then it follows:

$$1 + 3\alpha(Tk - T) = 1 + 3\alpha\Delta T = \frac{(1 - 3\alpha\Delta T)(1 + 3\alpha\Delta T)}{1 + 3\alpha\Delta T} = \frac{(1 - 9\alpha^2\Delta T^2)}{1 + 3\alpha\Delta T} = \frac{1}{1 + 3\alpha\Delta T}, \quad (5)$$

If α is extremely small, we can use an approximation and simplify equation (2) as follows by substituting $\frac{\rho}{\rho k}$:

$$E = \frac{T_k}{(1 + 3\alpha\Delta\mathrm{T})T_k}, \quad (6)$$

The formula shows that for a rubber vibration isolator, the modulus of elasticity increases when the temperature increases in a certain range. Other relationships are also available, such as formula (33).

In addition, due to the nonlinearity of rubber, the stiffness will gradually decrease with increasing temperature when the load is relatively high. Changes in modulus of elasticity and stiffness do not always correspond to each other. This will be discussed in detail: see conclusions, Fig. 5b formula (31).

3. CALCULATION OF VIBRATION ISOLATOR WITH A HOLE

Based on extensive experience, researchers have developed a simplified method for calculating the stiffness of vibration isolators with a certain accuracy. For a rubber vibration isolator with a round shape, at small deformations, the empirical formula for the static stiffness K is as follows:

$$K = \frac{A_c \mu E}{H}, \quad (7)$$

where A_c is the support area, E is the elasticity modulus, H is the height of the vibration isolator, μ is the form factor.

$$\mu = 1 + 2S^2. \quad (7.1)$$

This factor accounts for the ratio between the height and width of the vibration isolator, which directly affects its stiffness and deformation properties [26].

Let us assume the area factor S, which can be obtained from the following formula:

$$S = \frac{A_c}{A_f} = \frac{\pi(R^2 - r^2)}{2\pi(\mathrm{R} + \mathrm{r})\mathrm{H}} = \frac{R - r}{2\mathrm{H}}, \quad (8)$$

where Af is the free area, which is a sum of inner and external areas of vibration isolator with a hole, R is the outer radius of the vibration isolator, r is the inner radius of the vibration isolator.

Based on formulas (7) and (8), the empirical expression for the stiffness of the vibration isolator is as follows:

$$K = \frac{\pi r^2 E(H^2 + (\frac{1}{2})r^2)}{H^3} = \frac{\pi r^2 E}{\mathrm{H}} + \frac{\pi r^4 E}{2H^3}, \quad (9)$$

As a vibration isolator is compressing, the size of the rubber gasket is continuously changing. The stiffness K is related to the deformation and is not a fixed value. Thus, the static stiffness of the vibration isolator is nonlinear. In the calculation of the free area, we assume that the vibration isolator is compressed uniformly, but it has convex edges after deformation. Assuming that the change of the inner radius is the same as the outer radius, we obtain,

$$R_1 - R = r - r_1 = d, \quad (9.1)$$

where R_1 is the outer radius of the vibration isolator, r_1 is the inner radius after compression, R is the outer radius of the vibration isolator before compression, r is the inner radius of the vibration isolator before compression, d is the change in the radius. Since the volume remains constant, we get:

$$\pi({R_1}^2 - {r_1}^2)(\mathrm{H} - h_{def}) = \pi(R^2 - r^2)H,$$

$$d = \frac{1}{2}\frac{(R-r)h_{def}}{\mathrm{H}-h_{def}},$$

$$R_1 = R + \frac{1}{2}\frac{(R-r)h_{def}}{\mathrm{H}-h_{def}}, \qquad (10)$$

$$r_1 = r - \frac{1}{2}\frac{(R-r)h_{def}}{\mathrm{H}-h_{def}},$$

Where H is the initial height of the vibration isolator, and h_{def} is the deformation. Formulas (8) and (9) are modified as follows:

$$S_1 = \frac{A_{c1}}{A_{f1}} = \frac{\pi({R_1}^2 - {r_1}^2)}{2\pi(R_1 + r_1)(\mathrm{H}-h_{def})} = \\ = \frac{R_1 - r_1}{2(\mathrm{H}-h_{def})}, \qquad (11)$$

$$K_1 = \frac{\mu_1 A_{c1} E}{\mathrm{H}-h_{def}} = \frac{A_{c1}(1+2{S_1}^2)E}{\mathrm{H}-h_{def}} = \\ = \frac{\pi({R_1}^2 - {r_1}^2)\mathrm{E}}{\mathrm{H}-h_{def}} \cdot \left[1 + \frac{({R_1}^2 - {r_1}^2)}{2(\mathrm{H}-h_{def})^2}\right], \qquad (11)$$

where S_1 is the ratio of areas, A_{f1} is the free area, K_1 is the stiffness, A_{c1} is the support area, μ_1 is the form factor.
Static force F_1 is defined as follows:

$$F_1 = \int_0^{h_{def}} K_{c1}\,dz = \int_0^{h_{def}} \frac{\pi({R_1}^2 - {r_1}^2)\mathrm{E}}{\mathrm{H}-h_{def}} \cdot \\ \cdot \left[1 + \frac{({R_1}^2 - {r_1}^2)}{2(\mathrm{H}-h_{def})^2}\right] dz, \qquad (12)$$

Usually, the end friction causes the area change of the vibration isolator after deformation to be smaller than the calculated value, but the free area change is larger in the presence of the supporting steel plate.

$$A_{c1} = A_c = \pi(R^2 - r^2), \qquad (13)$$

As for rubber, the compression behavior of the sample between bonded surfaces can be estimated quantitatively by means of the elastic modulus. This parameter is related to the geometry of the rubber sample. In the case of compression without bonded surfaces, the rubber block exhibits axial and uniform lateral deformation as shown in Figure 1(a).
The deformation of the vibration isolator is non-uniform in compression. Therefore, the assumption of cylindrical deformation of the rubber gasket is unfeasible. It should be close to elliptical deformation because the lateral surface will take the shape of an ellipse. Figure 1(a) shows the initial state of the vibration isolator, and Figure 1(b) shows the hypothetical half-elliptical state, which is obtained in practice.
During deformation, the steel plate is treated as a rigid body, and hence the bearing area of the vibration isolator is not changed. However, the free area of the rubber gasket is changed. When the rubber pad is deformed, the side surface takes the shape of a semi-ellipse. It is assumed that the convex part is a semi-ellipse in the vertical section, and that the semi-axes of the inner and outer semi-ellipses are equal, as shown in Figure 1(b). By taking the center of the vibration isolator as the origin of the rectangular coordinate system, we denote the axis of the convex part as a and the axis to the steel plate as b.

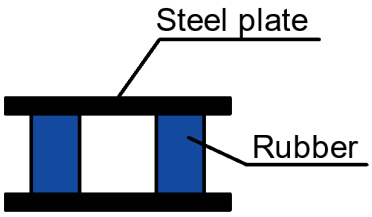

Figure 1a. Vibration isolator with a hole before loading

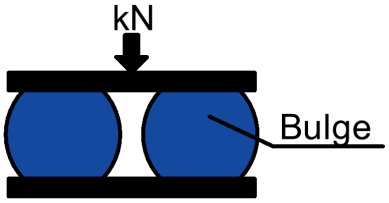

Figure 1b. Vibration isolator with a hole after loading

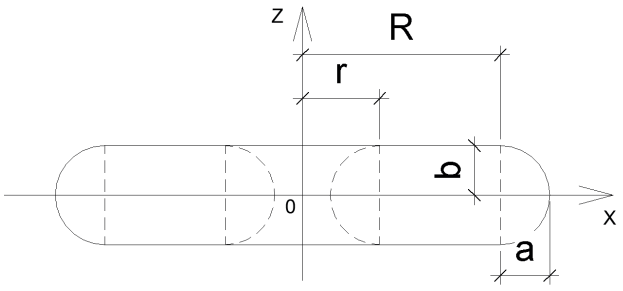

Figure 2. Diagram of geometrical characteristics of the vibration isolator

$$\begin{gathered}\frac{(x-R)^2}{a^2}+\frac{\mathrm{z}^2}{b^2}=1 \quad for\ R\le x\le R+a,\\ z=\pm b \quad for-R<x<-rUr<x<r,\\ \frac{(x-r)^2}{a^2}+\frac{\mathrm{z}^2}{b^2}=1 \quad for\ r-a\le x\le r,\\ \frac{(x+r)^2}{a^2}+\frac{\mathrm{z}^2}{b^2}=1 \quad for-r\le x\le -r+a,\\ \frac{(x+R)^2}{a^2}+\frac{\mathrm{z}^2}{b^2}=1 \quad for-R-a\le x\le -R,\end{gathered} \tag{14}$$

In the present paper, a vibration isolator with one central hole is considered. For further studies, the authors aim to derive formulas for a rectangular isolator with multiple holes.

The volume enclosed in the outer elliptic curve is represented as V_{out}, and the volume inside the elliptic curve is represented as V_{in}. Considering the right half, the following can be derived:

$$\begin{gathered}V=\pi(R^2-r^2)H=Vout-Vin=\\ =2\int_0^{\mathrm{b}}\pi({x_1}^2-{x_2}^2)dz=\\ =2\pi\int_0^b\left[R+\frac{a}{b}\sqrt{b^2-z^2}\right]^2-\\ -\left[r-\frac{\mathrm{a}}{b}\sqrt{b^2-z^2}\right]^2dz=\\ =2\pi(\mathrm{R}^2\mathrm{b}+\frac{2}{3}\mathrm{a}^2\mathrm{b}+\frac{1}{2}\mathrm{ab}\pi R)-2\pi(\mathrm{r}^2\mathrm{b}+\\ +\frac{2}{3}\mathrm{a}^2\mathrm{b}-\frac{1}{2}\mathrm{ab}\pi r)=\\ =2\pi b(R^2-r^2)+a\pi b(R+r),\end{gathered} \tag{15}$$

Thus, we have a:

$$a=\frac{(R-r)(H-2b)}{b}, \tag{16}$$

Since b satisfies

$$b=\frac{\mathrm{H}-h_{def}}{2}, \tag{17}$$

then

$$a=\frac{(R-r)h_{def}}{H-h_{def}}, \tag{18}$$

The free area of the vibration isolator, denoted as A_{f2}, can be calculated as follows:

$$\begin{gathered}A_{f2}=4\pi\int_0^{\mathrm{b}}\pi(x_1-x_2)dz=4\pi\int_0^{\mathrm{b}}\left[R+\right.\\ \left.\frac{\mathrm{a}}{b}\sqrt{b^2-z^2}\right]-\left[r-\frac{\mathrm{a}}{b}\sqrt{b^2-z^2}\right]dz=\\ =4b\pi R+ab\pi^2+(4b\pi r-ab\pi^2)=\\ 4b\pi(R+r)=2\pi(R+r)\left(H-h_{def}\right),\end{gathered} \tag{19}$$

Considering the free area in the cases of the elliptic deformation hypothesis, it can be seen that:

$$A_{f2}=A_{f1}=2\pi(R+r)\left(H-h_{def}\right), \tag{20}$$

Formula (20) is based on the assumption that the internal and external deformations are of the same elliptic shape. If this assumption is not fulfilled, then $A_{f2}\neq A_{f1}$. However, the difference between A_{f2} and A_{f1} is always extremely small.

In practice, the stiffness of rubber increases as the load increases. This is because an increase in load leads to a change in both the geometric shape and nonlinearity of the material. When the rubber element is compressed, the sample becomes anisotropic since the molecular chain is more oriented in the transverse direction.

As the compression ratio of the vibration isolator increases, the greater the degree of rubber bulging and the greater the change in rubber properties. This change can be expressed by the convexity factor μ_{bul}, which can be defined as follows:

$$\mu_{bul} = 1 + \frac{a}{b}\,, \qquad (21)$$

where a and b are accepted in accordance with (16) and (17).

Then the stiffness of the vibration isolator, K_2, taking into account the convexity coefficient, is defined as follows:

$$K_1 = \frac{A_{c1}\left(1 + 2{S_2}^2\right)E}{\mathrm{H} - h_{def}}\mu_2 = \\ = \frac{\pi(\mathrm{R}^2 - \mathrm{r}^2)\mathrm{E}}{\mathrm{H} - h_{def}} \cdot \left[1 + \frac{(\mathrm{R}^2 - \mathrm{r}^2)}{8\mathrm{b}^2(\mathrm{R} + \mathrm{r})^2}\right]\left(1 + \frac{a}{b}\right) = \\ = \frac{\pi(\mathrm{R}^2 - \mathrm{r}^2)\mathrm{E}}{\mathrm{H} - h_{def}} \cdot \\ \cdot \left[1 + \frac{(\mathrm{R}^2 - \mathrm{r}^2)}{2\left(\mathrm{H} - h_{def}\right)^2}\right]\left(1 + \frac{a}{b}\right), \qquad (22)$$

The applied force F_2 is determined by the formula:

$$F_{c2} = \int_0^{h_{def}} K_c dz = \int_0^{h_{def}} \frac{\pi(\mathrm{R}^2 - \mathrm{r}^2)\mathrm{E}}{\mathrm{H} - \mathrm{z}} \cdot \\ \cdot \left[1 + \frac{(\mathrm{R}^2 - \mathrm{r}^2)}{2(\mathrm{H} - \mathrm{z})^2}\right]\left(1 + \frac{a}{b}\right) dz, \qquad (23)$$

where $h_{def} = z$

During operation, the temperature of the vibration isolators may change, usually between -10°C and +10°C. If the temperature changes, the volume of the rubber will change due to thermal expansion and contraction.

Considering the room temperature TK as the standard condition, when the temperature change is ΔT, the volume of the round rubber part expands to

$$(1 + \alpha\Delta\mathrm{T})^3 3\pi(\mathrm{R}^2 - \mathrm{r}^2), \qquad (24)$$

and the height is as follows

$$(1 + \alpha\Delta\mathrm{T})H, \qquad (25)$$

However, because of the restraint imposed by the steel plate, the bearing surface is assumed to remain unchanged since the thermal expansion of steel is much lower than that of rubber. The lateral changes are limited to a certain extent. If the temperature increases, the rubber will protrude outward. Otherwise it will become concave inward.

Then equation (15) can be modified as follows:

$$(1 + \alpha\Delta T)^3 V = (1 + \alpha\Delta T)^3 3\pi(R^2 - r^2)H = \\ = Vout - Vin = 2\int_0^{\mathrm{b}} \pi({x_1}^2 - {x_2}^2)dz = \\ = 2\pi b(\mathrm{R}^2 - \mathrm{r}^2) + \mathrm{a}\pi b(R + r), \qquad (26)$$

From the equation (26) we can conclude that

$$a = \frac{(R - r)[(1 + \alpha\Delta\mathrm{T})^3 H - 2b)]}{b}, \qquad (27)$$

where

$$b = \frac{(1 + \alpha\Delta\mathrm{T})\mathrm{H} - h_{def}}{2}, \qquad (28)$$

then

$$A_{f2} = 2\pi(R + r)\left[(1 + \alpha\Delta\mathrm{T})\mathrm{H} - h_{def}\right], \qquad (29)$$

Form factor μ_2 is defined as follows

$$\mu_2 = 1 + 2{S_2}^2 = 1 + 2\left(\frac{A_c}{A_{f2}}\right)^2 = \\ 1 + \frac{(\mathrm{R} - \mathrm{r})^2}{2\left((1 + \alpha\Delta\mathrm{T})\mathrm{H} - h_{def}\right)^2}, \qquad (30)$$

As the temperature changes, equations (22) and (23) can be further modified as follows:

$$F_2 = \int_0^{h_{def}} K_{c2} dz = \\ \int_0^{h_{def}} \frac{\pi(\mathrm{R}^2 - \mathrm{r}^2)\mathrm{E}}{(1 + \alpha\Delta\mathrm{T})\mathrm{H} - \mathrm{z}} \cdot \\ \cdot \left[1 + \frac{(\mathrm{R}^2 - \mathrm{r}^2)}{2\left((1 + \alpha\Delta\mathrm{T})\mathrm{H} - \mathrm{z}\right)^2}\right]\left(1 + \frac{a}{b}\right) dz$$

$$K_2 = \frac{A_c\left(1+2{S_2}^2\right)E}{(1+\alpha\Delta\mathrm{T})\mathrm{H}-h_{def}}\mu_2 = \frac{\pi(\mathrm{R}^2-\mathrm{r}^2)\mathrm{E}}{(1+\alpha\Delta\mathrm{T})\mathrm{H}-h_{def}}\cdot \left[1+\frac{(\mathrm{R}^2-\mathrm{r}^2)}{2\left((1+\alpha\Delta\mathrm{T})\mathrm{H}-h_{def}\right)^2}\right]\left(1+\frac{a}{b}\right), \quad (31)$$

4. RESULTS AND DISCUSSION

At high temperatures, the degree of rubber crosslinking gradually increases with temperature, resulting in an increase in the hardness and elastic modulus of the rubber. If the temperature increases even further, the polymer molecular chain will fracture. There is no need to consider the role of material degradation, as the range of engineering applications is usually less than 60 °C. When the rubber temperature is lower, the molecular activity is weakened and the rubber crystallizes. This condition leads to an increase in the elastic modulus of the rubber at low temperatures.

When the rubber is above 0 °C, the crystallization effect is significantly weaker.

The elastic modulus and stiffness of the rubber increase significantly with decreasing temperature when the temperature is below 0 °C. Therefore, in some theoretical studies, 0 °C is chosen as the transition point. In this study, it is assumed that at temperatures above 0 °C, the modulus of elasticity changes according to equation (6), and at temperatures below 0 °C, the modulus of elasticity has a certain dependence on the ambient temperature.

To account for temperature as a variable, a coefficient φ is adopted. This coefficient is the ratio of the modulus of elasticity of rubber at low temperature to the modulus of elasticity at 0°C , which can be expressed as follows:

$$\varphi = \frac{E}{E_0}, \quad (32)$$

$$\Delta T_1 = T - T_0\,, \quad (32.1)$$

where E is the elasticity modulus at 0°C, and T0 is the temperature at 0°C.

Thus, we get:

$$E = \frac{TE_k}{(1+3\alpha\Delta\mathrm{T})T_k} \quad for\ T \geq 273\ K,$$
$$E = \frac{T_0E_k}{(1+75\alpha)T_k} \quad for\ T < 273\ K, \quad (33)$$

where $(1+75\alpha)$ have been previously derived in the study [27].

Consider the vibration isolator of the following sizes with and without hole.

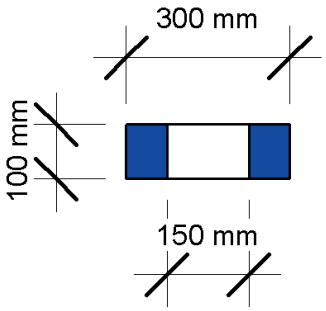

Figure 3a. Adopted vibration isolator with an aperture

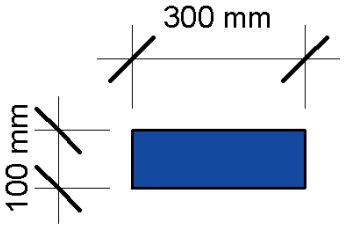

Figure 3b. Adopted vibration isolator without hole

The modulus of elasticity E is 2.28 MPa at room temperature [28].

For the isolator under consideration, the coefficient of thermal expansion is as follows

$$\alpha = 6.6\ \mathrm{x}\ 10^{-4}K^{-1}, \quad (34)$$

Using equation (33), the modulus of elasticity E can be calculated at different temperatures, which is shown in the diagrams below.

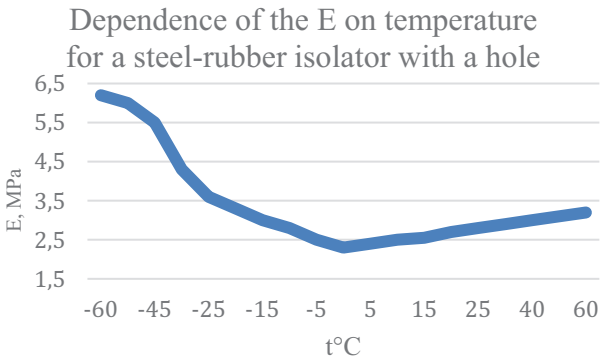

Figure 4a. Plot of elastic modulus versus temperature for a rubber-metal isolator

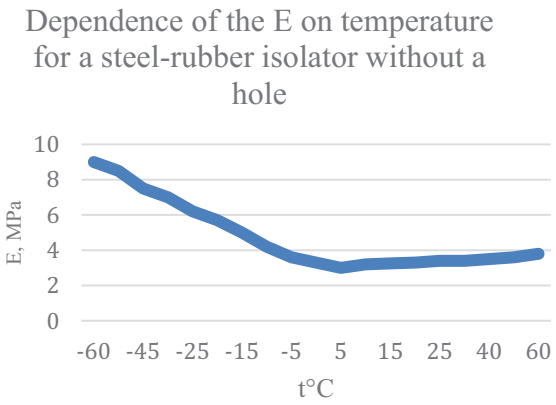

Figure 4b. Plot of elastic modulus versus temperature for a rubber-metal isolator without a hole

These figures show that at temperatures above 0°C, the modulus of elasticity E increases slowly with increasing temperature, and when the temperature drops below 0°C, the modulus of elasticity E increases rapidly with decreasing temperature. Although there are some uncertainties, the main trend of this curve reflects the theoretical analysis and the results of tests conducted by other authors [29].

These plots show the variation of stiffness obtained from formula (31) with convexity factor, as well as formulas (11) and (12) without convexity factor at T=25°C under different load.

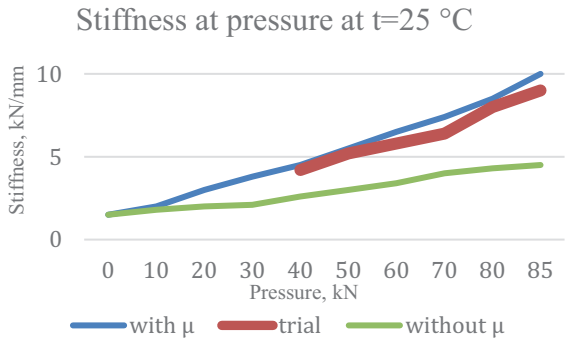

Figure 5a. Stiffness of the vibration isolator with a hole under different load at t=25C

Figure 5a shows that the difference between the original formula (11) and the formula with convexity factor (31) becomes more significant with increasing pressure. The maximum error is about 10.86% and the RMS error is 7.71%. The error increases with increase in pressure, but the accuracy is higher at low pressure. From the above analysis, it can be noted that the formula with convexity coefficient is effective and accurate in reflecting the change in stiffness caused by load variation. The experimental data shown in Fig.5 and Fig.5b are taken from [27] and [29].

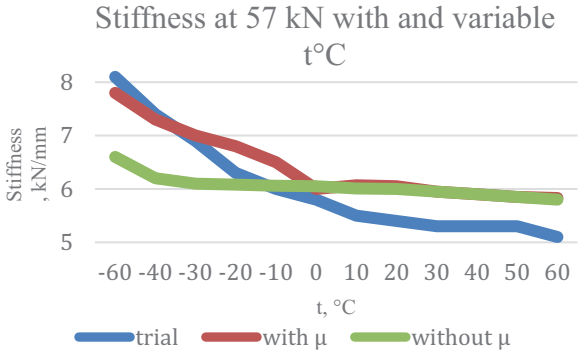

Figure 5b. Stiffness of vibration isolator with hole at different t under 57kN load

Figure 6 shows that formula (31) with the convexity factor is more accurate between -60°C and +60°C. If the temperature is above 0°C, the calculation result obtained using the modified formula (31) is close to the result obtained using the original (12) empirical formula. The maximum error with the modified formula (31) is

12% and the RMS error is 9%. Although the error gradually increases when the temperature is above 60°C, it is usually ignored. If the temperature is below 0°C, the maximum error with formula (31) is 5% and the RMS error is 3%. The maximum error with empirical formula (12) is 16% and the RMS error is 10%. From the above analysis, it can be seen that formula (31) can reflect the change in stiffness depending on temperature [28].

The stiffness of the vibration isolator changes as the pressure or compression amplitude changes. This is due to the nonlinearity of the stiffness. In particular, the stiffness decreases slightly with increasing temperature when the temperature is above 0°C and the preload is below 45 kN. The stiffness increases slightly with increasing temperature when the temperature is above 0°C and the preload is above 45 kN. This is mainly because the temperature affects not only the elastic modulus but also the geometric nonlinearity of the vibration isolator. When the temperature is below 0°C, changes in pressure have little effect on the stiffness trend. The stiffness hardly changes with temperature at the same load when the temperature is above 0°C. If the temperature is below 0°C, the greater the load, the more dramatic the change of stiffness with temperature [30, 31].

5. CONCLUSIONS

This study has examined the relationship between modulus of elasticity and rubber temperature. At low temperature, a more efficient formula for determining the modulus of elasticity (33) is proposed. The formula (31) with the convexity coefficient μ_{con} for more accurate calculation of the stiffness and modulus of elasticity of rubber vibration isolator is obtained.

There is a strong relationship between the modulus of elasticity and the temperature of the rubber. If the temperature is above 0°C, the modulus of elasticity gradually increases with increasing temperature. While the temperature is below 0°C, the modulus of elasticity increases significantly with decreasing temperature due to the effect of partial crystallization. Therefore, it is effective to use variable modulus of elasticity in calculations.

Thus, formula (31) with the correction by the convexity coefficient μ_{bul} has a good applied value. Formula (31) can also be applied to rubber vibration isolators of other sizes and types.

The modified formula (31) with convexity coefficient μ_{con} takes into account the effect of temperature and load simultaneously. The calculated values are close to the actual ones, and the calculation error under normal operating conditions is less than 10%. Therefore, it can be considered that formula (31) with convexity coefficient μ_{con} is effective for stiffness calculation. Consideration of the influence of temperature in formula (31) significantly increased the accuracy of the results compared to the original formula (11).

Different loads have the same effect on the stiffness trend at low temperature, and the stiffness increases significantly with decreasing temperature. However, the stiffness is less temperature dependent when the temperature is above 0°C, but still increases slightly with increasing temperature.

Theoretically, the elastic modulus increases with increasing temperature as can be seen from (6) and Fig. 4a. However, in most cases, the measured stiffness decreases with increasing temperature Fig. 6. This seemingly contradictory phenomenon is explained in the derived equation (31).

The theory of the static stiffness of rubber vibration isolator is of great importance in the study of the dynamic performance of rubber and provides a method for further derivation of the dynamic stiffness formula. The dynamic properties of rubber under temperature and pre-pressure will be given more attention in future research.

6. ACKNOWLEDGEMENTS

The study was funded by the Ministry of Science and Higher Education of the Russian Federation, project no. FSWG-2023-0004.

REFERENCES

1. **Dashevskij M.A., Mondrus V.L., Motorin V.V.** (2018) Koncepciya vibrozashchity zdanij i sooruzhenij v pole stroitel'nyh normativov [The concept of vibration protection of buildings and structures in the field of building regulations] // Academia. Arhitektura i stroitel'stvo. [Academia. Architecture and construction.]. №4. 109–115. (in Russian)
2. **Simbirkin V.N., Panasenko YU.V., Kurnavin V.V.** (2023) Sravnitel'nyj analiz primeneniya razlichnyh modelej dempfirovaniya pri raschete sejsmicheskoj reakcii sooruzhenij v PK STARK ES. [Analysis of Various Damping Models in The Simulation of the Seismic Response of Structures in the STARK ES Software] //ZHelezobetonnye konstrukcii. [Reinforced concrete structures] 2(2):58-64. https://doi.org/10.22227/2949-1622.2023.2.58-64 (in Russian)
3. **D.J. Thompson and C.J.C. Jones** (2000) A review of the modelling of wheel/rail noise generation / / Journal of Sound and Vibration,vol. 231, no. 3. https://doi.org/10.1006/jsvi.1999.2542
4. **J. Yao, R. Zhao, N. Zhang, and D. Yang** (2019) Vibration isolation effect study of infilled trench barriers to train-induced environmental vibrations // Soil Dynamics and Earthquake Engineering, vol. 125 https://doi.org/10.1016/j.soildyn.2019.105741
5. **Simbirkin V.N., Panasenko YU.V**. (2019) Uchet ukazanij SP 14.13330.2018 pri realizacii rascheta sooruzhenij na sejsmicheskie vozdejstviya v programmnom komplekse STARK ES. [Implementation of seismic structural analysis in Stark ES software according to the building code SP 14.13330.2018] // Vestnik NIC «Stroitel'stvo» [Bulletin of Science and Research Center of Construction.]; 21(2):103-113. (in Russian)
6. **Mondrus V.L., Sizov D.K., Kvasnikov T.M.** (2023) Raschet rezinometallicheskih vibroizolyatorov s otverstiyami v sisteme vibrozashchity zdanij s pomoshch'yu programmnogo kompleksa, realizuyushchego metod konechnyh elementov [Finite Element Modelling of Rubber-Metal Vibration Isolators with Holes for the Vibration Protection System of Buildings]// ZHelezobetonnye konstrukcii. [Reinforced concrete structures]; 4(4):43-51. (In Russian) https://doi.org/10.22227/2949-1622.2023.4.43-51
7. **Sizov D.K.** (2024) Variacionno-raznostnyj metod rascheta sloistyh rezinometallicheskih vibroizolyatorov, primenyaemyh dlya zashchity zhelezobetonnyh zdanij ot tekhnogennoj vibracii. [Variation-Difference Method of Calculation of Layered Rubber-Metal Vibration Isolators Used for Protection of Reinforced Concrete Buildings from Anthropogenic Vibration] // ZHelezobetonnye konstrukcii. [Reinforced concrete structures]. 5(1):68-78. (In Russian) https://doi.org/10.22227/2949-1622.2024.1.68-78
8. **Dashevskij M.A., Mondrus V.L., Motorin V.V.** (2017) Effektivnaya vibrozashchita verhnego stroeniya puti metropolitena [Effective vibration protection of the superstructure of the subway track]/ / Academia. Arhitektura i stroitel'stvo. [Academia. Architecture and construction.]. №4.
9. **C. Qingqing, G. Keqin.** (2010) Technical and economic analysis of seismic isolation structure // Building structure, 2010.
10. **S. Jiang, S. Yaoand D. Liu** (2021) Economic performance analysis of seismic isolation, energy dissipation, and traditional seismic structures // E3S Web of Conferences. https://doi.org/10.1051/e3sconf/202124801032
11. **L. Chen, G.-T. Yang, and Z.-Z. Huang** (2011) Constitutive equations of incompressible nonlinear super-elastic material. Transaction of Beijing Institute of Technology, vol. 31, no. 1, pp. 30–34.
12. **Y. Q. Li and X.-L. Gao** (2019), Constitutive equations for hyperelastic materials based on the upper triangular decomposition of the de-

formation gradient, Mathematics and Mechanics of Solids, vol. 24, no. 6, pp. 1785–1799. doi:10.1177/1081286518806950

13. **Ogden, R., Saccomandi, G. & Sgura, I.** (2004) Fitting hyperelastic models to experimental data. // Computational Mechanics 34, 484–502. https://doi.org/10.1007/s00466-004-0593-y
14. **Destrade, M., Saccomandi, G., & Sgura, I.** (2016). Methodical fitting for mathematical models of rubber-like materials. // Proceedings of the Royal Society A: Mathematical, Physical and Engineering Sciences, 473.
15. **Cheremisinoff, N.P., & Cheremisinoff, P.N.** (1993). Elastomer Technology Handbook (1st ed.). CRC Press. https://doi.org/10.1201/9780138758851
16. **Dickens, John D**. (1998) Dynamic characterisation of vibration isolators (PhD Thesis), Sydney: UNSW Canberra. https://doi.org/10.26190/unsworks/18020
17. **Hwang, J.S., & Hsu, T.** (2001). A fractional derivative model to include effect of ambient temperature on HDR bearings. Engineering Structures, 23, 484-490. DOI:10.1016/S0141-0296(00)00063-8
18. **Hou J. F., Bai H. B., Li D. W.** Test research of damping performance of metal rubber damper at high-low temperature. // Journal of Aeronautical Materials, Vol. 26, Issue 7, 2006, p. 50-55
19. **M. Gajewski, R. Szczerba, and S. Jemioło,** (2015) Modelling of elastomeric bearings with application of Yeoh hyperelastic material model, Procedia Engineering, vol. 111, pp. 220–227. https://doi.org/10.1016/j.proeng.2015.07.080
20. **M. Gajewski** (2018) Estimation of the energy dissipation capability for chosen elastomers with application of DMA, Polymer Testing, vol. 68, pp. 405–414. https://doi.org/10.1016/j.polymertesting.2018.04.037
21. **D. Cardone and G. Gesualdi** (2012) Experimental evaluation of the mechanical behavior of elastomeric materials for seismic applications at different air temperatures, International Journal of Mechanical Sciences, vol. 64, no. 1, pp. 127–143, https://doi.org/10.1016/j.ijmecsci.2012.07.008
22. **A. Stevenson** (1983), The influence of low-temperature crystallization on the tensile elastic modulus of natural rubber, Journal of Polymer Science: Polymer Physics Edition, vol. 21, no. 4, pp. 553–572, https://doi.org/10.1002/pol.1983.180210406
23. **P. Spanos** (2003) Cure system effect on low temperature dynamic shear modulus of natural rubber, Rubber World, vol. 229, no. 2, pp. 22–27, 2003
24. **T.L. Yu, D.Y. Yuan, and X.L. Sun**, (2012) The finished product of rubber bearing mechanical performance analysis in the low temperature, Applied Mechanics and Materials, vol. 178–181, pp. 2254–2259. https://doi.org/10.4028/www.scientific.net/AMM.178-181.2254
25. **L. Kari** (2002), The non-linear temperature dependent stiffness of precompressed rubber cylinders, KGK-Kautschuk und Gummi Kunststo2e, vol. 55, no. 3, pp. 76–81.
26. **Zaborov V.I., Klyachko P.N., Rosin G.S.** (1976) Zashchita ot shuma i vibracii v chernoj metallurgii [Protection against noise and vibration in ferrous metallurgy], Metallurgiya [Metallurgy] (in Russian)
27. **Xu, Chuanbo, Chi, Mao-Ru, Dai, Liangcheng, Guo, Zhaotuan**, (2020) Calculation of Nonlinear Stiffness of Rubber Pad under Different Temperatures and Prepressures, Shock and Vibration, 2020, 8140782, 10 pages, 2020. https://doi.org/10.1155/2020/8140782
28. D. Cheng, Mechanical Design Manual, Chemical Industry Press, Beijing, China, 2008, Fifth edition. (in Chinese)
29. **Y. Lu, L. Guo, Z. Deng, and Y. Wang** (2016) Temperature-dependent tensile behavior of silicon rubber using automated grid method, Polymeric Materials Science and Engineering, vol. 32, no. 2, pp. 104–108, doi:10.16865/j.cnki.1000-7555.2016.02.019
30. **S.L. Burtscher a, A. Dorfmann.** (2004) Compression and shear tests of anisotropic

high damping rubber bearings Engineering Structures, Volume 26, Issue 13 https://doi.org/10.1016/j.engstruct.2004.07.014.

31. **T. Sheng, G. Liu, X. Bian, W. Shi, Y. Chen**, (2022) Development of a three-directional vibration isolator for buildings subject to metro- and earthquake-induced vibrations // Engineering Structures, https://doi.org/10.1016/j.engstruct.2021.113576

СПИСОК ЛИТЕРАТУРЫ

1. **Дашевский М.А., Мондрус В.Л., Моторин В.В.** Концепция виброзащиты зданий и сооружений в поле строительных нормативов // Academia. Архитектура и строительство. 2018. №4. 109–115.
2. **Симбиркин В.Н., Панасенко Ю.В., Курнавин В.В.** Сравнительный анализ применения различных моделей демпфирования при расчете сейсмической реакции сооружений в ПК STARK ES. Железобетонные конструкции. 2023; 2(2):58-64. https://doi.org/10.22227/2949-1622.2023.2.58-64
3. **D.J. Thompson and C.J.C. Jones** A review of the modelling of wheel/rail noise generation / / Journal of Sound and Vibration, 2000, vol. 231, no. 3. https://doi.org/10.1006/jsvi.1999.2542
4. **J. Yao, R. Zhao, N. Zhang, and D. Yang** Vibration isolation effect study of in-filled trench barriers to train-induced environmental vibrations / / Soil Dynamics and Earthquake Engineering, 2019, vol. 125. https://doi.org/10.1016/j.soildyn.2019.105741
5. **Симбиркин В.Н., Панасенко Ю.В.** Учет указаний СП 14.13330.2018 при реализации расчета сооружений на сейсмические воздействия в программном комплексе STARK ES. Вестник НИЦ «Строительство». 2019;21(2):103-113.
6. **Мондрус В.Л., Сизов Д.К., Квасников Т.М.** Расчет резинометаллических виброизоляторов с отверстиями в системе виброзащиты зданий с помощью программного комплекса, реализующего метод конечных элементов. Железобетонные конструкции. 2023,4(4):43-51 https://doi.org/10.22227/2949-1622.2023.4.43-51
7. **Сизов Д.К.** Вариационно-разностный метод расчета слоистых резинометаллических виброизоляторов, применяемых для защиты железобетонных зданий от техногенной вибрации. Железобетонные конструкции. 2024 5(1):68-78. https://doi.org/10.22227/2949-1622.2024.1.68-78
8. **Дашевский М.А., Мондрус В.Л., Моторин В.В.** Эффективная виброзащита верхнего строения пути метрополитена // Academia. Архитектура и строительство. 2017. №4.
9. **C. Qingqing, G. Keqin.** Technical and economic analysis of seismic isolation structure / / Building structure, 2010.
10. **S. Jiang, S. Yaoand D. Liu** Economic performance analysis o fseismic isolation, energy dissipation, and traditional seismic structures / / E3S Web of Conferences, 2021. https://doi.org/10.1051/e3sconf/202124801032
11. **L. Chen, G.-T. Yang, and Z.-Z. Huang,** Constitutive equations of incompressible nonlinear super-elastic material, Transaction of Beijing Institute of Technology, vol. 31, no. 1, pp. 30–34, 2011
12. **Y. Q. Li and X.-L. Gao**, Constitutive equations for hyperelastic materials based on the upper triangular decomposition of the deformation gradient, Mathematics and Mechanics of Solids, vol. 24, no. 6, pp. 1785–1799, 2019 doi:10.1177/1081286518806950
13. **Ogden, R., Saccomandi, G. & Sgura, I.** Fitting hyperelastic models to experimental data. //Computational Mechanics 34, 484–502, 2004 https://doi.org/10.1007/s00466-004-0593-y
14. **Destrade, M., Saccomandi, G., & Sgura, I.** Methodical fitting for mathematical mod-

els of rubber-like materials. // Proceedings of the Royal Society A: Mathematical, Physical and Engineering Sciences, 473, 2016

15. **Cheremisinoff, N.P., & Cheremisinoff, P.N.** Elastomer Technology Handbook (1st ed.). CRC Press, 1993. https://doi.org/10.1201/9780138758851
16. **Dickens, John D**. (1998) Dynamic characterisation of vibration isolators (PhD Thesis), Sydney: UNSW Canberra. https://doi.org/10.26190/unsworks/18020
17. **Hwang, J.S., & Hsu, T.** A fractional derivative model to include effect of ambient temperature on HDR bearings. Engineering Structures, 23, 484-490, 2001 DOI:10.1016/S0141-0296(00)00063-8
18. **Hou J. F., Bai H. B., Li D. W.** Test research of damping performance of metal rubber damper at high-low temperature. // Journal of Aeronautical Materials, Vol. 26, Issue 7, 2006, p. 50-55
19. **M. Gajewski, R. Szczerba, and S. Jemioło,** Modelling of elastomeric bearings with application of Yeoh hyperelastic material model,Procedia Engineering, vol. 111, pp. 220–227, 2015 https://doi.org/10.1016/j.proeng.2015.07.080
20. **M. Gajewski,** Estimation of the energy dissipation capability for chosen elastomers with application of DMA, Polymer Testing, vol. 68, pp. 405–414, 2018 https://doi.org/10.1016/j.polymertesting.2018.04.037
21. **D. Cardone and G. Gesualdi,** Experimental evaluation of the mechanical behavior of elastomeric materials for seismic applications at different air temperatures, International Journal of Mechanical Sciences, vol. 64, no. 1, pp. 127–143, 2012 https://doi.org/10.1016/j.ijmecsci.2012.07.008
22. **A. Stevenson,** The influence of low-temperature crystallization on the tensile elastic modulus of natural rubber, Journal of Polymer Science: Polymer Physics Edition, vol. 21, no. 4, pp. 553–572, 1983 https://doi.org/10.1002/pol.1983.180210406
23. **P. Spanos,** Cure system effect on low temperature dynamic shear modulus of natural rubber, Rubber World, vol. 229, no. 2, pp. 22–27, 2003
24. **T.L. Yu, D.Y. Yuan, and X.L. Sun,** The finished product of rubber bearing mechanical performance analysis in the low temperature, Applied Mechanics and Materials, vol. 178–181, pp. 2254–2259, 2012 https://doi.org/10.4028/www.scientific.net/AMM.178-181.2254
25. **L. Kari,** The non-linear temperature dependent stiffness of pre compressed rubber cylinders," KGK-Kautschuk und Gummi Kunststo2e, vol. 55, no. 3, pp. 76–81, 2002
26. **Заборов В.И., Клячко П.Н., Росин Г.С.** Защита от шума и вибрации в черной металлургии. М., «Металлургия», 1976
27. **Xu, Chuanbo, Chi, Mao-Ru, Dai, Liangcheng, Guo, Zhaotuan,** (2020) Calculation of Nonlinear Stiffness of Rubber Pad under Different Temperatures and Prepressures, Shock and Vibration, 2020, 8140782, 10 pages, 2020. https://doi.org/10.1155/2020/8140782
28. **D. Cheng,** Mechanical Design Manual, Chemical Industry Press, Beijing, China, 2008, Fifth edition. (in Chinese)
29. **Y. Lu, L. Guo, Z. Deng, and Y. Wang** Temperature-dependent tensile behavior of silicon rubber using automated grid method, Polymeric Materials Science and Engineering, 2016, vol. 32, no. 2, pp. 104–108, doi:10.16865/j.cnki.1000-7555.2016.02.019
30. **S.L. Burtscher a, A. Dorfmann.** Compression and shear tests of anisotropic high damping rubber bearings Engineering Structures, 2004, Volume 26, Issue 13 https://doi.org/10.1016/j.engstruct.2004.07.014.
31. **T. Sheng, G. Liu, X. Bian, W. Shi, Y. Chen**, (2022) Development of a three-directional vibration isolator for buildings subject to metro- and earthquake-induced vibrations / / Engineering Structures, https://doi.org/10.1016/j.engstruct.2021.113576

Mondrus Vladimir Lvovich – Doctor of Technical Sciences, Professor, Corresponding Member. RAASN, Professor of the Department of Structural and Theoretical Mechanics, Institute of Industrial and Civil Engineering, National Research Moscow State University of Civil Engineering (NRU MGSU). 405, 26 Yaroslavskoe highway, Moscow, 129337, Russia. E-mail: mondeusvl@mgsu.ru

Sizov Dmitry Konstantinovich – Ph.D., Vibroseysmozashchita LLC,6 st. Bratislavskaya, Moscow, 109341, Russia. E-mail: newfff@mail.ru

Kvasnikov Timofei Mikhailovich - 3rd year graduate student of the Department of Structural and Theoretical Mechanics, Institute of Industrial and Civil Engineering, National Research Moscow State University of Civil Engi-neering (NRU MGSU). 405, 26 Yaroslavskoe shosse, Moscow, 129337, Russia. E-mail: ti-ma.kvasnikov@gmail.com

Мондрус Владимир Львович – д.т.н., профессор, член корр. РААСН, профессор кафедры строительной и теоретической механики, институт Промышленного и гражданского строительства, Национальный Исследовательский Московский Государственный Строительный Университет (НИУ МГСУ). 405, 26 Ярославское шоссе, Москва, 129337, Россия. E-mail: mondeusvl@mgsu.ru

Сизов Дмитрий Константинович – к.т.н., ООО «Вибросейсмозащита», ул. Братиславская, 6, Москва, 109341,Россия. E-mail: newfff@mail.ru,

Квасников Тимофей Михайлович -аспирант 3 курса кафедры строительной и теоретической механики, институт Промышленного и гражданского строительства, Национальный Исследовательский Московский Государственный Стро-ительный Университет (НИУ МГСУ). 405, 26 Ярославское шоссе, Москва, 129337, Россия. E-mail: tima.kvasnikov@gmail.com, https://orcid.org/0000-0002-7836-4918

International Journal for Computational Civil and Structural Engineering, 21(1) 136–145 (2025)

DOI:10.22337/2587-9618-2025-21-1-136-145

TORSION IN THE ELEMENTS OF THE METAL DOME FRAME, SUPPORTED BY SPARSELY INSTALLED COLUMNS

Evgeny V. Lebed

National Research Moscow State University of Civil Engineering, Moscow, RUSSIA

Annotation. The effect of torsion on the stress state of the main elements of a metal ribbed-annular dome was investigated. The dependence of the torsion effect on the increase in the distance between the columns supporting the dome was revealed. At the same time, the dependence of torsion on the type of nodal junctions of the frame elements among themselves was determined. The object of the study was a ribbed-ring dome, all elements of which are made of steel pipes. The dome had different support schemes on columns of steel pipes, installed not under each rib, but cyclically symmetrical along the contour. There were four such schemes. In addition, the type of nodal connections of the frame elements to each other has been changed for each scheme. There were five different types of conjugations. The research was carried out through calculations of various models. There were twenty models in total. During the calculations, the stresses in the main elements of the dome models were determined, which were compared with each other. In this case, comparative diagrams of the stress state dependences of the elements of the ribbed-ring dome are obtained. The effect of torsion on the stress state of the elements of the ribbed-ring dome of the considered models is estimated. The degree of change in the stress state of individual frame elements due to torsion has been established. According to the results of the study, significant stress changes due to torsion in the upper ring and noticeable in the meridional ribs were noted. The dependence of the nature of their changes on the type of nodal connections has been established. It is recommended to take into account the torsion effect when designing metal rib-ring domes.

Keywords: ribbed-ring dome, computer model, meridional ribs, upper and lower rings, columns, torsion, nodal connections, static calculation

КРУЧЕНИЕ В ЭЛЕМЕНТАХ КАРКАСА МЕТАЛЛИЧЕСКОГО КУПОЛА, ОПИРАЮЩЕГОСЯ НА РЕДКО УСТАНОВЛЕННЫЕ КОЛОННЫ

Е.В. Лебедь

Национальный исследовательский Московский государственный строительный университет, г. Москва, РОССИЯ

Аннотация. Исследовалось влияния кручения на напряженное состояние основных элементов металлического ребристо-кольцевого купола. Выявлялась зависимость эффекта кручения от увеличения расстояния между поддерживающими купол колоннами. Одновременно с этим определялась зависимость кручения от вида узловых сопряжений элементов каркаса между собой. Объектом исследования был ребристо-кольцевой купол, все элементы которого приняты из стальных труб. Купол имел разные схемы опирания на колонны из стальных труб, установленные не под каждым ребром, но циклически симметрично по контуру. Таких схем было четыре. Кроме того, для каждой расчетной схемы изменялся вид узловых сопряжений элементов каркаса между собой. Разных видов сопряжений было пять. Исследования проводились посредством расчетов разных моделей. Всего моделей насчитывалось двадцать. В процессе расчетов определялись напряжения в основных элементах купольных моделей, которые сравнивались между собой. При этом получены сравнительные диаграммы зависимостей напряженного состояния элементов ребристо-кольцевого купола. Дана оценка влияния кручения на напряженное состояние элементов ребристо-кольцевого купола рассмотренных моделей. Установлена степень изменения напряженного состояния отдельных элементов каркаса из-за кручения. По результатам исследования были отмечены значительные изменения напряжений из-за кручения в верхнем кольце и заметные в меридиональных ребрах. Установлена зависимость характера их изменений от типа узловых соединений. Рекомендовано учитывать эффект кручения при проектировании металлических ребристо-кольцевых куполов.

Ключевые слова: ребристо-кольцевой купол, компьютерная модель, меридиональные ребра, верхнее и нижнее кольца, колонны, кручение, узловые сопряжения, статический расчет

INTRODUCTION

Recently, publications have begun to actively pay attention to the study of the operation of metal structural elements taking into account torsion. The vast majority of publications are usually devoted to open-profile beams. For example, the article [1] studies the behavior of a cantilever beam during torsion, and the article [2] compares the results of a theoretical and experimental study of the operation of an I-beam during bending. In addition to beams, frame rod systems are being considered. For example, in the article [3], an L-shaped and U-shaped frame with channel elements is considered, and the subject of the study is the bimoment diagrams. The article [4] considers a U-shaped rod systems of I-beams, and the subject of the study is the angle of rotation of the cross-section elements at the node.

There are no publications in the open press on the study of torsion in the elements of metal domes. Due to the spatial rigidity and cost-effectiveness of metal consumption, domes occupy a leading place as long-span coatings [5]. Metal domes are used as load-bearing frames for building coverings due to the reliability of such core systems [6, 7].

The geometric schemes of metal dome frames depend on the covered spans and the purpose of the building [8, 9]. Ribbed-ring domes are considered to be the simplest according to the geometric scheme. But even in ribbed-ring domes, various geometric schemes are possible, related to the number of sectors around the circumference and tiers in height. In addition, an important factor in the operation of the dome frame is the curvature and the number of columns supporting them. The static scheme of the entire building frame and the internal forces in the elements of the dome frames depend on this, but there are no studies of metal domes supported by sparsely installed columns in the open press.

Usually columns in ribbed-ring domes are placed under each meridional rib. However, with a large number of sectors or edges in the dome frame, such a design solution may be inconvenient for various reasons. In this case, fewer columns are used compared to the number of meridional ribs, which leads, as shown by the previous study of the author [10], to a change in the nature of the dome, which is manifested by a change in internal forces in the elements of the dome frame. The same study showed that, despite the similarity of the shape of the dome deformations, with a decrease in the number of columns under the dome, there is a significant increase in deflections of the dome frame.

Studies of dome-type rod systems in various computer programs have been carried out by many scientists. For example, the stress state of dome frames was analyzed when its geometric parameters changed [11], with different ratios of dome height to diameter for different spans [12]. As well as when the roof is included in the work in the cells of the frame between the steel ribs and rings [13], with different dome height-to-diameter ratios and different cross-sections of the elements [14], with different heights compared to the span of the dome frame with connections [15]. Previously, the author performed a comparative study of ribbed-ring domes with different numbers of connections [16] and different sizes of the upper ring [17].

In addition to torsion, there are no publications (except for the author's) on the study of the dependence of the stress state on the increase in the distance between the columns supporting the dome. In addition, it is possible to use various types of coupling elements of dome frames with each other, which also affects the torsion in the elements. The effect of the stiffness of the nodal joints on the stressed state of the dome is discussed in the publication [18]. This article presents a comparative analysis of a low steel dome of a ribbed-ring type with a diameter of 41 m and a height of 7 m. The dome consisted of 20 ribs and 10 rings, supported on foundations directly by each meridional rib. Purlins with glass cladding were used as rings. The models of this frame were considered, which differ in two approaches to calculation – linear and nonlinear, as well as the type of connection – with rings at-

tached to the ribs and without attachment to them. There are no explanations about the specific interpretation of compounds in the computer model. In addition, in some models, cladding is included in the work, and in some– diagonal connections in all sectors. The publication analyzed dome deformations, internal forces, and stresses in the elements, but without torsion.

METHODS

In order to determine the effect of torsion on the stress state of the main elements of the metal rib-ring dome frame numerical studies using the finite element method using the SCAD software package were performed [19, 20]. Twenty variants of design models of a dome structure were considered for the study. They differed from each other, firstly, in the schemes of supporting the dome on the columns and, secondly, in the types of nodal connections of the frame elements to each other. Twenty different computer models of the dome structure frame were considered for the study. They differed from each other, firstly, by different schemes of supporting the dome on the columns and, secondly, by different types of nodal connections of the frame elements to each other.

The object of the study was the frame of a spherical ribbed-ring dome with a radius of curvature of 23 m, consisting of 36 ribs and 7 rings (Fig. 1). Thus, the dome is divided by ribs into 36 sectors. The diameter of the lower ring is 39.3 m, the diameter of the upper ring is 5.0 m, the height of the dome frame is 11 m. The parameters of the metal dome elements were adopted based on the results of a preliminary calculation for operational loads from electro-welded pipes: the meridional ribs are O 530×9, the upper ring is O 530×9, the lower ring is O 630×20, the remaining rings are O 273×7.

In the course of the study, four dome support schemes were considered, the distinguishing feature of which was the number of sectors between the columns. So, if the columns were installed under each riber of the dome, i.e. through one sector, then the scheme was designated as 1. If the columns were installed through two, four and six sectors, then the schemes were designated as 2, 4 and 6, respectively (Fig. 2). All support schemes are characterized by the cyclic symmetry of the arrangement of columns along the contour. The columns in all schemes have a height of 7.0 m and are made of electro-welded pipes O 402×10.

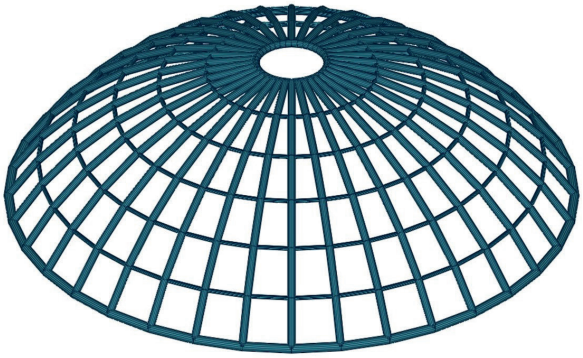

Figure 1. The ribbed-ring dome under study

The research was carried out on computational models of frameworks as spatial rod systems. In the calculated models, each structural element of the dome frame was represented by a single rod final element of the KE–10 with six degrees of freedom at the nodes. Calculations were performed for static impacts in a linear formulation. In the scheme 1 (Fig. 2, a), the number of elements 504, the number of nodes 288, total number of degrees of freedom 1728. In the scheme 2 (Fig. 2, b), the number of elements 486, the number of nodes 270, total number of degrees of freedom 1620. In the scheme 4 (Fig. 2, c), the number of elements 477, the number of nodes 261, total number of degrees of freedom 566. In the scheme 6 (Fig. 2, d), the number of elements 474, the number of nodes 258, total number of degrees of freedom 1548. In all schemes, restrictions on movement in the directions of all six degrees of freedom were imposed in the support nodes. In all schemes, the upper ring, the lower ring and the meridional ribs are integral, i.e. all 36 constituent rods of these rings and 6 rods of each rib are rigidly

connected to each other. And each of the intermediate rings is formed from separate rods between the ribs.

Nodes at the junctions of the ribs with the upper and lower rings, the joints of the columns with the lower ring, and the joints of the rods of the intermediate rings with the meridional ribs in the computational models of each of the schemes (see Fig. 2) were assigned both hinged and rigid. In the course of the study, five types of combinations of nodal connections were considered, which are conventionally called types of connections. Their designation and description of the allowed rotations in the joints in the normal (UY) and tangential (UZ) planes are given in Table 1. For example, for the S3 type (see Table 1) these joints are hinged in the normal (UY) and tangential (UZ) planes (Fig. 3). Type S2 (see Table 1) differs from S3 by prohibiting UY rotation only at the junctions of the ribs with the upper ring (see Fig. 3). Type S1 (see Table 1) differs from S2 by prohibiting the rotation of UY only at the junctions of the intermediate rings with the ribs (see Fig. 3). Type R1 (see Table 1) differs from S1 by prohibiting UY rotation at the joints of the ribs and columns with the lower ring (see Fig. 3). And for the R2 type of connection, they are rigid in the normal (UY) and tangential (UZ) planes (see Table 1). The torsion of rods around their axes (UX) has always remained prohibited.

Note that the rotation designations UY, UZ here and in Table 1 correspond to the local axes of the finite elements in the SCAD program.

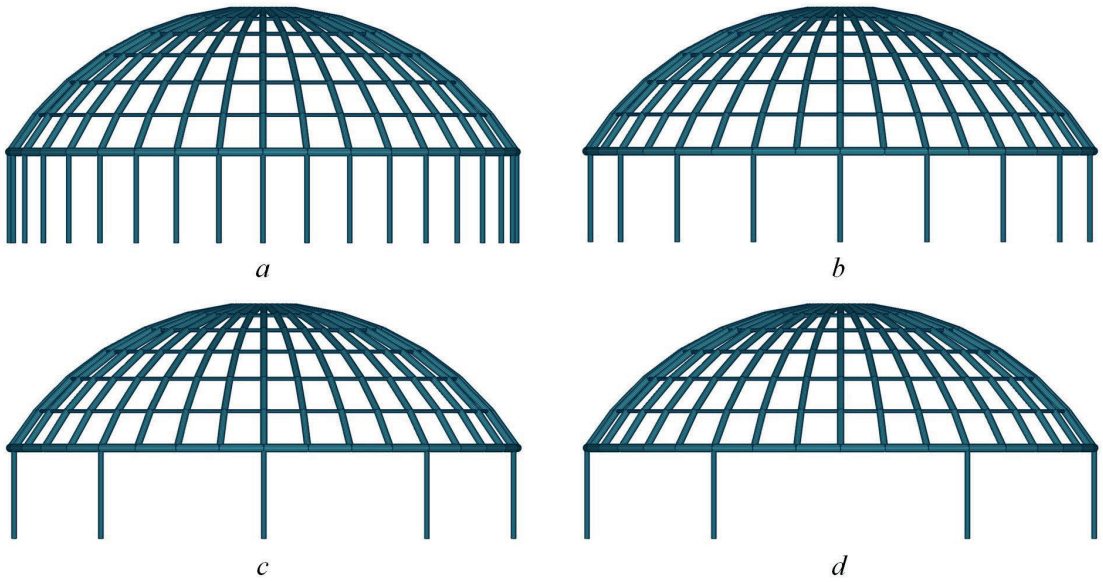

Figure 2. Schemes of frames with different numbers of sectors between the columns under the dome: a – 1 sector, b – 2 sectors, c – 4 sectors, d – 6 sectors.

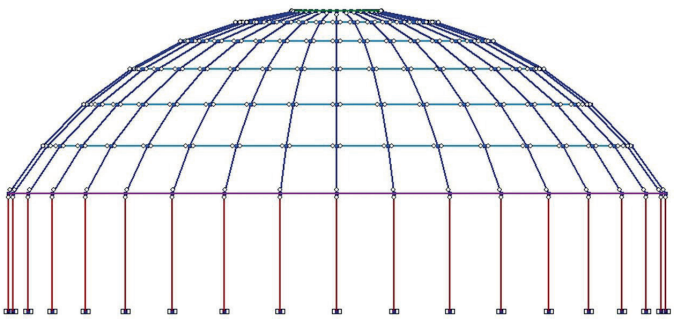

Figure 3. The initial calculation model of the frame with hinged nodal connections

Table 1. Resolution of rotations in nodes of various types of element connections of SCAD program

Types of nodes	Element connections							
	Ribs with upper ring		Ribs with lower ring		Columns with lower ring		Intermediate rings with ribs	
	UY	UZ	UY	UZ	UY	UZ	UY	UZ
S3	*	*	*	*	*	*	*	*
S2		*	*	*	*	*	*	*
S1		*	*	*	*	*		*
R1		*		*		*		*
R2								

The sign * means permission of rotation in node, and the absence of the sign means restrain of rotation.

The frames were calculated based on the combined effect of the load on the weight of the enclosing and load-bearing structures, as well as the asymmetric snow load acting on one side of the dome, as the most significant compared to the symmetrical one. All loads were applied at the nodes of the computational models of the framework.

In the course of the study internal forces N, M_x, M_y, M_t in the elements of the model frames were determined to calculate the stresses (in the SCAD program they were designated as N, M_y, M_z, M_k respectively), which were selected in the most stressed elements of the frame.

Since this study focuses on torsion, attention was focused on the torque M_t and the dependence of its magnitude on different frame schemes and types of connections elements in them.

Since the torsion of the elements causes tangential stresses in the sections, to assess the degree of influence of torsion on their stress state the reduced stresses were calculated using the formula

$$\sigma_t = \sqrt{\sigma^2 + 3\tau^2} \,. \qquad (1)$$

Here are the normal stresses σ for the tubular section

$$\sigma = \frac{N}{\mathrm{A}} \pm \frac{M}{\mathrm{W}_x}, \qquad (2)$$

where $M = \sqrt{M_x^2 + M_y^2}$ – this is the resultant of the moments M_x, M_y.

Tangential stresses τ in the presence of torque M_t in the pipes

$$\tau = \frac{M_t}{\mathrm{W}_t}. \qquad (3)$$

The effect of torsion on the stress state was determined by the difference between the reduced and normal stresses $\sigma_t - \sigma$.

RESULTS

The torques M_t manifests itself in all the elements of the framework, but in comparison with the moments M_x, M_y is characterized by relatively small values. In the columns and intermediate rings, the values of the torques M_t are insignificant. The meridional ribs of the dome the torques M_t are relatively small, but they show stable values by type of conjugation, with some increase with a decrease in the number of columns under the dome (Fig. 4).

In the upper ring of the dome the torque M_t values depend on the types of connections and increase with a decrease in the number of columns under the dome (Fig. 5). In the lower ring

of the dome, the torque M_t values significantly depend on the types of connections and increase with a decrease in the number of columns under the dome by several times (Fig. 6). In schemes with the number of sectors between columns 4 and 6, the moments in the upper and lower rings of the dome reach significant values.

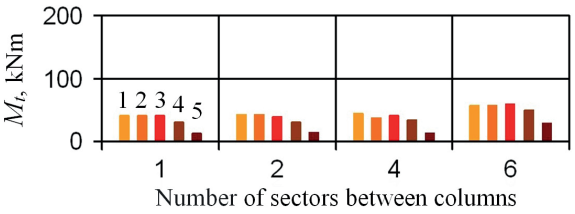

Figure 4. Maximum moments M_t in the meridional ribs of the dome. Types of connections: 1 – S3, 2 – S2, 3 – S1, 4 – R1, 5 – R2

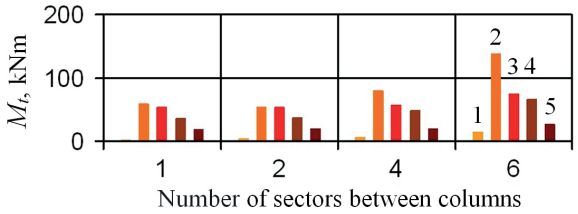

Figure 5. Maximum moments M_t in the upper ring of the dome. Types of connections: 1 – S3, 2 – S2, 3 – S1, 4 – R1, 5 – R2

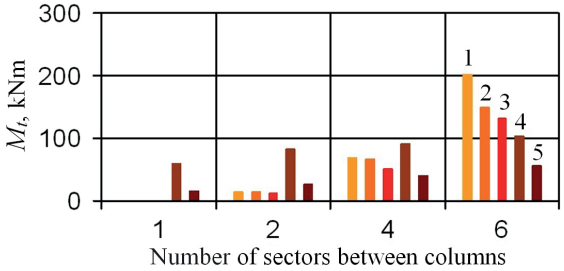

Figure 6. Maximum moments M_t in the lower ring of the dome. Types of connections: 1 – S3, 2 – S2, 3 – S1, 4 – R1, 5 – R2

Taking into account the identified torques M_t, a comparison of the reduced stresses σ_t calculated according to formula (1) was carried out. Note that these stresses are conditional, since their calculation uses the maximum values σ and the maximum values τ that occurred in different sections of the same type of elements. This is explained by the fact that in reality values are combined in a wide range of values – from maximum σ with minimum τ, to minimum σ with maximum τ.

In the meridional rings of the dome, the values of the reduced stresses σ_t depend on the types of connections and hardly change with a decrease in the number of columns under the dome (Fig. 7), with the exception of scheme 6. In the upper ring of the dome, the values of the reduced stresses σ_t also depend on the types of connections and clearly increase only when switching to scheme 6 with a reduced number of columns under the dome (Fig. 8).

The dependence of the reduced stresses σ_t on the number of columns under the dome is most reflected in the lower ring of the dome. The values σ_t increase several times when switching to schemes with a reduced number of columns (in schemes 2, 4 and 6) and, at the same time, depend on the types of connections (Fig. 9).

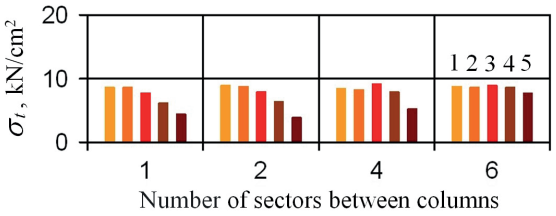

Figure 7. Reduced stresses σ_t in the meridional ribs of the dome. Types of connections: 1 – S3, 2 – S2, 3 – S1, 4 – R1, 5 – R2

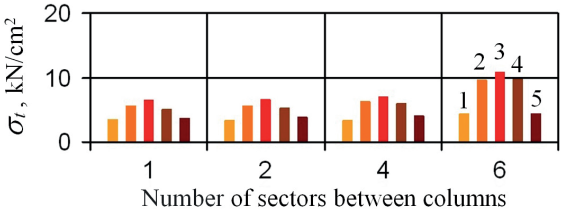

Figure 8. Reduced stresses σ_t in the upper ring of the dome. Types of connections: 1 – S3, 2 – S2, 3 – S1, 4 – R1, 5 – R2

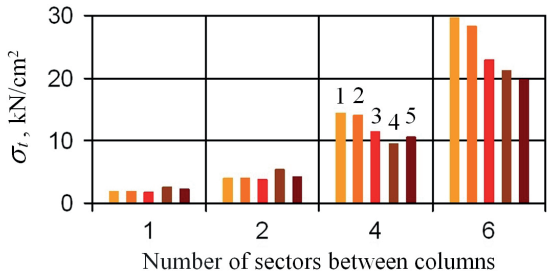

Figure 9. Reduced stresses σ_t in the lower ring of the dome. Types of connections: 1 – S3, 2 – S2, 3 – S1, 4 – R1, 5 – R2

To quantify the effect of torsion on the stress state of the dome elements, the ratio of the difference between reduced and normal stresses to reduced stresses, the so-called fractional effect of torsion, was calculated using the formula

$$\Delta_t = \frac{\sigma_t - \sigma}{\sigma_t}. \qquad (4)$$

In the meridional ribs of the dome the fractional effect of torsion Δ_t is relatively small and varies in the range from 1% to 5%. It depends on the type of node connections and increases slightly in scheme 6 with a reduced number of columns under the dome (Fig. 10).

In the upper ring of the dome, the fractional influence of torsion in one type of connections (S2), depending on the dome support scheme, is extremely high and varies from 11% to 26%, in the other (S1) – is not significant, since it does not exceed 1%. In other cases, the fractional effect of torsion Δ_t is relatively small and varies in the range from 3% to 8% (Fig. 11).

In the lower ring of the dome, the fractional effect of torsion Δ_t in only one type of connections (S1), depending on the dome support scheme, does not exceed 6%, and with the largest number of columns. In other types of connections, regardless of the support scheme, the torsion effect Δ_t does not reach even 1% (Fig. 12). This phenomenon, with a significant increase in torque M_t with a decrease in the number of dome support columns, is explained by the fact that the bending moments M_x, M_y increase much faster.

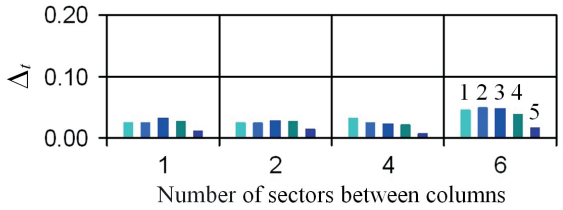

Figure 10. The fractional effect of torsion Δ_t on σ_t in the meridional ribs of the dome. Types of connections: 1 – S3, 2 – S2, 3 – S1, 4 – R1, 5 – R2

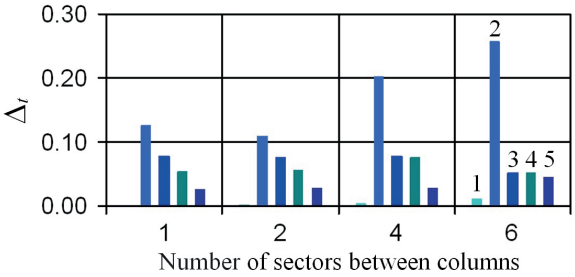

Figure 11. The fractional effect of torsion Δ_t on σ_t in the upper ring of the dome. Types of connections: 1 – S3, 2 – S2, 3 – S1, 4 – R1, 5 – R2

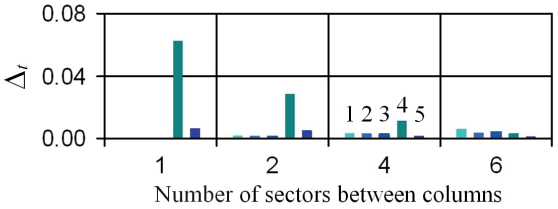

Figure 12. The fractional effect of torsion Δ_t on σ_t in the lower ring of the dome. Types of connections: 1 – S3, 2 – S2, 3 – S1, 4 – R1, 5 – R2

CONCLUSIONS

Based on the presented material, the following conclusions can be drawn:

1. With different types of nodal connections of the elements of the ribbed-ring dome, in combination with sparsely installed columns, torques

of different magnitudes arise in different elements.

2. In the meridional ribs of the dome, torsion has a noticeable (up to 5%) effect on their stress state in all dome support schemes and in various types of coupling elements, except for rigid ones.

3. Torsion has the most significant effect on the upper ring. When the nodes are swivel in the tangential and normal directions, with the exception of the junctions of the ribs with the upper ring, the voltage may increase by 11-26%, otherwise by no more than 1%. With other types of swivel connections, the torsion effect is limited to 8%, and with rigid connections - less than 5%.

4. In the lower ring of the dome, with hinged connections only in the tangential direction, torsion affects its stress state from 6% to 3% in schemes with columns under each rib and through the rib, respectively. In other types of nodes, regardless of the support scheme, the effect of torsion does not reach 1%.

5. Additional studies should be conducted to determine the possible effect of torsion on the stress state of metal ribbed-ring domes with non-tubular profile elements. It is also necessary to do this to evaluate the torsion in the intermediate rings of the dome, since it is necessary to take into account their work between the ribs along the beam circuit from a distributed load.

6. When designing metal ribbed-ring domes, it is recommended to take into account the effect of torsion on the bearing capacity of their elements, especially the upper ring.

REFERENCES

1. **Galishnikova V.V., Gebre T.H.** The behaviour of thin-walled beam with restrained torsion / Magazine of Civil Engineering. 2022. 110(2). Article No. 11009. 15 p.
2. **Tusnin A.R., Prokic M**. Experimental research of I-beams under bending and torsion actions / Magazine of Civil Engineering, 2015, №1. Pp. 24–31.
3. **Rybakov, V.A.; Jos, V.A.** Stress State of Г-Shaped Thin-Walled Rod Joints in Bending Torsion; 2022; Construction of Unique Buildings and Structures; 99 Article No 9903. 14 c.
4. **Serpik I.N., Shkolyarenko R.O.** Calculation of systems of thin-walled rods of a trough-shaped profile taking into account constrained torsion // Construction and reconstruction. 2018. Vol. 4, № 78. C. 31–41.
5. **Tur, V.I.** Dome Structures: Morphogenesis, Analysis, Design, Increase In Effectiveness. Moscow: ASV publ., 2004. – 96 p.
6. **Krivoshapko, S.N.** Metal ribbed-and-circular and lattice shells from the XIXth until the first half of the XXth centurie // Structural Mechanics of Engineering Constructions and Buildings, 2014, № 6 P. 4–15.
7. **Krivoshapko, S.N.** On application of parabolic shells of revolution in civil engineering in 2000-2017 // Structural Mechanics of Engineering Constructions and Buildings, 2017, № 4 P. 4–14.
8. Metal Structures. Vol. 2. Steel structures of buildings and constructions. Reference book the designer / *Under the general editorship of Kuznetsov, V.V.* Moscow: ASV publ., 1998. – 512 p.
9. **Lebed, E.V., Alukaev, A.U.** Large-span metal dome roofs and their construction // Structural Mechanics of Engineering Constructions and Buildings, 2018, 14(1): 4–16.
10. **Lebed E.V**. Behavior of metal frame of ribbed-ring dome with decrease in number of supporting columns // Structural Mechanics of Engineering Constructions and Buildings. 2024, 20(1):14–26.
11. **Chandiwala Anuj.** Analysis and design of steel dome using software // International Journal of Research in Engineering and Technology (IJRET). – eSAT Publishing House, Bangalore, India, 2014, Volume 03, Issue 03. Pp. 35–39.
12. **Peter Chacko, Dipu V.S., Manju P.M.** Finite Element Analysis of Ribbed Dome // International Journal of Engineering Re-

search and Applications (IJERA) – Kerala, India, 2014, ISSN: 2248-9622. Pp. 25–32.
13. **Nabeel Abdulrazzaq Jasim, Ihab Sabri Saleh, Saddam Khalaf Faleh.** Structural Analysis of Ribbed Domes Using Finite Element Method // International Journal of Civil Engineering Research. ISSN 2278-3652 – © Research India Publications, 2017, Volume 8, Number 2. Pp. 113-130.
14. **Anu J.S., Preethi M.** Parametric Analysis of Single layer Ribbed dome with Diagonal members // International Research Journal of Engineering and Technology (IRJET), 2017, Volume 04 Issue: 08. Pp. 870–877.
15. **Merilmol Eldhose, Rajesh A.K., Ramadass** *S.* Finite Element Analysis and Parametric Study of Schwedler Dome Using ABAQUS Software // International Journal of Engineering Trends and Technology (IJETT). 2015. Vol. 28. No. 7. – October 2015. Pp. 333–338.
16. **Lebed E.V.** The influence of bracing on the stress state of the ribbed-ring dome framework // Structural Mechanics of Engineering Constructions and Buildings. 2022; 18(5): 417–427.
17. **Lebed E.V**. Influence of the size of the upper ring on the stressed state of the ribbed-ring metal dome // Structural Mechanics of Engineering Constructions and Buildings. 2023; 19(5):450–458.
18. **Katarzyna Jeleniewicz, Jacek Jaworski, Mariusz Żółtowski, Izabela Uziębło, Anna Stefańska & Saurav Dixit.** Steel ribbed dome structural performance with different node connections and bracing system // Scientific Reports. Volume 14, Article number: 14013 (2024).
19. **Karpilovskiy V.S., Kriksunov E.Z., Malyarenko A.A., Perel'muter A.V., Perel'muter M.A.** SCAD Office. Computer system SCAD: – M.: Izdatel'stvo ASV, 2004. – 592 p.
20. **Gorodetskiy A.S., Evzerov I.D.** Computer models of structures – Kiev: Izdatel'stvo "Fakt", 2005. – 344 p.

СПИСОК ЛИТЕРАТУРЫ

1. **Galishnikova V.V., Gebre T.H.** The behaviour of thin-walled beam with restrained torsion / Magazine of Civil Engineering. 2022. 110(2). Article No. 11009. 15 p.
2. **Туснин А.Р., Прокич М.** Экспериментальные исследования работы балок двутаврового сечения при действии изгиба и кручения / Инженерно-строительный журнал, 2015, №1. С. 24–31.
3. **Rybakov, V.A.; Jos, V.A.** Stress State of Г-Shaped Thin-Walled Rod Joints in Bending Torsion; 2022; Construction of Unique Buildings and Structures; 99 Article No 9903. 14 c.
4. **Серпик И.Н., Школяренко Р.О.** Расчет систем тонкостенных стержней корытообразного профиля с учетом стесненного кручения // Строительство и реконструкция. 2018. Издание 4 № 78. С. 31–41.
5. **Тур В.И.** Купольные конструкции: формообразование, расчет, конструирование, повышение эффективности. – М.: Издательство АСВ, 2004. – 96 с.
6. **Кривошапко С.Н**. Металлические ребристо-кольцевые и сетчато-стержневые оболочки XIX – первой половины XX-го веков // Строительная механика инженерных конструкций и сооружений, 2014, № 6. С. 4–15.
7. **Кривошапко С.Н.** К вопросу о применении параболических оболочек вращения в строительстве в 2000-2017 годах // Строительная механика инженерных конструкций и сооружений, 2017, № 4 С. 4–14.
8. Металлические конструкции: справочник проектировщика. В 3-х т. / Под общ. ред. В.В. Кузнецова (ЦНИИпроектстальконструкция им. Н.П. Мельникова). Т. 2. Стальные конструкции зданий и сооружений. М.: Изд-во АСВ, 1998. – 512 с.
9. **Лебедь Е.В., Алукаев А.Ю.** Большепролетные металлические купольные покрытия и их возведение // Строительная механика инженерных конструкций и сооружений, 2018, Том 14, № 1. С. 4–16.

10. **Лебедь Е.В.** Работа металлического каркаса ребристо-кольцевого купола при уменьшении количества поддерживающих его колонн // Строительная механика инженерных конструкций и сооружений. 2024. Том 20. № 1. С. 14–26.
11. **Chandiwala Anuj.** Analysis and design of steel dome using software // International Journal of Research in Engineering and Technology (IJRET). – eSAT Publishing House, Bangalore, India, 2014, Volume 03, Issue 03. Pp. 35–39.
12. **Peter Chacko, Dipu V.S., Manju P.M.** Finite Element Analysis of Ribbed Dome // International Journal of Engineering Research and Applications (IJERA) – Kerala, India, 2014, ISSN: 2248-9622. Pp. 25–32.
13. **Jasim N.A., Saleh I.S., Faleh S.K**. Structural Analysis of Ribbed Domes Using Finite Element Method // International Journal of Civil Engineering Research. ISSN 2278-3652 – © Research India Publications, 2017, Volume 8, Number 2. Pp. 113-130.
14. **Anu J.S., Preethi M**. Parametric Analysis of Single layer Ribbed dome with Diagonal members // International Research Journal of Engineering and Technology (IRJET), 2017, Volume 04 Issue: 08. Pp. 870-877.
15. **Merilmol Eldhose, Rajesh A.K., Ramadass S.** Finite Element Analysis and Parametric Study of Schwedler Dome Using ABAQUS Software // International Journal of Engineering Trends and Technology (IJETT). 2015. Vol. 28. No. 7. – October 2015. ISSN: 2231-5381. Pp. 333–338.
16. **Лебедь Е.В.** Влияние связей на напряженное состояние каркаса ребристо-кольцевого купола // Строительная механика инженерных конструкций и сооружений. 2022. Т. 18. № 5. С. 417–427.
17. **Lebed E.V.** Influence of the size of the upper ring on the stressed state of the ribbed-ring metal dome // Structural Mechanics of Engineering Constructions and Buildings. 2023;19(5):450–458.
18. **Katarzyna Jeleniewicz, Jacek Jaworski, Mariusz Żółtowski, Izabela Uziębło, Anna Stefańska & Saurav Dixit.** Steel ribbed dome structural performance with different node connections and bracing system // *Scientific Reports* volume 14, Article number: 14013 (2024).
19. **Карпиловский В.С., Криксунов Э.З., Маляренко А.А., Перельмутер А.В., Перельмутер М.А.** SCAD Office. Вычислительный комплекс SCAD: – М.: Издательство АСВ. 2004. – 592 с.
20. **Городецкий А.С., Евзеров И.Д.** Компьютерные модели конструкций. – К.: Изд-во «Факт». 2005. – 344 с.

Evgeny V. Lebed – Candidate of Technical Science, Associate Professor, Department of Metal and Wooden Structures, Moscow State University of Civil Engineering (National Research University) (MGSU). Yaroslavskoye Shosse, Moscow, 129337, Russian Federation. E-mail: evglebed@mail.ru.

Лебедь Евгений Васильевич – кандидат технических наук, доцент, кафедра Металлических и деревянных конструкций, Национальный исследовательский Московский государственный строительный университет (НИУ МГСУ). 129337, Москва, Ярославское шоссе, д. 26. Электронная почта: evglebed@mail.ru

DOI:10.22337/2587-9618-2025-21-1-146-156

A CRITICAL REVIEW OF DEEP LEARNING APPLICATIONS, CHALLENGES, AND FUTURE DIRECTIONS IN STRUCTURAL ENGINEERING

Manaf Raid Salman[1], Marwan Al-Shaikhli [2], Hasan Ali Abbas [2], Hussain Hamed Ahmad [1], Sakhiah Abdul Kudus [3,4]

[1] Department of Building and Construction Techniques Engineering, Madent Alelem University College, Baghdad, IRAQ
[2] Department of Building and Construction Engineering Techniques, Middle Technical University, Baghdad, IRAQ
[3] School of Civil Engineering, College of Engineering, Universiti Teknologi MARA, 40450 Shah Alam, Selangor, MALAYSIA
[4] Institute for Infrastructure Engineering and Sustainable Management (IIESM), Universiti Teknologi MARA (UiTM), Shah Alam, Selangor, MALAYSIA

Abstract: Deep learning (DL), a major part of artificial intelligence (AI) is considered as a transformational technology in different areas of science, such as structural engineering. This critical review uncovers the potential contribution of deep learning in solving complex issues facing structural engineering, such as optimizing structural design, predicting and monitoring material behaviour, and monitoring in real-time the structural health. Through developed neural network architectures such as generative adversarial networks (GANs), recurrent neural networks (RNNs), and convolutional neural networks (CNNs), engineers can identify solutions based on traditional deterministic data extraction. However, issues like computational requirements, model interpretability and data scarcity are widely adopted. This review highlights recent advancements, practical applications, and the limitations of deep learning in structural engineering, proposing pathways for future research to enhance its efficacy and integration in real-world scenarios.

Keywords: Deep Learning, Machine Learning, Neural Networks, Structural Engineering, Structural Health Monitoring, Optimization of Structural Design

ОБЗОР ПРИМЕНЕНИЯ ГЛУБИННОГО ОБУЧЕНИЯ В СТРОИТЕЛЬНОМ ПРОЕКТИРОВАНИИ: ПРОБЛЕМЫ И БУДУЩИЕ НАПРАВЛЕНИЯ

Манаф Раид Салман [1], Марван Аль-Шайхли [2], Хасан Али Аббас [2], Хусейн Хамед Ахмад [1], Сахия Абдул Кудус [3,4]

[1] Кафедра строительства и инженерной техники, Университетский колледж Мадент Алем, г. Багдад, ИРАК
[2] Кафедра инженерных технологий строительства зданий и сооружений, Средний технический университет, г. Багдад, ИРАК
[3] Школа гражданского строительства, Инженерный колледж, Университет Текнологии МАРА, г. Селангор, МАЛАЙЗИЯ
[4] Институт инфраструктурной инженерии и устойчивого управления (IIESM), Университет Текнологии МАРА (UiTM), г. Селангор, МАЛАЙЗИЯ

Аннотация: Глубинное обучение (DL), основная часть искусственного интеллекта (AI), рассматривается как технология трансформации в различных областях науки, таких как строительное проектирование. Данный критический обзор раскрывает потенциальный вклад глубинного обучения в решение сложных проблем, стоящих перед строительным проектированием, таких как оптимизация конструкции, прогнозирование и мониторинг поведения материалов, а также мониторинг состояния конструкции в режиме реального времени. Благодаря разработанным архитектурам нейронных сетей, таким как генеративные адверсивные сети (GAN), рекуррентные нейронные сети (RNN) и конволюционные нейронные сети (CNN), инженеры могут находить решения на основе традиционного детерминированного извлечения данных. Однако при этом широко распространены такие проблемы, как вычислительные требования, интерпретируемость моделей и нехватка данных. В данном обзоре освещаются последние достижения, практические применения и ограничения глубинного обучения в

строительном проектировании, предлагаются пути будущих исследований для повышения его эффективности и интеграции в реальные практические задачи.

Ключевые слова: Глубинное обучение, машинное обучение, нейронные сети, проектирование конструкций, мониторинг состояния конструкций, оптимизация конструкций

1. INTRODUCTION

Structural engineering has long relied on tried-and-error methods such as finite element analysis [1, 2], deterministic models [3], and material science [4] to design safe and reliable structures [5]. Yet, with increasingly complex infrastructures and unpredictable environmental factors, the limits of these traditional techniques are being tested [6]. Therefore, deep learning, a cutting-edge technology rooted in artificial intelligence (AI), offer a new paradigm for problem-solving in structural engineering [7]. However, employing deep learning in this field is still in its nascent stages, yet its potential to revolutionize the industry is significant [8]. From optimizing the structural design to predicting the behavior of materials under stress, deep learning provides a data-driven approach to challenges that have historically been difficult to model using traditional engineering tools.

This review will explore the current applications for deep learning regarding structural engineering, discuss the advantages and limitations of integrating AI technologies, and suggest pathways for future research.

2. OVERVIEW OF DEEP LEARNING

Being a branch of Machine Learning, Deep Learning employs neural networks to execute various assignment like regression, classification, and learning [9]. It is known by this term because it has many layers of neurons similar to those in the human brain. Thus, it can also be called 'Artificial Neural Networks' [See Figure 1]. Its foundation is rooted in 1943 when McCulloch and Pitts published a paper that introduced the neural network first mathematical model [10].

A method called threshold logic (a combination of algorithms and mathematics) was used to simulate the human brain thought process. Later in 1957, a simple version of deep learning called Perceptron was suggested by Frank Rosenblatt which can learn from experience and adjust its weights to make precise predictions [11]. The breakthrough came in 1986 when backpropagation was introduced by Geoffrey Hinton [12]. This algorithm efficiently computes the network's weights gradients. Thus facilitating multi-layer neural networks training. Another progress was achieved in 2006 when scientists began applying deep learning models on the GPUs (graphics processing units) of computers, which eventually, led to the application of Convolutional Neural Networks (CNNs) in image recognition [13]. Till now, the demand for Deep Learning is still increasing and still improving with the introduction of new algorithms [14].

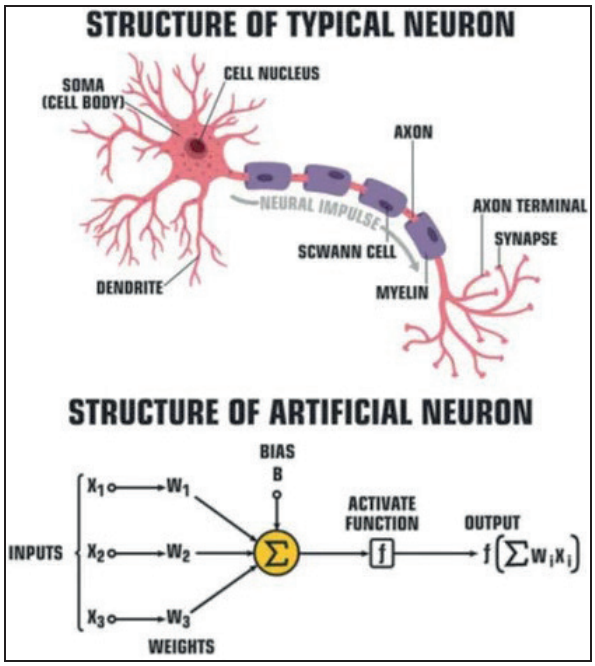

Figure 1. A compression between diagrams of biological neuron vs artificial neuron [14]

At its core, deep learning represents a dramatic departure from traditional machine learning

techniques. While conventional machine learning algorithms require structured data and manual feature selection, deep learning models excel at finding patterns in large, unstructured datasets like images, sensor data, or time-series signals from infrastructure monitoring systems. This makes them particularly suited for applications in structural engineering, where the real world rarely conforms to neat, clean data inputs.

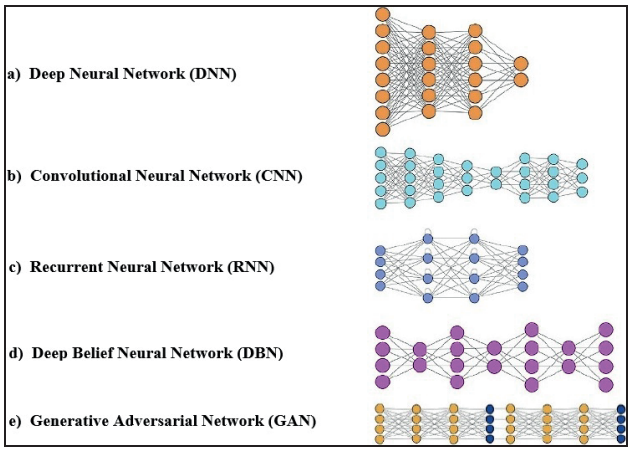

Figure 2. Different types of neural networks [15]

For instance, convolutional neural networks (CNNs) can detect minute cracks in bridges, while recurrent neural networks (RNNs) can forecast the behavior of buildings during seismic events. Moreover, generative adversarial networks (GANs) were utilized for generative design, automatically creating thousands of structural layouts that meet specific performance criteria. Figure 2 illustrates different types of neural networks used in structural engineering.

3. DEEP LEARNING APPLICATIONS IN STRUCTURAL ENGINEERING

3.1 Structural Health Monitoring

SHM has traditionally been a reactive process. However, deep learning is transforming it into a proactive discipline, using CNNs to process high-resolution images of structures to identify signs of damage such as cracks or corrosion. For instance, in Sydney Harbour Bridge, where CNNs were employed to analyze real-time sensor data, predicting damage before it occurs. These models can now offer early maintenance solutions, reducing downtime and enhancing infrastructure reliability [16, 17]. Dorafshan, Thomas [18] have conducted an image-based concrete crack detection by developing a Deep Convolutional Neural Network (DCCN). It was shown that it can predict and detect cracks better than the traditional edge detection methods (Gaussian, Butterworth Sobel, Prewitt, Roberts, and Laplacian of Gaussian).

Gao and Mosalam [19] have developed a Visual Geometry Group (VGG) based architecture to detect the damage in structural components [See Figure 3]. Furthermore, transfer learning was applied to obtain a robust recognition performance with a small training dataset, and collecting images for the training process was done by building an image dataset which is called Structural ImageNet. The acquired data have established the potential of using transfer learning in image-based structural damage recognition. Deng, Ju [20] have conducted an abnormal data recovery framework of an ancient palace wall by applying a gated recurrent unit (GRU). It was established that the selected method is adequate of obtaining accurate results of data recovery for ancient buildings.

3.2 Load Prediction and Structural Behavior Modeling

Several studies were conducted to determine the best AI techniques for forecasting loads. RNNs and long short-term memory (LSTM) models were found to be greatly adopted for load prediction, especially under dynamic conditions such as earthquakes. By analyzing historical data, these models can predict structural responses with high accuracy. This predictive power is crucial in regions prone to seismic activity, where deep learning has demonstrated an ability to improve the safety and resilience of buildings. Zhang, Chen [21] have employed a Deep LSTM to predict nonlinear seismic performance. Two different schemes (different input/output formats) were developed and it was shown that the

proposed network provides a reliable and efficient solution for nonlinear structural response prediction. Another research has demonstrated the accuracy of the LSTM algorithm in predicting the thermal loading of a building [22, 23].

Other studies have determined the efficiency of CNN in predicting the strength of concrete [24]. For instance, Deng, He [25] have suggested developing a CNN using a SoftMax regression model to predict the recycled concrete compressive strength before construction. The software has been trained using characteristics such as the water-cement ratio, the replacement ratio recycled fine aggregate, coarse aggregate, the fly ash and their mixtures. The suggested model has demonstrated efficient results and precision. Other researchers have determined that employing CNNs provides accurate and reliable results regarding the dynamic structural performance of reinforced concrete (R.C.) slabs under blast loads [25, 26].

3.2 Load Prediction and Structural Behavior Modeling

Several studies were conducted to determine the best AI techniques for forecasting loads. RNNs and long short-term memory (LSTM) models were found to be greatly adopted for load prediction, especially under dynamic conditions such as earthquakes. By analyzing historical data, these models can predict structural responses with high accuracy. This predictive power is crucial in regions prone to seismic activity, where deep learning has demonstrated an ability to improve the safety and resilience of buildings. Zhang, Chen [21] have employed a Deep LSTM to predict nonlinear seismic performance. Two different schemes (different input/output formats) were developed and it was shown that the proposed network provides a reliable and efficient solution for nonlinear structural response prediction.

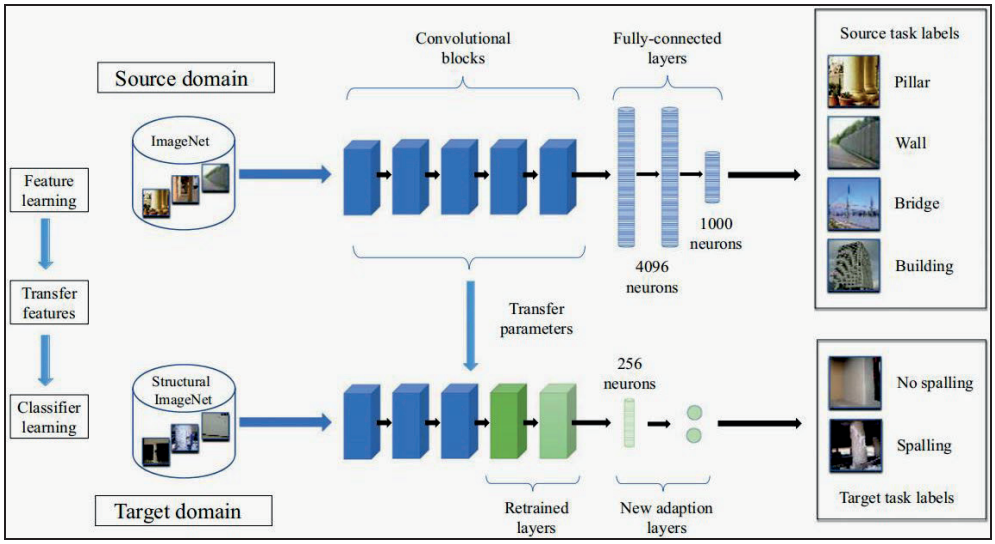

Figure 3. Detecting damage using Transfer Learning [19]

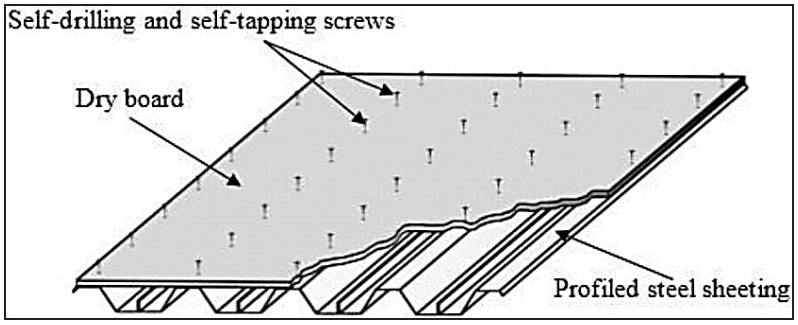

Figure 4. Typical PSSDB Floor panel [27]

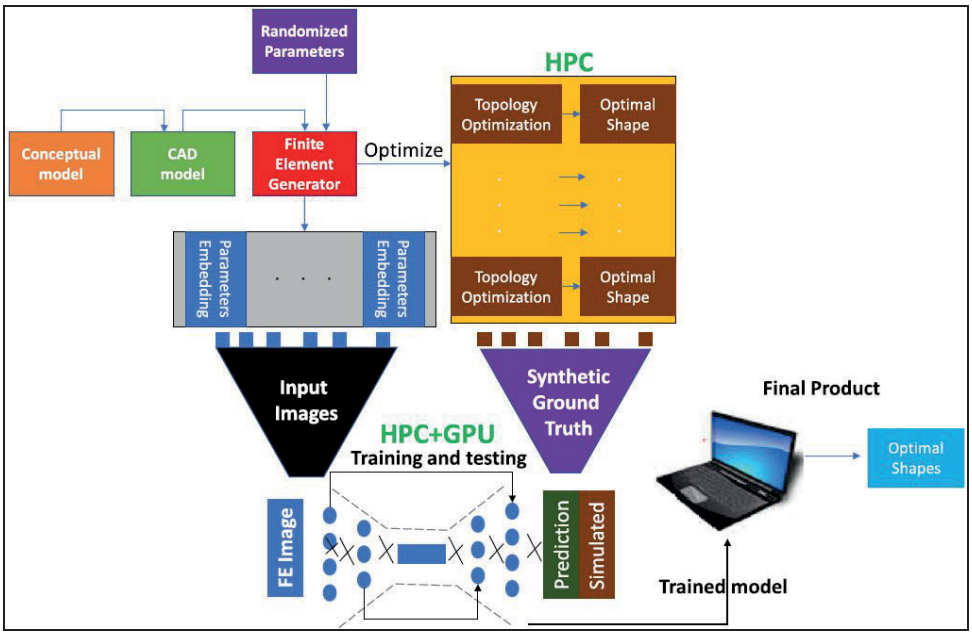

Figure 5. Flowchart used of CNN-based optimizer [28]

Another research has demonstrated the accuracy of the LSTM algorithm in predicting the thermal loading of a building [22, 23].

Other studies have determined the efficiency of CNN in predicting the strength of concrete [24]. For instance, Deng, He [25] have suggested developing a CNN using a SoftMax regression model to predict the recycled concrete compressive strength before construction. The software has been trained using characteristics such as the water-cement ratio, the replacement ratio recycled fine aggregate, coarse aggregate, the fly ash and their mixtures. The suggested model has demonstrated efficient results and precision. Other researchers have determined that employing CNNs provides accurate and reliable results regarding the dynamic structural performance of R.C. slabs under blast loads [25, 26].

3.3 Optimization of Structural Design

Optimization in design isn't just about making structures stronger; it's about making them smarter. Deep learning algorithms such as GANs enable engineers to generate and test thousands of design configurations in seconds, optimizing for parameters like material properties, load capacities, and cost constraints [29, 30]. A study conducted in 2018 by Vafa employed ANN to develop the optimum steel deck cross-sections for the Profiled Steel Sheeting Dry Board (PSSDB) floor panels [see Figure 4] [27]. Non-dominated Sorting Genetic Algorithm II (A multi-objective genetic algorithm) was employed for this research. It was shown the efficacy of ANNs in improving structural design [27].

Another study conducted by Ferreiro-Cabello, Fraile-Garcia [31] have employed deep learning techniques to develop metamodels with the aim to facilitate the optimization of one-way slabs. Five DNNs were developed which were capable of predicting CO_2 emissions, embodied energy, cost and deflection. The suggested method showed reliable results with only 0.5% error. Abueidda, Koric [28] have applied CNN to predict the optimized materials design subjected to small/large deformations (with/without stress constraints) Figure 5. The developed models demonstrate an accurate prediction of the optimized designs, and they can be employed in other design domains and nonlinear mechanics scenarios. Mai, Lieu [32] have applied a deep novel unsupervised learning (DUL)-based framework to optimize a truss structures design subjected to various constraints, and it was

shown that a computational cost in most problems can be saved using such algorithms.

4. CHALLENGES AND LIMITATIONS

Despite its potential, Deep Learning faces various challenges that can be summarized in the following:

4.1 Data Availability and Quality

High-quality and large datasets are essential for deep learning. Nevertheless, data scarcity is a major challenge in structural engineering, especially when it comes to rare events like structural failures [33]. Techniques like transfer learning, where models are adapted from similar domains, offer a potential solution [34].

4.2 Model Interpretability

One of the issues that discourage adapting deep learning in engineering applications is its "black box" nature [35]. Engineers must trust these models for safety-critical decisions, yet their inner workings are often opaque, making regulatory approval difficult.

4.3 Generalization and Scalability

Generalization to new environments and scalability to larger, more complex structures remain significant hurdles. Models trained on one type of structure may not perform as well on another, raising concerns about their robustness in real-world applications.

4.4 Underfitting & Overfitting

Both Overfitting & underfitting can pose an obstacle to deep learning. The former occurs when the models cannot capture the underlying patterns due to their simplicity, while the latter occurs when training the model demands a large amount of time and contains noisy data because of its complexity [36]. Therefore, it is important to provide an optimal solution by employing balanced-complex models to avoid either case Figure 6.

4.5 Ethical & Bias Issues

Biases can occur during the learning algorithm of the model to prioritize solutions with certain characteristics over others. Such an issue is considered unethical since it can cause unfair results. Thus, addressing such issues is essential to achieve fairness.

4.6 Hardware Limitations

High-performance CPUs are essential for training models. However, having access to such hardware is hard for many researchers.

5. FUTURE RESEARCH DIRECTIONS

5.1 Hybrid Models

Hybrid models that combine deep learning with traditional physics-based simulations hold significant promise for enhancing both accuracy and interpretability [37].

5.2 Transfer Learning

Transfer learning offers a way forward in addressing the issue of limited data availability, allowing models trained on one task to be adapted for another.

5.3 Real-Time Applications in Smart Cities

As cities become more connected, deep learning will significantly contribute in the real-time monitoring and management of infrastructure [38]. For instance, these models can optimize traffic flow or monitor structural health in real time. Consequently, decreasing the risk of catastrophic failures by capacitate predictive maintenance.

6. CONCLUSION

Deep learning is poised to transform structural engineering by improving prediction accuracy, optimizing designs, and enabling real-time monitoring. Although challenges remain particularly in data quality and model interpretability, the benefits of AI are too

significant to ignore. As deep learning continues to advance, it will become even more integrated into the field, leading to smarter, safer, and more resilient infrastructure.

REFERENCES

1. **Ereiz, S., I. Duvnjak, and J.F. Jiménez-Alonso**.(2022) Review of finite element model updating methods for structural applications. in Structures. Elsevier. of Conference.
2. **Liu, W.K., S. Li, and H.S. Park**,(2022) Eighty years of the finite element method: Birth, evolution, and future Archives of Computational Methods in Engineering, 29, no.6, p.p 4431-4453.
3. **Wu, B., S. Luo, and C.S. Suh**,(2024) A Comprehensive Review of Propagation Models in Complex Networks: From Deterministic to Deep Learning Approaches arXiv preprint arXiv:2410.02118.
4. **Fujinuma, N., et al.**,(2022) Why big data and compute are not necessarily the path to big materials science Communications Materials, 3, no.1, p.p 59.
5. Ditlevsen, O. and H.O. Madsen, *Structural reliability methods*. Vol. 178. 1996: Wiley New York.
6. **Ghosn, M., et al.**,(2016) Reliability-based performance indicators for structural members Journal of Structural Engineering, 142, no.9, p.p F4016002.
7. **Etim, B., et al.**,(2024) Machine Learning-Based Modeling for Structural Engineering: A Comprehensive Survey and Applications Overview Buildings, 14, no.11, p.p 3515.
8. **Li, Q., et al.**,(2024) Classification and Application of Deep Learning in Construction Engineering and Management–A Systematic Literature Review and Future Innovations Case Studies in Construction Materials, p.p e04051.
9. **Sarker, I.H.**,(2021) Deep learning: a comprehensive overview on techniques, taxonomy, applications and research directions SN computer science, 2, no.6, p.p 420.
10. **McCulloch, W.S. and W. Pitts**,(1943) A logical calculus of the ideas immanent in nervous activity The bulletin of mathematical biophysics, 5, p.p 115-133.
11. **Rosenblatt, F.**,(1958) The perceptron: a probabilistic model for information storage and organization in the brain Psychological review, 65, no.6, p.p 386.
12. **Rumelhart, D.E., G.E. Hinton, and R.J. Williams**,(1986) Learning representations by back-propagating errors nature, 323, no.6088, p.p 533-536.
13. **Zhao, X., et al.**,(2024) A review of convolutional neural networks in computer vision Artificial Intelligence Review, 57, no.4, p.p 99.
14. Sundaray, S. *History of Deep Learning*. 2023; Available from: https://medium.com/@sreyan806/history-of-deep-learning-c176e2d3cddf.
15. **Akinosho, T.D., et al.**,(2020) Deep learning in the construction industry: A review of present status and future innovations Journal of Building Engineering, 32, p.p 101827.
16. **Khoa, N.L., et al.**,(2014) Robust dimensionality reduction and damage detection approaches in structural health monitoring Structural Health Monitoring, 13, no.4, p.p 406-417.
17. **Abbas, H.A., Z. Mohamed, and S.A. Kudus**,(2023) Deformation behaviour, crack initiation and crack damage of weathered composite sandstone-shale by using the ultrasonic wave and the acoustic emission under uniaxial compressive stress International Journal of Rock Mechanics and Mining Sciences, 170, p.p 105497.
18. **Dorafshan, S., R.J. Thomas, and M. Maguire**,(2018) Comparison of deep convolutional neural networks and edge detectors for image-based crack detection in

concrete Construction and Building Materials, 186, p.p 1031-1045.
19. **Gao, Y. and K.M. Mosalam**,(2018) Deep transfer learning for image-based structural damage recognition Computer-Aided Civil and Infrastructure Engineering, 33, no.9, p.p 748-768.
20. **Deng, Y., et al.**,(2024) Abnormal data recovery of structural health monitoring for ancient city wall using deep learning neural network International Journal of Architectural Heritage, 18, no.3, p.p 389-407.
21. **Zhang, R., et al.**,(2019) Deep long short-term memory networks for nonlinear structural seismic response prediction Computers & Structures, 220, p.p 55-68.
22. **Wang, Z., T. Hong, and M.A. Piette**,(2020) Building thermal load prediction through shallow machine learning and deep learning Applied Energy, 263, p.p 114683.
23. **Lv, R., et al.**,(2022) Building thermal load prediction using deep learning method considering time-shifting correlation in feature variables Journal of Building Engineering, 61, p.p 105316.
24. **Raju, M.R., et al.**,(2023) Estimation of concrete materials uniaxial compressive strength using soft computing techniques Heliyon, 9, no.11.
25. **Deng, F., et al.**,(2018) Compressive strength prediction of recycled concrete based on deep learning Construction and Building Materials, 175, p.p 562-569.
26. **Ahmed, B., T. Park, and J.-S. Jeon**,(2023) Blast response and damage assessment of reinforced concrete slabs using convolutional neural networks International Journal of Damage Mechanics, p.p 10567895231204640.
27. Vafa, M., *Optimization of the Profiled Steel Sheeting Dry Board (PSSDB) floor system*, in *Civil Engineering* 2018, Universiti Kebangsaan Malaysia (UKM): Malaysia.
28. **Abueidda, D.W., S. Koric, and N.A. Sobh**, (2020) Topology optimization of 2D structures with nonlinearities using deep learning Computers & Structures, 237, p.p 106283.
29. **Almasri, W., et al.**(2021) Deep learning architecture for topological optimized mechanical design generation with complex shape criterion. in International Conference on Industrial, Engineering and Other Applications of Applied Intelligent Systems. Springer. of Conference.
30. **Long, T., Y. Zhang, and H. Zhang**,(2024) Generative deep learning for the inverse design of materials arXiv preprint arXiv:2409.19124.
31. **Ferreiro-Cabello, J., et al.**, (2018) Metamodel-based design optimization of structural one-way slabs based on deep learning neural networks to reduce environmental impact Engineering Structures, 155, p.p 91-101.
32. **Mai, H.T., et al.**,(2023) A novel deep unsupervised learning-based framework for optimization of truss structures Engineering with Computers, 39, no.4, p.p 2585-2608.
33. **Nandy, A., C. Duan, and H.J. Kulik**, (2022) Audacity of huge: overcoming challenges of data scarcity and data quality for machine learning in computational materials discovery Current Opinion in Chemical Engineering, 36, p.p 100778.
34. **Rather, I.H., S. Kumar, and A.H. Gandomi**, (2024) Breaking the data barrier: a review of deep learning techniques for democratizing AI with small datasets Artificial Intelligence Review, 57, no.9, p.p 226.
35. **Qamar, T. and N.Z. Bawany**,(2023) Understanding the black-box: towards interpretable and reliable deep learning models PeerJ Computer Science, 9, p.p e1629.
36. **Ying, X.**(2019) An overview of overfitting and its solutions. in Journal of physics: Conference series. IOP Publishing. of Conference.
37. **Giabbanelli, P.J.**,(2022) Hybrid Models That Combine Machine Learning and Simulations Computing in Science & Engineering, 24, no.5, p.p 72-76.

38. **Rane, N., et al.**,(2024) Artificial intelligence, machine learning, and deep learning for enabling smart and sustainable cities and infrastructure Artificial Intelligence and Industry in Society, 5, p.p 2-25.

СПИСОК ЛИТЕРАТУРЫ

1. **Ereiz, S., I. Duvnjak, and J.F. Jiménez-Alonso**.(2022) Review of finite element model updating methods for structural applications. in Structures. Elsevier. of Conference.
2. **Liu, W.K., S. Li, and H.S. Park**,(2022) Eighty years of the finite element method: Birth, evolution, and future Archives of Computational Methods in Engineering, 29, no.6, p.p 4431-4453.
3. **Wu, B., S. Luo, and C.S. Suh**,(2024) A Comprehensive Review of Propagation Models in Complex Networks: From Deterministic to Deep Learning Approaches arXiv preprint arXiv:2410.02118.
4. **Fujinuma, N., et al.**,(2022) Why big data and compute are not necessarily the path to big materials science Communications Materials, 3, no.1, p.p 59.
5. Ditlevsen, O. and H.O. Madsen, *Structural reliability methods*. Vol. 178. 1996: Wiley New York.
6. **Ghosn, M., et al.**,(2016) Reliability-based performance indicators for structural members Journal of Structural Engineering, 142, no.9, p.p F4016002.
7. **Etim, B., et al.**,(2024) Machine Learning-Based Modeling for Structural Engineering: A Comprehensive Survey and Applications Overview Buildings, 14, no.11, p.p 3515.
8. **Li, Q., et al.**,(2024) Classification and Application of Deep Learning in Construction Engineering and Management–A Systematic Literature Review and Future Innovations Case Studies in Construction Materials, p.p e04051.
9. **Sarker, I.H.**,(2021) Deep learning: a comprehensive overview on techniques, taxonomy, applications and research directions SN computer science, 2, no.6, p.p 420.
10. **McCulloch, W.S. and W. Pitts**,(1943) A logical calculus of the ideas immanent in nervous activity The bulletin of mathematical biophysics, 5, p.p 115-133.
11. **Rosenblatt, F.**,(1958) The perceptron: a probabilistic model for information storage and organization in the brain Psychological review, 65, no.6, p.p 386.
12. **Rumelhart, D.E., G.E. Hinton, and R.J. Williams**,(1986) Learning representations by back-propagating errors nature, 323, no.6088, p.p 533-536.
13. **Zhao, X., et al.**,(2024) A review of convolutional neural networks in computer vision Artificial Intelligence Review, 57, no.4, p.p 99.
14. Sundaray, S. *History of Deep Learning*. 2023; Available from: https://medium.com/@sreyan806/history-of-deep-learning-c176e2d3cddf.
15. **Akinosho, T.D., et al.**,(2020) Deep learning in the construction industry: A review of present status and future innovations Journal of Building Engineering, 32, p.p 101827.
16. **Khoa, N.L., et al.**,(2014) Robust dimensionality reduction and damage detection approaches in structural health monitoring Structural Health Monitoring, 13, no.4, p.p 406-417.
17. **Abbas, H.A., Z. Mohamed, and S.A. Kudus**,(2023) Deformation behaviour, crack initiation and crack damage of weathered composite sandstone-shale by using the ultrasonic wave and the acoustic emission under uniaxial compressive stress International Journal of Rock Mechanics and Mining Sciences, 170, p.p 105497.
18. **Dorafshan, S., R.J. Thomas, and M. Maguire**,(2018) Comparison of deep convolutional neural networks and edge detectors for image-based crack detection in

concrete Construction and Building Materials, 186, p.p 1031-1045.
19. **Gao, Y. and K.M. Mosalam**,(2018) Deep transfer learning for image-based structural damage recognition Computer-Aided Civil and Infrastructure Engineering, 33, no.9, p.p 748-768.
20. **Deng, Y., et al.**,(2024) Abnormal data recovery of structural health monitoring for ancient city wall using deep learning neural network International Journal of Architectural Heritage, 18, no.3, p.p 389-407.
21. **Zhang, R., et al.**,(2019) Deep long short-term memory networks for nonlinear structural seismic response prediction Computers & Structures, 220, p.p 55-68.
22. **Wang, Z., T. Hong, and M.A. Piette**,(2020) Building thermal load prediction through shallow machine learning and deep learning Applied Energy, 263, p.p 114683.
23. **Lv, R., et al.**,(2022) Building thermal load prediction using deep learning method considering time-shifting correlation in feature variables Journal of Building Engineering, 61, p.p 105316.
24. **Raju, M.R., et al.**,(2023) Estimation of concrete materials uniaxial compressive strength using soft computing techniques Heliyon, 9, no.11.
25. **Deng, F., et al.**,(2018) Compressive strength prediction of recycled concrete based on deep learning Construction and Building Materials, 175, p.p 562-569.
26. **Ahmed, B., T. Park, and J.-S. Jeon**,(2023) Blast response and damage assessment of reinforced concrete slabs using convolutional neural networks International Journal of Damage Mechanics, p.p 10567895231204640.
27. Vafa, M., *Optimization of the Profiled Steel Sheeting Dry Board (PSSDB) floor system*, in *Civil Engineering* 2018, Universiti Kebangsaan Malaysia (UKM): Malaysia.
28. **Abueidda, D.W., S. Koric, and N.A. Sobh**, (2020) Topology optimization of 2D structures with nonlinearities using deep learning Computers & Structures, 237, p.p 106283.
29. **Almasri, W., et al.**(2021) Deep learning architecture for topological optimized mechanical design generation with complex shape criterion. in International Conference on Industrial, Engineering and Other Applications of Applied Intelligent Systems. Springer. of Conference.
30. **Long, T., Y. Zhang, and H. Zhang**,(2024) Generative deep learning for the inverse design of materials arXiv preprint arXiv:2409.19124.
31. **Ferreiro-Cabello, J., et al.**, (2018) Metamodel-based design optimization of structural one-way slabs based on deep learning neural networks to reduce environmental impact Engineering Structures, 155, p.p 91-101.
32. **Mai, H.T., et al.**,(2023) A novel deep unsupervised learning-based framework for optimization of truss structures Engineering with Computers, 39, no.4, p.p 2585-2608.
33. **Nandy, A., C. Duan, and H.J. Kulik**, (2022) Audacity of huge: overcoming challenges of data scarcity and data quality for machine learning in computational materials discovery Current Opinion in Chemical Engineering, 36, p.p 100778.
34. **Rather, I.H., S. Kumar, and A.H. Gandomi**, (2024) Breaking the data barrier: a review of deep learning techniques for democratizing AI with small datasets Artificial Intelligence Review, 57, no.9, p.p 226.
35. **Qamar, T. and N.Z. Bawany**,(2023) Understanding the black-box: towards interpretable and reliable deep learning models PeerJ Computer Science, 9, p.p e1629.
36. **Ying, X.**(2019) An overview of overfitting and its solutions. in Journal of physics: Conference series. IOP Publishing. of Conference.
37. **Giabbanelli, P.J.**,(2022) Hybrid Models That Combine Machine Learning and Simulations Computing in Science & Engineering, 24, no.5, p.p 72-76.

38. **Rane, N., et al.**,(2024) Artificial intelligence, machine learning, and deep learning for enabling smart and sustainable cities and infrastructure Artificial Intelligence and Industry in Society, 5, p.p 2-25.

Manaf Raid Salman, M.Sc., Assistant Lecturer, Department of Building and Construction Techniques Engineering, Madenat Alelem University College (MAUC), 10006, Baghdad, Iraq. E-mail: munaf.raad@mauc.edu.iq

Marwan Al-Shaikhli, Ph.D., Lecturer, Department of Building and Construction Engineering Techniques, Middle Technical University, Baghdad, Iraq. E-mail: Marwan.samir@mauc.edu.iq. ORCID ID: 0000-0002-3497-0043

Hasan Ali Abbas, Ph.D., Lecturer, Department of Building and Construction Engineering Techniques, Middle Technical University, Baghdad, Iraq. ORCID ID: 0000-0001-8909-4346. E-mail: hassan_2007a@yahoo.com

Hussain Hamed Ahmad, Ph.D., Assistant Prof., Department of Building and Construction Techniques Engineering, Madenat Alelem University College (MAUC), 10006, Baghdad, Iraq. E-mail: hhahmad2006@mauc.edu.iq

Sakhiah binti Abdul Kudus, Ph.D., Lecturer, School of Civil Engineering, College of Engineering, Universiti Teknologi MARA, Shah Alam, 40450, Selangor, Malaysia; Institute for Infrastructure Engineering and Sustainable Management (IIESM), Universiti Teknologi MARA (UiTM), Shah Alam, Selangor, Malaysia. E-mail: sakhiah@uitm.edu.my

Манаф Раид Салман, магистр наук, ассистент преподавателя, кафедра строительства и инженерных технологий, Университетский колледж Маденат Алем (MAUC), 10006, Багдад, Ирак. E-mail: munaf.raad@mauc.edu.iq

Марван Аль-Шайхли, доктор философии, преподаватель кафедры инженерных технологий строительства зданий и сооружений, Средний технический университет, Багдад, Ирак. E-mail: Marwan.samir@mauc.edu.iq. ORCID ID: 0000-0002-3497-0043

Хасан Али Аббас, доктор философии, преподаватель, Кафедра технологии строительства зданий и сооружений, Средний технический университет, Багдад, Ирак. ORCID ID: 0000-0001-8909-4346. E-mail: hassan_2007a@yahoo.com

Хусейн Хамед Ахмад, доктор философии, доцент, кафедра инженерных технологий строительства зданий и сооружений, Университетский колледж Маденат Алем (MAUC), 10006, Багдад, Ирак. E-mail: hhahmad2006@mauc.edu.iq

Сахия бинти Абдул Кудус, доктор философии, преподаватель, Школа гражданского строительства, Инженерный колледж, Университет Технология МАРА, Шах Алам, 40450, Селангор, Малайзия; Институт инженерии инфраструктуры и устойчивого управления (IIESM), Университет Технологии МАРА (UiTM), Шах-Алам, Селангор, Малайзия. E-mail: sakhiah@uitm.edu.my

International Journal for Computational Civil and Structural Engineering, 21(1) 157–176 (2025)

DOI:10.22337/2587-9618-2025-21-1-157-176

CREEP EFFECT ON BEHAVIOR OF ECCENTRICALLY LOADED REINFORCED CONCRETE COLUMNS MADE OF HIGH-STRENGTH CONCRETE

Dmitry A. Strakhov, Aleksey O. Baranov

Peter the Great St. Petersburg Polytechnic University, St. Petersburg, RUSSIA

Abstract: The focus of the research is on eccentrically loaded reinforced concrete elements made of high-strength concrete with mineral additives such as fly ash and silica fume. The behavior of eccentrically loaded reinforced concrete elements was studied on a reinforced concrete column. At the age of 90 days the reinforced concrete column was subjected to a compressive force of 66 kN with an eccentricity of 12.5 cm. The loading duration was 245 days. During the tests, the average strains caused by eccentric loading, shrinkage, and creep concrete on the column were measured. In addition, the deflections and crack opening widths were measured. Experimental data were compared to theoretical data obtained using a stepwise version of the elastic solutions method (the stepwise method). In this method, the continuous change of stresses and strains of reinforced concrete elements under loading is replaced with a stepwise change. The considered loading time is divided into specific intervals (steps). Due to the creep of concrete, the conditions for compatibility of deformations are violated at the end of each step. The restoration of the conditions is carried out due to elastic deformations while simultaneously satisfying the conditions of static equivalence. The results of the comparison demonstrate that the stepwise meth-od adequately describes the changes of strains and deflections of eccentrically loaded reinforced concrete columns made from high-strength concrete over time. For the first time, the stepwise method was used to calculate the crack opening width. The calculation results are in good agreement with the experiments and show a significantly smaller increase in crack opening over time compared to that calculated according to Russian Building Codes.

Keywords: high-strength concrete, fly ash, silica fume, reinforced concrete, creep, eccentric loading, deflection, strain

НАПРЯЖЕННО-ДЕФОРМИРОВАННОЕ СОСТОЯНИЕ ВНЕЦЕНТРЕННО СЖАТЫХ ЭЛЕМЕНТОВ ИЗ ВЫСОКОПРОЧНОГО БЕТОНА ПРИ ДЛИТЕЛЬНОМ НАГРУЖЕНИИ

Д.А. Страхов, А.О. Баранов

Санкт-Петербургский политехнический университет Петра Великого, г. Санкт-Петербург, РОССИЯ

Аннотация: Объектом исследования в данной работе являются железобетонные внецентренно сжатые элементы из высокопрочного бетона с использованием минеральных добавок (зола уноса, микрокремнезем). Исследование напряжено-деформированного состояния внецентренно сжатых элементов выполнялось на примере железобетонной колонны. Колонна в возрасте бетона 90 суток подвергалась длительному нагружению в пружинной установке сжимающей силой, равной 66 кН, с эксцентриситетом 12.5 см. Продолжительность нагружения составила 245 суток. В период выдерживания под нагрузкой измерялись средние деформации в сжатой зоне, средние деформации сжатой и растянутой арматур, перемещения (прогибы) и ширина раскрытия трещин. Опытные данные сопоставлялись с теоретическими, полученными в соответствии с шаговым вариантом метода упругих решений (метод ступенек). В этом методе непрерывное изменение напряжений и деформаций в железобетонных элементах под нагрузкой заменяется на ступенчатое изменение. Весь исследуемый период времени разбивается на отдельные интервалы (шаги). В конце каждого интервала условия совместности деформаций нарушаются из-за ползучести бетона. Восстановление условий осуществляется за счет упругих деформаций при выполнении условий статического равновесия.

Результаты сравнения показали, что рассмотренный метод удовлетворительно описывает изменения деформаций и прогибов внецентренно сжатых колонн из высокопрочного бетона при длительном нагружении. Кроме того, впервые шаговый вариант метода упругих решений использовался для вычисления ширины раскрытия трещин.

Ключевые слова: высокопрочный бетон, зола уноса, микрокремнезем, железобетон, ползучесть, внецентренно сжатые элементы, прогибы, деформации

INTRODUCTION

The creep of high-strength concrete is of particular importance in the design of reinforced concrete structures of high-rise buildings [1,2]. The use of high-strength concrete allows for the creation of structural elements with smaller cross-sectional areas. This has a positive economic impact as it reduces the amount of material required to construct a structure and increases the usable space within the building. However, this leads to a reduction in their rigidity and an increase in the deflection. This trend is particularly noticeable during prolonged loading, when creep deformation occurs, which has not yet been fully studied for high-strength concrete.

It is known that the addition of mineral additives to concrete, such as fly ash [3–5], silica fume [6–8], ground granulated blast furnace slag [9,10], metakaolin [11,12], can reduce creep. However, a different outcome was achieved in the studies [7,13,14].

The article [7] reported that replacing 10% of the cement with silica fume (SF) increased the creep of concrete during the early stages of loading (0 to 60 days) compared to a control mixture (without silica fume). However, after 60 days of loading, the rate of creep deformation decreased, and after 360 days, the creep deformation of concrete with 10% SF was approximately 85% that of concrete without added SF.

In [14], creep deformation after 150 days of observation was 16%, 33%, and 55% higher for concrete mixes containing 20%, 40%, and 60% ground granulated blast furnace slag (GGBFS) respectively, compared to the control mix without slag. In the study [13], the deflections of reinforced concrete beams in the middle part of the span caused by concrete creep were 30%, 70%, and 100% higher for concrete mixes containing 20%, 40%, and 60% GGBFS, respectively, compared to beams made from control concrete mixes, after 150 days of observation. The values of the long-term load during the tests were 25% of the load values at the time of crack formation.

Steel and basalt fibers can reduce creep strains in concrete, both under compressive and tensile loads [15–17]. Reinforcing fibers with a low modulus of elasticity, such as polypropylene fibers or polyvinyl alcohol fibers, can increase creep in concrete [18,19].

The use of aggregates made from recycled materials [20–22] and industrial waste [23,24] as a substitute for natural aggregates increases the creep of concrete.

In work [25], short reinforced concrete columns were loaded with a long axial load. The creep coefficient of reinforced concrete columns decreased as the compressive strength of concrete and the reinforcement ratio increased. An expression is proposed to account for the effect of longitudinal reinforcement on the creep of concrete in reinforced concrete columns. In articles [26,27], it is noted that longitudinal reinforcement has a retarding effect on the creep of concrete.

In the study [28], reinforced concrete cantilever columns were subjected to long-term loading with a force applied at an eccentricity. Axial shortening and deflection increase over time due to creep and shrinkage of concrete. However, this increase decreased rapidly as time increased. Axial shortening and deflection of eccentrically loaded cantilever columns in experiments agreed well with the predictions based on existing models for concrete creep and shrinkage, as proposed in ACI 209R-92 [29].

In the article [30], the experimental values of the specific creep of high-strength concrete

were compared with the calculated values obtained using different theoretical models. The CEB-FIP [31], GL2000 [32], B4 [33], and ACI 209 [29] models significantly overestimate the specific creep strains compared to the experimental values. The B4 model satisfactorily predicts the creep of high-strength concrete. The articles [34,35] note that existing models for predicting creep in conventional concrete cannot be applied to high-strength concrete.

The analytical model presented in the article [36] takes into account the effects of creep, geometric nonlinearity, cracking, shrinkage, and aging in concrete. Numerical research has shown that creep in reinforced concrete columns leads to an increase in internal forces and deflections over time. The article [37] presents a new approach to calculating the behavior of reinforced concrete shells. The method is based on replacing the actual shell with an equivalent elastic shell.

In [38], reinforced concrete beams made from high-strength concrete were tested for pure bending. The experimental values of the destructive load were slightly higher than predicted by the calculations. Studies [39,40] contain the results of experimental studies of high-strength fiber reinforced concrete beams with round cross-sections under combined bending and torsion. Article [41] proposes expressions that make it possible to consider force and temperature effects jointly in calculations of reinforced concrete bending elements.

The article [42] compares the experimental data on strains and deflections of a reinforced concrete beam made of ordinary concrete under prolonged loading with calculated data obtained using the stepwise elastic solution method (the stepwise method). The results of the comparison showed good agreement.

The creep of high-strength concrete has not yet been fully studied. Additionally, the behavior of different types of reinforced concrete structures made from high-strength concrete under prolonged loads has not been adequately studied. The above-mentioned stepwise method can quite accurately describe the behavior of most types of rods reinforced concrete structures made of ordinary concrete. However, no studies have compared the calculated values with experimental data of reinforced concrete elements made from high-strength concrete under prolonged loading. Therefore, this study aimed to investigate the behavior of eccentrically loaded reinforced concrete elements made of high-strength concrete under prolonged loading and to compare experimental data with theoretical data obtained using a stepwise version of the elastic solutions method.

METHODS AND MATERIALS

Experimental research

The study of the behavior of eccentrically loaded compressed elements was conducted on a reinforced concrete column made from high-strength concrete with a cross-section of 15 x 10 cm and a height of 120 cm.

The following materials, with their respective characteristics, were used to create high-strength concrete: Portland cement CEM I 42.5 N from JSC "CEMROS" from the Peterburgcement plant in St. Petersburg, Russia; natural sand with a SiO_2 content of at least 81.4% and a fineness modulus of 2.3 produced by the "REMIKS" company in St. Petersburg, Russia; granite crushed stone (fractions from 5-10 mm and 10-20 mm), JSC "Semiozerskoe kar'eroupravlenie", quarry "Perovskij", Leningrad region, Russia; tap water; modifier for concrete "MB10-30S A I-2", LC "Predprijatie Master Beton", Moscow, Russia.

The modifier "MB10-30S A I-2" [43] was added to the concrete mix in an amount of 20% of the cement weight. The modifier contains the indicated ingredients in the following quantities (in % of total weight): silica fume 63%, fly ash 27%, and superplasticizer based on naphthalene-formaldehyde polycondensation 10%.

Table 1. Chemical composition of modifier "MB10-30S A I-2" and Portland cement CEM I 42.5N

Chemical composition by weight, %	Materials	
	Modifier	Cement
SiO_2	70.8	21.2
Al_2O_3	12.2	4.6
Fe_2O_3	2.1	4.2
CaO	0.7	62.9
MgO	0.6	1.7
SO_3	0.5	2.8
K_2O	0.6	0.6
Na_2O	0.4	0.3

Table 2. Mix proportions of concrete (kg/m³)

Ingredient	Proportions
Cement	490
Sand	790
Crushed stone	850
Water	170
Modifier	100
W/C	0.35
Density of compacted fresh concrete, kg/m³	2367

The modifier is a gray powdered material with a bulk density of 776 kg/m³. Table 1 shows the chemical composition of the modifier "MB10-30S A I-2" and Portland cement CEM I 42.5N. Table 2 provides basic information on the composition of high strength concrete.

The concrete mixture was poured into the moulds in a horizontal position. After that, it was compacted by tamping and vibration on a laboratory vibration table, model C279, manufactured by "Matest" in Italy (**Ошибка! Источник ссылки не найден.**). The specimens were kept in moulds for 24 hours at room temperature 20 ± 5°C. Afterward, they were demoulded and placed in a standard curing room with a controlled temperature of 20 ± 2°C and relative humidity of more than 95%. After 27 days, the specimens were removed from the standard curing room and stored in laboratory conditions at a temperature of 20 ± 2 ° C and an air humidity of 60 ± 5% until testing.

Figure 1. Production of concrete mix

The concrete mixture was prepared in a forced concrete mixer, model C162, manufactured by "Matest" in Italy (Fig. 1). The workability of the concrete mixture was determined using a concrete slump test in accordance with the Russian State Standard GOST 10181-2014 [44]. The slump of fresh concrete cone was 18 cm.

Figure 2. Compacting fresh concrete with tamper and vibration on laboratory vibrating table

Table 3. Mechanical properties of high-strength concrete at age 28 and 90 days

Mechanical properties	Age of concrete	
	28 days	90 days
Compressive strength, MPa	90.4	93.6
Splitting tensile strength, MPa	3.26	3.90
Prismatic compressive strength, MPa	68.2	70.5
Modulus of elasticity, GPa	36.5	38.3

Table 3 shows the mechanical properties of high-strength concrete at 28 and 90 days, as determined according to the Russian State Standards GOST 10180-2012 [45] and GOST 24452-80 [46]. The compressive strength and splitting tensile strength of concrete were determined on cubes with a side length of 10 cm. The values of strength obtained in tests were multiplied by coefficients of 0.95 and 0.88 respectively to calculate the compressive and splitting tensile strengths of concrete for cubes with a basic dimension of 15 cm in accordance with the Russian State Standard GOST 10180-2012 [45]. The prismatic compressive strength and modulus elasticity of concrete were determined on prism specimens with dimensions of 10x10x40 cm.

The characteristics of the mechanical properties of high-strength concrete were used as initial data to calculate the behavior of an eccentrically loaded reinforced concrete column using a stepwise version of the elastic solutions method.

Laminated plywood with a thickness of 18 mm was used to create the formwork for the reinforced concrete column. The formwork was previously lubricated with engine oil. Fig. 3 shows a general view of the formwork and reinforcement frame. There were two bars of tensile reinforcement with a diameter of 12 mm and two bars of compressed reinforcement installed with 6 mm in the column. The class of longitudinal steel reinforcement bars was A400, with a yield strength of 400 MPa. Steel bars with a diameter of 6 mm and class A 240 with a yield strength of 240 MPa were used as transverse reinforcement. The reinforcement bars in the frame were joined by welding.

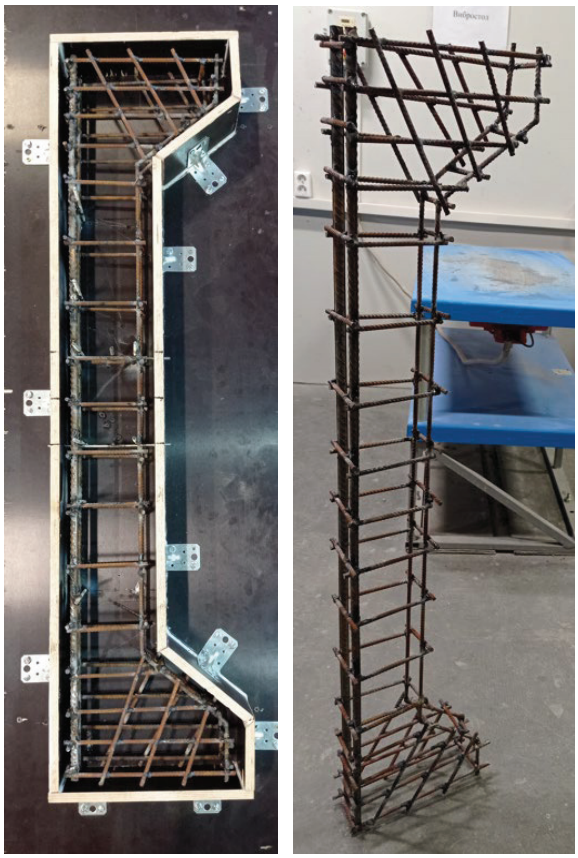

Figure 3. General view of formwork, reinforcement frame

After 24 hours of production, the column was removed from the formwork. Then it was placed in laboratory conditions with a temperature of 20 ± 5 °C and an air humidity of 60 ± 5% until testing.

Fig. 4 shows a general view of the reinforced concrete column in the testing setup. The age of the concrete at the time of testing was 90 days. A compressive force (P) of 66 kN was applied with an eccentricity (e) of 12.5 cm from the longitudinal axis of the element, as shown in Fig. 5. A hydraulic jack (LLC "Belak-Rus", in Russia) with a capacity of 50 tons was used to apply a compressive force to the column. The load on the column was applied in steps of 15% of the total load value (66 kN) during testing. At each stage, the load was maintained for 10 minutes.

Figure 4. General view of reinforced concrete column and testing setup

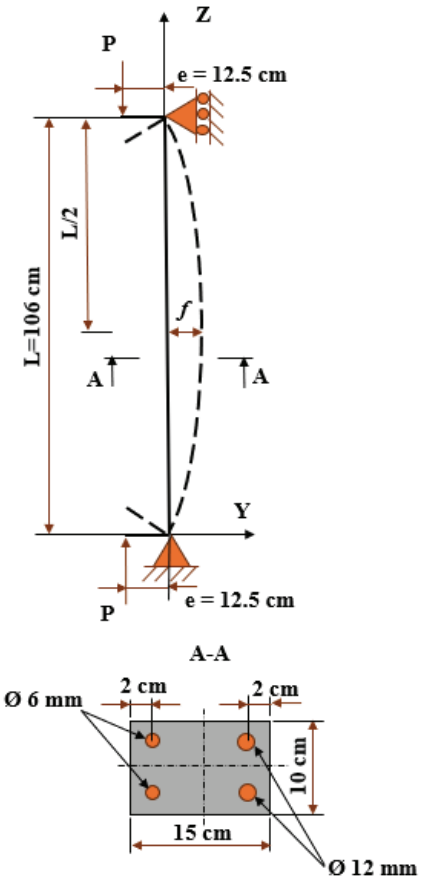

Figure 5. Testing scheme

The strains were measured in the middle of the column using dial indicators with a graduation of 0.001 mm (produced by "Micron" in the Czech Republic). The strains of the extreme fiber in the compression zone and the compressed reinforcement were measured using a base length of 15 cm. The strains of tensile reinforcement were measured using a base length of 35 cm.

The deflections of the reinforced concrete column were measured in the middle of the height using dial indicators with a graduation of 0.01 mm (produced by "Micron" in the Czech Republic). In addition, dial indicators were installed at the intended support points (70 mm from the column ends) to monitor possible movements of the test setup.

The width of the crack of the reinforced concrete column was measured using a microscope with the price of division of 0.02 mm.

Numerical method

To compare the experimental results with the calculated ones, a stepwise version of the method of elastic solutions was used, which is based on the following principles:

– the distribution of concrete and reinforcement strain along the depth of the element section is assumed according to a linear law (hypothesis of plain sections);

– the resistance of concrete in the tensile zone is not taken into account; all tensile force is taken by the reinforcement;

– the relationship between stresses and instantaneous strains is linear, i.e., stresses under instantaneous loading are determined as for an elastic body;

– increments of creep strain (over a short time interval) are determined without considering the change in stress over the same interval.

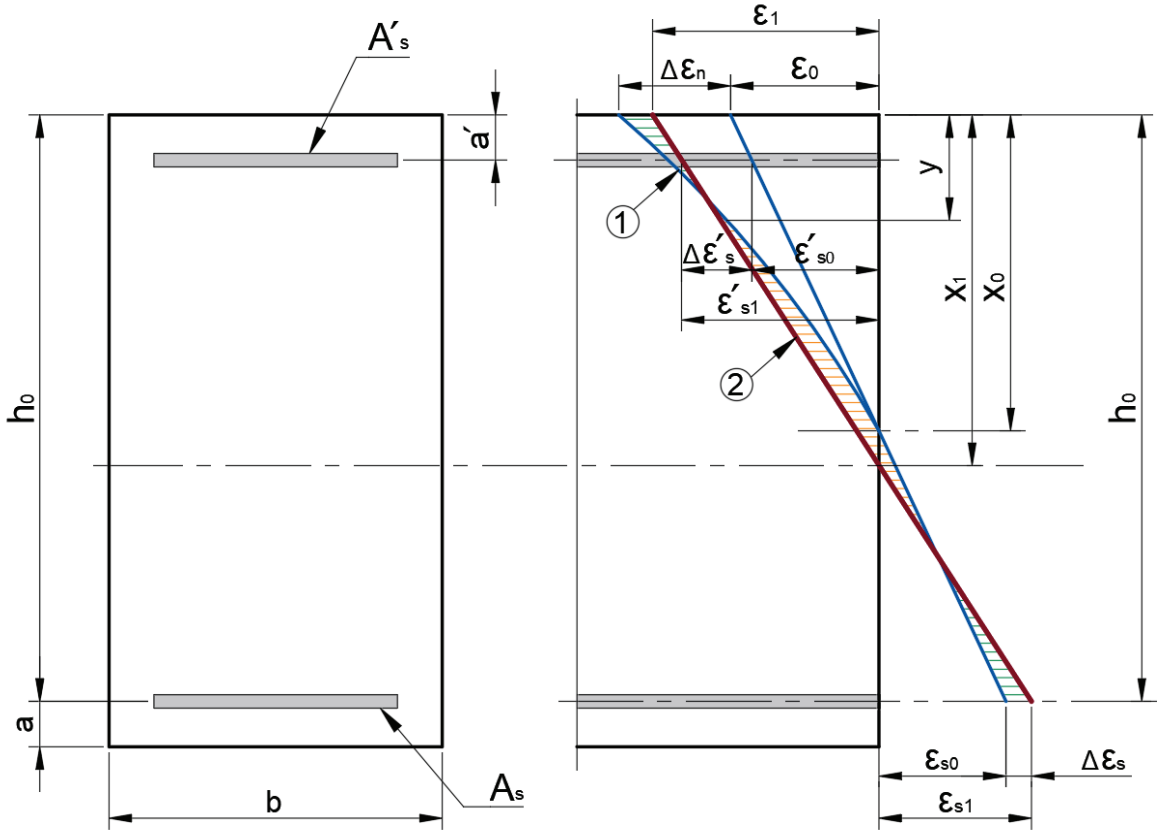

Figure 6. Transformation scheme ensuring implementation of condition of compatibility of deformations (hypothesis of plane sections)

The stepwise version of the method of elastic solutions (stepwise method) allows one to quite accurately take into consideration the main features of the strains of reinforced concrete elements under long-term load action [42]. The ability to consider the actual duration of each load component is a significant advantage of this method both when analyzing the stress-strain state and when calculating displacements (deflections) and crack opening width.

Calculation of the behavior using the stepwise method is carried out as follows.

1. The continuous change in stress and strain is replaced by a step change. The entire time period under study is divided into intervals Δt, that are quite small and not necessarily equal in size.

2. At the beginning of the first interval, stress and strain are determined by solving the corresponding elastic problem. The resistance of tensile concrete is not considered.

3. Creep strains during the interval are determined under the assumption of constant stresses during this interval.

4. Due to creep, the conditions for compatibility of deformations are violated. They can be satisfied only through instantaneous strains, for which it is necessary to apply such a stress state that would restore the conditions of compatibility while simultaneously satisfying the conditions of static equivalence.

Next, the following time interval is considered, taking into account stress changes during the previous interval.

For a reinforced element of arbitrary cross-section with a double reinforcement, the transformation that ensures the fulfillment of the condition of compatibility of deformations is presented in the diagram below (see Fig. 6).

During the interval Δt, creep strain develops. At each point of the compressed zone at the end of the interval, the strain is expressed

$$\varepsilon(y) = \varepsilon_0(y) + \Delta\varepsilon_n(y), \quad (1)$$

where y is the distance from the compressed edge of the section to the point in question; $\varepsilon(y)$ is the total strain at a point with a coordinate y until the condition of compatibility of strains is satisfied.

A total strain diagram is formed at the end of the interval, indicated by the number 1 (Fig. 6), which does not satisfy the condition of compatibility of deformations. The purpose of the transformation is to find a strain diagram (indicated by number 2 in Fig. 6) that would satisfy the compatibility condition (the hypothesis of plane sections), as well as the equilibrium conditions.

When implementing the stepwise method, the following notations are adopted: x_0 is the height of the compressed zone at the beginning of the interval Δt; x_1 is the depth of the compressed zone at the end of the interval after the transformation has been carried out; ε_0 is the shortening deformation in the upper fiber of the section at the beginning of the interval (at the beginning of the first interval it is elastic strain, while at the beginning of subsequent intervals it contains both elastic and creep strain); $\Delta\varepsilon_n$ is the increment of creep strain in the top fiber of the section during the interval Δt; ε_1 is the shortening deformation in the upper fiber of the section at the end of the interval Δt after the transformation has been carried out; ε_{s0} and ε'_{s0} are the strains of tensile and compressed reinforcement at the beginning of the interval Δt; $\Delta\varepsilon_{s0}$ and $\Delta\varepsilon'_{s0}$ is the increment in strains of tensile and compressed reinforcement during the interval; ε_{s1} and ε'_{s1} are the strains of tensile and compressed reinforcement at the end of the interval after the transformation.

To solve the problem, it is necessary to determine the following quantities $x_1, \varepsilon_1, \varepsilon_{s1}$ and ε'_{s1}. The first two can be found from two static equations, and the last two can be expressed through and from the condition of compatibility of deformations. Using the latter, we get:

$$\varepsilon_{s1} = \frac{\varepsilon_1(h_0 - x_1)}{x_1}; \quad (2)$$

$$\varepsilon'_{s1} = \frac{\varepsilon_1(x_1 - a')}{x_1}. \quad (3)$$

The equality to zero of the projections of the stress increments sum on the horizontal axis gives

$$\begin{aligned} &E_b\int_0^{x_1}\frac{\varepsilon_1(x_1-y)}{x_1}b(y)dy - \\ &-E_b\int_0^{x_0}\varepsilon(y)b(y)dy - E_b n A_s\Delta\varepsilon_s + \\ &+E_b n A'_s\Delta\varepsilon'_s = 0\ , \end{aligned} \quad (4)$$

where $n = \frac{E_s}{E_b}$,

E_b is the initial modulus of elasticity of concrete (under instantaneous loading);

E_s is the modulus of elasticity of the reinforcement.

Using the equality to zero of a sum of the static moments of stress increments relative to the axis of the tensile reinforcement, we have

$$\begin{aligned} &E_b\int_0^{x_1}\frac{\varepsilon_1(x_1-y)}{x_1}(h_0-y)b(y)dy - \\ &-E_b\int_0^{x_0}\varepsilon(y)(h_0-y)b(y)dy + \\ &+E_b n A'_s\Delta\varepsilon'_s(h_0-a') = 0. \end{aligned} \quad (5)$$

The universal form of writing equations (4) and (5) allows us to have the same forms for bending, eccentric compression, and eccentric tension.

Having determined the values of x_1 and ε_1, the stresses at any point in the compressed zone at the end of the interval can be obtained using the formula

$$\sigma(y,t) = \overline{\sigma}(y,t) + \\ + E_b\left[-\varepsilon(y,t) + \frac{\varepsilon_1(x_1 - y)}{x_1}\right], \quad (6)$$

where $\overline{\sigma}(y,t)$ are the stresses at the beginning of the interval; $\varepsilon(y,t)$ are total strain at the end of the interval before transformation.

Stresses in the tensile and compressed reinforcement in a section with a crack at the end of the interval are determined using the formulas:

$$\sigma_s = \varepsilon_{s1} E_b n; \quad (7)$$

$$\sigma'_s = \varepsilon'_{s1} E_b n. \quad (8)$$

With a time-varying external load, within the framework of this method, the continuous load change should be replaced by a step change, and individual steps should be applied "instantaneously" at the boundaries of time intervals. In this case, the resulting strains must satisfy the law of linear distribution over the depth of the section, and the stress state must satisfy the equilibrium conditions. The implementation of these conditions leads to the fact that with an instantaneous increase in load, the depth of the compressed zone decreases, and the neutral axis in terms of stress is located closer to the compressed face of the element than the neutral axis in terms of total strain. With an instantaneous decrease in load, the depth of the compressed zone of the section increases, and the neutral axes in terms of stress and total strain coincide.

The element deflections due to the total strains (instantaneous and creep strains) at the end of each time interval can be determined using the Mohr integral according to the formula

$$f = \sum_{j=1}^{n} \int_{a_j}^{b_j} \omega_j(t) \bar{M}_j dx, \quad (9)$$

where n is the number of integration sections along the length of the element; j is the integration section number; $\omega_j(t)$ is the average curvature of the axis of the corresponding section of the element; $\bar{M}_j$ is the bending moment in the section with the index j from a unit force applied at the point and in the direction of the determined displacement.

In accordance with the considered calculation method, at the end of each time interval, the total strains of the extreme compressed concrete fiber and tensile reinforcement) in the section with a crack are known. In calculations, cross sections in the middle of each section along the length should be considered; the corresponding curvatures can be calculated using the formula

$$\omega_j(t) = \frac{\varepsilon_{bj}\psi_b + \varepsilon_{sj}\psi_{sj}}{h_0}, \quad (10)$$

where ψ_b and ψ_{sj} are the coefficients of transition from strains in the section with a crack to average strains in the area between the cracks.

The coefficient ψ_b can be taken as equal to 0.9.

The coefficient ψ_{sj} is calculated using the formula

$$\psi_{sj} = 1 - 0.8\frac{\sigma_{s,crc(j)}}{\sigma_{s(j)}}, \quad (11)$$

where $\sigma_{s,crc(j)}$ is the stress in the longitudinal tensile reinforcement in the section with a crack immediately after the formation of normal cracks for the section with index j.

The stress $\sigma_{s,crc(j)}$ can be determined by using a first approximation under instantaneous loading (without taking creep into account), and the values in accordance with the considered step method are known at the end of each time interval.

The crack opening a_{crc} in the calculations below was determined in accordance with the methodology adopted in the current standards, with the exception of the strains of the tensile reinforcement and the area of the tensile zone of concrete, which are known directly from the calculation using the step method, and the duration coefficient for prolonged action of the load, since its actual duration was taken into consideration in the calculations.

RESULTS AND DISCUSSION

Fig. 7 shows the experimental data of the average concrete strains in the compressed zone and the average strains of tensile and compressive reinforcement in a reinforced concrete column. By average, we mean strains averaged over the length of the indicator base, including strains in cross sections with cracks. In addition, the strains obtained in the experiment are complete, i.e., elastic strains and strains caused by creep and shrinkage of concrete.

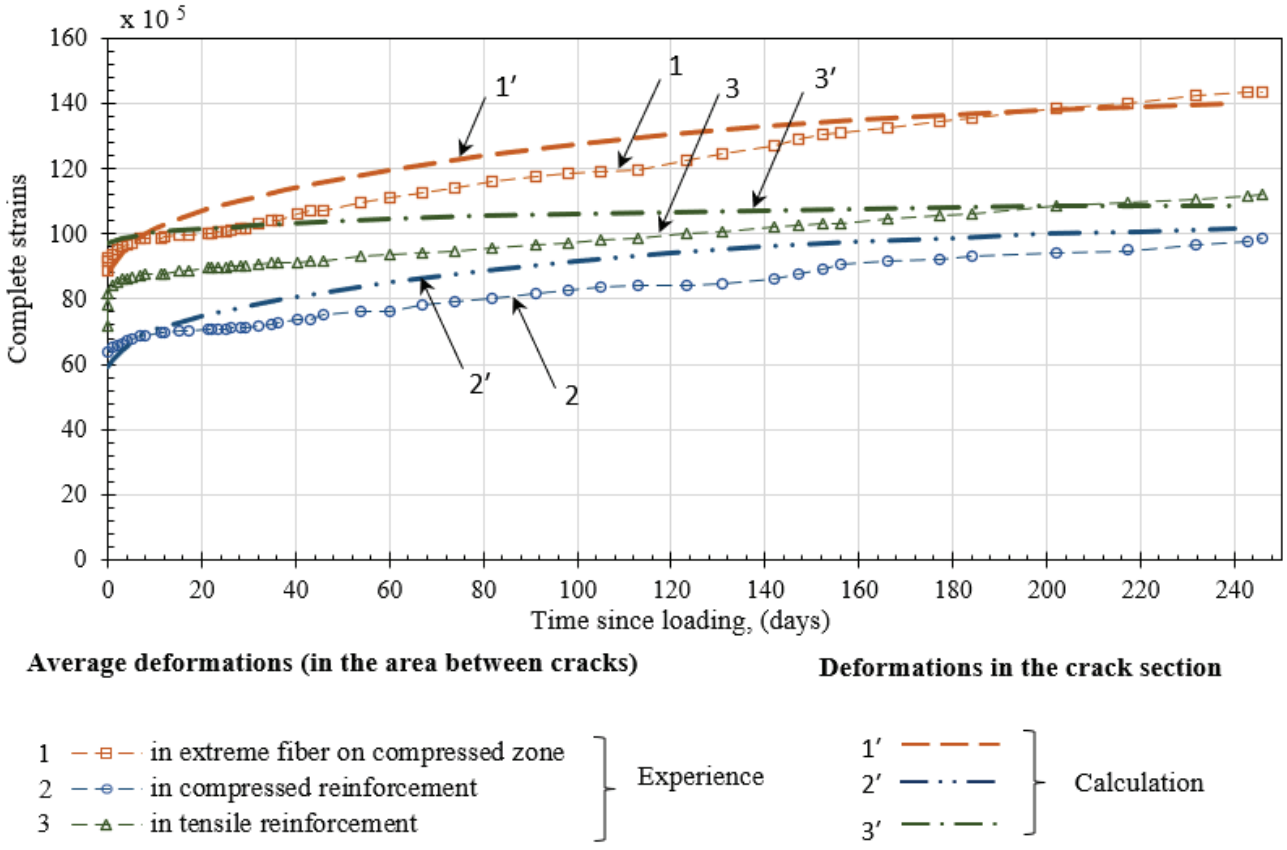

Figure 7. Comparison of experimental average strains and calculated strains in section with crack (using the stepwise method) for reinforced concrete column made of high-strength concrete

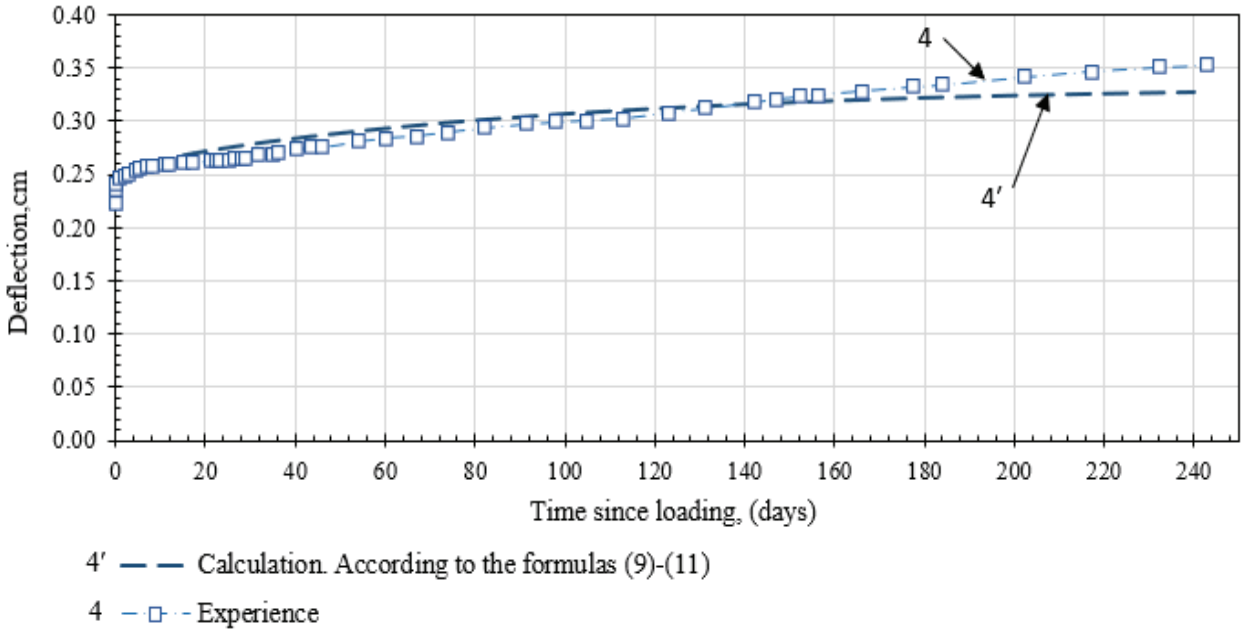

Figure 8. Comparison of experimental and calculated values of deflections in middle part of height of reinforced concrete column made of high strength concrete

It should be noted that Fig. 7 shows experimental strain values of compressed and tensile reinforcement according to direct readings of dial indicators installed on the side faces of the column (see Fig. 4). The readings of indicators installed on the end surface to determine the average strains of concrete in the compressed zone (the outermost fiber of the section) should be considered as overestimated by approximately 25% due to the indicator being located 30 mm from the outermost compressed fiber. Therefore, Fig. 7 (number 1) shows the results extrapolated from the experimental strain values of tensile and compressed reinforcement based on the law of plane sections.

For comparison, Fig. 7 shows the calculation results obtained using the stepwise method described above. The experimental strain characteristics and analytical dependencies approximating them, given in [47], were taken as the initial data for the calculation. As can be seen from examining the curves in the figure, there is satisfactory agreement between the results. The calculated values are slightly higher than the experimental ones, which can be partly explained by the fact that the averaged strains are recorded in the experiment, while in the calculations, the strains were obtained in the cross-section with a crack. It is also impossible to exclude some in-fluence of room temperature changes on the creep of concrete. The relatively low increase in strains over time is due to the low level of compressive stresses in concrete and, accordingly, the linear nature of creep.

Fig. 8 shows experimental data on changes in column deflections over time, measured in the middle part of its height. As previously noted for concrete and reinforcement average strains, the measured deflections are total, i.e., include both deflections from an external load with a conditionally instantaneous application and deflections caused by strains of shrinkage and creep of concrete.

In fig. 8, the experimental values of deflections are compared with the calculated ones, obtained using expressions (9) and (10) considering (11). It should be noted that, despite the fact that the calculations do not take into account concrete shrinkage strains, the results are quite satisfactory. Although these strains are small (when the concrete is 90 days old at the time of

loading), they could nevertheless affect the magnitude of the deflections.

The crack opening width in the tensile concrete zone, measured in the middle part of the column height, was 0.05 mm when the column was loaded with a full compressive force (66 kN) and a loading duration of approximately 1 hour. The moment of crack formation corresponded to the moment during the period of loading with a compressive force of up to 40 kN (the previous load level was 30 kN). During the observation period, the crack opening width increased slightly, and after 245 days of being under load, the crack width was approximately 0.06 mm.

Table 4 shows the values of the crack opening width a_{crc} and coefficient ψ_s depending on the duration of the load obtained by calculation. As can be seen, over a period of 245 days, the coefficient ψ_s values changed very little, and the crack opening width increased by approximately 12% and, at the same time, practically stabilized. In addition, calculated values of the crack opening width itself agree quite well with experimental data, considering measurement inaccuracies and the approximate nature of the calculation formulas. Russian Building Codes SP 63.13330.2018 [48] assumes an increase in opening under prolonged load action by 40% compared to short-term action. This difference is not surprising since the standards are focused on a certain margin of crack resistance and cannot consider the specifics of each structure.

Table 4. Values of crack opening width a_{crc} and coefficient ψ_s

Time since loading, (days)	Coefficient ψ_s	a_{crc}, mm	ε_s x 10^5
0	0.8748	0.0451	97.10
1	0.8758	0.0455	97.86
7	0.8783	0.0466	99.96
28	0.8813	0.0479	102.42
70	0.8843	0.0493	105.06
100	0.8857	0.0500	106.36
160	0.8873	0.0508	107.87
245	0.8883	0.0514	108.89

CONCLUSIONS

This study aimed to investigate the behavior of eccentrically loaded reinforced concrete elements made of high strength with mineral additives concrete under prolonged loading and to compare experimental data with theoretical data obtained using a stepwise version of the elastic solutions method. The behavior of eccentrically loaded reinforced concrete elements was studied on a reinforced concrete column. Comparison was made for stresses and strains in the compressed zone of concrete, as well as in tensile and compressed reinforcement. In addition, a comparison was made of the experimental and calculated values of the maximum deflections and crack opening width, which allows us to formulate the following conclusions.

1. The relatively low increase in strains over time is due to the low level of compressive stresses in concrete and, accordingly, the linear nature of creep. A certain excess of the calculated values of strains of the compressed zone of concrete, tensile, and compressed reinforcement over the corresponding experimental values was obtained. This excess is probably explained by the fact that in the experiments, the averaged strains were recorded along the length of the section between the cracks, while in the calculations, strains were obtained for the cross-section with a crack.
2. A comparison of the experimental values of deflections with the values obtained by calculation based on the deformed state in accordance with (9) - (11) showed quite satisfactory agreement with the results.
3. For the first time, using a stepwise version of the method of elastic solutions, the calculation of the opening width of normal cracks for elements made of high-strength concrete with a mineral additive was carried out according to formulas (2), (3), (6) - (11). The calculation results are in good agreement with the experiments and show a significantly smaller increase in crack opening over time compared to that calculated according to Russian Building Codes SP 63.13330.2018.

REFERENCES

1. **Mahmoud, K.A., Abdel Raheem, S.E. and Mansour, M.H.** (2024) Deformational Behavior of Eccentrically Loaded Slender RC Columns Subjected to Sustained Loads. Structures, Elsevier, 59, 105675. https://doi.org/10.1016/J.ISTRUC.2023.105675.
2. **Vasilenko, A., Chernogorsky, D., Strakhov, D. and Sinyakov, L.** (2019) High-Strength Concrete Eccentrically Compressed Elements. E3S Web of Conferences, EDP Sciences, 140. https://doi.org/10.1051/E3SCONF/201914002017.
3. **Harinadha Reddy, D. Ramaswamy, A**. (2018) Experimental and Numerical Modeling of Creep in Different Types of Concrete. Heliyon, Elsevier, 4, e00698. https://doi.org/10.1016/J.HELIYON.2018.E00698.
4. **Liu, Z., Takasu, K., Koyamada, H. and Suyama, H.** (2022) A Study on Engineering Properties and Environmental Impact of Sustainable Concrete with Fly Ash or GGBS. Construction and Building Materials, Elsevier, 316, 125776. https://doi.org/10.1016/J.CONBUILDMAT.2021.125776.
5. **Liu, Y., Li, Y., Mu, J., Li, H. and Shen, J.** (2023) Modeling and Analysis of Creep in Concrete Containing Supplementary Cementitious Materials Based on Machine Learning. Construction and Building Materials, Elsevier, 392, 131911. https://doi.org/10.1016/J.CONBUILDMAT.2023.131911.
6. **Gedam, B.A., Bhandari, N.M. and Upadhyay, A.** (2015) Influence of Supplementary Cementitious Materials on Shrinkage, Creep, and Durability of High-Performance Concrete. Journal of Materials in Civil Engineering, American Society of Civil Engineers, 28, 04015173. https://doi.org/10.1061/(ASCE)MT.1943-5533.0001462.
7. **Li, Y., Liu, Y., Li, Y., Li, Y. and Wang, R.** (2021) Evaluation of Concrete Creep Properties Based on Indentation Test and Multiscale Homogenization Method. Cement and Concrete Composites, Elsevier, 123, 104135. https://doi.org/10.1016/J.CEMCONCOMP.2021.104135.
8. **Korsun, V., Baranov, A., Khon, K. and Ha, Q.** (2021) The Influence of Temperature and Duration of Heating on the Properties of High-Strength Concrete Modified by Organo-Mineral Components. Lecture Notes in Civil Engineering, Springer Science and Business Media Deutschland GmbH, 150 LNCE, 515–524. https://doi.org/10.1007/978-3-030-72404-7_50.
9. **Cao, J., Zeng, P., Liu, T. and Tu, B.** (2023) Influence of Mineral Powder Content and Loading Age on Creep Behavior of Concrete Members under Axial Compression. Results in Engineering, Elsevier, 19, 101304. https://doi.org/10.1016/J.RINENG.2023.101304.
10. **Tangadagi, R.B., M, M., Seth, D. and S, P.** (2021) Role of Mineral Admixtures on Strength and Durability of High Strength Self Compacting Concrete: An Experimental Study. Materialia, Elsevier, 18, 101144. https://doi.org/10.1016/J.MTLA.2021.101144.
11. **He, Z., Qian, C., Li, L. and Du, S.** (2016) Creep Analysis of Concrete with Different Mineral Admixtures. Materials Express, American Scientific Publishers, 6, 328–336. https://doi.org/10.1166/MEX.2016.1319.
12. **Usanova, K., Barabanshchikov, Y.G., Krasova, A. V., Akimov, S. V. and Belyaeva, S. V.** (2021) Plastic Shrinkage of Concrete Modified by Metakaolin. Magazine of Civil Engineering, St. Petersburg Polytechnic University of Peter the Great, 103, 10314–10314. https://doi.org/10.34910/MCE.103.14.
13. **Faridmehr, I., Shariq, M., Plevris, V. and Aalimahmoody, N.** (2022) Novel Hybrid Informational Model for Predicting the Creep and Shrinkage Deflection of Reinforced Concrete Beams Containing GGBFS. Neural Computing and Applications, Springer Science and

Business Media Deutschland GmbH, 34, 13107–13123. https://doi.org/10.1007/S00521-022-07150-3/FIGURES/10.

14. **Shariq, M., Prasad, J. and Abbas, H.** (2016) Creep and Drying Shrinkage of Concrete Containing GGBFS. Cement and Concrete Composites, Elsevier, 68, 35–45. https://doi.org/10.1016/J.CEMCONCOMP.2016.02.004.
15. **Pena, P.V.C., Ferreira, R.A. dos R., Santos, A.C. dos and Oliveira, A.M. de.** (2023) Analysis of the Compressive Creep Strain of the Concretes with Steel Fibers: A Holistic View in Micro and Macro Scale. Journal of Building Engineering, Elsevier, 71, 106436. https://doi.org/10.1016/J.JOBE.2023.106436.
16. **Chen, P., Zheng, W., Wang, Y. and Chang, W.** (2018) Analysis and Modelling of Shrinkage and Creep of Reactive Powder Concrete. Applied Sciences (Switzerland), MDPI AG, 8. https://doi.org/10.3390/APP8050732.
17. **González, L., Gaute, Á., Rico, J. and Thomas, C.** (2021) Effect of Fibre Reinforcement on Creep in Early Age Concrete. Applied Sciences 2022, Vol. 12, Page 257, Multidisciplinary Digital Publishing Institute, 12, 257. https://doi.org/10.3390/APP12010257
18. **Zhao, Q., Yu, J., Geng, G., Jiang, J. and Liu, X.** (2016) Effect of Fiber Types on Creep Behavior of Concrete. Construction and Building Materials, Elsevier, 105, 416–422. https://doi.org/10.1016/J.CONBUILDMAT.2015.12.149.
19. **Kleshchevnikova, V., Belyaeva, S. and Baranov, A.** (2021) Optimization of Mix Designs and Experimental Study of the Properties of Concrete Mix for 3D Printing. Lecture Notes in Civil Engineering, Springer Science and Business Media Deutschland GmbH, 150 LNCE, 151–160. https://doi.org/10.1007/978-3-030-72404-7_16.
20. **Nakararoj, N., Nhat Ho Tran, T., Sukontasukkul, P., Attachaiyawuth, A., Tangchirapat, W., Chee Ban, C., Rattanachu, P. and Jaturapitakkul, C.** (2022) Effects of High-Volume Bottom Ash on Strength, Shrinkage, and Creep of High-Strength Recycled Concrete Aggregate. Construction and Building Materials, Elsevier, 356, 129233. https://doi.org/10.1016/J.CONBUILDMAT.2022.129233.
21. **He, Z.** (2023) Creep and Shrinkage Performance of High-Performance Recycled Aggregate Concrete. Multi-functional Concrete with Recycled Aggregates, Woodhead Publishing, 145–177. https://doi.org/10.1016/B978-0-323-89838-6.00012-8.
22. **Bompa, D. V. and Elghazouli, A.Y.** (2019) Creep Properties of Recycled Tyre Rubber Concrete. Construction and Building Materials, Elsevier, 209, 126–134. https://doi.org/10.1016/J.CONBUILDMAT.2019.03.127.
23. **Usanova, K., Vatin, N. and Barabanshchikov, Y.** (2024) Properties of Cold-Bonded Lightweight Aggregate Based on High Calcium Fly Ash. Lecture Notes in Networks and Systems, Springer, Cham, 733, 187–197. https://doi.org/10.1007/978-3-031-37978-9_18.
24. **Gesoğlu, M., Özturan, T. and Güneyisi, E.** (2006) Effects of Cold-Bonded Fly Ash Aggregate Properties on the Shrinkage Cracking of Lightweight Concretes. Cement and Concrete Composites, Elsevier, 28, 598–605. https://doi.org/10.1016/J.CEMCONCOMP.2006.04.002.
25. **Chen, P., Zhang, G., Cao, S., Lv, X. and Shen, B.** (2023) Creep and Post-Creep Mechanical Properties of Reinforced Concrete Columns. Journal of Building Engineering, Elsevier, 63, 105521. https://doi.org/10.1016/J.JOBE.2022.105521.
26. **Cao, G., Yang, L., Zhang, K. and Peng, X.** (2017) Analysis of Reinforcement

Influence on Concrete Creep. Zhongnan Daxue Xuebao (Ziran Kexue Ban)/Journal of Central South University (Science and Technology), Central South University of Technology, 48, 506–511. https://doi.org/10.11817/J.ISSN.1672-7207.2017.02.031.

27. **Shariff, M.N., Menon, D. and Saravanan, U.** (2023) Experimental and Analytical Studies on Shrinkage and Creep Behavior of RC Walls and Prisms. Structural Concrete, John Wiley and Sons Inc, 24, 6157–6169. https://doi.org/10.1002/SUCO.202300170.
28. **Eom, T.S., Kim, C.S., Zhang, X. and Kim, J.Y.** (2018) Time-Dependent Deformations of Eccentrically Loaded Reinforced Concrete Columns. International Journal of Concrete Structures and Materials, Korea Concrete Institute, 12, 1–12. https://doi.org/10.1186/S40069-018-0312-1/FIGURES/11.
29. **Rhodes, J.A., Carreira, D.J., Bazant, Z.P., Beaudoin, J.I., Branson, D.E., Gamble, B.R., Gcymaycr, H.G., Goyal, B.B., Hope, B.B., Keeton, J.R., Kesler, C.E., Lorman, W.R., Means, J.A., Meyers, B.L., Hills, R.H., Nasser, K.H., Neville, A.H., Roll, F., Timusk, J. and Hard, M.A.** (1982) Prediction of Creep, Shrinkage, and Temperature Effects in Concrete Structures: Reported by ACI Committee 209. American Concrete Institute, ACI Special Publication, American Concrete Institute, 193–300.
30. **Zhou, Y., Chen, W. and Yan, P.** (2022) Measurement and Modeling of Creep Property of High-Strength Concrete Considering Stress Relaxation Effect. Journal of Building Engineering, Elsevier, 56, 104726. https://doi.org/10.1016/J.JOBE.2022.104726.
31. **Wicke, M., Siviero, E., Hilsdorf, H., Müller, H.S., Walraven, J. and Foraboschi, P.** (1999) Structural Concrete. Textbook on Behaviour, Design and Performance. Updated Knowledge of the CEB/FIP Model Code 1990. Volume 1: Introduction-Design Process-Materials. Bulletin-FIB, 1.
32. **Gardner, N.J. and Lockman, M.J.** (2001) Design Provisions for Drying Shrinkage and Creep of Normal-Strength Concrete. Materials, 98, 159–167. https://doi.org/10.14359/10199.
33. **Bažant, Z., Jirasek, M.** (2015) RILEM Draft Recommendation: TC-242-MDC Multi-Decade Creep and Shrinkage of Concrete: Material Model and Structural Analysis. Model B4 for Creep, Drying., CarolMaterials and structures. https://doi.org/10.1617/s11527-014-0485-2.
34. **Huang, Y., Wang, J., Wei, Q., Shang, H. and Liu, X.** (2023) Creep Behaviour of Ultra-High-Performance Concrete (UHPC): A Review. Journal of Building Engineering, Elsevier, 69, 106187. https://doi.org/10.1016/J.JOBE.2023.106187.
35. **Liu, Y., Wang, L., Wei, Y., Sun, C. and Xu, Y.** (2024) Current Research Status of UHPC Creep Properties and the Corresponding Applications – A Review. Construction and Building Materials, Elsevier, 416, 135120. https://doi.org/10.1016/J.CONBUILDMAT.2024.135120.
36. **Hamed, E. and Lai, C.** (2016) Geometrically and Materially Nonlinear Creep Behaviour of Reinforced Concrete Columns. Structures, Elsevier, 5, 1–12. https://doi.org/10.1016/J.ISTRUC.2015.07.001.
37. **Mussabayev, T.T., Nuguzhinov, Z.S., Nemova, D., Kayupov, T., Tolkynbaev, T.A., Akmakanova, A.Z. and Khafizova, G.S.** (2023) Creep of Concrete in Shell Structures: Nonlinear Theory. Materials 2023, Vol. 16, Page 5587, Multidisciplinary Digital Publishing Institute, 16, 5587. https://doi.org/10.3390/MA16165587
38. **Travush, V.I., Kaprielov, S.S., Konin, D. V., Krylov, A.S. and Chilin, I.A.** (2017) Experimental Study of Composite Structures for Bending Elements. Building

and Reconstruction, 63–71. https://doi.org/ZHHHJJ.

39. **Travush, V.I., Karpenko, N.I., Kolchunov, V.I., Kaprielov, S.S., Demyanov, A.I., Bulkin, S.A. and Moskovtseva, V.S.** (2020) Results of Experimental Studies of High-Strength Fiber Reinforced Concrete Beams with Round Cross-Sections under Combined Bending and Torsion. Structural Mechanics of Engineering Constructions and Buildings, Peoples' Friendship University of Russia, 16, 290–297. https://doi.org/10.22363/1815-5235-2020-16-4-290-297.
40. **Travush, V.I., Karpenko, N.I., Kolchunov, V.I., Kaprielov, S.S., Dem'yanov, A.I. and Konorev, A. V.** (2019) Main Results of Experimental Studies of Reinforced Concrete Structures of High-Strength Concrete B100 Round and Circular Cross Sections in Torsion with Bending. Structural Mechanics of Engineering Constructions and Buildings, Peoples' Friendship University of Russia, 15, 51–61. https://doi.org/10.22363/1815-5235-2019-15-1-51-61.
41. **Korsun, V.I., Morozov, V.I., Tamrazyan, A.G. and Alekseytsev, A. V.** (2023) Nonlinear Deformation Model for Analysis of Temperature Effects on Reinforced Concrete Beam Elements. Buildings 2023, Vol. 13, Page 2734, Multidisciplinary Digital Publishing Institute, 13, 2734. https://doi.org/10.3390/BUILDINGS13112734.
42. **Vorobeva, A., Strakhov, D. and Semenov, K.** (2021) Calculation of Reinforced Concrete Elements Taking into Account Nonlinear Creep at Different Loading Mode. Lecture Notes in Civil Engineering, Springer Science and Business Media Deutschland GmbH, 150 LNCE, 73–84. https://doi.org/10.1007/978-3-030-72404-7_8/TABLES/5.
43. **Bezgodov, I., Kaprielov, S. and Sheynfeld, A.** (2023) Relationship Between Strength and Deformation Characteristics of High-Strength Self-Compacting Concrete. Lecture Notes in Civil Engineering, Springer Science and Business Media Deutschland GmbH, 282, 459–468. https://doi.org/10.1007/978-3-031-10853-2_43/FIGURES/4.
44. International Technical Standard GOST 10181-2014. Concrete Mixtures. Methods of Testing. Russian Federation. https://docs.cntd.ru/document/1200115733?section=text.
45. International Technical Standard GOST 10180-2012. Concretes. Methods for Strength Determination Using Reference Specimens. Russian Federation. https://docs.cntd.ru/document/1200100908.
46. International Technical Standard GOST 24452-80 Concretes. Methods of Prismatic, Compressive Strength, Modulus of Elasticity and Poisson's Ratio Determination. Russian Federation. https://kodeks.library.spbstu.ru/docs/
47. **Baranov, A.O. and Strakhov, D.A.** (2023) Creep of High Strength Concrete at Elevated Temperatures. Construction of Unique Buildings and Structures, 108, 10704–10704. https://doi.org/10.4123/CUBS.107.4.
48. Russian Building Codes SP 63.13330.2018. Concrete and Reinforced Concrete Structures. General Provisions. Russian Federation. https://docs.cntd.ru/document/554403082.

СПИСОК ЛИТЕРАТУРЫ

1. **Mahmoud, K.A., Abdel Raheem, S.E. and Mansour, M.H.** (2024) Deformational Behavior of Eccentrically Loaded Slender RC Columns Subjected to Sustained Loads. Structures, Elsevier, 59, 105675. https://doi.org/10.1016/J.ISTRUC.2023.105675.
2. **Vasilenko, A., Chernogorsky, D., Strakhov, D. and Sinyakov, L.** (2019) High-Strength Concrete Eccentrically Compressed Elements. E3S Web of

Conferences, EDP Sciences, 140. https://doi.org/10.1051/E3SCONF/201914002017.

3. **Harinadha Reddy, D. Ramaswamy, A**. (2018) Experimental and Numerical Modeling of Creep in Different Types of Concrete. Heliyon, Elsevier, 4, e00698. https://doi.org/10.1016/J.HELIYON.2018.E00698.
4. **Liu, Z., Takasu, K., Koyamada, H. and Suyama, H.** (2022) A Study on Engineering Properties and Environmental Impact of Sustainable Concrete with Fly Ash or GGBS. Construction and Building Materials, Elsevier, 316, 125776. https://doi.org/10.1016/J.CONBUILDMAT.2021.125776.
5. **Liu, Y., Li, Y., Mu, J., Li, H. and Shen, J.** (2023) Modeling and Analysis of Creep in Concrete Containing Supplementary Cementitious Materials Based on Machine Learning. Construction and Building Materials, Elsevier, 392, 131911. https://doi.org/10.1016/J.CONBUILDMAT.2023.131911.
6. **Gedam, B.A., Bhandari, N.M. and Upadhyay, A.** (2015) Influence of Supplementary Cementitious Materials on Shrinkage, Creep, and Durability of High-Performance Concrete. Journal of Materials in Civil Engineering, American Society of Civil Engineers, 28, 04015173. https://doi.org/10.1061/(ASCE)MT.1943-5533.0001462.
7. **Li, Y., Liu, Y., Li, Y., Li, Y. and Wang, R.** (2021) Evaluation of Concrete Creep Properties Based on Indentation Test and Multiscale Homogenization Method. Cement and Concrete Composites, Elsevier, 123, 104135. https://doi.org/10.1016/J.CEMCONCOMP.2021.104135.
8. **Korsun, V., Baranov, A., Khon, K. and Ha, Q.** (2021) The Influence of Temperature and Duration of Heating on the Properties of High-Strength Concrete Modified by Organo-Mineral Components. Lecture Notes in Civil Engineering, Springer Science and Business Media Deutschland GmbH, 150 LNCE, 515–524. https://doi.org/10.1007/978-3-030-72404-7_50.
9. **Cao, J., Zeng, P., Liu, T. and Tu, B.** (2023) Influence of Mineral Powder Content and Loading Age on Creep Behavior of Concrete Members under Axial Compression. Results in Engineering, Elsevier, 19, 101304. https://doi.org/10.1016/J.RINENG.2023.101304.
10. **Tangadagi, R.B., M, M., Seth, D. and S, P.** (2021) Role of Mineral Admixtures on Strength and Durability of High Strength Self Compacting Concrete: An Experimental Study. Materialia, Elsevier, 18, 101144. https://doi.org/10.1016/J.MTLA.2021.101144.
11. **He, Z., Qian, C., Li, L. and Du, S.** (2016) Creep Analysis of Concrete with Different Mineral Admixtures. Materials Express, American Scientific Publishers, 6, 328–336. https://doi.org/10.1166/MEX.2016.1319.
12. **Usanova, K., Barabanshchikov, Y.G., Krasova, A. V., Akimov, S. V. and Belyaeva, S. V.** (2021) Plastic Shrinkage of Concrete Modified by Metakaolin. Magazine of Civil Engineering, St. Petersburg Polytechnic University of Peter the Great, 103, 10314–10314. https://doi.org/10.34910/MCE.103.14.
13. **Faridmehr, I., Shariq, M., Plevris, V. and Aalimahmoody, N.** (2022) Novel Hybrid Informational Model for Predicting the Creep and Shrinkage Deflection of Reinforced Concrete Beams Containing GGBFS. Neural Computing and Applications, Springer Science and Business Media Deutschland GmbH, 34, 13107–13123. https://doi.org/10.1007/S00521-022-07150-3/FIGURES/10.
14. **Shariq, M., Prasad, J. and Abbas, H.** (2016) Creep and Drying Shrinkage of Concrete Containing GGBFS. Cement and Concrete Composites, Elsevier, 68, 35–45. https://doi.org/10.1016/J.CEMCONCOMP.2016.02.004.

15. **Pena, P.V.C., Ferreira, R.A. dos R., Santos, A.C. dos and Oliveira, A.M. de.** (2023) Analysis of the Compressive Creep Strain of the Concretes with Steel Fibers: A Holistic View in Micro and Macro Scale. Journal of Building Engineering, Elsevier, 71, 106436. https://doi.org/10.1016/J.JOBE.2023.106436.
16. **Chen, P., Zheng, W., Wang, Y. and Chang, W.** (2018) Analysis and Modelling of Shrinkage and Creep of Reactive Powder Concrete. Applied Sciences (Switzerland), MDPI AG, 8. https://doi.org/10.3390/APP8050732.
17. **González, L., Gaute, Á., Rico, J. and Thomas, C.** (2021) Effect of Fibre Reinforcement on Creep in Early Age Concrete. Applied Sciences 2022, Vol. 12, Page 257, Multidisciplinary Digital Publishing Institute, 12, 257. https://doi.org/10.3390/APP12010257
18. **Zhao, Q., Yu, J., Geng, G., Jiang, J. and Liu, X.** (2016) Effect of Fiber Types on Creep Behavior of Concrete. Construction and Building Materials, Elsevier, 105, 416–422. https://doi.org/10.1016/J.CONBUILDMAT.2015.12.149.
19. **Kleshchevnikova, V., Belyaeva, S. and Baranov, A.** (2021) Optimization of Mix Designs and Experimental Study of the Properties of Concrete Mix for 3D Printing. Lecture Notes in Civil Engineering, Springer Science and Business Media Deutschland GmbH, 150 LNCE, 151–160. https://doi.org/10.1007/978-3-030-72404-7_16.
20. **Nakararoj, N., Nhat Ho Tran, T., Sukontasukkul, P., Attachaiyawuth, A., Tangchirapat, W., Chee Ban, C., Rattanachu, P. and Jaturapitakkul, C.** (2022) Effects of High-Volume Bottom Ash on Strength, Shrinkage, and Creep of High-Strength Recycled Concrete Aggregate. Construction and Building Materials, Elsevier, 356, 129233. https://doi.org/10.1016/J.CONBUILDMAT.2022.129233.
21. **He, Z.** (2023) Creep and Shrinkage Performance of High-Performance Recycled Aggregate Concrete. Multi-functional Concrete with Recycled Aggregates, Woodhead Publishing, 145–177. https://doi.org/10.1016/B978-0-323-89838-6.00012-8.
22. **Bompa, D. V. and Elghazouli, A.Y.** (2019) Creep Properties of Recycled Tyre Rubber Concrete. Construction and Building Materials, Elsevier, 209, 126–134. https://doi.org/10.1016/J.CONBUILDMAT.2019.03.127.
23. **Usanova, K., Vatin, N. and Barabanshchikov, Y.** (2024) Properties of Cold-Bonded Lightweight Aggregate Based on High Calcium Fly Ash. Lecture Notes in Networks and Systems, Springer, Cham, 733, 187–197. https://doi.org/10.1007/978-3-031-37978-9_18.
24. **Gesoğlu, M., Özturan, T. and Güneyisi, E.** (2006) Effects of Cold-Bonded Fly Ash Aggregate Properties on the Shrinkage Cracking of Lightweight Concretes. Cement and Concrete Composites, Elsevier, 28, 598–605. https://doi.org/10.1016/J.CEMCONCOMP.2006.04.002.
25. **Chen, P., Zhang, G., Cao, S., Lv, X. and Shen, B.** (2023) Creep and Post-Creep Mechanical Properties of Reinforced Concrete Columns. Journal of Building Engineering, Elsevier, 63, 105521. https://doi.org/10.1016/J.JOBE.2022.105521.
26. **Cao, G., Yang, L., Zhang, K. and Peng, X.** (2017) Analysis of Reinforcement Influence on Concrete Creep. Zhongnan Daxue Xuebao (Ziran Kexue Ban)/Journal of Central South University (Science and Technology), Central South University of Technology, 48, 506–511. https://doi.org/10.11817/J.ISSN.1672-7207.2017.02.031.
27. **Shariff, M.N., Menon, D. and Saravanan, U.** (2023) Experimental and Analytical

Studies on Shrinkage and Creep Behavior of RC Walls and Prisms. Structural Concrete, John Wiley and Sons Inc, 24, 6157–6169. https://doi.org/10.1002/SUCO.202300170.

28. **Eom, T.S., Kim, C.S., Zhang, X. and Kim, J.Y.** (2018) Time-Dependent Deformations of Eccentrically Loaded Reinforced Concrete Columns. International Journal of Concrete Structures and Materials, Korea Concrete Institute, 12, 1–12. https://doi.org/10.1186/S40069-018-0312-1/FIGURES/11.
29. **Rhodes, J.A., Carreira, D.J., Bazant, Z.P., Beaudoin, J.I., Branson, D.E., Gamble, B.R., Gcymaycr, H.G., Goyal, B.B., Hope, B.B., Keeton, J.R., Kesler, C.E., Lorman, W.R., Means, J.A., Meyers, B.L., Hills, R.H., Nasser, K.H., Neville, A.H., Roll, F., Timusk, J. and Hard, M.A.** (1982) Prediction of Creep, Shrinkage, and Temperature Effects in Concrete Structures: Reported by ACI Committee 209. American Concrete Institute, ACI Special Publication, American Concrete Institute, 193–300.
30. **Zhou, Y., Chen, W. and Yan, P.** (2022) Measurement and Modeling of Creep Property of High-Strength Concrete Considering Stress Relaxation Effect. Journal of Building Engineering, Elsevier, 56, 104726. https://doi.org/10.1016/J.JOBE.2022.104726.
31. **Wicke, M., Siviero, E., Hilsdorf, H., Müller, H.S., Walraven, J. and Foraboschi, P.** (1999) Structural Concrete. Textbook on Behaviour, Design and Performance. Updated Knowledge of the CEB/FIP Model Code 1990. Volume 1: Introduction-Design Process-Materials. Bulletin-FIB, 1.
32. **Gardner, N.J. and Lockman, M.J.** (2001) Design Provisions for Drying Shrinkage and Creep of Normal-Strength Concrete. Materials, 98, 159–167. https://doi.org/10.14359/10199.
33. **Bažant, Z., Jirasek, M.** (2015) RILEM Draft Recommendation: TC-242-MDC Multi-Decade Creep and Shrinkage of Concrete: Material Model and Structural Analysis. Model B4 for Creep, Drying., CarolMaterials and structures. https://doi.org/10.1617/s11527-014-0485-2.
34. **Huang, Y., Wang, J., Wei, Q., Shang, H. and Liu, X.** (2023) Creep Behaviour of Ultra-High-Performance Concrete (UHPC): A Review. Journal of Building Engineering, Elsevier, 69, 106187. https://doi.org/10.1016/J.JOBE.2023.106187.
35. **Liu, Y., Wang, L., Wei, Y., Sun, C. and Xu, Y.** (2024) Current Research Status of UHPC Creep Properties and the Corresponding Applications – A Review. Construction and Building Materials, Elsevier, 416, 135120. https://doi.org/10.1016/J.CONBUILDMAT.2024.135120.
36. **Hamed, E. and Lai, C.** (2016) Geometrically and Materially Nonlinear Creep Behaviour of Reinforced Concrete Columns. Structures, Elsevier, 5, 1–12. https://doi.org/10.1016/J.ISTRUC.2015.07.001.
37. **Mussabayev, T.T., Nuguzhinov, Z.S., Nemova, D., Kayupov, T., Tolkynbaev, T.A., Akmakanova, A.Z. and Khafizova, G.S.** (2023) Creep of Concrete in Shell Structures: Nonlinear Theory. Materials 2023, Vol. 16, Page 5587, Multidisciplinary Digital Publishing Institute, 16, 5587. https://doi.org/10.3390/MA16165587
38. **Травуш В.И., Каприелов С.С., Конин Д.В., Крылов А.С., Чилин И.А.** Экспериментальные исследования сталежелезобетонных конструкций, работающих на изгиб // Строительство и реконструкция, 2017, №4 (72). С.63-71.
39. **Травуш В.И., Карпенко Н.И., Колчунов В.И., и др.** Результаты экспериментальных исследований сложнонапряженных балок круглого поперечного сечения из высокопрочного фиброжелезобетона // Строительная

механика инженерных конструкций и сооружений, 2020. Т. 16. №4. С. 290-297. doi: 10.22363/1815-5235-2020-16-4-290-297

40. **Травуш В.И., Карпенко Н.И., Колчунов В.И., и др.** Основные результаты экспериментальных исследований железобетонных конструкций из высокопрочного бетона В100 круглого и кольцевого сечений при кручении с изгибом // Строительная механика инженерных конструкций и сооружений, 2019, Т. 15. №1. С. 51-61 https://doi.org/10.22363/1815-5235-2019-15-1-51-61.
41. **Korsun, V.I., Morozov, V.I., Tamrazyan, A.G. and Alekseytsev, A. V.** (2023) Nonlinear Deformation Model for Analysis of Temperature Effects on Reinforced Concrete Beam Elements. Buildings 2023, Vol. 13, Page 2734, Multidisciplinary Digital Publishing Institute, 13, 2734. https://doi.org/10.3390/BUILDINGS13112734.
42. **Vorobeva, A., Strakhov, D. and Semenov, K.** (2021) Calculation of Reinforced Concrete Elements Taking into Account Nonlinear Creep at Different Loading Mode. Lecture Notes in Civil Engineering, Springer Science and Business Media Deutschland GmbH, 150 LNCE, 73–84. https://doi.org/10.1007/978-3-030-72404-7_8/TABLES/5.
43. **Bezgodov, I., Kaprielov, S. and Sheynfeld, A.** (2023) Relationship Between Strength and Deformation Characteristics of High-Strength Self-Compacting Concrete. Lecture Notes in Civil Engineering, Springer Science and Business Media Deutschland GmbH, 282, 459–468. https://doi.org/10.1007/978-3-031-10853-2_43/FIGURES/4.
44. ГОСТ 10181-2014. Смеси бетонные. Методы испытаний. https://docs.cntd.ru/document/1200115733?section=text.
45. ГОСТ 10180-2012. Бетоны. Методы определения прочности по контрольным образцам. https://docs.cntd.ru/document/1200100908.
46. ГОСТ 24452-80. Бетоны. Методы определения призменной прочности, модуля упругости и коэффициента Пуассона. https://kodeks.library.spbstu.ru/docs/
47. **Baranov, A.O. and Strakhov, D.A.** (2023) Creep of High Strength Concrete at Elevated Temperatures. Construction of Unique Buildings and Structures, 108, 10704–10704. https://doi.org/10.4123/CUBS.107.4.
48. СП 63.13330.2018. Бетонные и железобетонные конструкции. Основные положения. https://docs.cntd.ru/document/554403082.

Dmitry Alexandrovich Strakhov, Candidate of Technical Sciences, Assistant Professor at Higher School of Industrial, Civil and Road Construction, Peter the Great St. Petersburg Polytechnic University, Russia, St. Petersburg, 195251, Politechnicheskaya str., 29B, sdaleks2008@rambler.ru

Aleksey Olegovich Baranov, Senior Lecturer at the Higher School of Industrial, Civil and Road Construction, Peter the Great St. Petersburg Polytechnic University, Russia, St. Petersburg, 195251, Politechnicheskaya str., 29B, baranov_ao@spbstu.ru

Дмитрий Александрович Страхов, кандидат технических наук, доцент, доцент Высшей школы промышленно-гражданского и дорожного строительства (ВШПГиДС), Санкт-Петербургский политехнический университет Петра Великого (СПбПУ), Россия, Санкт-Петербург, 195251, ул. Политехническая, д. 29 литера Б, sdaleks2008@rambler.ru

Алексей Олегович Баранов, старший преподаватель Высшей школы промышленно-гражданского и дорожного строительства (ВШПГиДС), Санкт-Петербургский политехнический университет Петра Великого (СПбПУ), Россия, Санкт-Петербург, 195251, ул. Политехническая, д. 29 литера Б, baranov_ao@spbstu.ru

International Journal for Computational Civil and Structural Engineering, 21(1) 177–187 (2025)

DOI:10.22337/2587-9618-2025-21-1-177-187

EXPERIMENTAL IDENTIFICATION OF THE MEASURE OF INTERNAL FRICTION IN PLATES WITH A TWO-DIMENSIONAL AUXETIC STRUCTURE

Marina V. Shitikova [1,2], Ivan A. Soloviev [2], Artem V. Levchenko [2]

[1] National Research Moscow State University of Civil Engineering, Moscow, RUSSIA
[2] Voronezh State Technical University (VSTU), Voronezh, RUSSIA

Abstract: The analysis of relaxation processes occurring in metals, alloys and composites is an important problem of modern materials science. This paper presents the results of experiments to determine the measure of internal friction by impulse excitation technique (IET) in samples with different two-dimensional auxetic structures, namely, tetrachiral and re-entrant. IET is an advanced method for measuring material characteristics such as dynamic elastic and shear moduli, dynamic Poisson's ratio and internal friction to study deformation, softening, relaxation mechanisms and phase transformations in various materials. In the present research, five series of specimens of each structure have been made from photopolymer resin by sterlitography technology, which differ from each other in relative density. According to the test results, the dependence of internal friction on the sample density was determined. From the analysis of the obtained data, it was found that the re-entrant structure has a higher measure of internal friction, which indicates more pronounced viscoelastic properties, which in turn means a greater ability of the re-entrant structure to dampen the energy generated by the dynamic excitation. The values of the internal friction measure for the re-entrant structure at the peak point exceed the similar values for the tetrachiral structure by a factor of 6.44, in so doing with the increase in the relative density of the structure, the measure of the internal friction decreases irrespective of the type of the considered structures.

Keywords: Stereolithographic printing, tetrachiral honeycomb structure, re-entrant honeycomb structure, internal friction, impulse excitation technique

ЭКСПЕРИМЕНТАЛЬНОЕ ОПРЕДЕЛЕНИЕ МЕРЫ ВНУТРЕННЕГО ТРЕНИЯ В ПЛАСТИНКАХ С ДВУМЕРНОЙ АУКСЕТИЧЕСКОЙ СТРУКТУРОЙ

М.В. Шитикова [1,2], И.А. Соловьев [2], А.В. Левченко [2]

[1] Национальный исследовательский Московский государственный строительный университет, г. Москва, РОССИЯ
[2] Воронежский государственный технический университет, г. Воронеж, РОССИЯ

Аннотация: Анализ релаксационных явлений, происходящих в металлах, сплавах и композитах, является важной проблемой современного материаловедения. В данной статье представлены результаты экспериментов по определению меры внутреннего трения по технике импульсного возбуждения (IET) в образцах с различной двумерной ауксетической структурой, а именно тетракиральной и повторно-входящей. IET – это продвинутый метод измерения таких характеристик материалов, как динамические модули упругости и сдвига, динамический коэффициент Пуассона и внутреннее трение, для исследования процессов деформации, разупрочнения, механизмов релаксации и фазовых превращений в различных материалах. Образцы изготавливаются по технологии стерлитографии из фотополимерной смолы. Авторами были испытаны по пять серий образцов каждой структуры, которые отличаются между собой относительной плотностью. По результатам испытаний определена зависимость внутреннего трения от плотности образца. Из анализа полученных данных установлено, что повторно-входящая структура обладает более высокой мерой внутреннего трения что говорит о более выраженных вязкоупругих свойствах, что в свою очередь означает о большей способности повторно-входящей структуры гасить энергию, возникающую при динамическом воздействии. Значения меры внутреннего трения для повторно-входящей структуры в пиковой точке превышает аналогичные значения для тетракиральной структуры в 6.44 раза.

При этом с увеличением относительной плотности структуры мера внутреннего трения уменьшается независимо от вида рассмотренных структур.

Ключевые слова: Стереолитографическая печать, тетракиральная сотовая структура, повторно-входящая сотовая структура, внутреннее трение, метод импульсного возбуждения

1. INTRODUCTION

The analysis of relaxation phenomena occurring in metals, alloys and composites is an important problem of modern materials science. The results obtained as a result of such studies provide extensive information on the kinetics of crystal structure defects and allow one to predict the behaviour of structural elements made of these materials under various operating conditions. For the phenomenological description of relaxation processes in materials subjected to sufficiently weak external excitation, which is not reduced to plastic deformations, the hereditary theory of elasticity is usually adopted.

Recent trends are aimed at a wider use of fractional derivatives and other fractional operators in hereditary models of viscoelasticity, a detailed review of which could be found in [1-4]. In the last two decades, various fractional calculus models have also been widely used to describe the rheological properties of various building materials such as concrete [5, 8, 9, 10], asphalt [11, 12] and bituminous [13, 14] mixtures, asphalt concrete [15, 16], polymer concrete [17], rubber concrete [18], fibrocomposites [18, 19], polymer foams [20] and polyurethanes [21]. In this case, the order of the fractional derivative, or the so-called fractional parameter, is an additional microstructural characteristic of the material describing the level of its viscosity and microstructural changes [22], and for solid materials it varies from 0 (corresponding to a purely elastic material) to 1 (corresponding to a material described by the traditional viscoelastic model).

Fractional calculus models are nowadays widely applied in materials science, rheology and mechanics not only because they allow one to describe a whole range of dissipative mechanisms (including creep and relaxation phenomena [3, 4, 11]). with fewer parameters compared to traditional rheological formulations involving time derivatives of a whole order [17]. The fractional parameter variation could also allow one to account for a wide range of other important properties occurring over time in materials, such as ageing effects [19], chloride resistance of concrete and others. composites and their cohesion [9], concrete fracture [5], internal friction [10, 20], the phenomenon of second, or volume, relaxation [3, 10], which should be considered together with the first, or shear, relaxation for advanced composite materials, and would also enable modelling the properties of viscoelastic materials with negative Poisson's ratios [3, 23], which are called auxetics.

In order to incorporate fractional calculus models into engineering applications, it is necessary to define their characteristics [12, 21, 24-26], in particular the orders of fractional operators, for real structural materials, and/or structural elements, and/or engineering structures. The fractional parameter is of great interest not only from a computational but also from a physical point of view.

Several methods for fractional parameter estimation have been proposed, and the majority of them are based on quasi-static experimental tests such as pre-peak steady bending tests [5], uniaxial dynamic modulus tests [16]. creep tests [8, 24], stress relaxation tests [20, 24], and three-point bending tests of beams [12, 15]. While minimizing the errors between the numerical model and measurements provides the opportunity to estimate the material model parameters by analyzing the behaviour of materials to impulsive loading over a long period of

time [25], dynamic methods take the response to variable loading into account. According to [26], dynamic methods could be referred to Dynamic Mechanical Analysis (DMA) [14, 19] based on the measurement of amplitude and lag in the stress-strain relationship caused by oscillating force, vibration testing [26] and Impulse Excitation Technique (IET) [27] based on the measurement of resonant frequencies during shock excitation, allowing the evaluation of damping characteristics [28]. Using numerical modelling of experimental data from external vibration studies of suspension bridges, which led to the analysis of the model using the fast Fourier transform, a fractional parameter identification procedure was proposed in [29], allowing the authors to obtain damping coefficients dependent on natural frequencies of vibrations.

There are several ways to measure internal friction in different materials. Pavlova et al. [4] measured damping as the logarithmic damping of oscillations of an inverted torsion pendulum

$$Q^{-1}=\frac{1}{\pi n}\ \ln\frac{A_i}{A_{i+n}}, \tag{1}$$

where A_i and A_{i+n} are the amplitudes of the i-th and (i+n)-th periods of vibrations, respectively.

Recently, devices capable of direct measuring the internal friction in different materials have been proposed. Huang et al. [6] used a DTM-II-J dynamic elastic modulus internal friction analyzer manufactured by Hunan Zhenhua Analysis Instrument Co. Ltd., China. The device is based on the bending resonance method according to GB/T13665-2007 [7].

The principle of the bending resonance method is as follows: the frequency is increased until the strain amplitude reaches half of the resonance value, which corresponds to the frequency ω_2 and the period T_2. When the frequency is decreased until the strain amplitude reaches half of the resonance value, this frequency is denoted as ω_1, and the period as T_1. In so doing, $\Delta\omega$ is the difference value of $\omega_2-\omega_1$, and ΔT is the difference value of T_2-T_1. Then the damping could be evaluated as

$$Q^{-1}=\frac{|\Delta\omega|}{\sqrt{3}\omega_r}=\frac{|\omega_2-\omega_1|}{\sqrt{3}\omega_r}, \tag{2}$$

or

$$Q^{-1}=T_r\frac{|\Delta T|}{\sqrt{3T_2T_1}}=T_r\frac{|T_2-T_1|}{\sqrt{3T_2T_1}}, \tag{3}$$

where ω_r is the resonant frequency, and T_r is the resonant period [6].

The current study is focused on the experimental detection of the measure of internal friction of a metamaterial with a two-dimensional auxetic structure. For this purpose, plates with two different honeycomb structures would be considered, namely: tetrachiral and re-entrant. Auxetics have several advantages over conventional materials, among them, increased energy dissipation, increased resistance to crack formation and opening, better resistance to indentation. In this study, the effect of such factors as the internal dimensions of the honeycomb filler on the internal friction and fractional parameter would be investigated for metamaterials using a resonant frequency and damping analyzer (RFDA Basic) implementing the impulse excitation technique (IET) [27, 28].

2. MATERIALS AND METHODS

2.1. Materials for experiment

Samples for the study are made by additive manufacturing using Formlabs Form 3 3D printer. Formlabs Clear photopolymer resin with the following characteristics is used for manufacturing: tensile strength $\sigma_t=65$ MPa, tensile modulus $E_t=2.8$ GPa, and flexural modulus $E_f=2.2$ GPa. This resin is transparent, what

provides good quality control of the manufactured samples.

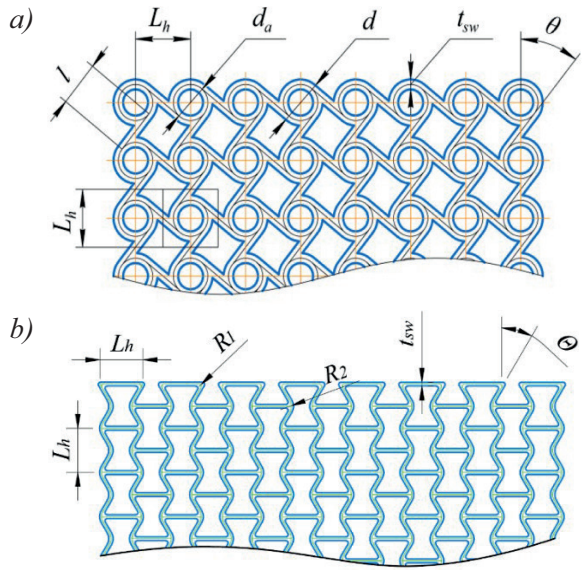

Figure 1. Type of tested structures: (a) tetrachiral (b) re-entrant

For laboratory experiments, samples of tetrachiral structure (Figures 1a, 2a) and re-entrant structure (Figures 1b, 2b) were produced, the geometrical parameters of which are given in Table 1. The variable parameter is the relative density of the cell:

$$\rho = A_{str}/A, \tag{4}$$

where A_{str} is the amount of material used to manufacture the structure, and A is the amount of material required to manufacture a full-body plate of the same dimensions.

Five series of samples for each honeycomb structure were designed.

The production of specimens includes the following steps:

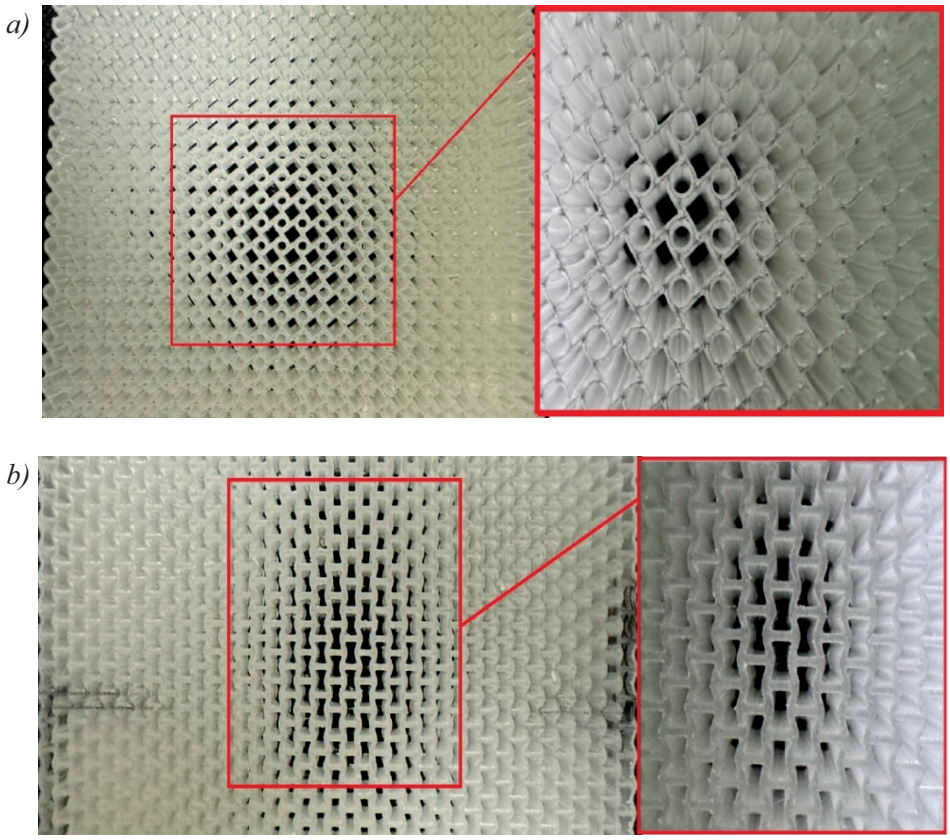

Figure 2. General view of produced samples: (a) tetrachiral (b) re-entrant

Table 1. Geometrical parameters of the samples.

Relative density ρ, %	l, mm	L_h, mm	d_a, mm	d, mm	t_{sw}, mm	R_1, mm	R_2, mm	Θ, ^{o}
Tetrachiral structure								
14	1.6227	2.08	1.3	1.3541	0.1082	-	-	20
21.1	1.6227	2.08	1.3	0.08485	0.1697	-	-	20
28.2	1.6227	2.08	1.3	0.11775	0.2355	-	-	20
35.3	1.6227	2.08	1.3	0.1529	0.3058	-	-	20
42.4	1.6227	2.08	1.3	0.19085	0.3817	-	-	20
Re-entrant structure								
14	-	1.97	-	-	0.1082	0.1	0.5	30
21.1	-	1.97	-	-	0.1697	0.1	0.5	30
28.2	-	1.97	-	-	0.2355	0.1	0.5	30
35.3	-	1.97	-	-	0.3058	0.1	0.5	30
42.4	-	1.97	-	-	0.3817	0.1	0.5	30

1. Printing the honeycomb structures on a 3D printer;
2. Cleaning the printed elements in an ultrasonic bath using isopropyl alcohol;
3. Pre-curing in an ultraviolet chamber;
4. Bringing the honeycomb structures to the required dimensions and surface flatness by grinding;
5. Cleaning of the ground elements from dust;
6. Final curing of the samples in an ultraviolet chamber.

2.2. Impulse excitation method

In this work, internal friction measurements were performed using the Impulse Excitation Technique (IET). The Impulse Excitation Technique (IET) is an advanced method for measuring material characteristics such as dynamic elastic and shear moduli, dynamic Poisson's ratio and internal friction to investigate deformation, softening, relaxation mechanisms and phase transformations in various materials. Experimental studies can be carried out both at room and high temperatures.

The method is based on the following. A specimen of a strictly defined shape and dimensions is freely rested on a wire support (Figure 3). The contact between the wire and the surface of the specimen must be established at certain points, so-called nodes. The location of the support plays a key role in the measurement of internal friction. If the support points do not coincide with the nodes, the internal friction will be significantly increased. In such a situation, the damping is generated not by the material but by the test machine.

The position of nodes is calculated separately for each sample shape with specific dimensions. After a small impact on the sample, it starts to vibrate. The signal is picked up by a microphone and transmitted to a personal computer, where the Resonant Frequency and Damping Analyzer (RFDA) software performs a Fast Fourier Transform (FFT), in order to calculate resonant frequencies, dynamic elastic and shear moduli, dynamic Poisson's ratio, damping factor, and internal friction.

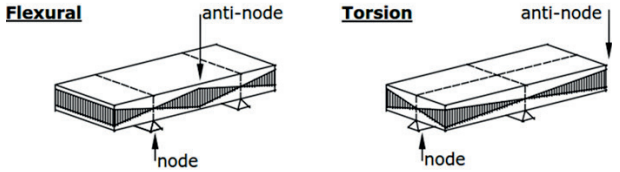

Figure 3. Schemes of bending and torsional vibrations of rectangular rods

For this experiment, specimens with dimensions l = 10 cm, b = 5 cm, t = 1 cm were produced. The RFDA Basic program obtained nodes at a distance of ≈22.54 mm from the edge

of the plate. Then the specimens were mounted on wire supports located at the distance of ≈54.92 mm from each other. After that a metal ball attached to a flexible rod was used to impact the plates. Figure 4 shows a photo of the experiment to determine the internal friction of the plates. Figure 5 shows the window of the initial data.

Internal friction is characterized by the following relationship:

$$Q^{-1} = \frac{k}{\pi \omega_r}, \tag{5}$$

where k is the damping coefficient (the inverse of the relaxation time).

Figure 4. Process of the experiment to determine the internal friction.

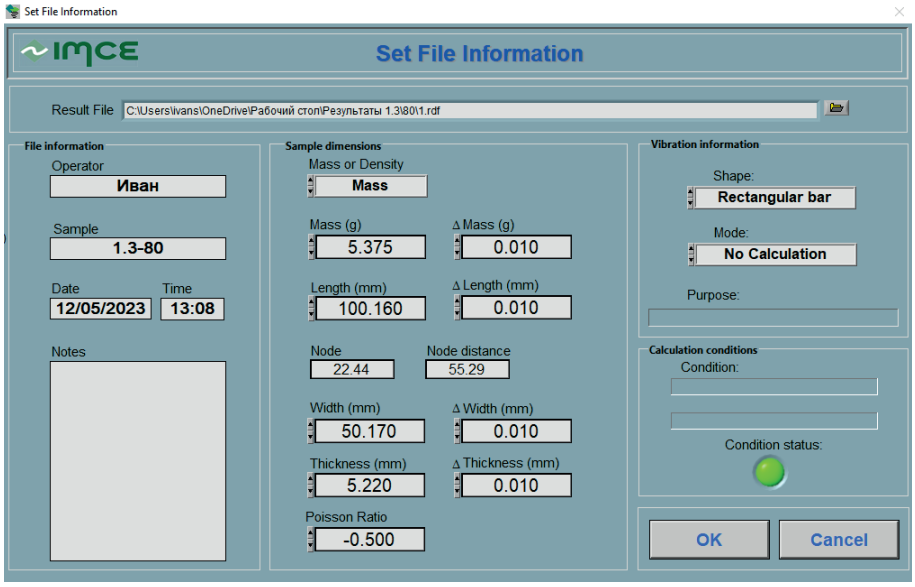

Figure 5. Input data task screen

3. RESULTS

According to the test results, the data necessary for calculations according to formula (5) were obtained, which are given in Tables 2 and 3, and the graph of internal friction dependence on the relative density of a honeycomb filler was plotted (Figure 6).

Table 2. Results of damping tests of tetrachiral structure

Relative density ρ, %	k, c^{-1}	ω_r, Hz	Q^{-1}
14	5.07	38.50	0.0487
21.1	7.18	39.05	0.0528
28.2	5.80	44.19	0.0434
35.3	280.86	12178.94	0.0073
42.4	251.35	11622.32	0.0069

Table 3. Results of damping tests of re-entrant structure

Relative density ρ, %	k, c^{-1}	ω_r, Hz	Q^{-1}
14	15.68	20.31	0.24
21.1	23.05	21.76	0.34
28.2	15.22	22.20	0.22
35.3	14.90	22.13	0.21
42.4	13.18	22.22	0.19

From the analysis of the graphs in Figure 6, it could be seen that the re-entrant structure has a higher measure of internal friction, which indicates more pronounced viscoelastic properties, what, in its turn, means that the re-entrant structure has a greater ability to dissipate the energy arising from the dynamic action. It is observed in both graphs that the highest internal friction is exhibited by the second set of samples with the relative density of 21.1%. In the tetrachiral structure with relative density greater than 35.3%, the measure of internal friction becomes close to 0, resulting in the decrease of the auxetic properties in structures with this relative density. However, in the re-entrant structures the values of Q^{-1}, although it goes to decrease after the relative density value of 28.2%, remain at a rather high level. The values of the measure of internal friction for the re-entrant structure at the peak point exceed the same values for the tetrachiral structure by a factor of 6.44.

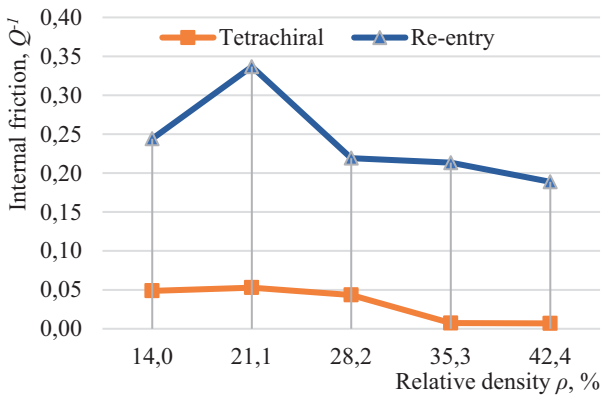

Figure 6. Graph of the dependence of internal friction on the relative density of honeycomb

4. CONCLUSION

The authors have validated the impulse excitation technique for non-destructive analysis of viscoelastic properties of metamaterials with two-dimensional auxetic structures. The following conclusions could be formulated:

1. the re-entrant structure has more pronounced viscoelastic properties compared to the tetrachiral structure;
2. as the relative density of the structure increases, the measure of internal friction decreases independent of the type of the considered structures;
3. the use of the impulse excitation method enables preliminary estimation of the damping properties of the selected honeycomb structures;
4. according to the results obtained it could be deduced that these plates are not pure elastic, but are viscoelastic, and it is recommended to apply the standard linear solid body model with fractional derivatives to describe the mechanical behaviour of such honeycomb plates.

ACKNOWLEDGEMENT

This research has been supported by the Ministry of Science and High Education of the Russian Federation, Project No 075-03-2023-132 (FZGM-2023-0006).

REFERENCES

1. **Rossikhin Yu.A., Shitikova M.V.** Applications of fractional calculus to dynamic problems of linear and nonlinear hereditary mechanics of solids // Applied Mechanics Reviews, 1997, vol. 50, no. 1, pp. 15–67.
2. **Rossikhin Yu.A., Shitikova M.V.** Application of fractional calculus for dynamic problems of solid mechanics: Novel trends and recent results // Applied Mechanics Reviews, 2010, vol. 63, no. 1, pp. 1–52.
3. **Shitikova M.V**. Fractional operator viscoelastic models in dynamic problems of me-

chanics of solids: A review // Mechanics of Solids, 2022, vol. 57, pp. 1–33.
4. **Shitikova M.V., Krusser A.I.** Models of viscoelastic materials: A review on historical development and formulation // Advanced Structured Materials, 2022, vol. 175, pp. 285–326.
5. **Barpi F., Valente S.** Creep and fracture in concrete: a fractional order rate approach // Engineering Fracture Mechanics, 2002, vol. 70, no. 5, pp. 611–623.
6. **Huang W., Zhan H., Xu L., Xu Z., Zeng J.** Investigation on microstructure and internal friction for low density TiB2/ZL114 composites // Acta Metallurgica Sinica, 2009, vol. 22, pp. 211–218.
7. **GB/T 13665-2007 2007** Test Method for Damping Capacity of Metallic Damping Materials – Torsion Pendulum Method and Bending Vibration Method (Standardization Administration of China)
8. **Zhang C., Zhu Z., Zhu S., He Z., Zhu D., Liu J., Meng S.** Nonlinear creep damage constitutive model of concrete based on fractional calculus theory // Materials, 2019, vol. 12, no. 9, Article ID 1505.
9. **Yao L., Ren L., Gong G.** Time-fractional model of chloride diffusion in concrete: analysis using meshless method // Advanced Materials and Science Engineering, 2020, vol. 2020, pp. 1–9.
10. **Shitikova M.V., Popov I.I., Rossikhin Yu.A.** Theoretical and experimental evidence of the bulk relaxation peak on the loss tangent versus frequency diagrams for concrete // Mechanics of Advanced Materials and Structures, 2022, vol. 30, no. 2, pp. 332–341.
11. **Oeser M., Pellinen T., Scarpas T., Kasbergen C.** Studies on creep and recovery of rheological bodies based upon conventional and fractional formulations and their application on asphalt mixture // International Journal of Pavement Engineering, 2008, vol. 9, no. 5, pp. 373–386.
12. **Yin Y., Yang Z., Shi M.** Circular arc rules of complex plane plot for model parameters determination of viscoelastic material // Mechanics of Time-Dependent Materials, 2021, vol. 25, no. 4, pp. 631–643.
13. **Olard F., Di Benedetto H.** General "2S2P1D" model and relation between the linear viscoelastic behaviours of bituminous binders and mixes // Road Materials and Pavement Design, 2003, vol. 4, pp. 185–224.
14. **Yin Y., Yang Z., Shi M.** Dynamic mechanical response for bituminous mixtures in wide frequency range // IOP Conference. Series Materials and Science Engineering, 2019, vol. 592, ArticleID 012059.
15. **Yin Y., Yang Z., Shi M.** Analytical expression of complex modulus for viscoelastic material // International Journal of Applied Mechanics, 2020, vol. 12, no. 5, ArticleID 20500
16. **Katicha S.W., Apeagyei A.K., Flintsch G.W., Loulizi A.** Universal linear viscoelastic approximation property of fractional viscoelastic models with application to asphalt concrete // Mechanics of Time-Dependent Materials, 2014, vol. 18, no. 3, pp. 555–571.
17. **Quan W., Zhao K., Ma X., Dong Z.** Fractional viscoelastic models for asphalt concrete: from parameter identification to pavement mechanics analysis // Journal of Engineering Mechanics, 2022, vol. 148, ArticleID 04022036.
18. **Popov I.I., Levchenko A.V.** Experimental investigation of internal friction in rubber concrete and fiber-reinforced rubber concrete // Russian Journal of Building Construction and Architecture, 2021, vol. 52, pp. 53–62.
19. **Wang X., Petru M., Xia L.** Modeling the dynamics behavior of flax fiber reinforced composite after water aging using a modified Huet-Sayegh viscoelastic model with fractional derivatives // Construction and Building Materials, 2021, vol. 290, pp. 122879–122876.
20. **Guo X., Yan G., Benyahia L., Sahraouri F.** Fitting stress relaxation experiments with

fractional Zener model to predict high frequency moduli of polymeric acoustic foams // Mechanics of Time-Dependent Materials, 2016, vol. 20, no. 4, pp. 523–533.
21. **Pawlak Z.M., Denisiewicz A.** Identification of the fractional Zener model parameters for a viscoelastic material over a wide range of frequencies and temperatures // Materials, 2021, vol. 14, no. 22, ArticleID 7024.
22. **Popov I.I., Rossikhin Yu.A., Shitikova M.V., Chang T.-P.** Impact response of a viscoelastic beam considering the changes of its microstructure in the contact domain // Mechanics of Time-Dependent Materials, 2015, vol. 19, no. 4, pp. 455–481.
23. **Rossikhin Yu.A., Shitikova M.V.** Fractional calculus models in dynamic problems of viscoelasticity. In: D. Baleanu, A.M. Lopes, (Eds.) // Handbook of Fractional Calculus with Applications. Vol. 7: Applications in Engineering, Life and Social Sciences, Part A, De Gruyter, Berlin, Boston, 2019. pp. 139–158.
24. **Yang X., Cai W., Liang Y., Holm S.** A novel representation of time-varying viscosity with power-law and comparative study // International Journal of Non-Linear Mechanics, 2020, vol. 119, ArticleID 103372.
25. **Prem M. S., Klanner M., Ellermann K.** Identification of fractional damping parameters in structural dynamics using polynomial chaos expansion // Applied Mechanics, 2021, vol. 2, no. 4, pp. 956–975.
26. **Ren Z., Atalla N., Ghinet S.** Optimization based identification of the dynamic properties of linearly viscoelastic materials using vibrating beam techniques // Journal of Vibration and Acoustics, 2011, vol. 133, no. 4, ArticleID 041012.
27. **Roebben G., Bollen B., Brebels A., Van Humbeeck J., Van der Biest O.** Impulse excitation apparatus to measure resonant frequencies, elastic moduli, and internal friction at room and high temperature // Review of Scientific Instruments, 1997, vol. 68, no. 12, pp. 4511–4515.
28. **Popov I.I., Shitikova M.V.** Impulse excitation technique and its application for identification of material damping: an overview // IOP Conference Series Material Science and Engineering, 2020, vol. 962, ArticleID 022025.
29. **Rossikhin Yu.A., Shitikova M.V.** Application of fractional calculus for analysis of non-linear damped vibrations of suspension bridges // Journal of Engineering Mechanics, 1998, vol. 124, pp. 1029–1034.

СПИСОК ЛИТЕРАТУРЫ

1. **Rossikhin Yu.A., Shitikova M.V.** Applications of fractional calculus to dynamic problems of linear and nonlinear hereditary mechanics of solids // Applied Mechanics Reviews, 1997, vol. 50, no. 1, pp. 15–67.
2. **Rossikhin Yu.A., Shitikova M.V.** Application of fractional calculus for dynamic problems of solid mechanics: Novel trends and recent results // Applied Mechanics Reviews, 2010, vol. 63, no. 1, pp. 1–52.
3. **Шитикова М.В.** Обзор вязкоупругих моделей с операторами дробного порядка, используемых в динамических задачах механики твердого тела // Известия РАН. Механика твердого тела. 2022. № 1. С. 3-40.
4. **Shitikova M.V., Krusser A.I.** Models of viscoelastic materials: A review on historical development and formulation // Advanced Structured Materials, 2022, vol. 175, pp. 285–326.
5. **Barpi F., Valente S.** Creep and fracture in concrete: a fractional order rate approach // Engineering Fracture Mechanics, 2002, vol. 70, no. 5, pp. 611–623.
6. **Huang W., Zhan H., Xu L., Xu Z., Zeng J.** Investigation on microstructure and internal friction for low density TiB2/ZL114 composites // Acta Metallurgica Sinica, 2009, vol. 22, pp. 211–218.

7. **GB/T 13665-2007 2007** Test Method for Damping Capacity of Metallic Damping Materials – Torsion Pendulum Method and Bending Vibration Method (Standardization Administration of China)
8. **Zhang C., Zhu Z., Zhu S., He Z., Zhu D., Liu J., Meng S.** Nonlinear creep damage constitutive model of concrete based on fractional calculus theory // Materials, 2019, vol. 12, no. 9, Article ID 1505.
9. **Yao L., Ren L., Gong G.** Time-fractional model of chloride diffusion in concrete: analysis using meshless method // Advanced Materials and Science Engineering, 2020, vol. 2020, pp. 1–9.
10. **Shitikova M.V., Popov I.I., Rossikhin Yu.A.** Theoretical and experimental evidence of the bulk relaxation peak on the loss tangent versus frequency diagrams for concrete // Mechanics of Advanced Materials and Structures, 2022, vol. 30, no. 2, pp. 332–341.
11. **Oeser M., Pellinen T., Scarpas T., Kasbergen C.** Studies on creep and recovery of rheological bodies based upon conventional and fractional formulations and their application on asphalt mixture // International Journal of Pavement Engineering, 2008, vol. 9, no. 5, pp. 373–386.
12. **Yin Y., Yang Z., Shi M.** Circular arc rules of complex plane plot for model parameters determination of viscoelastic material // Mechanics of Time-Dependent Materials, 2021, vol. 25, no. 4, pp. 631–643.
13. **Olard F., Di Benedetto H.** General "2S2P1D" model and relation between the linear viscoelastic behaviours of bituminous binders and mixes // Road Materials and Pavement Design, 2003, vol. 4, pp. 185–224.
14. **Yin Y., Yang Z., Shi M.** Dynamic mechanical response for bituminous mixtures in wide frequency range // IOP Conference. Series Materials and Science Engineering, 2019, vol. 592, ArticleID 012059.
15. **Yin Y., Yang Z., Shi M.** Analytical expression of complex modulus for viscoelastic material // International Journal of Applied Mechanics, 2020, vol. 12, no. 5, ArticleID 20500
16. **Katicha S.W., Apeagyei A.K., Flintsch G.W., Loulizi A.** Universal linear viscoelastic approximation property of fractional viscoelastic models with application to asphalt concrete // Mechanics of Time-Dependent Materials, 2014, vol. 18, no. 3, pp. 555–571.
17. **Quan W., Zhao K., Ma X., Dong Z.** Fractional viscoelastic models for asphalt concrete: from parameter identification to pavement mechanics analysis // Journal of Engineering Mechanics, 2022, vol. 148, ArticleID 04022036.
18. **Попов И.И., Левченко А.В.** Экспериментальное исследование внутреннего трения в каутоне и фиброкаутоне // Научный журнал строительства и архитектуры, 2021, №4 (64), С. 83-92.
19. **Wang X., Petru M., Xia L.** Modeling the dynamics behavior of flax fiber reinforced composite after water aging using a modified Huet-Sayegh viscoelastic model with fractional derivatives // Construction and Building Materials, 2021, vol. 290, pp. 122879–122876.
20. **Guo X., Yan G., Benyahia L., Sahraouri F.** Fitting stress relaxation experiments with fractional Zener model to predict high frequency moduli of polymeric acoustic foams // Mechanics of Time-Dependent Materials, 2016, vol. 20, no. 4, pp. 523–533.
21. **Pawlak Z.M., Denisiewicz A.** Identification of the fractional Zener model parameters for a viscoelastic material over a wide range of frequencies and temperatures // Materials, 2021, vol. 14, no. 22, ArticleID 7024.
22. **Popov I.I., Rossikhin Yu.A., Shitikova M.V., Chang T.-P.** Impact response of a viscoelastic beam considering the changes of its microstructure in the contact domain // Mechanics of Time-Dependent Materials, 2015, vol. 19, no. 4, pp. 455–481.

23. **Rossikhin Yu.A., Shitikova M.V.** Fractional calculus models in dynamic problems of viscoelasticity. In: D. Baleanu, A.M. Lopes, (Eds.) // Handbook of Fractional Calculus with Applications. Vol. 7: Applications in Engineering, Life and Social Sciences, Part A, De Gruyter, Berlin, Boston, 2019. pp. 139–158.
24. **Yang X., Cai W., Liang Y., Holm S.** A novel representation of time-varying viscosity with power-law and comparative study // International Journal of Non-Linear Mechanics, 2020, vol. 119, ArticleID 103372.
25. **Prem M. S., Klanner M., Ellermann K.** Identification of fractional damping parameters in structural dynamics using polynomial chaos expansion // Applied Mechanics, 2021, vol. 2, no. 4, pp. 956–975.
26. **Ren Z., Atalla N., Ghinet S.** Optimization based identification of the dynamic properties of linearly viscoelastic materials using vibrating beam techniques // Journal of Vibration and Acoustics, 2011, vol. 133, no. 4, ArticleID 041012.
27. **Roebben G., Bollen B., Brebels A., Van Humbeeck J., Van der Biest O.** Impulse excitation apparatus to measure resonant frequencies, elastic moduli, and internal friction at room and high temperature // Review of Scientific Instruments, 1997, vol. 68, no. 12, pp. 4511–4515.
28. **Popov I.I., Shitikova M.V.** Impulse excitation technique and its application for identification of material damping: an overview // IOP Conference Series Material Science and Engineering, 2020, vol. 962, ArticleID 022025.
29. **Rossikhin Yu.A., Shitikova M.V.** Application of fractional calculus for analysis of non-linear damped vibrations of suspension bridges // Journal of Engineering Mechanics, 1998, vol. 124, pp. 1029–1034.

Marina V. Shitikova, Prof., Dr.Sc., Department of High Mathematics, Moscow State University of Civil Engineering, Moscow; Yaroslavskoye Shosse 26, Moscow, Russia; Research Center on Dynamics of Solids and Structures; Voronezh State Technical University; 20-letiya Oktyabrya 84, Voronezh, 394006, Russia; E-mail: mvs@cchgeu.ru; ORCID: 0000-0003-2186-1881.

Ivan A. Soloviev, research engineer, Voronezh State Technical University, 84, 20 letiya Oktyabrya st. Voronezh, 394006. Russia, E-mail: ivansolovev3112@gmail.com; ORCID: 0000-0002-0748-1922

Artem V. Levchenko, Candidate of Technical Sciences, Associate Professor, Voronezh State Technical University, 84, 20 letiya Oktyabrya st. Voronezh, 394006. Russia, E-mail: alevchenko@cchgeu.ru; ORCID: 0000-0002-6875-754X

Шитикова Марина Вячеславовна, профессор, доктор физико-математических наук; зав. кафедрой высшей математики НИУ МГСУ, Ярославское шоссе 26, Москва, Россия; руководитель международного научного центра по фундаментальным исследованиям в области естественных и строительных наук имени Заслуженного деятеля науки РФ, профессора Россихина Ю.А.; Воронежский государственный технический университет; 394006, Россия, г. Воронеж, ул. 20 лет Октября, д. 84, E-mail: mvs@cchgeu.ru; ORCID: 0000-0003-2186-1881.

Соловьев Иван А., инженер-исследователь Воронежского государственного технического университета, 394006. Россия, г. Воронеж, ул. 20-летия Октября. 84, E-mail: ivansolovev3112@gmail.com; ORCID: 0000-0002-0748-1922

Левченко Артем Владимирович, к.т.н., доцент Воронежского государственного технического университета, 394006. Россия, г. Воронеж, ул. 20-летия Октября. 84, E-mail: alevchenko@cchgeu.ru; ORCID: 0000-0002-6875-754X

International Journal for Computational Civil and Structural Engineering, 21(1) 188–201 (2025)

DOI:10.22337/2587-9618-2025-21-1-188-201

STRENGTH ANALYSIS OF STEAM TURBINE BLADES FOR A NUCLEAR POWER PLANT

Patrick L. Kiprotich, Mariia V. Volkova, Robert F. Siro

National Research Nuclear University NRNU IATE MEPhI, Obninsk, RUSSIA

Abstract: The blade is an aerofoil-shaped component of a steam turbine that has a root attached to the rotor. The root is the base of the blade that supports the entire structure and transmits the torque generated by the steam flow to the rotor. The root must be designed in a manner that takes into account its removal during maintenance and positional maintenance on-the-fly during turbine operation. This essentially ensures a safe working environment for the operators and other personnel in the nuclear power plant.

Strength analysis of a steam turbine blade is a prerequisite procedure in the steam turbine design process during which the strength and durability of the blades under various operating conditions are evaluated. Such operating conditions include elevated temperatures, intense pressure and high rotational speeds. The purpose of this scientific work is to demonstrate that the blades can withstand such extreme conditions with little or no degradation over time. The adopted methodology involves modeling of the steam turbine blade using SolidWorks, and using the Finite Element Analysis (FEA) software to simulate the mechanical behavior of the associated blade material under various stress and strain conditions. The analysis takes into account factors such as stress distribution and concentration to predict the response of the blade under high pressure steam jets. The results of the analysis are adopted in the optimization of blade design and material selection to ensure safe and efficient blade operation throughout the entire lifespan of the turbine blade. The results are also useful in the identification of potential areas of weakness or failure that can be addressed through design changes and material improvements.

Keywords: Strength analysis, steam turbine blade, finite element analysis, SolidWorks, Ansys, static structural analysis, nuclear power plant

РАСЧЕТ ПРОЧНОСТИ ЛОПАТОК ПАРОВОЙ ТУРБИНЫ ДЛЯ АТОМНОЙ ЭЛЕКТРОСТАНЦИИ

П.Л. Кипротич, М.В. Волкова, Р.Ф. Сиро

Национальный исследовательский ядерный университет «НИЯУ ИАТЭ МИФИ», г. Обнинск, РОССИЯ

Аннотация: Лопатка является компонентом паровой турбины в форме аэродинамического профиля, который имеет корень, прикрепленный к ротору. Корень — это основание лопатки, которое поддерживает всю конструкцию и передает крутящий момент, создаваемый потоком пара, на ротор. Корень должен быть спроектирован таким образом, чтобы учитывать возможность его демонтажа во время обслуживания и сохранение его положения в процессе работы турбины. Это, по сути, обеспечивает безопасные условия труда для операторов и другого персонала на атомной электростанции. Анализ прочности лопатки паровой турбины является обязательной процедурой в процессе проектирования паровой турбины, в ходе которой оцениваются прочность и долговечность лопаток при различных условиях эксплуатации. К таким условиям относятся повышенные температуры, интенсивное давление и высокие обороты. Целью данной научной работы является демонстрация того, что лопатки могут выдерживать такие экстремальные условия с минимальным или отсутствующим ухудшением прочности со временем. Принятая методология включает моделирование лопатки паровой турбины с использованием Solidworks и применение программного обеспечения, использующего метод конечных элементов (FEA) для симуляции механического поведения связанного материала лопатки при различных условиях напряжения и деформации. Расчет учитывает такие факторы, как распределение напряжений и их концентрация, чтобы предсказать напряженно-деформированное состояние лопатки под воздействием струй пара под высоким давлением. Результаты расчета используются для оптимизации проектирования лопаток и выбора материалов, чтобы обеспечить безопасную и эффективную работу лопаток на

протяжении всего срока их службы. Результаты также полезны для выявления потенциальных зон слабости или отказа, которые могут быть устранены за счет изменения конструкции и улучшения материалов.

Ключевые слова: расчет на прочность, лопатка паровой турбины, метод конечных элементов, Solidworks, Ansys, статический расчет на прочность, атомная электростанция

1. INTRODUCTION

A steam turbine is a fundamental subsystem in every power generation complex, particularly in nuclear power plants in which they convert the potential energy stored in high pressure steam into kinetic energy associated with the rotating turbine blades, generating a rotary motion for driving electrical generators which ultimately results into electrical power. The efficiency and reliability of the turbine is critically dependent on the performance of the blades, which are subjected to extreme operating conditions associated with very high temperatures, pressures and rotational speeds. In this scientific work, we perform a strength analysis of the last-stage reaction-type steam turbine blades. Understanding the mechanical behavior of these blades under operational stresses is essential in preventing failures and ensuring the longevity of the turbine.

The primary objective of this scientific work is to model, analyze and validate the stresses associated with the steam turbine blade subjected to the extreme conditions formerly mentioned. In the analysis, it is assumed that the manifestation of such conditions is uniform on all the blades and so the results associated with a single blade can be replicated to give a whole picture of the condition of all the blades in the turbine. By conducting a detailed analysis of the impact of these conditions on the blade, we get results that are crucial in the enhancement of the design and material selection for the turbine blades.

By integrating advanced modeling and simulation techniques, the study provides a comprehensive understanding of the stresses manifesting on the turbine blades, a prerequisite stage in informed decision making on the basis of the adopted materials and design improvements. Additionally, the analysis procedure adopted in this scientific work can easily be applied in other types of turbines and components, contributing to the broader field of engineering and power generation. The findings in the study are expected to have practical implications in the maintenance and design of steam turbines, ultimately enhancing the stability and efficiency of power plants.

1.1 A Brief Description of the Steam Turbine Blade and the Investigated Conditions

A steam turbine operates under the fundamental principle of the Rankine Cycle, a thermodynamic cycle that transforms heat energy into mechanical work. In the Rankine cycle, high-pressure steam is generated in the steam generator. The steam is subjected to expansion in a series of turbine stages to create a rotary motion needed to facilitate the motion of conductive material through the magnetic field lines associated with permanent magnets of the electrical generator. The steam is then condensed and reintroduced into the cycle.

The blade causes the rotation of the rotor by the action of reactionary or impulsive forces when a jet of steam traverses over its surface. It's installed in slots on discs connected to a rapidly rotating shaft. The blade is engineered to allow steam to flow smoothly over its surface, altering direction and generating a force that induces rotary motion. In a nuclear power plant (NPP), the turbine operates at extreme conditions associated with high temperatures, oxidation, cavitation, corrosion, bending and centrifugal forces associated with the flowing steam, necessitating the selection of materials that can withstand such conditions. The design of the steam turbine blades must therefore take all these factors into consideration.

Materials such as INCONEL 718, a precipitation-hardened nickel-based superalloy, are capable of withstanding these conditions but require rigorous testing before use [1,2].

The blade consists of 3 main parts; the leaf type, the blade root, and the blade tip, normally mounted in a disc containing shaft as illustrated in figure 1 [3].

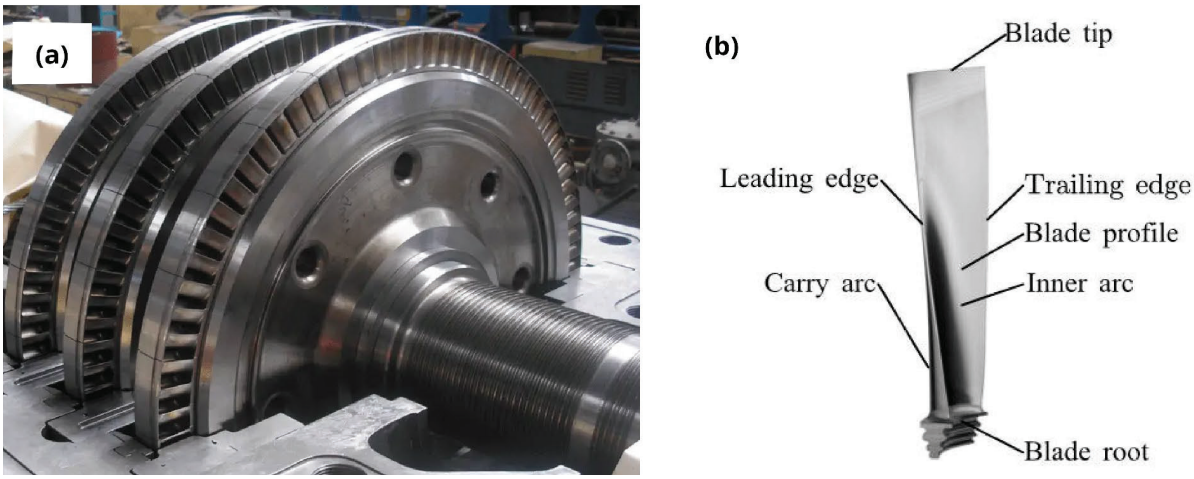

Figure 1. Turbine blades: (a) The shaft and disc with turbine blades, (b) Basic structure of a twisted blade

Each edge of a cross-section is referred to as a profile line, which, along with the section profile line and the leaf height parameters, adheres to gas dynamics requirements and ensures structural strength. Due to multi-axial stress state from the load, the blade must be modeled using 3-dimensional (3D) solid elements. The 3D model allows for detailed views of the maximum stresses, ensuring the design remains within safe limits. The blade's shape is determined by the minimum inertia of the section, while its strength and vibration performance are influenced by several aerodynamic parameters, including the impeller's suiting mode on the main shaft, the geometric inlet angle, and the exit angle [4].

1.2 Steam Turbine Blade Material Strength Analysis

Numerous studies have been conducted to analyze the strength and life expectancy of steam turbine blades under various loading scenarios. Researchers have employed a range of analytical, numerical and experimental techniques to investigate the complex stress distributions, material behaviors and failure mechanisms associated with these components.

Analytical methods, such as beam theory and energy methods, have been widely used to estimate the stresses and deformations in turbine blades subjected to centrifugal, thermal, and aerodynamic loads. These methods provide closed-form solutions and offer insights into the dominant failure modes, such as high-cycle fatigue, creep, and low-cycle fatigue [5].

Numerical techniques, particularly the FEA, have proven to be powerful tools for detailed stress analysis and turbine blade lifespan prediction. This method can incorporate complex blade geometries, material properties and loading conditions to accurately simulate the blade's structural response and identify critical stress concentration regions [6].

Experimental investigations have played a crucial role in validating analytical and numerical models, as well as understanding the underlying failure mechanisms. Static, fatigue, creep and thermal cycling tests have been conducted on actual blade specimens or scaled models to provide valuable data on material behavior, crack initiation and propagation, and

the effects of the environmental factors such as temperature and corrosion [7].
Strength analysis has led to the development of new alloys and coatings designed to enhance the strength and durability of turbine blades. Such materials exhibit superior high-temperature strength, creep resistance, and oxidation resistance, enabling longer service life and improved performance in nuclear power plant applications [8].
To achieve reliable performance, it is essential that the working stress manifesting on the turbine blades does not exceed the maximum allowable stress associated with the material.

1.3 Principles of Operation of Turbines

Turbines can be categorized based on the principle of their operation. In this case, we consider the categorization into impulse turbine and the reaction turbine. The impulse turbine operates by utilizing high-pressure steam that enters a stationary nozzle, consequently experiencing a decrease in pressure and a corresponding increase in velocity. The high-velocity steam is directed towards properly shaped turbine blades, generating an impulse force as it changes the steam flow direction upon impact. The resultant force instigates blade movement, initiating a rotary motion. The impulse turbine maintains a constant pressure across the moving blades. While the stationary nozzles facilitate a pressure drop and an increase in velocity, the moving blades do not experience any changes in pressure. On the other hand, the reaction turbine consists of rows of fixed and moving blades. Initially, the steam expands in the fixed blades, increasing in velocity while its pressure decreases. As the steam gets to the moving blades, its direction changes, creating an impulse force on the blades. While traversing through the moving blades, it continues to expand and its pressure further drops, generating a reaction force that drives the turbine. A key characteristic of the reaction turbine is the pressure differential between the inlet and the outlet of the moving blades, indicating a significant pressure drop across the blades [5].

2. MATERIALS AND METHODOLOGY

The adopted methodology entailed creation of the 3D model of the turbine blade using SolidWorks, adoption of the analytical computation scheme for the stress, adoption of the ANSYS supported numerical computation in simulating stress, and validation of results by comparing the adopted numerical and analytical computation models. The implementation workflow diagram is presented in figure 2.

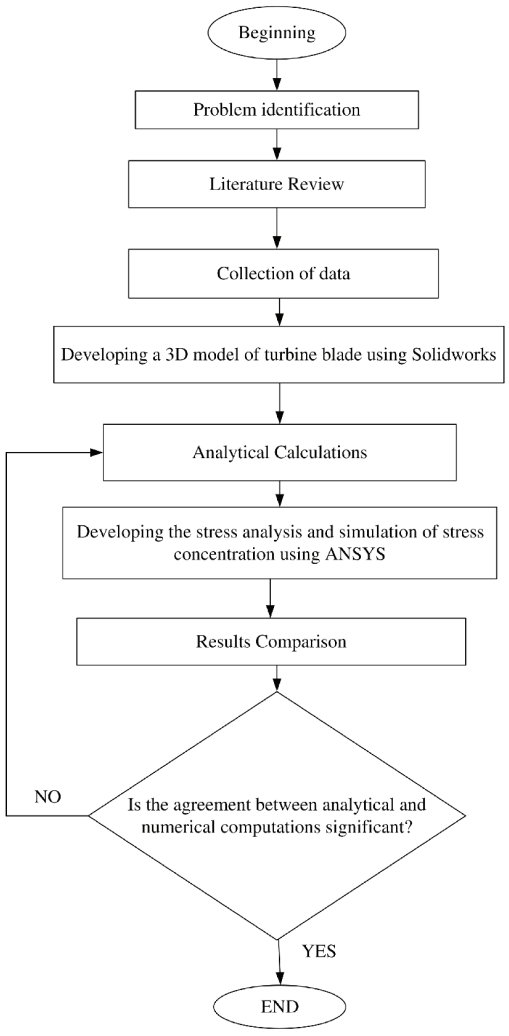

Figure 2. Implementation workflow

2.1 Steam Turbine Blade Material Characteristics, Properties and Physical Parameters

The steam turbine blade considered in this scientific work is made of INCONEL Alloy 718, a nickel-based superalloy whose mechanical characteristics are outlined in table 1 [11].

Table 1. Mechanical characteristics of INCONEL Alloy 718

Material characteristic	Value/comment
Physical density, g cm^{-3}	8,221
Melting point, ^{0}C	1380-1425
Modulus of elasticity, GPa	205
Tensile strength, MPa	869.4
Yield strength, MPa	761,2
Creep resistance	Excellent
Corrosion resistance	Excellent in air, water and steam
Oxidation resistance	Good up to 1200 ^{0}C
Wear resistance	Good
Fatigue resistance	Good

The INCONEL Alloy 718 turbine material constitutes a blend of diverse elements, each with specified percentage composition as outlined in table 2. These element compositions impart favorable characteristics, enabling the turbine to operate effectively under high-pressure steam conditions within the steam turbine system.

Table 2. Percentage composition of materials in INCONEL Alloy 718

Element	Composition , %
Nickel (Ni)	50-55
Chromium (Cr)	17-21
Iron (Fe)	18-22
Niobium (Nb)	4,75-5,5
Tantalum (Ta)	4,75-5,5
Molybdenum (Mo)	2,8-3,3
Titanium (Ti)	0,65-1,15
Aluminium (Al)	0,2-0,8
Columbium (Cb)	0,3-0,7
Others	Trace amounts

The material properties and physical parameters of the turbine blade adopted in the analysis are presented in table 3.

Table 3. Material properties and physical parameters

Material properties	Magnitude
Physical density, Kg m^{-3}	8221
Modulus of elasticity, E, MPa	$1{,}95 \cdot 10^5$
Yield strength, σ_y, MPa	761,20
Ultimate tensile strength, MPa	869,40
Elongation, %	40,00
Radius of the rotor disc, m	0,30
Height of the blade, mm	150,00
Cross-sectional area of the root of the blade, mm^2	1195,82
Blade rotation speed, ω, rad s^{-1}	314,16
Steam mass flowrate, t hr^{-1}	1602

2.2 Analytical Solution

2.2.1 Centrifugal Stress on the Turbine Blade

The rotating blades encounter centrifugal forces as a consequence of their circular motion within the turbine. These forces exert an outward pressure on the blades, directly proportional to the square of the rotational speed and the distance on the blade from the center of rotation. Considering a simplified two-dimensional (2D) representation of the blade as depicted in figure 3 [9], the centrifugal force acting on the turbine blade, denoted by F_C is calculated using equation (1).

$$F_C = m \cdot r \cdot \omega^2 \tag{1}$$

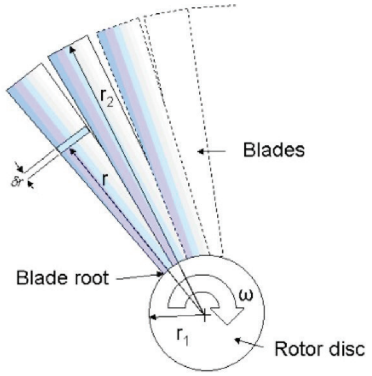

Figure 3. Load acting rotor blade

Where m is the mass of the blade, r is the radial distance from the center of rotation to the blade tip, and ω the angular velocity of the blade.
Considering an infinitesimal mass segment, denoted by δm, with a width dr, located at a distance r from the center of rotation, the centrifugal force acting on this point, represented by δF_C takes the form of equation (2).

$$\delta F_c = \delta m \cdot r \cdot \omega^2 \tag{2}$$

Given the cross-sectional area of the blade is A, mm^2, and the material physical density ρ, kg mm^{-3}, then the infinitesimal mass of the element takes the form of equation (3).

$$\delta m = \rho \cdot A \cdot dr \tag{3}$$

Substituting equation (3) into (2), and assuming that both the material physical density and the cross-sectional area are constant, we get equation (4).

$$\delta F_c = \rho \cdot A \cdot \omega^2 \cdot r \cdot dr \tag{4}$$

Integrating equation (4) from the centroid of the turbine shaft to the blade tip [10] gives the force exerted on the entire turbine blade in the form of equation (5).

$$F_C = \rho \cdot A \cdot \omega^2 \int_{r_1}^{r_2} r dr \tag{5}$$

So that the resultant centrifugal force is determined using the equation (6).

$$F_C = \rho \cdot A \cdot \omega^2 \cdot \frac{r_2^2 - r_1^2}{2} \tag{6}$$

Where r_1 is the radius of the rotor disc, and r_2 is the sum of the height of the blade and the radius of the rotor disc, as shown in figure 2.
Considering the data provided in table 3, we calculate the total radius of the blade by summing up the radius of the rotor disc (r_1 = 0,3 m) and the height of the turbine blade, so that, r_2 = 0,45 m. Substituting all the known parameters into equation (6) gives the centrifugal force on the blade, F_C = 54600 N.

2.2.2 The Centrifugal and Bending Stresses on the Turbine Blades

The centrifugal stress σ_c at the blade root is then calculated using the relation (7).

$$\sigma_c = \frac{F_c}{A_{root}} \tag{7}$$

Where A_{root} is the cross-sectional area of the blade root. So that the resulting centrifugal force acting on the blade root, σ_c = 45,50 MPa.
We must also take into account the bending stress on the steam turbine blade due to the steam pressure. This stress is sensitive to various factors, including the blade geometry, material properties, operating conditions, and the aerodynamic forces acting on the blade. On a beam-like structure, this stress takes the form of equation (8).

$$\sigma_B = \sqrt{\sigma_t^2 + \sigma_a^2} \tag{8}$$

The tangential bending stress on the blade takes the form of equation (9).

$$\sigma_t = \frac{M}{I_x} \cdot y \tag{9}$$

The axial bending stress on the blade takes the form of equation (10).

$$\sigma_a = \frac{M}{I_y} \cdot x \tag{10}$$

Where M is the bending moment due to steam pressure, x, y are the distances from the neutral axis to the outermost part of the blade in the x and y directions respectively, I_x, I_y are the

moments of inertia in the x and y directions respectively.

Formulation of the bending stress requires scrutiny of the combined velocity triangle for steam turbine illustrated in the figure 4 [12]. This is a graphical assessment of the velocity distribution of steam as it traverses through the steam turbine blade. The velocities are represented using velocity triangles, which illustrate the magnitudes and directions of various velocity components.

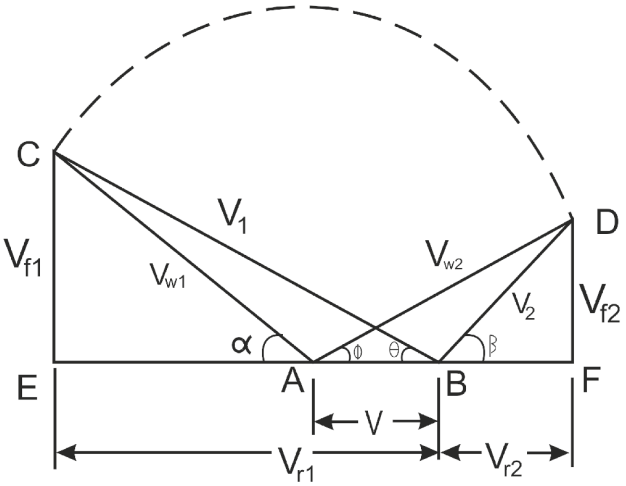

Figure 4. Combined velocity triangle for steam turbine

The free body diagram of the steam turbine blade adopted in the analysis is given in figure 5.

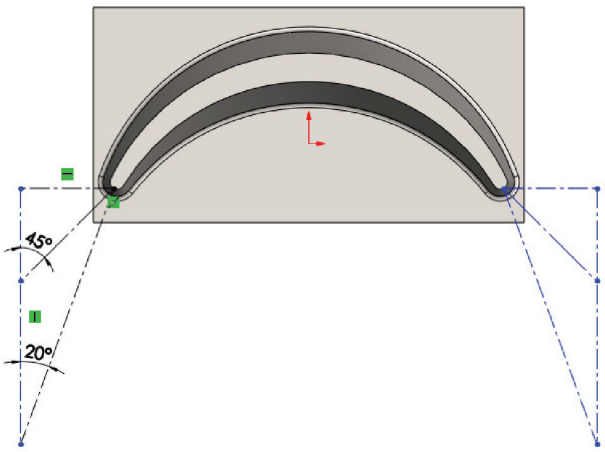

Figure 5. Steam turbine blade cross-section with velocity diagram

The mass flowrate, $\dot{M}$, associated with all the blades in a circular section of the steam turbine under scrutiny is given in table 3. The total number of turbine blades in each circular section is given as, n = 90, therefore, the mass flowrate associated with a turbine blade takes the form of equation (11).

$$\dot{m} = \frac{\dot{M}}{n} \tag{11}$$

So that, on substituting into equation (11), $\dot{M} = 4{,}94\ \mathrm{kgs}^{-1}$.

With reference to the depiction in figure 4, we generate a combined velocity triangle diagram for the steam turbine blade adopted in the analysis as shown in figure 6.

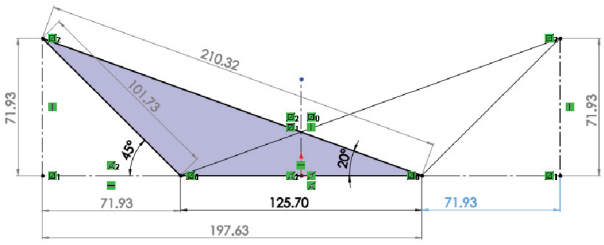

Figure 6. Combined velocity diagram of the turbine blade

The approximate values for the tangential and axial components are obtained from figure 6. The dimensional lengths correspond to relative velocities in m s^{-1}. From this figure, we retrieve the angles $\alpha = \beta = 45^0$, and $\theta = \Phi = 20^0$; representing the angle the incoming steam makes with the tangent of the wheel at the steam inlet, the angle the discharging steam makes with the tangent of the wheel at the steam outlet, the inlet angle of the moving blades, and the outlet angle of the moving blades respectively. The linear velocity V is calculated from the angular velocity of the rotor.

At the entrance, the vertical component velocity of flow V_{f1} corresponds to the axial component velocity V_1, while the velocity of flow at the exit V_{f2} aligns with the axial component V_2. Since both V_{f1} and V_{f2} are identical at a velocity of

71,93 m s^{-1}, the axial force acting on the blade becomes zero, implying that only the tangential force is exerted on the blade. From the figure 6, the velocity of the steam relative to the moving blade V_{r1} = 197,63 m s^{-1} at the inlet and the velocity of steam relative to the moving blade V_{r2} = 71,93 m s^{-1} at the outlet are used to calculate the tangential force using equation (12).

$$F_t = \dot{m}(V_{r1} + V_{r2}) \quad (12)$$

So that, the tangential force F_t = 1332,82 N.
The tangential moment M_t caused by the tangential force takes the form of equation (13).

$$M_t = F_t(r_2 - r_1) \quad (13)$$

So that M_t = 199,92 N m.

Table 4. Principal moment of inertia at the centroid, I_y and the depth of the blade from the central axis

Centroid relative to output coordinate system origin, mm		x = 0,00 y = 1,00 z = -9,11	
Moments of inertia of the area, at the centroid, mm^4	L_{xx}=74635,33 L_{yx}=0,00 L_{zx}=-24,44	L_{xy}=0,00 L_{yy}=731171,07 L_{zy}=0,00	L_{xz}=-24,44 L_{yz}=0,00 L_{zz}=656535,74
Polar moment of inertia of the area, at the centroid = 731171,07 mm^4		Angle between principal axes and part axes = 90^0	
Principal moments of inertia of the area, at the centroid , mm^4		I_x = 74635,33 I_y = 656535,74	
Moments of inertia of the area , at the output coordinate system, mm^4	L_{xx}=174679,60 L_{yx}=0,83 L_{zx}=16,86	L_{xy}=0,83 L_{yy}=830024,43 L_{zy}=-10850,11	L_{xz}=16,86 L_{yz}=-10850,11 L_{zz}=657726,64

Table 4 entails the principal moment of inertia at the centroid, I_y and the depth of the blade from the central axis. The measurements are based on sectioned model. The cross-sectional area of the selected face, A = 1190,91 mm^2. The value of the principal moment of inertia along the y-axis, I_y, and its corresponding length, y from the neutral axis is used to calculate the tangential stress by substituting these values into equation (9), so that σ_t = 50,65 MPa. Due to the fact that the axial force acting on the blade is zero, the bending stress on the turbine blade, σ_B = σ_t = 50,65 MPa.
The total stress acting on the turbine blade is determined by summing up the tangential and centrifugal stresses on the blade, equating to 96,15 MPa.

2.3 ANSYS Supported Numerical Solution

The Ansys Workbench's static structural analysis module was used in the numerical computation of centrifugal and bending stresses. This module utilizes the FEA techniques, which involve breaking down a complex structure into smaller, simpler elements. The equations governing the motion and behavior of each individual element are then solved numerically to determine the stress, strain, and displacement distributions throughout the entire structure [13]. By discretizing the problem, the program effectively analyzes the centrifugal and bending stresses acting on the blade.
The 3D model of the steam turbine blade subjected to numerical simulation is given in figure 7.

2.3.1 Meshing and Solving for Centrifugal Stress

In the static structural analysis module, the geometry file of the steam turbine blade is imported, the material properties of the blade defined, in this case, Nickel alloy INCONEL 718 is chosen from the ANSYS material database, the coordinate system for the analysis is defined, and the meshing processes initiated. The FEA technique solves the equations governing the motion of the structures on

infinitesimal volume elements of the solid domain. The meshing process divides the supplied geometry into infinitesimal elements linked by nodes. The resulting mesh is given in figure 8. The mesh element size for this analysis was chosen based on several critical factors, taking into account the distinction between critical and non-critical regions of the blade.

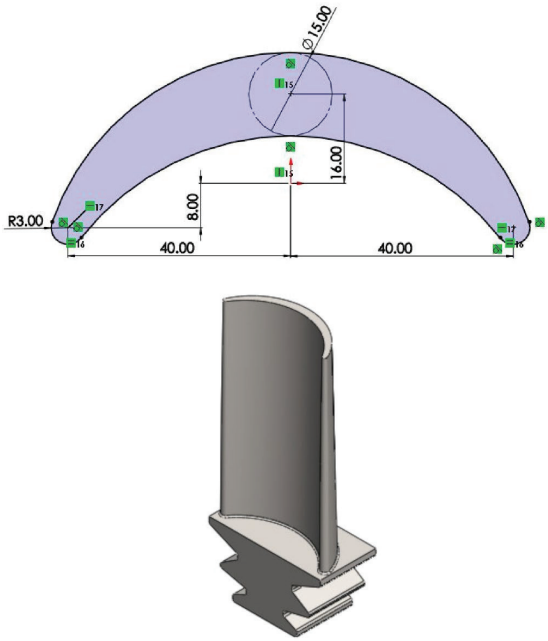

Figure 7. 3D model of the steam turbine blade adopted in the numerical solution

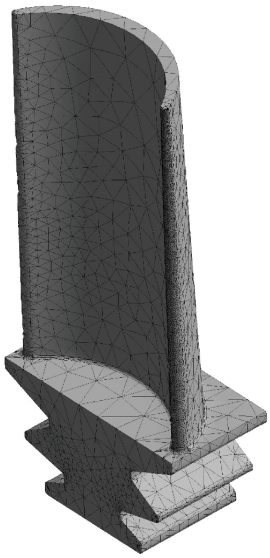

Figure 8. Steam turbine blade mesh

The blade's geometry has both simple and complex features, necessitating a variable mesh density approach, considering:

a) High stress gradient areas such as the root, trailing edge, and the leading edge of the blade, in which finer mesh elements were adopted. This facilitated accurate analysis of stress concentrations.

b) Uniform material regions such as the inner and outer arc of the blade, in which coarser mesh elements were considered. The homogeneous nature of the blade material allowed for coarser mesh in less critical areas without compromising the required accuracy.

This strategy reduced computational time and facilitated optimization on resource usage while maintaining the necessary accuracy.

The meshing process is proceeded by definition of boundary conditions on the mesh as depicted in the figure 9. This process involves applying a fixed support condition to the region where the blade attaches to the rotor disc section. Additionally, a rotational velocity of 3000 rpm is specified, which generally corresponds to the operating speed of the NPP steam turbines.

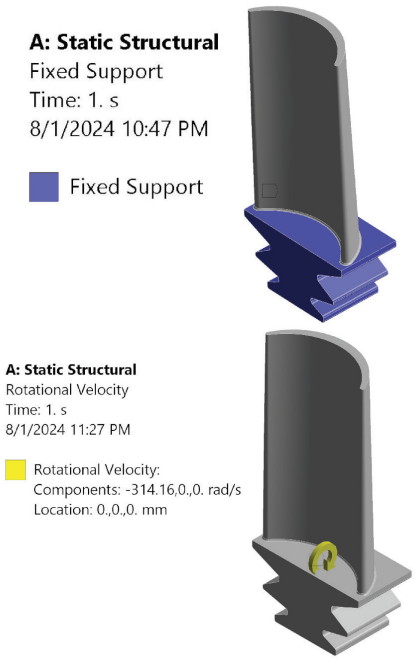

Figure 9. Boundary conditions

With the setup completed; including the material properties, coordinate system, mesh, and the boundary conditions, the Ansys static structural analysis module solution is run to evaluate the stresses and deformations on the turbine blade under the specified centrifugal loading conditions.

2.3.2 Solving for Bending Stress

Given that the simulation of steam flow using Ansys Computational Fluid Dynamics (CFD) is beyond the scope of the primary objective of this scientific work, the adopted approach in the computation of bending stress is not as straightforward as it would be if CFD is integrated in the solution. Instead of performing CFD simulation to determine the bending force acting on the blade, this value is arrived at by an analytical means. The bending force is then directly supplied as the primary bending load in the boundary conditions within the static structural analysis module. While a comprehensive CFD simulation would have provided a detailed and accurate representation of the steam-blade interaction, the adopted approach strikes a balance between computational feasibility and capturing the essential bending stress effects within the scope of the primary objective of the scientific work. The static structural module is then used to compute the bending stress in the same manner as previously executed in the case of the centrifugal stress. All the boundary conditions in this case are the same except for the bending force on the blade.

The notable difference in the boundary conditions is the introduction of the bending force acting on the blade. The analysis setup; including the geometry, material properties, coordinate system, and the mesh remain identical. Figure 10 is a depiction of the bending force applied to the turbine blade, with the fixed support constraint applied at the region where the blade attaches to the rotor section. From this we determine the equivalent force exerted by the steam jet impinging on the blade's surface.

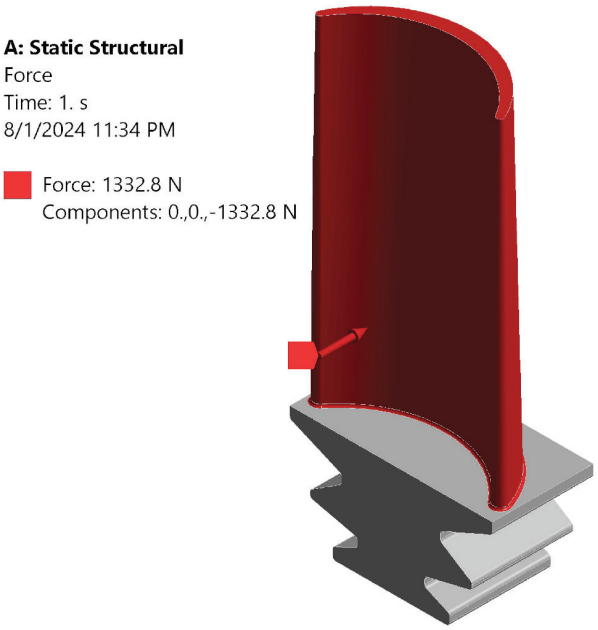

Figure 10. Equivalent force exerted by the steam jet impinging on the blade surface

3. RESULTS

Figure 11 is a depiction of the equivalent (Von-Mises) stress distribution and total deformation in the model; the results of the numerical computation of centrifugal stress. The color scale indicates the stress values, ranging from a minimum of 0,00 MPa to a maximum of 45,33 MPa. The areas with higher stress concentrations are highlighted in red and orange, while the lower stress regions are highlighted in blue and green. Figure 12 is a depiction of the bending stress and the associated total deformation force on the blade. The maximum bending stress experienced by the steam blade is 52,80 MPa. The comparison is given in the table 5.

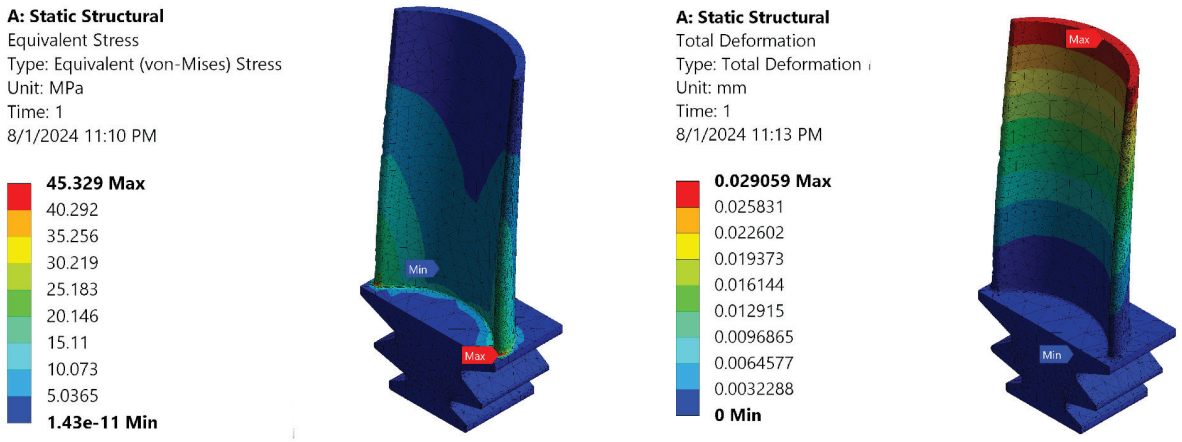

Figure 11. Centrifugal stress and associated total deformation

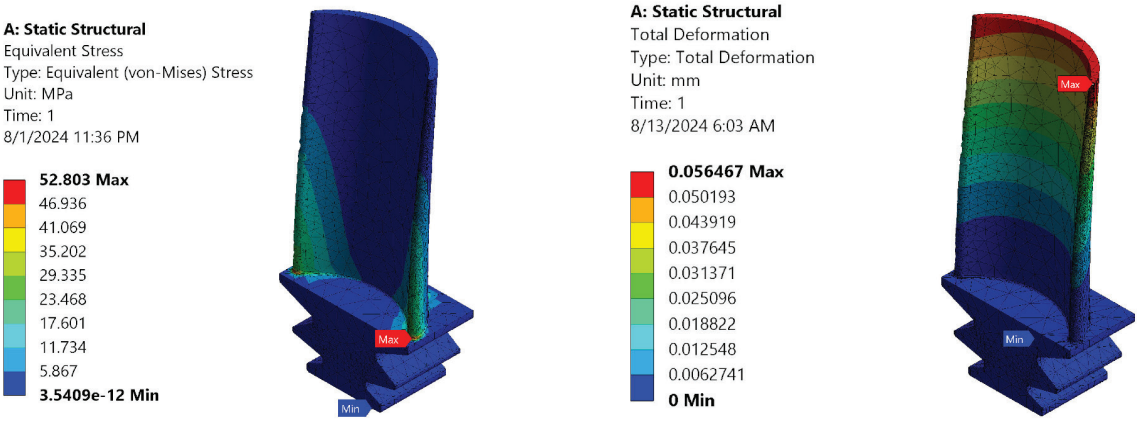

Figure 12. Bending stress and associated total deformation

Table 5. Comparison of analytical and numerical results

	Analytical	Numerical	% difference
Centrifugal stress, MPa	45,50	45,33	0,38
Bending stress, MPa	50,65	52,80	4,07
Total, MPa	96,15	98,13	2,02

CONCLUSION

The analytical technique yielded a total stress of 96,15 MPa, arrived at by summing up the centrifugal stress and bending moment stress caused by the impingement of steam jet on the blade. The total stress registered by the numerical technique is 98,13 MPa, slightly higher than the analytical results. The discrepancy in the computation of total stress by these two techniques represents 2,02% difference.

The resulting discrepancy, even though slightly significant, underscores the importance of

conducting comparative studies. While in this case the analytical method offers a simplified approach, a computational simulation provides a more comprehensive and potentially more reliable means of assessing the structural integrity and performance of the steam turbine blade under realistic operation conditions.

The difference in the results could be attributed to the limited scope of this scientific work, i.e., the decision not to incorporate the CFD analysis functionality into the static structural analysis workflow for purposes of computing the bending stress associated with the steam jet on the blade. However, the manifesting difference is one that is insignificant in the validation of the agreement between numerical and analytical computation techniques.

REFERENCES

1. **Verde C., Sánchez-Parra M.** Monitorability Analysis for a Gas Turbine Using Structural Analysis // IFAC Proceedings Volumes. – 2006.– Vol. 39, Issue 13. – P. 675-680. – ISSN 1474-6670. – DOI: 10.3182/20060829-4-CN-2909.00112
2. **Sinha, A., Swain, B., Behera, A., Mallick, P., Samal, S.K., Vishwanatha, H.M., Behera, A.** A Review on the Processing of Aero-Turbine Blade Using 3D Print Techniques // Journal of Manufacturing and Materials Processing. – 2022.– Vol. 6, Issue 1. – P. 16. – ISSN 2504-4494. – DOI: 10.3390/jmmp6010016
3. Thermal Engineering. (2019). What is Turbine Blade — Definition [online] Available at: https://www.thermal-engineering.org/what-is-turbine-blade-definition/ (Retrieved — 02/08/2024)
4. **Mingyu Zhu**. Design and Analysis of Steam Turbine Blades // Journal of Physics: Conference Series. – 2019.– Vol. 1300, Issue 1. – P. 012056. – DOI: 10.1088/1742-6596/1300/1/012056
5. Impulse Turbine and Reaction Turbine Working Principle [online] Available at: https://mechanicalengineeringsite.com/impulse-turbine-and-reaction-turbine-working-principle/ (Retrieved — 02/08/2024)
6. **Tateki Nakamura Kiyoshi Segawa Nobuhiro Isobe, Takashi Saito**. Highly-reliable Design Technology of Steam Turbine for Nuclear Power Plant, 2009
7. **Prabhunandan G.S, C., Byregowda H.V**. Static and Fatigue Analysis of a Steam Turbine Blade // International Journal of Latest Technology in Engineering, Management & Applied Science. – 2016.– Vol. 5, Issue 10. – P. 60-62. – ISSN 2278-2540
8. **Naveen kumar S., Konduru Sivaprasad Raju, Bhakiyaraja S., Vijayaganapathy D.** Static and Design Analysis of a Steam Turbine Blade // International Journal of Pure and Applied Mathematics. – 2018.– Vol. 120, Issue 6. – P. 3989-3996. – ISSN 1314-3395
9. **Anilkumar Konderu, Ganesh Purushothaman**. Determination of Thermal Stresses on Turbine Blades of Gas Turbine with NACA Airfoils by Finite Element Analysis // International Journal of Innovative Science and Research Technology. – 2017.– Vol. 2, Issue 12. – P. 393-398. – ISSN 2456-2165
10. **Swarnalata Naga Durga K., Sesha Talpa Sai P.H.V.** Design and Analysis of Steam Turbine Blade Using FEA // International Journal of Scientific Engineering and Technology Research. – 2015.– Vol. 4, Issue 29. – P. 5661-5665. – ISSN 2319-8885
11. ASM Aerospace Specification Metals Inc. – Special Metals INCONEL Alloy 718 [online] Available at: https://asm.matweb.com/search/SpecificMaterial.asp?bassnum=NINC34 (Retrieved – 02/08/2024)
12. Steam Turbine – Steam Turbine Velocity Diagram [online] Available at: https://www.mechanicaltutorial.com/steam-turbine-velocity-diagram (Retrieved — 03/08/2024)

13. Physics Forums: Science Discussion, Homework Help, Articles. (2017). Ansys Workbench Static Structural Analysis. [online] Available at: https://www.physicsforums.com/threads/ansys-workbench-static-structural-analysis.934410/ (Retrieved — 12/08/2024)

СПИСОК ЛИТЕРАТУРЫ

1. **Verde C., Sánchez-Parra M.** Monitorability Analysis for a Gas Turbine Using Structural Analysis // IFAC Proceedings Volumes. – 2006.– Vol. 39, Issue 13. – P. 675-680. – ISSN 1474-6670. – DOI: 10.3182/20060829-4-CN-2909.00112
2. **Sinha, A., Swain, B., Behera, A., Mallick, P., Samal, S.K., Vishwanatha, H.M., Behera, A.** A Review on the Processing of Aero-Turbine Blade Using 3D Print Techniques // Journal of Manufacturing and Materials Processing. – 2022.– Vol. 6, Issue 1. – P. 16. – ISSN 2504-4494. – DOI: 10.3390/jmmp6010016
3. Thermal Engineering. (2019). What is Turbine Blade — Definition [online] Available at: https://www.thermal-engineering.org/what-is-turbine-blade-definition/ (Retrieved — 02/08/2024)
4. **Mingyu Zhu**. Design and Analysis of Steam Turbine Blades // Journal of Physics: Conference Series. – 2019.– Vol. 1300, Issue 1. – P. 012056. – DOI: 10.1088/1742-6596/1300/1/012056
5. Impulse Turbine and Reaction Turbine Working Principle [online] Available at: https://mechanicalengineeringsite.com/impulse-turbine-and-reaction-turbine-working-principle/ (Retrieved — 02/08/2024)
6. **Tateki Nakamura Kiyoshi Segawa Nobuhiro Isobe, Takashi Saito**. Highly-reliable Design Technology of Steam Turbine for Nuclear Power Plant, 2009
7. **Prabhunandan G.S, C., Byregowda H.V**. Static and Fatigue Analysis of a Steam Turbine Blade // International Journal of Latest Technology in Engineering, Management & Applied Science. – 2016.– Vol. 5, Issue 10. – P. 60-62. – ISSN 2278-2540
8. **Naveen kumar S., Konduru Sivaprasad Raju, Bhakiyaraja S., Vijayaganapathy D.** Static and Design Analysis of a Steam Turbine Blade // International Journal of Pure and Applied Mathematics. – 2018.– Vol. 120, Issue 6. – P. 3989-3996. – ISSN 1314-3395
9. **Anilkumar Konderu, Ganesh Purushothaman**. Determination of Thermal Stresses on Turbine Blades of Gas Turbine with NACA Airfoils by Finite Element Analysis // International Journal of Innovative Science and Research Technology. – 2017.– Vol. 2, Issue 12. – P. 393-398. – ISSN 2456-2165
10. **Swarnalata Naga Durga K., Sesha Talpa Sai P.H.V.** Design and Analysis of Steam Turbine Blade Using FEA // International Journal of Scientific Engineering and Technology Research. – 2015.– Vol. 4, Issue 29. – P. 5661-5665. – ISSN 2319-8885
11. ASM Aerospace Specification Metals Inc. — Special Metals INCONEL Alloy 718 [online] Available at: https://asm.matweb.com/search/SpecificMaterial.asp?bassnum=NINC34 (Retrieved — 02/08/2024)
12. Steam Turbine – Steam Turbine Velocity Diagram [online] Available at: https://www.mechanicaltutorial.com/steam-turbine-velocity-diagram (Retrieved — 03/08/2024)
13. Physics Forums: Science Discussion, Homework Help, Articles. (2017). Ansys Workbench Static Structural Analysis. [online] Available at: https://www.physicsforums.com/threads/ansys-workbench-static-structural-analysis.934410/ (Retrieved — 12/08/2024)

Patrick Kiprotich Langat, 14.03.01 Nuclear Power Engineering and Thermal Physics, Bachelor's degree holder from the Institute of Nuclear Physics and Engineering, National Research Nuclear University MEPhI (NRNU MEPhI), Obninsk Institute for Nuclear Power Engineering (IATE), 249039, Kaluga Region, Obninsk City District, Obninsk, Studgorodok Territory, 1. E-mail: info@iate.obninsk.ru; ORCID: 0009-0005-6450-8692

Mariia Vladimirovna Volkova, PhD, Associate professor, Department of Nuclear Physics and Engineering, National Research Nuclear University MEPhI (NRNU MEPhI), Obninsk Institute for Nuclear Power Engineering (IATE), 249039, Kaluga Region, Obninsk City District, Obninsk, Studgorodok Territory, 1. E-mail: marissa36@yandex.ru ORCID: 0009-0005-1168-8247

Robert Folkenberg Siro, 14.04.01 Nuclear Power Engineering and Thermal Physics, Master's student of the Institute of Nuclear Physics and Engineering, National Research Nuclear University (NRNU MEPhI), 31, Kashirskoe Shosse, Moscow, 115409, Russian Federation, e-mail: sr008@campus.mephi.ru; ORCID: 0009-0008-1830-5677

Патрик Кипротич Лангат, 14.03.01 Ядерная энергетика и теплофизика, обладатель степени бакалавра Института ядерной физики и технологий, Национальный исследовательский ядерный университет МИФИ (НИЯУ МИФИ), Обнинский институт атомной энергетики (ИАТЭ), 249039, Калужская область, городской округ Обнинск, г. Обнинск, территория Студгородок, 1. Эл. почта: info@iate.obninsk.ru; ORCID: 0009-0005-6450-8692

Мария Владимировна Волкова, к.т.н., доцент, отделение Ядерной физики и технологий, Национальный исследовательский ядерный университет МИФИ (НИЯУ МИФИ), Обнинский институт атомной энергетики (ИАТЭ), 249039, Калужская область, городской округ Обнинск, г. Обнинск, территория Студгородок, 1. Эл. почта: marissa36@yandex.ru; ORCID: 0009-0005-1168-8247

Роберт Фолкенберг Сиро, 14.04.01 Ядерная энергетика и теплофизика, магистрант Института ядерной физики и технологий, Национальный исследовательский ядерный университет (НИЯУ МИФИ), 31, Каширское шоссе, Москва, 115409, Российская Федерация, E-mail: sr008@campus.mephi.ru, ORCID: 0009-0008-1830-5677

International Journal for Computational Civil and Structural Engineering, 21(1) 202–221 (2025)

DOI:10.22337/2587-9618-2025-21-1-202-221

LONGITUDINAL DEFORMATIONS OF SHORTENING OF STEEL-REINFORCED CONCRETE STRUCTURES UNDER COMPRESSION FROM SHORT-TERM LOADS

Denis V. Konin

TSNIISK named after V. A. Koucherenko JSC Research Center of Construction, Moscow, RUSSIA

Abstract: Determination and investigation of longitudinal deformations of shortening of steel-reinforced concrete structures is an important step in the calculation of complex spatial schemes of buildings. Ignoring these deformations can make it difficult to operate the facility and, in some cases, lead to the failure of adjacent structures. The study of longitudinal deformations of shortening of steel-reinforced concrete structures has not been given due attention before. The longitudinal deformations of shortening for steel-reinforced concrete compressed elements using a large range of heavy concretes (from B25 to B80) and percentages of reinforcement (from 0 to 22%) are estimated. The deformations were calculated. The analysis of experimental data obtained during testing of conditionally centrally compressed models of columns of steel-reinforced concrete structures is presented. It is shown that the existing diagrams of concrete work do not accurately describe the work of a composite steel-reinforced concrete structure, it is its shortening and reduced rigidity. When the structure is compressed, concrete loses its destruction at earlier stages of loading than it would be for concrete or reinforced concrete. This fact is caused by the stress-strain state of the concrete section separated by steel elements, as well as the effects of early detachment and slippage along the «steel-concrete» contact surface. It is necessary to use a system of additional coefficients to eliminate the established discrepancy in determining the magnitude of longitudinal deformation (shortening) under the action of short-term loads and experimentally obtained data. These coefficients should increase the theoretical value of the expected relative deformations and consider the features of the work of conventional and high-strength concrete as part of compressible steel-reinforced concrete structures. When determining the stiffness values for steel-reinforced concrete structures under the action of short-term loads and bringing the calculated longitudinal stiffness to a value close to experimental data, it is proposed to introduce an additional coefficient. This coefficient further reduces the longitudinal rigidity of the structure depending on the stress level in concrete and steel.

Keywords: central compression, off-center compression, vertical deformation, longitudinal stiffness, steel-reinforced concrete structure, column, high-rise building

ПРОДОЛЬНЫЕ ДЕФОРМАЦИИ УКОРОЧЕНИЯ СТАЛЕЖЕЛЕЗОБЕТОННЫХ КОНСТРУКЦИЙ ПРИ СЖАТИИ ОТ НЕПРОДОЛЖИТЕЛЬНЫХ НАГРУЗОК

Д.В. Конин

ЦНИИСК им. В.А. Кучеренко АО «НИЦ «Строительство», г. Москва, РОССИЯ

Аннотация: Определение и исследование продольных деформаций укорочения сталежелезобетонных конструкций является важным этапом в вопросе расчета сложных пространственных схем зданий, поскольку их игнорирование может затруднить эксплуатацию объекта и, в некоторых случаях, привести к выходу из строя примыкающих конструкций. Ранее исследованию продольных деформаций укорочения сталежелезобетонных конструкций не уделялось должного внимания. Дана оценка продольных деформаций укорочения для сталежелезобетонных сжатых элементов с применением большого диапазона тяжелых бетонов (от В25 до В80) и процентов армирования (от 0 до 22%), произведен расчет деформаций. Представлен анализ экспериментальных данных, полученных при испытании условно центрально сжатых моделей колонн сталежелезобетонных конструкций. Показано, что существующие диаграммы рабо-

ты бетона не вполне точно описывают работу составной сталежелезобетонной конструкции, в частности, ее укорочение и приведенную жесткость. При работе конструкции на сжатие бетон теряет разрушается на более ранних этапах нагружения, чем это было бы для бетона или железобетона. Этот факт вызван напряженно-деформированным состоянием разделенного стальными элементами бетонного сечения, а также эффектами раннего отслоения и проскальзывания по контактной поверхности «сталь-бетон». Для того, чтобы устранить установленное разночтение в определении величины продольной деформации (укорочения) при действии кратковременных нагрузок и экспериментально полученных данных, необходимо использовать систему дополнительных коэффициентов, которые должны увеличивать теоретическую величину ожидаемых относительных деформаций, а также должны учитывать особенности работы бетонов обычной и высокой прочности в составе сжимаемых сталежелезобетонных конструкций. При определении значений жесткостей для сталежелезобетонных конструкций под действием кратковременных нагрузок и приведении расчетной продольной жесткости к величине, близкой к экспериментальным данным, предложено ввести дополнительный коэффициент, который дополнительно понижает продольную жесткость конструкции в зависимости от уровня напряжений в бетоне и стали.

Ключевые слова: центральное сжатие, внецентренное сжатие, вертикальная деформация, продольная жесткость, сталежелезобетонная конструкция, колонна, высотное здание

INTRODUCTION

The columns of high-rise buildings and the supporting structures of stadium coverings, where the elements are subjected to significant compression forces, are usually designed in steel-reinforced concrete structures, in particular, columns with rigid reinforcement. For correct analysis of complex spatial schemes of buildings, it is extremely important to correctly determine the longitudinal deformations of steel-reinforced concrete structures. Despite the fact that the current normative documents on analysis and design of such structures SP 63.13330 “Concrete and Reinforced Concrete Structures”, SP 267.1325800 “Buildings and High-Rise Complexes...”, SP 266. 1325800 “Steel-reinforced concrete structures...” do not regulate the ultimate values of shortening for eccentrically compressed elements. Ignoring these deformations can complicate the operation of the facility and in some cases lead to the failure of adjacent structures. The effect of longitudinal deformations in multi-storey and high-rise buildings can result in misalignment of the vertical cells of the frame, which should have deformations no greater than those specified in clause D.1.9 of SP 20.13330 and clause 8.2.4.16 of SP 267.1325800 “Buildings and high-rise complexes...” where the allowed displacements are of 1/300 of the floor height and less.

Cells skew is calculated by the formula f1/hs + f2/l, where f1 and f2 are horizontal and vertical displacements respectively, and hs and l - cell height and its span as can be seen from Figure E.3 in SP 20.13330 “Loads and Actions". In addition, during construction and operation of high-rise buildings the standards GOST 27751-2014 “Reliability of building structures and foundations. Main provisions” and GOST 31937-2011 ”Buildings and structures. Rules for inspection and monitoring of technical condition” stipulate monitoring of deformations of structures.

Shear deformations of the frame cell can cause damage to the exterior structural components, facade modules, partition walls. It can also impede the operation of elevators. The drift of the top of the building from the vertical, as well as standard formulas for cell deformation only regulate the slab shear relative to each other and do not include estimates of potential additional vertical deformation. For example, damage can also occur in high-rise and multi-floor buildings due to varying column shortening. In the U.S. structural design codes [1, 19], the shortening effect is accounted for by the so-called Drift Measurement Index (DMI = Drift Measurement Index) for high-rise structures. This value is essentially the average shear deformation of a vertical rectangular cell. Its influence on envelope structures for their main types is taken with regard to [2].

It is obvious that in the absence of experimentally and theoretically substantiated methodology for calculation of vertical longitudinal deformations of complex composite steel reinforced concrete structures almost impossible to reliably determine the values of controlled vertical deformations of the entire building frame and its structural components, misalignments of frame cells, which are permissible for a particular facility. For large-span structures, correct determination of longitudinal deformations of steel- reinforced concrete support structures guarantee normal operation of coverings and grandstand structures resting on them.

The papers [3, 4] demonstrate the results of tests of eccentrically compressed steel-reinforced concrete elements with a ratio of longitudinal reinforcement from 3 to 20 percent. The elements are made of concrete with compressive strength class up to B90 and fiber-reinforced concrete. In these articles, as well as in [5], devoted to the calculation of columns for oblique eccentric compression, the test results and calculations for the ultimate limit states are presented in detail.

The design of frames of unique buildings and structures with steel-reinforced concrete elements is based on the use of certified software systems that implement the finite element method. Columns and supports of these structures, as a rule, are modeled as bars of reduced stiffness, or as a "combined" design by solid elements (separately steel, separately concrete and rebars), combined by common nodes. Such models, even in calculations with respect to nonlinear deformation diagrams of steel and reinforced concrete, cannot fully account for the behavior of the composite structure, in particular, the possibility of slippage of concrete relative to the steel core [4].

The review of experimental studies in Russia and the world and normative documents [6, 13] shows that earlier the issue of studying longitudinal shortening deformations of steel-reinforced concrete structures was not paid proper attention to. In contrast to long-term shortening due to creep and shrinkage of concrete [14, 15, 16, 19, 20, 21], which have been extensively studied in recent years, the regularities of deformations of steel-reinforced-concrete structures under short-term loads are poorly studied.

RESEARCH METHODS

The laboratories of the V.A. Kucherenko Central Research Institute of Steel and Concrete Structures have carried out large-scale tests of steel-reinforced concrete structures for central and off-centered compression. Detailed test results are given in [3, 4]. The paper [7] provides a methodology for calculating the strength of steel reinforced concrete compression-bending elements (columns) using a nonlinear deformation model, which corresponds to the current standards for the analysis of reinforced concrete structures such as SP 63.13330. The ultimate limit state of the structure is determined by reaching the ultimate longitudinal strains of concrete, reinforcement and rigid reinforcing steel. The ultimate value of longitudinal strains of concrete $\varepsilon_{b,ult}$ is accepted depending on the ratio of concrete edge strains ε_1 and ε_2 by linear interpolation from -0.002 at $\varepsilon_1/\varepsilon_2=1$ to -0.0035 at $\varepsilon_1/\varepsilon_2\leq 0$, where ε_2 is the concrete strain at the most compressed edge with the minus sign. In this case, the strength of the tensile concrete is not accounted for in the calculation. The ultimate value of the strain of the steel of the core and tensile reinforcement is assumed to be 0.025 for central and eccentric compression.

In actual norms for the calculation of steel structures SP 16.13330 "Steel structures" a generalized diagram of steel deformation under load action is given for different steels. Clause 4.2.4 establishes the possibility of modeling of nonlinear operation of steel according to the diagram of Figure B.1 and Table B.9 in SP 16.13330.2017. Figure 1a,b shows stress vs. strain relationships for steels from C255 to C550 in accordance with the normative parameters. The ultimate strain of steel should be taken corresponding to the end of the yield plane. For steels with yield strengths

from 255 to 550 MPa, the value of the ultimate strain will vary from 0.017 to 0.047 respectively. In this connection, it is obvious that it is incorrect to take the ultimate strain as 0.025 as for reinforcing steel, regardless of the yield strength of the steel. Since for steels C235, C245, C255 this value will correspond to the steel performance in the self-strengthening region above the yield point, and for C355 and above the plastic properties of the steel will not be fully utilized. It is important to note that ignoring the performance of steel in the elastic-plastic deformation region in calculations using a two-line diagram of steel performance (the so-called "Prandtl diagram") can lead to a distorted picture of strain distribution in the cross-section of the steel-reinforced concrete element and inaccurate results of the shortening calculation.

In order to properly account for concrete strains in steel and reinforced concrete structures, several variants of diagrams of behavior under load can be adopted. In recent standards it is allowed to use two- and three-line diagrams (clauses 6.1.19...6.1.21 in SP 63.13330), as well as curvilinear diagram of concrete deformation (Appendix G in SP 63.13330), which is developed on the basis of the works summarized in the monograph by Academician N.I. Karpenko [8, 12, 16]. Also, Prof. G.V. Murashkin and co-authors developed and presented in [9, 10] an exponential version of the concrete deformation diagram. In addition to those listed above, it is possible to use the curvilinear diagram given in the European Union standards (Eurocode 2). In the present work we will limit ourselves to consideration of three-line diagrams (Figure 1 c) and curvilinear diagrams (Figure 1 d), since by now they are reflected in normative documents, implemented in finite element program complexes, tested by a large number of experimental data and many years of experience in design and operation of real buildings and structures.

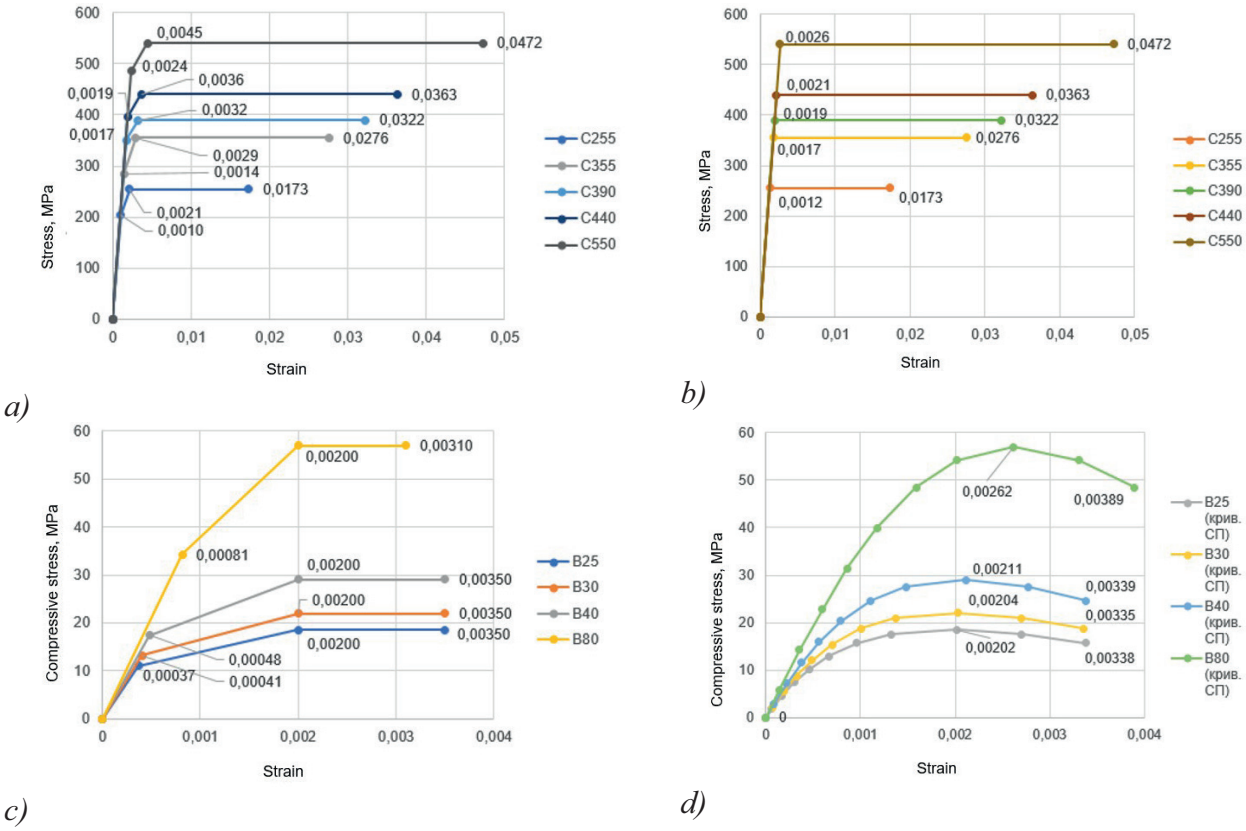

a) *b)* *c)* *d)*

Figure 1. Deformation diagrams for steel and concrete: a - three-linear for steel (S3L), b - bilinear for steel (S2L), c - three-linear for concrete according to SP 63.13330 (B3L), d - curvilinear for concrete according to SP 63.13330 (BCL)

Calculation of theoretical longitudinal deformations of a bar subjected to compression without moments is carried out in the following way to construct theoretical curves. At the break points of each diagram, the boundaries of the loading stages (I, II, III...) are drawn, within which the shortenings of the structure are calculated. Thus, Figure 2 shows an example of splitting two- and three-line diagrams into stages for concrete B80 and steel C255, Figure 3 shows an example of splitting a curvilinear diagram of concrete B80 with a three-linear diagram of steel C255 performance. The longitudinal deformation of the bar at the first (I) Δl_I and subsequent stages (II, III, ...) and the total longitudinal deformation (shortening) ΔL are calculated as follows:

$$\Delta l_{I,\ II,\ III\ldots} = \Delta\varepsilon_{I,\ II,\ III\ldots} L, \quad \Delta L = \sum_{m=I}^{VIII} \Delta l_m \qquad (1)$$

where L is the effective design length of the bar, $\Delta\varepsilon_{I,\ II,\ III\ldots}$ is the range of strain on the considered section of the diagram.

For each stage, the corresponding moduli of deformation for steel, concrete, and reinforcement are determined. For stage I, these moduli will be denoted as $E_{st,I}, E_{b,I}, E_{s,I}$ respectively. For each stage of the steel-reinforced concrete structure, the concrete reduction factors are calculated, and then the area of the reduced section A_{red}, the longitudinal stiffness of the reduced section within the stage ΔD_a using stage I as an example is calculated by the formula:

$$\alpha_{st,I} = \frac{E_{st,I}}{E_{b,I}}, \alpha_{s,I} = \frac{E_{s,I}}{E_{b,I}}, \qquad (2)$$

$$A_{red,I} = A_b + A_{st}\alpha_{st,I} + A_s\alpha_{s,I} \qquad (3)$$

$$\Delta D_{a,I} = E_{b,I} A_{red,I} \qquad (4)$$

where A_b, A_{st}, A_s are the areas of concrete cross-section, steel core cross-section and rebars' cross-section respectively. The increments of longitudinal force ΔN up to the corresponding strain stage boundaries and the limiting value of longitudinal force N at which the strain increases without increasing the load are calculated using the formulas:

$$\Delta N_I = \Delta\varepsilon_I\ \Delta D_{a.I}\ ,\ N = \sum_{m=I}^{VIII} \Delta N_m \qquad (5)$$

By performing calculations using the above formulas allows us to estimate the value of shortening in compression and compare it with the corresponding results of numerical modeling and experimental data.

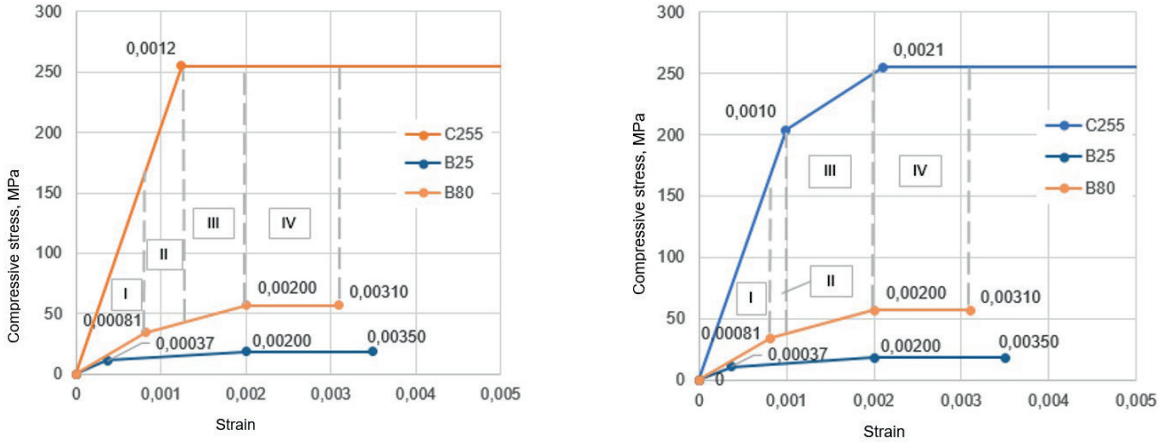

a) *b)*

Figure 2. To the description of the stages of performance of steel-reinforced concrete compressed bar: a - superposition of two-line diagram of steel and three-line diagram of concrete (S2L+B3L), b - superposition of three-line diagrams of steel and concrete (S3L+B3L).

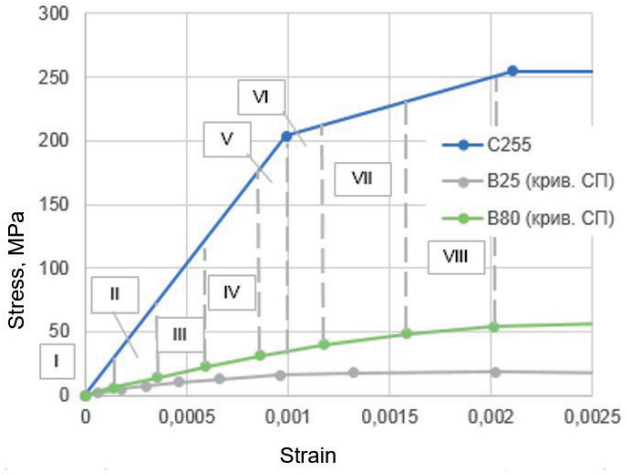

Figure 3. To the description of the stages of steel-reinforced concrete compressed bar performance: combination of three-line diagram for steel and curvilinear diagram for concrete respectively (S3L+BCL)

To verify the solution of this problem, the results of central compression tests of columns with I-beam rigid reinforcement and concrete prisms without reinforcement have been examined. The study of only centrally compressed models, centering of which is performed with special care during the tests, allows us to reliably assess the degree of joint operation of the structure and correctly measure the actual shortening of the models without the effects of buckling at eccentric compression and non-uniform loading of different materials in the cross-section. Models K-3 and K-13 have a nominal cross-sectional dimension of 400x400 mm in concrete, the length of the column model is 1640 mm. The cross section of the steel core is a welded I-beam made of sheet steel C255 according to GOST 27772. Concrete was of compressive strength class B25. Calculated longitudunal reinforcement was of class A400, diameter - 8 mm (8 pcs.). Transverse reinforcement was of class A240, 120 mm spacing, 4 mm diameter. The reinforcement ratio is 10.7%. To provide joint performance of the steel core with concrete it is envisaged to install studs on the walls of the I-beams made of short pieces of reinforcement with diameter of 8 mm, length of 90...120 mm and spacing of about 200 mm. The general view of the steel core and location of the studs is shown in Figure 4, a. Models K10-3, K10-8, K10-11 have smaller concrete cross-sectional dimensions of 150x150 mm. The length of the column model is 600 mm. The steel core is an I-beam made of two channels No.10 reinforced with sheet steel along the wall to achieve a higher ratio of reinforcement. For this purpose, steel C255 according to GOST 27772-88 and concrete of class B80 were used. Working reinforcement was of class A400C; 4 pcs number of bars, 8 mm diameter. Transverse reinforcement was of class A240, 50 mm spacing, 4 mm diameter. The ratio of reinforcement is from 10% to 17.5%. The cross-section is shown in Figure 4, b. In addition to the steel reinforced concrete models, concrete prisms without additional reinforcement were tested with characteristics corresponding to the K10 model group made of B80 concrete. Also, 3 cube specimens with a side of 100 mm were prepared for each concrete casting batch, that is 39 specimens tested in total. The characteristics of the tested models are summarized in Table 1. The calculated shortenings according to formulas 1...5 are given in Table 2 for different curves, the designations of which are adopted in accordance with Figure 1.

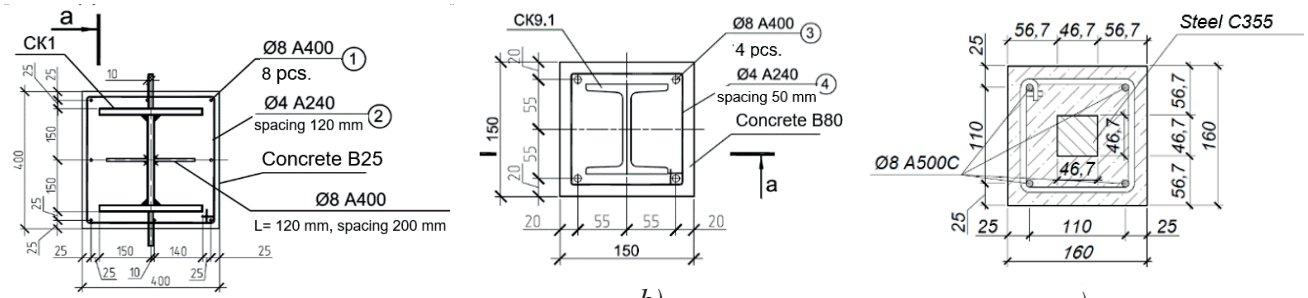

Figure 4. Tested cross sections: a - K-3, K-13, b - K10-3, K10-8, K10-11, K-9-7, c - SQ type model with square core (FEM only)

Table 1. Parameters of the tested specimens

No	μ, % reinf.	Core steel	Concrete	Additional anchorage of the core	Concrete age at test, days	Compress. Strength of cubes, MPa	*h*, cm	*b*, cm	*L*, cm	Ultimate load N_{ult}, rN		
										Characteristic	FEM	Test (mean)
1	2	3	4	5	6	7	8	9	10	11	12	13
K-3	10.7	C255	B25	+	135	28.55	39.7	39.9	164	6481	6480	6592
K-13	10.7	C255	B25	+	135	28.55	40.0	39.9	164			
K10-3	22.0	C255	B80	-	27	93.8	15.1	15.1	60	2037	2038	2423
K10-8	22.0	C255	B80	-	27	93.8	15.1	15.2	60			
K10-11	22.0	C255	B80	-	94	104.4	15.2	14.9	60			
CP 1	0.0	-	B80	-	90	97.9	15.0	14.9	60	1258	-	1733
CP 2	0.0	-	B80	-	90	97.9	15.0	15.0	60			
CP 3	0.0	-	B80	-	90	97.9	15.0	15.0	60			
SQ	22.0	C255	B80	-	-	-	15.0	15.0	60	2037	2037	-

Notes:
μ is the ratio of reinforcement equal to the ratio of the area of steel in the cross-section to the area of flexible and rigid reinforcement; *h*, *b* is the dimensions of the cross-section of the concrete part, *L* is the length of the specimen, along the axis of which the external load is transferred; N_{ult} is the ultimate load, determined by characteristic values of strength of materials (characteristic), by FE-modeling (FEM), Test - by the results of the experiment.

Table 2. Theoretical shortening according to different diagrams, mm

No	At failure (for ε_{b2})			At appearing of plastic strain in concrete (for ε_{b0})		
	S2L+B3L	S3L+B3L	S3L+BCL	S2L+B3L	S3L+B3L	S3L+BCL
1	2	3	4	5	6	7
K3 K13	5.74	5.74	5.54	3.28	3.28	3.31
K-10-11 K-10-8 K-10-3	1.86	1.86	1.99	1.20	1.20	1.21
CP 1 CP 2 CP 3	1.86		2.75	1.86		1.85
SQ	1.55	1.55	1.31	1.00	1.00	1.01

The tests were carried out using a calibrated hydraulic jack creating axial load up to 1000 tf (10 MN) in the V.A. Kucherenko Central Research Institute for Structural Engineering. Loading was carried out in accordance with GOST 8829-94 "REINFORCED CONCRETE AND PREFABRICATED CONCRETE BUILDING PRODUCTS. Loading test methods. Assesment of strength, rigidity and crack resistance". According to standard methodic, the load was applied by steps, each step was not more than 10% of the failure load. The endurance for 10 minutes was carried out at each step. When the design (control load) was reached, the endurance was carried out for 30 minutes. Instrument readings were reading continuously at each step of loading with a frequency of 1 Hz. The "central" compression of the model was ensured by centering the column model relative to the marks on the press tables, as well as by monitoring the readings of strain gauges during the first steps of loading. If the corresponding strain gauges showed significant strain differences, the model was additionally aligned to the table. Thus, all the stress non-uniformities arising as a result of the tests at "central" compression in cross-sections are caused only by random internal eccentricities of the model. In the course of the tests under stepwise application of compressive load, the stresses in steel and concrete elements of column models in longitudinal and transverse directions, vertical absolute shortening of the models by means of digital displacement sensors fixed on the upper and lower tables of the press with a measurement accuracy of 0.001 mm were recorded at each step.

Finite element numerical simulation in ATENA PC was performed for models similar in size and material properties, taking into account the nonlinear behavior of materials: curvilinear diagram for concrete and three-linear diagram for steel. The number of steps and mesh size for each model was also selected separately. The minimum number of loading steps was at least 20...30 and the mesh size was about 20 mm. To describe the performance of concrete, the material model Fracture-Plastic Constitutive Model (CC3DCementitious2) was utilized. It is based on the combination of the tensile fracture model with the compressive fracture model of the material. The FE models completely replicated the geometry and mechanical properties of materials of the tested structures as shown in Figure 4 and Table 1. In addition, bars with a square core as shown in Figure 4,c were modeled to verify the effect of cross-sectional shape on concrete performance. Structures with contact interaction between steel and concrete were also modeled. It was found that for models with small or zero eccentricities, the presence of a finite contact interaction at the steel-concrete joint practically does not affect the results of calculations of longitudinal deformations of the column. That is, there is no influence of the contact on the value of the ultimate load and on the value of the ultimate longitudinal deformation of the bar. The difference between forces and deformations for similar models with and without modeling of contact interaction is less than 0.5%. Therefore, the contact interaction at the joint "steel-concrete" was not modeled in a special way, and the finite elements of steel and concrete had common nodes in the calculation scheme. The view of FE models is shown in Figure 5.

Capacity calculation according to the nonlinear deformation model [3] practically does not depend on the type of concrete state diagram to determine the cracking moment M_crc and ultimate moment M_ult in reinforced concrete eccentrically compressed and bent elements, as shown in [11, 12]. When comparing the results of calculation according to SP 63.13330 and experimental data, the authors of [11] found differences of no more than 7.8% and 6.8% of the above moments, respectively, for different variants of concrete constitutive diagrams.

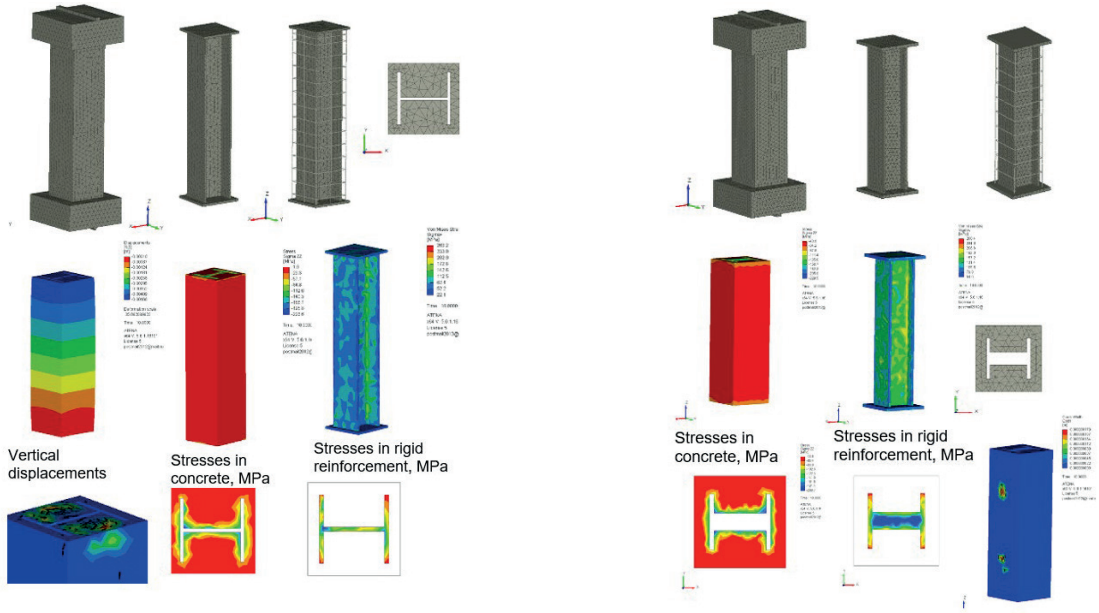

a) b)

Figure 5. FE models: a - model K3; b - model K10-3

RESULTS AND DISCUSSION

The comparative analysis of theoretical, numerical calculations and experimental data on shortening deformations are shown in Figures 6, 7. The comparison of models was performed in the dimensionless coordinate by force, since it is necessary to compare the theoretical calculation, in which the characteristic values of strength and deformation properties of materials are used, and experimental data, in which the values of destructive loads are slightly overestimated relative to the characteristic values. That is, one of the coordinates of the graphs was the value $N/N_{(u,n)}$, where N is the current compressive load in tests or calculations, and $N_{(u,n)}$ is the characteristic ultimate compressive load, which is calculated by the formula:

$$N_{u,n} = R_{bn}A_b + R_{yn}A_{st} + R_{sn}A_s, \quad (6)$$

where R_{bn}, R_{yn}, R_{sn} are the characteristic values of concrete compressive strength, yield strength of steel, design strength of reinforcement, respectively. Thus, the value of $N/N_{u,n}$=1 corresponds to the standard strength of the cross-section ignoring the material and operational condition partial factors. For the tested concrete prisms without reinforcement, $N_{u,n}=R_{bn}A_b$. Also in the plots, horizontal dashed lines show the load level corresponding to the design values of material strength R_b, R_y, R_s calculated by the formula:

$$N_u = R_bA_b + R_yA_{st} + R_sA_s \quad (7).$$

Table 3 summarizes the typical points of the theoretical and experimental curves with each other, and below are figures with strain plots (Figures 6, 7, 8) for the respective models.

A. Axial deformations (shortening)

Figure 6,a shows the shortening deformations for unreinforced models (concrete prism - CP) made of concrete of compressive strength class B80. In this figure and further gray dashed lines show the experimental data for the same type of models. Blue and green lines respectively indicate theoretical deformations calculated by formulas 1...5, based on three-line and curvilinear diagrams of concrete performance according to SP 63.13330. Fractures of the models during tests occurred with explosive release of energy. It can be seen that the deformation sections from 0 to $N/N_{u,n}$=1.0...1.1 are practically linear.

This corresponds to the actual concrete deformation diagrams obtained by other authors (e.g., [17, 18]) in the section from 0 to the characteristic compressive strength for B80 concrete (R_{bn}=57 MPa; $N_{u,n}$=1). In this case, the actual "straightness" of the experimental curves indicates that a certain margin will be obtained when calculating the shortening strains using the normative curves. At the same time, the curvilinear diagram gives a slightly larger reserve than the three-line diagram at stresses close to the calculated values of concrete strength.

Table 3. Experimental shortenings

No.	Experimental shortening, mm				Shortening by FEM, mm	
	At failure		At the initiation of plastic deformation in concrete		Max	The initiation of plastic deformation in concrete
	For unit test	Mean	For unit test	Mean		
1	2	3	4	5	6	7
K3	6.33	6.24	3.51	3.69	5.16	2.85
K13	6.15		3.87			
K-10-11	2.38	2.17	1.84	1.78	1.68	1.06
K-10-8	2.33		1.81			
K-10-3	1.80		1.68			
CP 1	2.03	1.96	1.40	1.41	-	-
CP 2	2.15		1.51			
CP 3	1.69		1.31			
SQ	-	-	-	-	1.36	1.04

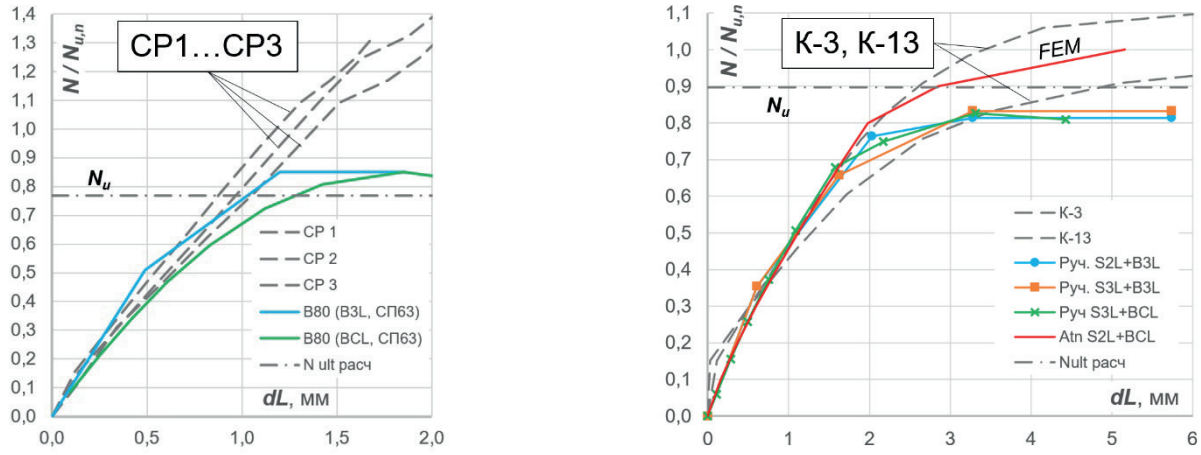

a) b)

Figure 6. Comparison of shortening diagrams: a - concrete models (B80), b - steel reinforced concrete models K3 and K13 (B25)

Figures 6, b and 7 present the shortening strains for the models with rigid reinforcement made of concrete of compressive strength classes B25 and B80 (gray dashed lines). The blue, orange and green lines show the theoretical shortenings determined by formulas 1...5 for various combinations of steel and concrete diagrams. The red line shows the results of FEM analysis utilizing bilinear steel diagram and curvilinear concrete diagram. All theoretical curves follow practically the same trajectory. This circumstance indicates insignificant influence of the diagram type on the linear shortening of the structure.

Experimental shortening curves for the models with concrete B25 have the form of smooth curves (Figure 6, b) with gradually increasing shortening with increasing load. In this case, we can state a good agreement of theoretical assumptions for calculations by formulas 1...5 and by FEM (red solid line).

Models with B80 concrete are shortened according to a slightly different law close to linear (Figure 7), as it was shown above for concrete models without reinforcement (CP) in Figure 6, a. That is, the presence of rigid reinforcement (μ=22%) in the cross-section of the model significantly changes the shortening strain pattern. At load $N/N_{u,n}$=0.5...0.6 the average shortening strain according to the experiment is about 0.85 mm, while the theoretically determined one is about 0.55 mm. At the same time, the values of shortening at load levels $N/N_{u,n}$=0.87, corresponding to the beginning of concrete failure and strains ε_{b0}=0.002, agree with the theoretical values satisfactorily.

Figure 8, a shows a comparison of theoretical and finite element calculations of linear deformations for a structure with a square core. It can be seen that at loads $N/N_{u,n}$=0.7...0.9 the finite element model performs somewhat differently than expected theoretically by formulas 1-5. Comparing the curves obtained by FEM for the structure with I-beam and square cores (Figure 8, b) it can be concluded that the square core operates more efficiently and the structure with it deforms less by about 20-25% at loads close to the calculated values of material strength.

Comparison of experimental results and calculations are summarized in Table 4. Formulas for determining the difference of the compared values are given in the head of the table, where [Teor.] denotes the values calculated by formulas 1...5; [Test] are the values obtained from the results of experiment; [FEM] are the values obtained from the results of FEM simulation.

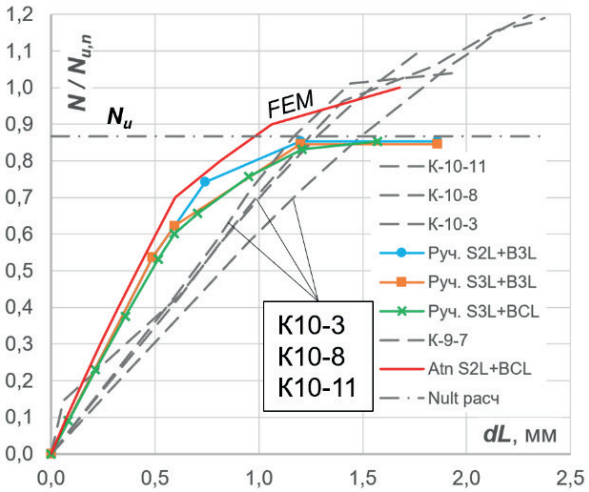

Figure 7. Comparison of shortening diagrams of steel-reinforced concrete models K10 (B80)

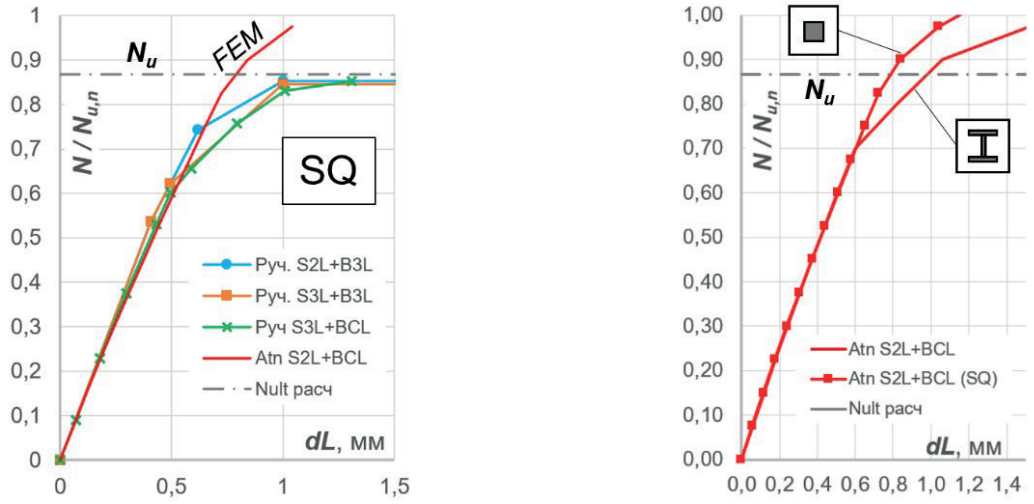

a) *b)*

Figure 8. Comparison of shortening diagrams of steel-reinforced concrete models: a - with square core SQ (B80), b - comparison of structure performance with square and I-beam core

It can be seen that the values in columns 2...7 and 8...9 are negative, which means that the calculation of linear shortening deformations using formulas 1...5 or FEM using characteristic diagrams does not provide a reserve relative to the experimental data. That is, if the shortening is calculated according to the standards, underestimated values will be obtained than those obtained by experiment. Thus, the difference for concrete of ordinary strength (type B25) will be 11...17%, and for high-strength it is 14...32%. This circumstance cannot be considered satisfactory. Let's pay attention to the fact that the results of comparison of capacity calculations excluding stability effects with the experiment provide a relatively good convergence and the calculation method according to the formulas of SP 266 or FEM gives the necessary and expected reserve. To illustrate this fact, one can compare the values of columns 11...13 in Table 1.

To eliminate the revealed discrepancy in the value of longitudinal shortening deformation under the action of short-term (short-term, e.g., wind) loads and experimentally obtained data, it is necessary to use a system of additional coefficients. These coefficients should increase the theoretical value of the strains, and should also take into account the peculiarities of concrete of ordinary and high strength as part of compressible steel and reinforced concrete structures. It is established that the following formulas should be used to plot concrete deformation diagrams in accordance with the methodology of SP 63.13330:

$$\varepsilon_{b0(composite)} = 1{,}15\varepsilon_{b0},\ \varepsilon_{b2(composite)} = 1{,}15\varepsilon_{b2}$$ – for concrete class B25, (8)

$$\varepsilon_{b0(composite)} = 1{,}54\varepsilon_{b0},\ \varepsilon_{b2(composite)} = 1{,}18\varepsilon_{b2}$$ for concrete of class B80 (9)

If the coefficients specified in formulas 8, 9 are used, the necessary reliability and reserve of 2 to 6% for B25 concrete and 1 to 8% for B80 concrete will be realized in structures under short-term loads (see the values in brackets in Table 4). For other intermediate concretes it is allowed to interpolate the presented coefficients by strain values.

Table 4. Comparison of obtained values, %

No.	$\frac{[Teor.]-[Test]}{[Test]}$						$\frac{[FEM]-[Test]}{[Test]}$		$\frac{[Teor.]-[FEM]}{[FEM]}$	
	At failure			At the initiation of plastic deformation of concrete			At failure	At the initiation of plastic deformation of concrete	At failure	At the initiation of plastic deformation of concrete
	Data used									
	Table 2 Table 3	Table 2 Table 3	Table 2 Table 3	Table 2 Table 3	Table 2 Table 3	Table 2 Table 3	Table 3	Table 3	Table 2 Table 3	Table 2 Table 3
	Type of theoretical material deformation curve (S - steel according to SP 16, B - concrete according to SP 63)									
	S2L+ B3L	S3L+ B3L	S3L+ BCL	S2L+ B3L	S3L+ B3L	S3L+ BCL	S3L+ B3L	S3L+ B3L	S3L+ B3L	S3L+ B3L
1	2	3	4	5	6	7	8	9	10	31
K3 K13	-8,0 (5,8)	-8,0 (5,8)	-11,2 (2,1)	-11,2 (2,1)	-11,2 (2,1)	-10,3 (3,1)	-17,3	-22,9	11,3	15,2
K-10-11 K-10-8 K-10-3	-14,2 (0,9)	-14,2 (0,9)	-8,3 (7,9)	-32,6 (3,7)	-32,6 (3,7)	-32,1	-22,6	-40,3	10,8	13,0
CP 1 CP 2 CP 3	-4,9		-	-	-	-	-	-	-	-
SQ	-	-	-	-	-	-	-	-	14,0	-4,0
Note: values in parentheses are given by using the proposed factors for the construction of material deformation diagrams										

B. Axial stiffness of compressed bars

The effective geometric characteristics of the cross-sections must be utilized and the stiffnesses of the elements must be calculated. Due to the active inclusion in spatial performance, including the action of wind loads, it is extremely important to correctly determine the stiffness of the elements when assessing the overall deformation of the building. Based on the results of the conducted experiments, it is possible to estimate the reduced (total) axial stiffness of compressed steel-reinforced concrete structures at each design or loading stage. It is possible to plot the diagram "force vs. axial stiffness" ($N/N_{u,n}$) - $D_{a.i}$) on the basis of the adopted approach of division of diagrams into stages by transforming formulas 4, 5:

$$\Delta D_{a.i} = \frac{\Delta N_i L}{\Delta l_i} \ , \qquad (10)$$

where Δl_i is the shortening according to the results of the experiment at load N_i at the i^{th} stage of loading. The graphs of stiffness variation depending on the applied load are shown in Figures 9...11. On the horizontal axis of the graphs the value $N/N_{u,n}$ is plotted, where N is the current compressive load at tests or calculations, and $N_{u,n}$ is the normative ultimate compressive load, which is calculated according to the formula 6. The vertical dashed line corresponds to

the load level corresponding to the design strength values of materials R_b, R_y, R_s, calculated by formula 7. Experimental data are shown in gray dashed lines. Blue, orange, green lines show the theoretical values of stiffnesses according to formula 10. Red line shows the stiffness of the compressed structure according to the numerical model. The horizontal black dashed line on the graphs shows the value of the reduced normative axial stiffness of the section $D_{a,n}$, calculated by the formula similar to G.11 of SP 266.1325800, where instead of the moment of inertia the cross-sectional areas are taken, and the coefficients k_s=k_b=1 and the concrete deformation modulus - E_{b1}=0.85E_b, as under short-term load action.

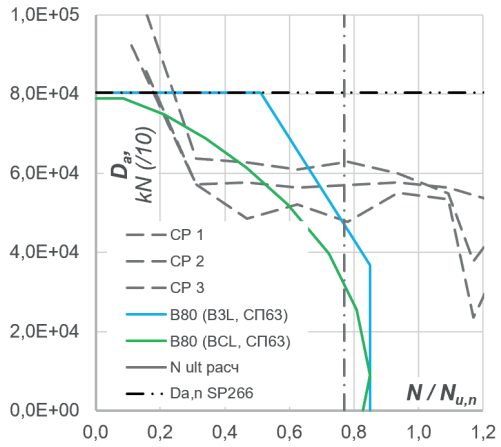

Figure 9. Diagrams of change in stiffness D_a as a function of load for concrete models (B80)

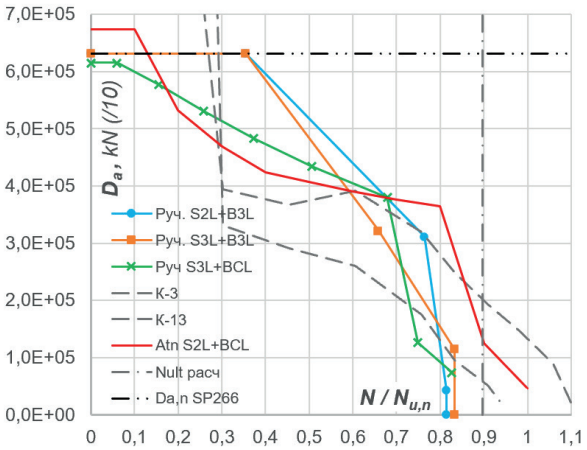

Figure 10. Diagrams of change in stiffness D_a as a function of load for steel reinforced concrete models K3 and K13 (B25)

The stiffness of unreinforced models (concrete prisms CP1...CP3 - gray dashed line in Figure 9) at the initial stages of loading of structures (at $N/N_{u,n}$=0...0.3) is much higher than the value of $D_{a,n}$. Further, after initial compression, the stiffness begins to drop to a value of about 0.75$D_{a,n}$ and remains stable up to a load of about $N/N_{u,n}$=1.1. The stiffness graph goes sharply downward to a value of about 0.4...0.5$D_{a,n}$. Failure ($D_{a,n}$=0) occurs at about the load level $N/N_{u,n}$=1.4. The utilization of nonlinear strain diagrams will allow a fairly accurate modeling of the behavior of concrete under load and the graph shows that the curvilinear diagram is obviously more accurate in describing the performance of concrete under load (green line), compared to the tri-linear diagram (blue line).

The stiffness of steel-reinforced concrete models made of B25 concrete (gray dashed line in Figure 10) at the initial stages of structural loading (at $N/N_{u,n}$=0...0.3) is much higher than the value of $D_{a,n}$. Further, after the initial compression, the stiffness starts to drop sharply to a value of about 0.56$D_{a,n}$. At the load range $N/N_{u,n}$=0.3...1.05 it steadily decreases almost to 0. Failure ($D_{a,n}$=0) occurs approximately at the load level $N/N_{u,n}$=1.07. The comparison shows that the use of the curvilinear diagram also shows a good convergence with the experimental curves (green line), while the three-line diagram of concrete and steel (orange) and even more so the two-line diagram (blue) give an unjustified overestimation of the stiffness at loads $N/N_{u,n}$=0...0.5. Numerical modeling using the curvilinear concrete deformation diagram (red line) also shows a good convergence with the experimental stiffness diagram.

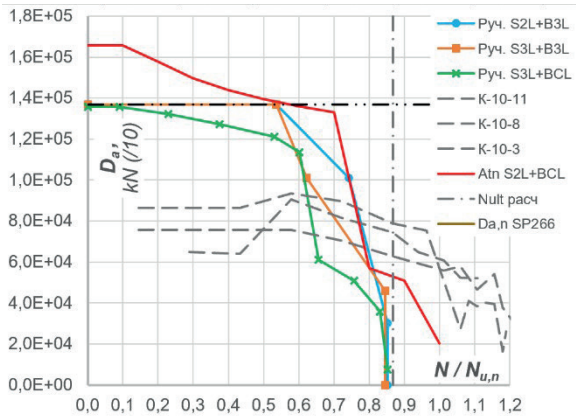

Figure 11. Diagrams of change in stiffness D_a as a function of load for steel-reinforced concrete models K10 (B80)

The stiffness of steel-reinforced concrete models made of B80 concrete (gray dashed line in Figure 11) at the initial stages of loading of the structures (at $N/N_{u,n}$=0...0.3), as well as for the above considered models, is significantly higher than the value of $D_{a,n}$. Further, after the initial compression, the stiffness begins to drop to a value of about $0.57D_{a,n}$ and remains stable up to a load of about $N/N_{u,n}$=0.7. After the plastic deformations start to develop in the steel core at the load range $N/N_{u,n}$=0.7...1.2 the stiffness of the element decreases smoothly to the value of $0.3D_{a,n}$. Here cracks actively develop and separation of concrete from steel takes place and the stiffness diagram sharply goes down to the value of about $0.14D_{a,n}$. Failure ($D_{a,n}$=0) occurs at approximately the load level $N/N_{u,n}$=1.4. It can be seen that the diagram of stiffness change in steel-reinforced concrete structure made of high-strength concrete (B80) and with high ratio of reinforcement (model type K10) practically repeats the diagram for unreinforced concrete (Figure 9). There are the same characteristic steps of stiffness drop and then a stable stiffness value without significant decrease over the load range $N/N_{u,n}$=0.3...0.7. At the same time, modeling of stiffness by formulas 4, 5, 10 (orange line), as well as by the finite element method (red) using curvilinear diagram of concrete deformation and three-linear diagram for steel do not provide an accurate description of the change of stiffness (as well as deformation) of the structure in the range of loads $N/N_{u,n}$=0.3...0.7.

In order to bring the axial stiffness to a value close to the experimental data, it is proposed to introduce an additional coefficient $k_{composite}$ in accordance with Formula 11, Table 5 and Figure 12 when calculating stiffnesses for steel-reinforced concrete structures under the action of short-term loads:

$$D_{a,composite} = k_{composite}(0.85E_bA_b + E_sA_s + E_{st}A_{st}), \quad (11)$$

Table 5. Correction factor to modulus of deformation

$N/N_{u,n}$	$k_{composite}$ for steel reinforced concrete structures with reinforcement ratio μ≤22% and heavy concrete of compressive strength class	
	B25	B80
1	2	3
0	1	1
0.3	0.55	0.55
0.7	-	0.55
1	0.1	0.3
1	0	0

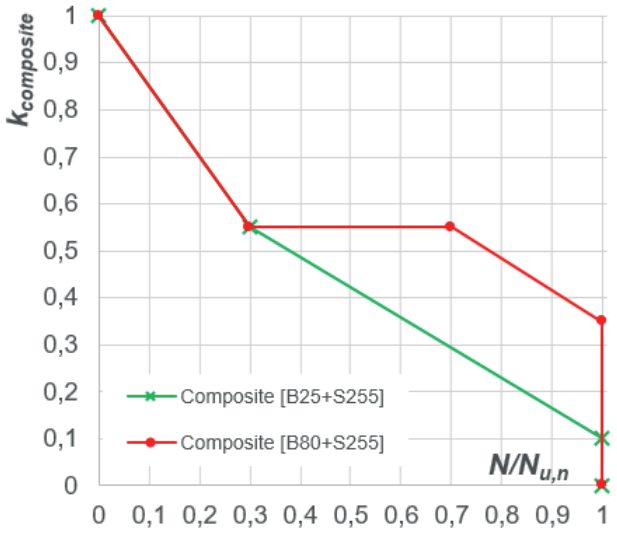

Figure 12. Diagram if the coefficient $k_{composite}$

CONCLUSION

1. Longitudinal shortening deformations for steel-reinforced concrete compressed members have been evaluated with a wide range of heavy concretes (from B25 to B80) and reinforcement ratios (from 0 to 22%). Deformations were calculated manually using modified formulas of SP 63.13330 taking into account three types of concrete deformation diagrams (two- and three-line, curvilinear) and two types of steel deformation diagrams (two- and three-line according to SP 16.13330). Finite element method analysis of structural models has been performed. These calculations take into account the characteristic diagrams of materials performance, as well as the possibility of slippage at the steel-concrete contact in accordance with [4]. Experimental data obtained during testing of conditionally centrally compressed column models of steel-reinforced concrete structures have been analyzed.
2. It has been found that the existing concrete performance diagrams do not accurately describe the performance of a composite steel-reinforced concrete structure, namely its shortening and reduced stiffness. When the concrete structure operates in compression, its failure at earlier stages of loading than it would be for concrete or reinforced concrete. This circumstance is due to the stress-strain state of the concrete section separated by steel elements, as well as to the effects of early delamination and slippage on the steel-concrete contact surface.
3. To eliminate the identified discrepancy in determining the value of longitudinal deformation (shortening) under the action of short-term loads and experimentally obtained data, it is necessary to use a system of additional coefficients. These coefficients should increase the theoretical value of the expected strains ε_{b0} and ε_{b2}, and should also account for the peculiarities of the operation of concrete of ordinary and high strength as part of compressible steel and reinforced concrete structures.
4. To bring the calculated axial stiffness to a value close to the experimental data, it is suggested to introduce an additional coefficient $k_{composite}$, which additionally reduces the axial stiffness of the structure depending on the level of stresses in concrete and steel, when calculating the stiffness values for steel-reinforced concrete structures under the action of short-term loads.
5. Considering the curvilinear diagram of concrete in compression provides more accurate results of the serviceability limit state (for deformations) than two- and three-line diagrams when performing calculations of spatial schemes of complex structures taking into ac-

count physical nonlinearity on the deformed scheme. Curvilinear diagrams more accurately describe the deformations of the structure operating in compression at the initial stages of deformation and loading.

REFERENCES

1. ANSI/AISC 360-16 An American National Standard. Specification for Structural Steel Buldings. (2016) Chicago: American Institute of Steel Construction. 676 p.
2. **Griffis, L.G.** (1993) Serviceability Limit States Under Wind Load. *Engineering Journal. American Institute of Steel Construction*. Q1. pp. 1-16.
3. **Travush V.I., Konin D.V., Rozhkova L.S., Krylov A.S., Kaprielov S.S., Chilin I.A., Fimkin A.I** (2016) Eksperimental'nye issledovaniya stalezhelezobetonnyh konstrukcij, rabotayushchih na vnecentrennoe szhatie [Experimental studies of steel-reinforced concrete structures operating on off-center compression]. *Academia. Architecture and construction*, no 3, pp. 127-135.
4. **Travush V.I., Kaprielov S.S., Konin D.V., Krylov A.S., Kashevarova G.G., Chilin I.A** (2016) Opredelenie nesushchej sposobnosti na sdvig kontaktnoj poverhnosti «stal'-beton» v stalezhelezobetonnyh konstrukciyah dlya betonov razlichnoj prochnosti na szhatie i fibrobetona [Determination of the bearing capacity for shear of the contact surface "steel-concrete" in steel-reinforced concrete structures for concretes of various compressive strength and fiber concrete]. *Construction and reconstruction*, no 4 (66), pp. 45-55.
5. **Desyatkin M.A., Konin D.V., Martirosyan A.S., Travush V.I**. (2015) Raschet stalezhelezobetonnoj kolonny vysotnogo doma na kosoe vnecentrennoe szhatie [Calculation of a steel-reinforced column of a high-rise building for oblique off-center compression] *Housing construction,* no 5, pp. 92-95.
6. **Travush V.I., Rozhkova L.S., Krylov A.S.** (2016) Otechestvennyj i zarubezhnyj opyt issledovanij raboty stalezhelezobetonnyh konstrukcij na vnecentrennoe szhatie [Domestic and foreign experience in researching the operation of steel-reinforced concrete structures for non-central compression] *Construction and reconstruction,* no 5, pp. 31-44.
7. **Mukhamediev T.A., Starchikova O.I.** (2016) Raschet prochnosti stalezhelezobetonnyh kolonn s ispol'zovaniem deformacionnoj modeli [Calculation of the strength of steel-reinforced concrete columns using a deformation model] *Concrete and reinforced concrete*, no 4, pp. 18-21.
8. **Karpenko N.I.** (1996) Obshchie modeli mekhaniki zhelezobetona [General models of reinforced concrete mechanics] Moscow: Stroyizdat, 416 p. (In Russian)
9. **Murashkin G.V., Murashkin V.G.** (1997) Modelirovanie diagrammy deformirovaniya betona i skhemy napryazhenno-deformirovannogo sostoyaniya [Modeling of the deformation diagram of concrete and the scheme of the stress-strain state] *Izvestiya vysshih uchebnyh zavedenij. Stroitel'stvo*, no 10, pp. 4-6.
10. **Mordovsky S.S., Murashkin V.G.** (2012) Napryazhyonnoe sostoyanie eksperimental'nyh obrazcov pri vnecentrennom nagruzhenii [The stressed state of experimental samples under extreme loading]. *Sovremennye problemy nauki i obrazovaniya,* no 4. Available at: http://science-education.ru/ru/article/view?id=6794 (accessed 03 January 2018).
11. **Karpenko N.I., Sokolov B.S., Radaykin O.V**. (2013) K raschyotu prochnosti, zhyostkosti i treshchinostojkosti vnecentrenno szhatyh zhelezobetonnyh elementov s primeneniem nelinejnoj deformacionnoj modeli [On the calculation of strength, stiffness and crack resistance of non-centrally compressed reinforced concrete elements using a nonlinear deformation model]. *Izvestiya Kazanskogo gosudar-*

stvennogo arhitekturno-stroitel'nogo universiteta, no 4(26), pp. 113-120.
12. **Karpenko N.I., Karpenko S.N.** (2012) O diagrammnoj metodike rascheta deformacij sterzhnevyh elementov i ee chastnyh sluchayah [On the diagrammatic methodology for calculating deformations of rod elements and its special cases] *Concrete and iron-concrete*, no 6, pp. 20-27.
13. **Arleninov P.D.** (2016) Deformation and stability of compressed and non-centrally compressed core reinforced concrete elements, taking into account creep and cracking (PhD thesis), Moscow, JSC "SIC "Construction" (NIIZHB named after A.A. Gvozdev). – 143 p. (In Russian)
14. **Krylov S.B.** (2012) Kriticheskaya sila dlya zhelezobetonnyh sterzhnevyh elementov [Critical force for reinforced concrete core elements] *Academia. Architecture and Construction*, no 2, pp. 136-138.
15. **Arleninov P.D.** (2015) Analiz razlichnyh metodik sozdaniya raschetnyh skhem pri komp'yuternom modelirovanii nesushchih konstrukcij [Analysis of various methods for creating computational schemes for computer modeling of load-bearing structures] *BST: Byulleten' stroitel'noj tekhniki*, no 5(969), pp.58-59.
16. **Karpenko N.I., Sokolov B.S., Radaykin O.V.** (2013) Analiz i sovershenstvovanie krivolinejnyh diagramm deformirovaniya betona dlya rascheta zhelezobetonnyh konstrukcij po deformacionnoj modeli [Analysis and improvement of curvilinear diagrams of concrete deformation for the calculation of reinforced concrete structures according to the deformation model] *Industrial and civil construction*, no.1, pp.28-30.
17. **Bezgodov, I., Kaprielov, S., & Sheynfeld, A.** (2022) Relationship between strength and deformation characteristics of high-strength self-compacting concrete. *International Journal for Computational Civil and Structural Engineering*, no 18(2), pp. 175–183.
18. **Kaprielov, S., Sheinfeld, A., Selyutin, N.** (2022) Control of heavy concrete characteristics affecting structural stiffness. *International Journal for Computational Civil and Structural Engineering*, no18(1), pp. 24–39.
19. **Chiorino M.A., Carreira J.** (2012) Factors Affecting Creep and Shrinkage of Hardened Concrete and Guide for Modelling. *The Indian Concrete Journal,* no 12(86), pp.11-24.
20. **Guilin Zhang, Pang Chen, Xiaoyu Si, Jingde Wang, Yang Han** (2022) Research on Shrinkage and Shrinkage Models of Reinforced Concrete Specimens. *The Open Civil Engineering Journal*, no 16(1), pp. 1-10.
21. **Darko Nakov** (2024) Early-age thermal and shrinkage cracking in reinforced concrete structures. Proceedings of the *Contemporary Civil Engineering Practice 2024*, *June 2024, Ruma, Serbia*, pp. 40-51.

СПИСОК ЛИТЕРАТУРЫ

1. ANSI/AISC 360-16 An American National Standard. Specification for Structural Steel Buldings. – Chicago: American Institute of Steel Construction. 2016. 676 p.
2. **Griffis, L.G.** Serviceability Limit States Under Wind Load // Engineering Journal. American Institute Of Steel Construction, 1993, Q1. pp. 1-16.
3. **Травуш В.И., Конин Д.В., Рожкова Л.С., Крылов А.С., Каприелов С.С., Чилин И.А., Фимкин А.И.** Экспериментальные исследования сталежелезобетонных конструкций, работающих на внецентренное сжатие // Academia. Архитектура и строительство. 2016, № 3, С. 127-135.
4. **Травуш В.И., Каприелов С.С., Конин Д.В., Крылов А.С., Кашеварова Г.Г., Чилин И.А.** Определение несущей способности на сдвиг контактной поверхности «сталь-бетон» в сталежелезобетонных конструкциях для бетонов различной прочности на сжатие и фибробетона // Строительство и реконструкция, 2016, №4 (66), С. 45-55.

5. **Десяткин М.А., Конин Д.В., Мартиросян А.С., Травуш В.И.** Расчет сталежелезобетонной колонны высотного дома на косое внецентренное сжатие // Жилищное строительство, 2015, № 5, С. 92-95.
6. **Травуш В.И., Рожкова Л.С., Крылов А.С.** Отечественный и зарубежный опыт исследований работы сталежелезобетонных конструкций на внецентренное сжатие // Строительство и реконструкция, 2016, №5, С. 31-44.
7. **Мухамедиев Т.А., Старчикова О.И.** Расчет прочности сталежелезобетонных колонн с использованием деформационной модели // Бетон и железобетон, 2006, №4, С. 18-21.
8. **Карпенко Н.И.** Общие модели механики железобетона. – М.: Стройиздат, 1996. – 416 с.
9. **Мурашкин Г.В., Мурашкин В.Г**. Моделирование диаграммы деформирования бетона и схемы напряженно-деформированного состояния // Известия высших учебных заведений. Строительство, 1997, №10, С. 4-6.
10. **Мордовский С.С., Мурашкин В.Г.** Напряжённое состояние экспериментальных образцов при внецентренном нагружении // Современные проблемы науки и образования, 2012, № 4. URL: http://science-education.ru/ru/article/view?id=6794 (дата обращения: 01.03.2018).
11. **Карпенко Н.И., Соколов Б.С., Радайкин О.В.** К расчёту прочности, жёсткости и трещиностойкости внецентренно сжатых железобетонных элементов с применением нелинейной деформационной модели // Известия Казанского государственного архитектурно-строительного университета, 2013, №4(26), С. 113-120.
12. **Карпенко Н.И., Карпенко С.Н.** О диаграммной методике расчета деформаций стержневых элементов и ее частных случаях // Бетон и железобетон, 2012, №6, С. 20-27.
13. **Арленинов П.Д.** Деформирование и устойчивость сжатых и внецентренно сжатых стержневых железобетонных элементов с учетом ползучести и трещинообразования – Кандидатская диссертация, АО «НИЦ «Строительство» (НИИЖБ им. А.А. Гвоздева), 2016, С. 143.
14. **Крылов С.Б.** Критическая сила для железобетонных стержневых элементов // Academia. Архитектура и строительство, 2012, №2, С. 136-138.
15. **Арленинов П.Д.** Анализ различных методик создания расчетных схем при компьютерном моделировании несущих конструкций // БСТ: Бюллетень строительной техники, №5(969), 2015, С.58-59.
16. **Карпенко Н.И., Соколов Б.С., Радайкин О.В.** Анализ и совершенствование криволинейных диаграмм деформирования бетона для расчета железобетонных конструкций по деформационной модели // Промышленное и гражданское строительство, 2013, №1, С.28-30.
17. **Bezgodov, I., Kaprielov, S., & Sheynfeld, A.** Relationship between strength and deformation characteristics of high-strength self-compacting concrete // International Journal for Computational Civil and Structural Engineering, 2022, №18(2), pp. 175–183.
18. **Kaprielov, S., Sheinfeld, A., Selyutin, N.** Control of heavy concrete characteristics affecting structural stiffness // International Journal for Computational Civil and Structural Engineering, 2022, №18(1), pp. 24–39.
19. **Chiorino M.A., Carreira J.** Factors Affecting Creep and Shrinkage of Hardened Concrete and Guide for Modelling // The Indian Concrete Journal, 2012, № 12(86), pp. 11-24.
20. **Guilin Zhang, Pang Chen, Xiaoyu Si, Jingde Wang, Yang Han**. Research on Shrinkage and Shrinkage Models of Reinforced Concrete Specimens // The Open Civil Engineering Journal, 2022, no 16(1), pp. 1-10.

21. **Darko Nakov.** Prsline usled rane termičke kontrakcije i skupljanja u armirano-betonskimkonstrukcijama // Proceedings of the Contemporary Civil Engineering Practice 2024, 2024, Ruma, Serbia, pp. 40-51.

Denis Vladimirovich Konin - PhD, deputy director for scientific work Research Institute of Building Constructions (TSNIISK) named after V. A. Koucherenko JSC Research Center of Construction: 6, 2nd Institutskaya street, Moscow, 109428, Russia; konden@inbox.ru

Денис Владимирович Конин - кандидат технических наук, заместитель директора по научной работе Центрального научно-исследовательского института строительных конструкций (ЦНИИСК) им. В.А. Кучеренко АО «Научно-исследовательский центр (НИЦ) «Строительство»): д. 6, 2-я Институтская ул., г. Москва, 109428, Россия; konden@inbox.ru

International Journal for Computational Civil and Structural Engineering, 21(1) 222–232 (2025)

DOI:10.22337/2587-9618-2025-21-1-222-232

DESIGN OF FOUNDATION STRENGTHENING WITH PILES FOR THE RECONSTRUCTION OF BUILDINGS ON CLAY SOILS

Anatoly I. Polishchuk [1], Arkady A. Petukhov [1], Nadezhda S. Nikitina [2], Ivan V. Semenov [1]

[1] Kuban State Agrarian University named after I.T. Trubilin. Krasnodar, RUSSIA
[2] National Research Moscow State University of Civil Engineering, Moscow, RUSSIA

Abstract. The paper presents the main stages of designing the strengthening of shallow foundations with piles made in clay soil (injection and bored-injection) for reconstructed buildings. Such foundations are often called combined foundations. The basic methods for installing these piles as part of reinforced foundations are presented, including injection cylindrical piles, bored-injection cylindrical piles of Titan and Atlant types, and bored-injection conical piles. The methodology of foundation strengthening design with the use of such piles is discussed. As a result of investigations of soil properties, lithologic structure of the base and other parameters the procedure of evaluation of soil conditions of construction sites is shown. The data on assessment of technical condition of bases and foundations of reconstructed buildings are presented. The article presents the main results of tests of injection piles, provides guidelines for determining their load-bearing capacity. It provides information on verification calculations performed while designing foundations reinforced by injection (bored-injection) piles, including the determination of the design resistance of the compacted soil of the base. An engineering method for calculating the settlement of reinforced foundations with injected, bored-injected piles in clay soils, which can be used in the design practice of reconstructed buildings, has been presented. The method allows accounting for the displacement (settlement) of the soil due to its weakening in the places of wells for the piles and data on the change in the stress state of the base under the bottom of the slab part of the foundation.

Keywords: strengthened foundation, injection and bored-injection piles, reconstruction of buildings, assessment of soil conditions of construction, foundation strengthening solutions

ПРОЕКТИРОВАНИЕ УСИЛЕНИЯ ФУНДАМЕНТОВ С ИСПОЛЬЗОВАНИЕМ СВАЙ ПРИ РЕКОНСТРУКЦИИ ЗДАНИЙ В ГЛИНИСТЫХ ГРУНТАХ

А.И. Полищук [1], А.А. Петухов [1], Н.С. Никитина [2], И.В. Семёнов [1]

[1] Кубанский государственный аграрный университет им. И. Т. Трубилина, г. Краснодар, РОССИЯ
[2]Национальный исследовательский Московский государственный строительный университет, г. Москва, РОССИЯ

Аннотация. Приведены основные этапы проектирования усиления фундаментов мелкого заложения сваями, изготавливаемыми в глинистом грунте (инъекционные и буроинъекционные) для реконструируемых зданий. Такие фундаменты часто называют комбинированными. Представлены основные способы устройства указанных выше свай в составе усиливаемых фундаментов, включая инъекционные цилиндрические сваи, буроинъекционные цилиндрические сваи конструкции «*Titan*», «*Атлант*», буроинъекционные конические сваи. Дана методика проектирования усиления фундаментов с использованием таких свай. По результатам исследований свойств грунтов, литологического строения основания и других параметров показан порядок выполнения оценки грунтовых условий площадок строительства. Представлены данные по оценке технического состояния оснований и фундаментов реконструируемых зданий. Приведены основные результаты испытаний инъекционных свай, даны указания по определению их несущей способности. Приведены сведения о поверочных расчетах, выполняемых при проектировании фундаментов, усиливаемых инъекционными, буроинъекционными сваями, в том числе по определению

расчетного сопротивления уплотненного грунта основания. Представлен инженерный метод расчета осадок усиливаемых фундаментов с инъекционными, буроинъекционными сваями в глинистых грунтах, который может использоваться в проектной практике реконструируемых зданий. Метод позволяет учитывать перемещения (осадки) грунта за счет его ослабления в местах устройства скважин под рассматриваемые сваи и данные об изменении напряженного состояния основания под подошвой плитной части фундамента.

Ключевые слова: усиливаемый фундамент, инъекционные и буроинъекционные сваи, реконструкция зданий, оценка грунтовых условий строительства, решения по усилению фундаментов

BASIC PROVISIONS

A way to increase the load-bearing capacity of shallow foundations is to change the scheme of operation by transferring part of the load from the building to the piles. The foundation thus formed is often called a combined foundation. In this case, the piles can be arranged under the footing of the foundation through its slab part or adjacent to its perimeter (Fig. 1).

In recent years, injection and bored-injection piles have been increasingly used to strengthen the foundations of reconstructed buildings. Injection piles are defined as structures that are formed in prepared (ready-made) boreholes by injecting into them under pressure a mixture of fine-grained concrete with subsequent pressure testing of the system “pile - base soil” (Polischuk A.I., Petukhov A.A. et al., 2003). In the case of such piles, the borehole is constructed by preliminary pushing into the ground steel tubular injectors of special design (Fig. 2) [1, 2, 3]. If the borehole is drilled using auger or other equipment such piles are usually called Titan cylindrical bored injection piles [4, 5]. [4, 5]. They were introduced in construction by Ishebek (Germany, 1956). The considered bored-injection cylindrical piles are used mainly for the action of vertical compressive and pulling (anchor) loads. Sometimes they are called Titan bored-injection anchor piles (Fig.3). In Russia, the Titan piles have been used since about 1985-1990. As a development of Titan bored-injection piles, the company InzhProektStroy (Russia) in 2006-2008 proposed a design solution of Atlant bored-injection piles for compressive and pull-out (anchor) loads, as well as for moment forces (Fig. 4).

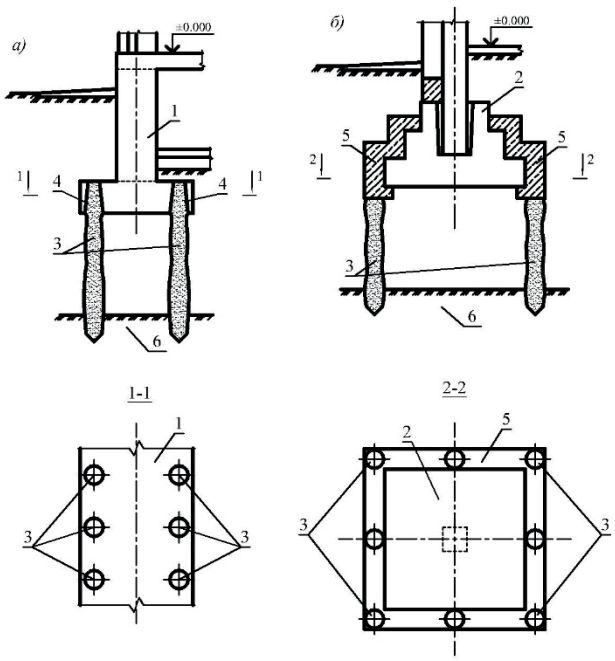

Figure 1. Foundations reinforced by injection (bored-injection) piles: a - under the bottom of the existing strip foundation; b - adjacent to the slab part of the existing separate foundation; 1 - existing strip foundation; 2 - existing separate foundation; 3 - injection (bored-injection) piles; 4 - cone hole in the slab part of the foundation; 5 - reinforced concrete cage; 6 - bearing layer of the foundation soil

As part of the development of design solutions for bored-injection cylindrical piles, D.A. Chernyavskiy, O.Y. Yeschenko (2010), and later G.G. Solonov, D.A. Chernyavskiy et al. (2024) proposed a device and a method for manufacturing bored-injection conical piles, which are now increasingly used in new construction and building reconstruction (Fig. 5) [6, 24].

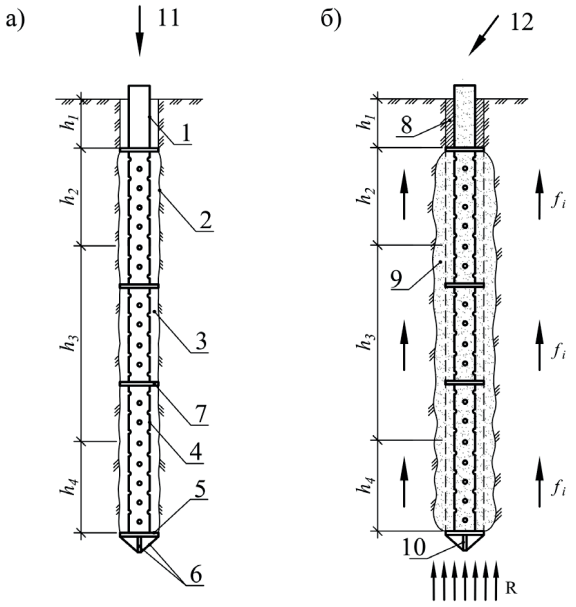

Figure 2. Injection piles and schemes of their formation in the soil (authors A.I. Polishchuk, A.A. Petukhov et al.).: a - Injector immersion; b - Arrangement of injection pile by injecting fine-grained concrete; 1 - Injector section without perforation; 2 - Well side surface; 3 - Air gap between injector and well wall; 4 - Injector section with perforation; 5 - Injector pipe widening at the bottom of the injection pile for air gap arrangement; 6 - Cutting plates; 7 - injection pipe widening along the injection pile; 8 - well plugging; 9 - expandable part of the injection pile during concrete mixture injection; 10 - lower end of the pile; 11 - injector push-in force; 12 - direction of concrete mixture injection

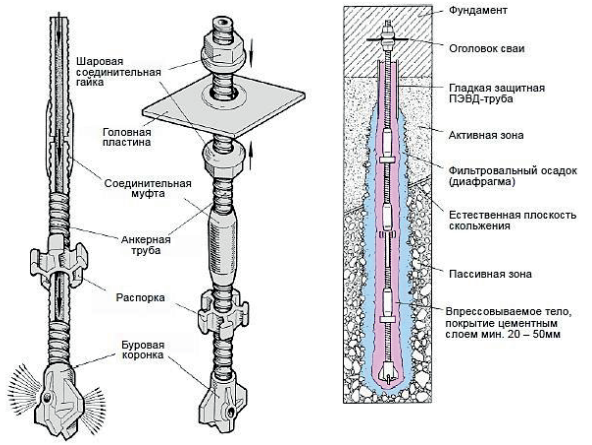

Figure 3. Structural elements of Titan cylindrical (anchor) bored injection pile (Germany)

Figure 4. General view of constituent structural elements of the Atlant bored-injection pile (Russia)

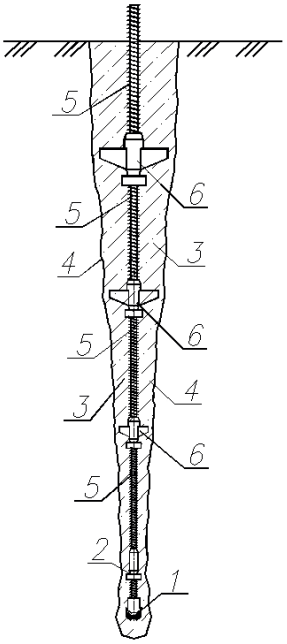

Figure 5. Scheme of bored-injection conical pile (authors D.A. Chernyavskiy, O.Y. Yeschenko): 1 - drill bit; 2 - connecting coupling; 3 - fine-grained concrete mixture; 4 - lateral surface of the borehole; 5 - hollow steel rod; 6 - drill bit with drilling blades

METHODOLOGY FOR FOUNDATION STRENGTHENING DESIGN AND PILE PERFORMANCE STUDIES

The design methodology for strengthening of shallow foundations of reconstructed buildings includes the following stages: selection of experimental sites for testing of full-scale injection (bored-injection) piles; performance of engineering and geological surveys; manufacturing of structural elements of piles; preparation of fine-grained concrete mixture and its experimental injection into boreholes; construction of injection, bored-injection piles at the selected site; investigation of physical and mechanical properties of soils in the pile space; testing of

injection (bored-injection) piles by static indentation load. The experience of the above methodology can be borrowed from the authors' publications and technical literature [1, 7, 8, 9] for the period from 2003-2023.

For example, experimental studies at the experimental sites in Tomsk and Kemerovo were grouped into series of experiments [1, 10]. Injection piles with lengths of 1.5, 3.5, 5.0 m without widening injectors and with extensions at the level of their lower ends in the form of tips to form an air gap were applied (Fig. 6). Each injector pipe had two sections: a "blind" section, usually up to 1.5 m long, and a section with 15-20 mm diameter holes staggered at 80-100 mm spacing. At the boundary between these sections, a ring of the same diameter as the tip widening was provided.

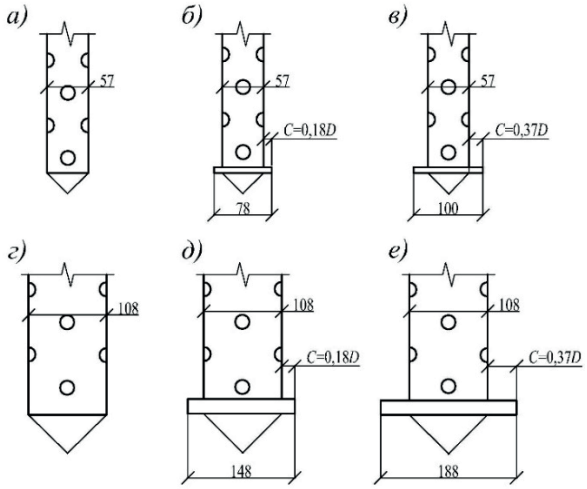

Figure 6. Design solution of tips for 57 mm (a, b, c) and 108 mm (d, e, f) diameter injectors used in the production of injection piles: a, d - tips for piles without widening; b, e - the same with widening diameter (1.37-1.4)D; c, f - the same with widening diameter (1.75-1.8)D, where D is the injector diameter

Injectors were immersed up to the design level using a hydraulic long-rod jack due to the cramped conditions at the experimental site in Tomsk and a drilling rig UGB-1BC at the experimental site in Kemerovo. Injection of fine-grained concrete was carried out with the help of a CO-49 m and CO-180 pump, providing a constant rate of its supply of about 2.5 m^3/h. The maximum pressure created by the pump was 1.5-2.0 MPa. The concrete mixture was injected into the boreholes in portions of 0.1 m^3 with technological breaks for 5-10 min for "intermediate" pressing of the soil mass with working pressure (Fig. 7). The concrete mixture was injected up to the specified volume calculated on the basis of the geometry of the piles being constructed. After injection of the concrete mixture, the soil in the pile space was pressurized by maintaining the working pressure in the borehole for a specified period of time to ensure soil compaction around the pile shaft.

KEY RESULTS AND THEIR ANALYSIS

Results of assessment of soil properties and soil conditions of construction. The evaluation of base soils enables designers to choose the most rational solution for the reconstruction of buildings in terms of their reliability and cost-effectiveness [1, 11]. Studies of changes in physical and mechanical properties of soils around the shaft of injection piles were carried out on the selected soil monoliths from pilot sites (Kemerovo, Tomsk). The change of soil density ρ in the surrounding massif along the length of the pile was revealed. In the natural state, the soil density (ρ) was 1.70-1.73 g/cm^3, while at the boundary of the pile shaft with the soil mass the soil density changed and reached 1.97-1.98 g/cm^3.

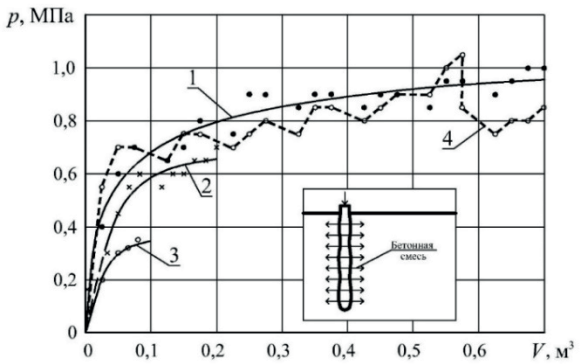

Figure 7. Changes in injection pressure p (MPa) of the concrete mixture for injection piles: 1 - 5.0 m long piles (site 1); 2 - 3.5 m long piles (site 1); 3 - 1.5 m long piles (site 2); 4 - 5.0 m long piles (site 1 - with soil fracturing)

The specific cohesion of the clayey soil after pile placement increased from 13.3-15.0 kPa to 18.2-18.6 kPa within a distance of up to 500 mm from the lateral surface of the piles. At the same time, the angle of internal friction of clayey soil increased insignificantly, by 1-3 deg [1, 9, 10]. According to the results of static soil probing, it was found that after pile arrangement the soil resistance under the probe tip within the length of the arranged pile q_c increased 1.5-2.0 times and amounted to 1.5-2.2 MPa. Soil resistance on the lateral surface of the probe f_s. within the depth of the pile increased by 1.4-1.5 times. Based on the results of studies of soil properties, lithologic structure of the foundation and other parameters, the soil conditions of the test sites under consideration were evaluated [20, 22].

Assessment of the technical condition of foundations. For reconstructed buildings, the condition of foundations shall be established based on the results of inspection, including the examination of the base soils and verification calculations [1, 12]. Based on the results of the work performed, considering the identified defects, damages and verification calculations, their technical condition can be assessed in accordance with the requirements of GOST 31937-2011 and other technical literature [13, 14].
Since 2011 there have been 4 groups for assessing the category of technical condition of building structures, including base soils, according to GOST 31937-2011 in Russia. According to this standard, load-bearing building structures and foundation soils may be in: normative technical condition, serviceable condition, limited serviceable condition and emergency condition.

Test results of injection piles and justification of their bearing capacity. Tests of injection piles were carried out in accordance with GOST 5686-2020. Analysis of the results of injection pile tests allowed to reveal the nature of their operation performance under load. For example, in the considered tests at pilot sites (Kemerovo, Tomsk) it was found that for injection piles with injectors without tips (Fig. 6) the bearing capacity F_d was the lowest. For piles having injectors with bottom end extensions in clayey soils their bearing capacity F_d increases. Significant increase of up to 20-30 % and more in the bearing capacity F_d of injection piles was detected if the diameter of the widening D_y exceeded the injector diameter D by a distance C = (0.37-0.4)D.
To substantiate the bearing capacity of injection piles, the requirements of regulatory documents and technical literature (SP 24.13330.2021; Mangushev R.A. et al., 2015; Handbook of Geotechnical Engineering, 2023; Polishchuk A.I. et al., 2023) have been utilized. The value of external load $N = F_d$, which corresponded to their settlement equal to 10 mm, was taken as the bearing capacity F_d of injection piles at the pilot sites in the cities of Kemerovo and Tomsk [1]. In the absence of data on in-situ tests of piles, their bearing capacity can be determined using formulas and methods presented in regulatory and technical documentation and publications of authors [2, 9, 14, 15, 16, etc.].

Loading assessment of strengthened foundations. Loading assessment of strengthened (combined) foundations means the analysis of initial data and calculation results, which reveals the compliance of their design solution with the current loads (N, M, Q) and ground conditions of the construction site of the building being reconstructed [17, 18]. During the loading assessment, verification calculations are first performed for shallow foundations before they are strengthened (before the building is reconstructed). In particular, the design resistance of the compacted base soil R_{up} must be determined and compared with the pressure at the bottom of the shallow foundations p ($p \leq R_{up}$) before and after reconstruction [22]. In addition, the foundation settlement S and its irregularity ΔS are also determined. If the pressure p exceeds the design resistance R_{up} ($p > R_{up}$) or the settlement S or the irregularity of settlement ΔS of the foundations exceeds the permissible limits, the foundation should be strengthened with piles ("strengthened founda-

tion") [9, 19]. The strengthened foundation is then designed [7, 14, 22].

Verification calculations of the final settlement of the foundation S strengthened by injection (bored-injection) piles should be performed according to the requirements of SP 22.13330.2016. The engineering calculation method developed by the authors can also be utilized, according to which the foundation settlement S_{req} (mm) of the reconstructed building is determined considering the nonlinear relationship between stresses and deformations in the soil [2, 21, 23] using the formula:

$$S_{rec} = S_o \cdot k_n + S_f(k_{tech} - 1), \qquad (1)$$

where S_o is the final settlement of single injection piles (injection pile), mm [19, 20]; S_f is the design settlement of the existing shallow foundation (before strengthening with piles), determined by calculation mm; $k_{tech} = 1.01 - 1.13$ is the coefficient, which takes into account soil displacement (settlement) due to soil shrinkage along the borehole walls during injection pile installation; k_n = 0.93–0.98 – coefficient, which takes into account the data on the change in the stress state of the soil in the basement under the bottom of the slab part of the foundation after the installation of injection piles.

Thus, the proposed sequence of actions in the design of foundation reinforcement with the use of piles (injection, bored-injection) allows to properly organize the main stages of work of specialists and create an effective design solution that ensures its reliable operation for reconstructed buildings in clay soils.

CONCLUSIONS

1. The paper provides data on the performance of reinforced concrete foundations formed from shallow foundations when their slab part is reinforced with injection or bored-injection piles of 3...8 m length. The scope of application of the considered structural solutions of foundations extends mainly to reconstructed buildings in clay soils, including weak soils.

2. It has been found that injection and bored-injection piles made of fine-grained concrete are now increasingly used for strengthening foundations of reconstructed buildings. In particular, the introduction of injection piles was carried out at the objects of reconstructed buildings in Tomsk and Kemerovo (2005-2008), and bored-injection piles at the objects in Sochi and Krasnodar (2020).

3. The proposed engineering method for calculating settlements of foundations strengthened by injection, bored-injection piles in clayey soils can be used for the conditions of building reconstruction. The method allows to account for the displacement (settlement) of the soil from the external load at the locations of wells and data on the change in the stress state of the foundation soil under the bottom of the slab part of the foundation.

REFERENCES

1. **Polishchuk A.I., Petuhov A.A., Semyonov I.V.** Usilenie fundamentov in"ekcionnymi svayami pri rekonstrukcii zdanij [Strengthening foundations with injection piles during reconstruction of buildings] 2-nd edition, added. M.: Publishing house ASV, 2023. 212 p. м
2. **Polishchuk A.I., Semyonov I.V.** Raschet osadki kombinirovannogo fundamenta dlya rekonstruiruemogo zdaniya v glinistyh gruntah [Calculation of the settlement of a combined foundation for a reconstructed building in clay soils] *Osnovaniya, fundamenty i mekhanika gruntov*. 2022, No 6, pp.7-11.
3. **Polishchuk A.I., Gerasimov O.V., Petukhov A.A., Andriyenko YU.B., Nuykin S.S.** Sposob ustroystva in"yektsionnoy svai [Method for the device of injection piles]. Patent Rossiiskaia Federatsiia no. 2238366 (2014).

4. **Bruce, D.A., Bruce, M.E.C., and Traylor, R.P.** (1999). «High Capacity Mi-cropiles – Basic Principals and Case Histories» GeoEngineering for Underground Facilities.Proc. of the 3rd National Conference of the Geo-Institute of the American Society of Civil Engineers. Geotechnical Special Publication No. 90, Urbana-Champaign, IL, June 13-17, pp. 188-199.
5. **Jeon, S., and Kulhawy, F.H.** (2002). «Evaluation of axial compression be-havior of micropiles» Proceeding of a Specialty Conference – Foundation and ground improvement, Blacksburg VI, ASCE, pp. 460-471.
6. **CHernyavskij D.A.** Ocenka vliyaniya prochnostnyh harakteristik glinistyh gruntov na nesushchuyu sposobnost' odinochnyh konicheskih buroin"ekcionnyh svaj [Assessment of the influence of the strength characteristics of clay soils on the bearing capacity of single conical drilled injection piles] *Vestnik PNIPU. Stroitel'stvo i arhitektura,* 2018, No 4, pp.69-79. DOI: 10.15593/2224-9826/2018.4.07.
7. **Mangushev R.A., Gotman A.L., Znamenskij V.V., Ponomarev A.B**. Svai i svajnye fundamenty. Konstrukcii, proektirovanie i tekhnologii [Piles and pile foundations. Structures, design and technology] M.: Publishing house ASV, 2018, 320 p.
8. **Tarasov A.A.** Razvitiye metodov raschota in"yektsionnykh svay v slabykh glinistykh gruntakh dlya fundamentov rekonstruiruyemykh zdaniy [Development of methods for calculating injection piles in weak clay soils for the foundations of reconstructed buildings]: avtoref. dis. … cand. tech. sc. Tomsk, 2015, 23 p.
9. Directory geotechnics. Bases, foundations and underground structures. 3rd ed. Eds. V.A. Ilichev, R.A. Mangushev. Moscow, ASV, 2023, 1084 p.
10. **Petuhov A.A.** Sovershenstvovanie sposoba ustrojstva in"ekcionnyh svaj v slabyh glinistyh gruntah dlya uslovij rekonstrukcii zdanij [Improving the method of installing injection piles in weak clay soils for building reconstruction conditions]: avtoref. dis. … cand. tech. sc. Tomsk, 2006, 23 p.
11. **Zakharov M.S., Mangushev R.A.** Inzhenerno-geologicheskiye i inzhenerno-geotekhnicheskiye izyskaniya v stroitel'stve [Engineering-geological and engineering-geotechnical surveys in construction] Edited by R. A. Mangushev. Moscow, Saint-Peterburg : Publishing ASV, 2014, 176 p.
12. **Zemlianskii A.A**. Obsledovanie i ispytanie zdanii i sooruzhenii [Inspection and testing of buildings and structures] M.: Publishing house ASV, 2002, 240 p.
13. **Plevkov V.S., Mal'ganov A.I., Baldin I.V.** Otsenka tekhnicheskogo sostoyaniya, vosstanovleniye i usileniye stroitel'nykh konstruktsiy inzhenernykh sooruzheniy: uchebnoye posobiye [Assessment of the technical condition, restoration and strengthening of building structures of engineering structures] / Edited by V. S. Plevkov. 2-nd edition, remastered and added. Moscow: Publishing ASV, 2014, 328 p.
14. **Polishchuk A.I., Semyonov I.V., Demchenko V.A.** Main reasons for strengthening foundations and base soil stabilizations of used buildings. *Journal of Physics: Conference Series : 2*, Perm, 26–28 may 2021. Perm, 2021. P. 012029. – DOI 10.1088/1742-6596/1928/1/012029. – EDN QJREFB.
15. **Gotman A.L.** Svai i svaynyye fundamenty. Izbrannyye Trudy [Piles and pile foundations. Selected works: monograph] Ufa : IDPO UGNTU, 2015, 384 p.
16. **Pronozin, YA.A., Samokhvalov M.A.** Raschet vzaimodeystviya buroin"yektsionnykh svay s gruntovym osnovaniyem [Calculation of the interaction of bore-injection piles with a soil foundation] *Osnovaniya, fundamenty i mekhanika gruntov*. 2018, No 2, pp. 14-17.
17. **Filippovich A.A.** Vzaimodejstvie lentochnyh fundamentov rekonstruiruemyh zdanij s glinistym gruntom osnovaniya pri ih usilenii in"ekcionnymi svayami [Interaction of strip foundations of reconstructed buildings with clay foundation soil when

they are reinforced with injection piles]: avtoref. dis. … cand. tech. sc. Volgograd, 2014, 23 p.
18. **Konovalov P.A., Konovalov V.P.** Osnovaniya i fundamenty rekonstruiruemyh zdanij [Foundations and foundations of reconstructed buildings] M.: Publishing house ASV, 2011, 384 p.
19. **Polishchuk A.I.** Razrabotka metoda rascheta osadki odinochnoj in"ekcionnoj svai v glinistyh gruntah [Development of a method for calculating the settlement of a single injection pile in clayey soils]. *IV Mezhdunarodnaya nauchno-prakticheskaya molodezhnaya konferenciya po geotekhnike : sbornik materialov, Tyumen'*, 28–30 September 2018. Tyumen', Tyumen Industrial University, 2018, pp. 67-69. – EDN XZPKYP
20. **Polishchuk A.I., Nikitina N.S., Petukhov A.A., Semyonov I.V.** Strengthening of the Foundations of Renovated Buildings With Injection Piles. *International Journal for Computational Civil and Structural Engineering.* 2021, Vol. 17, No. 1, pp. 75-86. DOI 10.22337/2587-9618-2021-17-1-75-86. – EDN RCSPAE.
21. **Malyshev M.V., Nikitina N.S.** Raschet osadok fundamentov pri nelinejnoj zavisimosti mezhdu napryazheniyami i deformaciyami v gruntah [Calculation of foundation settlements with a nonlinear relationship between stresses and deformations in soils] *Osnovaniya, fundamenty i mekhanika gruntov*. 1982, No 2, pp.21-24.
22. **Nikitina N.S., Kravchenko D.A., Remizova N.V.** Sravnitel'nyj analiz metodov vozvedeniya fundamentov na prosadochnyh gruntah [Comparative analysis of methods for constructing foundations on subsidence soils] *Vestnik MGSU*. 2025, Vol. 20, No 3.
23. **Polishchuk A.I., Marinichev M.B.** Osnovaniya i fundamenty, podzemnye sooruzheniya [Foundations and bases, underground structures] Krasnodar, Kuban State Agrarian University, 2024. 612 p.
24. **Maksimov F.A.** Sovershenstvovanie konstrukcii i metodov rascheta vintovyh dvuhlopastnyh svaj v glinistyh gruntah [Improving the design and calculation methods of screw two-blade piles in clay soils]: avtoref. dis. … cand. tech. sc. Volgograd, 2018, 24 p.
25. **Polishchuk A.I., CHernyavskij D.A., Solonov G.G.** Osobennosti ustrojstva buroin"ekcionnyh konicheskih svaj v glinistyh gruntah [Features of the device of bored conical piles in clay soils]. *Sbornik statej po materialam konferencii, posvyashchennoj 50-letiyu arhitekturno-stroitel'nogo fakul'teta, posvyashchennoj 50-letiyu arhitekturno-stroitel'nogo fakul'teta*, 28 March 2024. Krasnodar, Kuban State Agrarian University, 2024, pp. 97-101. – EDN DUYBFA

СПИСОК ЛИТЕРАТУРА

1. **Полищук А.И.** Усиление фундаментов инъекционными сваями при реконструкции зданий: монография / А. И. Полищук, А. А. Петухов, И. В. Семёнов; под ред. д-ра техн. наук, профессора А. И. Полищука / 2-е изд., доп. – М.: Изд-во АСВ, 2023. – 212 с.
2. **Полищук А.И.** Расчет осадки комбинированного фундамента для реконструируемого здания в глинистых грунтах / А. И. Полищук, И. В. Семёнов // Основания, фундаменты и механика грунтов. – 2022. – №6. – С.7-11.
3. Пат. 2238366. Российская Федерация, МПК E 02 D 5/34. Способ устройства инъекционной сваи / Полищук А.И., Герасимов О.В., Петухов А.А., Андриенко Ю.Б., Нуйкин С.С. ; заявитель и патентообладатель ЗАО «Научно-производственное объединение «Георекнструкция»» - № 2003106150/03; заявл. 04.03.2003; опубл. 20.10.2004, Бюл. № 29. – 10 с.
4. **Bruce, D.A., Bruce, M.E.C., and Traylor, R.P.** (1999). «High Capacity Mi-cropiles – Basic Principals and Case Histories» GeoEngineering for Underground Facilities.Proc. of the 3rd National Conference

of the Geo-Institute of the American Society of Civil Engineers. Geotechnical Special Publication No. 90, Urbana-Champaign, IL, June 13-17, pp. 188-199.
5. **Jeon, S., and Kulhawy, F.H**. (2002). «Evaluation of axial compression be-havior of micropiles» Proceeding of a Specialty Conference – Foundation and ground improvement, Blacksburg VI, ASCE, 460-471.
6. **Чернявский Д.А.** Оценка влияния прочностных характеристик глинистых грунтов на несущую способность одиночных конических буроинъекционных свай / Д. А. Чернявский // Вестник ПНИПУ. Строительство и архитектура. – 2018. – Т. 9, № 4. – с. 69–79. – DOI: 10.15593/2224-9826/2018.4.07.
7. **Мангушев Р.А.** Сваи и свайные фундаменты. Конструкции, проектирование и технологии / Р. А. Мангушев, А. Л. Готман, В. В. Знаменский, А. Б. Пономарев. – М.: Изд-во АСВ, 2018. – 320 с.
8. **Тарасов А.А.** Развитие методов расчёта инъекционных свай в слабых глинистых грунтах для фундаментов реконструируемых зданий: автореф. дис. … канд. техн. наук. – Томск, 2015. – 23 с.
9. Справочник геотехника. Основания, фундаменты и подземные сооружения: 3-е издание, дополненное и переработанное / Под общ. ред. В.А. Ильичева и Р.А. Мангушева. – М.: Изд-во АСВ, 2023. С.1084.
10. **Петухов А.А.** Совершенствование способа устройства инъекционных свай в слабых глинистых грунтах для условий реконструкции зданий: автореф. дис. … канд. техн. наук. – Томск, 2006. – 23 с.
11. **Захаров М.С**. Инженерно-геологические и инженерно-геотехнические изыскания в строительстве : учеб. пособие / М. С. Захаров, Р. А. Мангушев; под ред. Р. А. Мангушева. – М., СПб. : Изд-во АСВ, 2014. – 176 с.
12. **Землянский А.А**. Обследование и испытание зданий и сооружений / А.А. Землянский. – М.: Изд-во АСВ, 2002. – 240 с.
13. **Плевков В. С., Мальганов А.И., Балдин И.В.** Оценка технического состояния, восстановление и усиление строительных конструкций инженерных сооружений: учебное пособие / Под ред. В. С. Плевкова. 2-е изд. перераб. и доп. – М.: Изд-во АСВ, 2014. – 328 с.
14. **Polishchuk, A.I.** Main reasons for strengthening foundations and base soil stabilizations of used buildings / A.I. Polishchuk, I.V. Semyonov, V.A. Demchenko // Journal of Physics: Conference Series : 2, Perm, 26–28 мая 2021 года. – Perm, 2021. – P. 012029. – DOI 10.1088/1742-6596/1928/1/012029. – EDN QJREFB.
15. **Готман А.Л.** Сваи и свайные фундаменты. – Уфа: ИДПО УГНТУ, 2015. – 384 с.
16. **Пронозин Я.А.** Расчет взаимодействия буроинъекционных свай с грунтовым основанием / Я. А. Пронозин, М. А. Самохвалов // Основания, фундаменты и механика грунтов. – 2018. – № 2. – С. 14-17.
17. **Филиппович А.А.** Взаимодействие ленточных фундаментов реконструируемых зданий с глинистым грунтом основания при их усилении инъекционными сваями: автореф. дис. … канд. техн. наук. – Волгоград, 2014. – 23 с.
18. **Коновалов П. А.** Основания и фундаменты реконструируемых зданий / П. А. Коновалов, В. П. Коновалов. – 5-е изд. перераб. и доп. – М.: Изд-во АСВ, 2011. – 384 с.
19. **Полищук А.И.** Разработка метода расчета осадки одиночной инъекционной сваи в глинистых грунтах / А. И. Полищук, И. В. Семенов // IV Международная научно-практическая молодежная конференция по геотехнике : сборник материалов, Тюмень, 28–30 сентября 2018 года / Тюменский индустриальный университет. – Тюмень: Тюменский индустриальный университет, 2018. – С. 67-69. – EDN XZPKYP.

20. Strengthening of the Foundations of Renovated Buildings With Injection Piles / A. I. Polishchuk, N. S. Nikitina, A. A. Petukhov, I. V. Semyonov // International Journal for Computational Civil and Structural Engineering. – 2021. – Vol. 17, No. 1. – P. 75-86. – DOI 10.22337/2587-9618-2021-17-1-75-86. – EDN RCSPAE.
21. **Малышев М.В., Никитина Н.С.** Расчет осадок фундаментов при нелинейной зависимости между напряжениями и деформациями в грунтах / М.В. Малышев, Н.С. Никитина // Основания, фундаменты и механика грунтов. – 1982. – №2. – С.21–24.
22. **Никитина Н.С., Кравченко Д.А., Ремизова Н.В.** Сравнительный анализ методов возведения фундаментов на просадочных грунтах / Н.С. Никитина, Д.А. Кравченко, Н.В. Ремизова // Вестник МГСУ. 2025 Том 20, № 3.
23. **Полищук, А.И**. Основания и фундаменты, подземные сооружения : учебник / А. И. Полищук, М. Б. Мариничев. – Краснодар : Кубанский государственный аграрный университет, 2024. – 612 с. – EDN TQRMTU.
24. **Максимов, Ф.А.** Совершенствование конструкции и методов расчета винтовых двухлопастных свай в глинистых грунтах [Текст]: автореф. дис. … канд. техн. наук. – Волгоград, 2018. – 24 с.
25. **Полищук, А. И.** Особенности устройства буроинъекционных конических свай в глинистых грунтах / А. И. Полищук, Д. А. Чернявский, Г. Г. Солонов // Современные векторы развития архитектуры и строительства : Сборник статей по материалам конференции, посвященной 50-летию архитектурно-строительного факультета, посвященной 50-летию архитектурно-строительного факультета, Краснодар, 28 марта 2024 года. – Краснодар: Кубанский государственный аграрный университет им. И.Т. Трубилина, 2024. – С. 97-101. – EDN DUYBFA.

Anatoly I. Polishchuk, Professor at the Department of Bases and Foundations, Kuban State Agrarian University named after I.T. Trubilin (Krasnodar), Honored Builder of the Russian Federation, Honorary Worker of Higher Professional Education of the Russian Federation, holder of the Honorary Diploma of the President of the Russian Federation, Doctor of Technical Sciences, Professor. Specialist in the field of foundation construction, building inspection and reconstruction. Member of the Presidium of the Russian Society for Soil Mechanics, Geotechnics and Foundation Construction, holder of the N.M. Gersevanov Medal. Author, co-author of 8 monographs, 2 regional normative documents, 18 educational and scientific-practical manuals, 3 reference books, 40 patents of the Russian Federation for inventions, in total more than 260 scientific printed works. (Russia, 350044, Krasnodar, 13, Kalinina str., E-mail: ofpai@mail.ru).

Arkady A. Petukhov. Director of LLC “Stroytechinovations TDSK” (Tomsk), Associate Professor of the Department of “Foundations and Foundations” of I.T. Trubilin Kuban State Agrarian University (Krasnodar), Candidate of Technical Sciences, Associate Professor. He is a specialist in the field of engineering-geological surveys, reconstruction of buildings and geotechnical construction. Author and co-author of more than 80 scientific works, 30 patents of the Russian Federation for inventions and utility models. (Russia, 350044, Krasnodar, 13, Kalinina str. E-mail: paa5579@mail.ru)

Полищук Анатолий Иванович, Профессор кафедры «Основания и фундаменты» Кубанского государственного аграрного университета им. И. Т. Трубилина (г. Краснодар), заслуженный строитель РФ, почетный работник высшего профессионального образования РФ, обладатель почетной грамоты Президента РФ, докт. техн. наук, профессор. Специалист в области фундаментостроения, обследования и реконструкции зданий. Член Президиума Российского общества по механике грунтов, геотехнике и фундаментостроению, обладатель медали Н.М. Герсеванова. Автор, соавтор 8 монографий, 2 региональных нормативных документов, 18 учебных и научно-практических пособий, 3 справочников, 40 патентов РФ на изобретения, всего более 260 научных печатных работ. (Россия, 350044, г. Краснодар, ул. Калинина, 13, E-mail: ofpai@mail.ru).

Петухов Аркадий Александрович. Директор предприятия ООО «Стройтехинновации ТДСК» (г. Томск), доцент кафедры «Основания и фундаменты» Кубанского государственного аграрного университета им. И. Т. Трубилина (г. Краснодар), канд. техн. наук, доцент. Специалист в области инженерно-геологических изысканий, реконструкции зданий и геотехнического строительства. Автор, соавтор более 80 научных работ, 30 патентов РФ на изобретения и полезные модели. (Россия, 350044, г. Краснодар, ул. Калинина, 13, E-mail: paa5579@mail.ru).

Nadezhda S. Nikitina, Director of the Publishing House of the Association of Universities for Civil Engineering (Moscow), Professor of the Department of Soil Mechanics and Geotechnics of the National Research Moscow State University of Civil Engineering (NRU MGSU), Candidate of Technical Sciences, Professor. Scientific and practical interests: soil mechanics, foundation engineering, geotechnical construction; educational activity in the field of training of scientific and pedagogical personnel in postgraduate studies. Honorary worker of higher professional education of the Russian Federation, author of more than 50 scientific works. (Russia, 129337, Moscow, Yaroslavskoe Shosse, 26, High-Rise Building, office. 511; E-mail: nsnikitina@mail.ru).

Ivan V. Semenov. Senior lecturer, postgraduate student at the Department of "Bases and Foundations" of Kuban State Agrarian University named after I.T. Trubilin. Scientific and practical interests: improvement of constructive solutions of injection, bored-injection piles and methods of their calculation, computer support of scientific and design works in construction. Author, co-author of 5 scientific-practical and educational-methodical manuals, 1 monograph, 25 scientific articles and 4 patents of the Russian Federation for inventions. (Russia, 350044, Krasnodar, 13, Kalinina str., E-mail: amigos_siv@mail.ru)

Никитина Надежда Сергеевна. Директор издательства Ассоциации строительных ВУЗов (Москва), профессор кафедры механики грунтов и геотехники Национального исследовательского Московского государственного строительного университета (НИУ МГСУ), канд. техн. наук, профессор. Научно-практические интересы: механика грунтов, фундаментостроение, геотехническое строительство; образовательная деятельность в сфере подготовки научно-педагогических кадров в аспирантуре. Почетный работник высшего профессионального образования РФ, автор более 50 научных работ. (Россия, 129337, Москва, Ярославское шоссе, д. 26, Высотное здание, оф. 511; E-mail: nsnikitina@mail.ru).

Семёнов Иван Владимирович. Старший преподаватель, аспирант кафедры «Основания и фундаменты» Кубанского государственного аграрного университета им. И. Т. Трубилина. Научно-практические интересы: совершенствование конструктивных решений инъекционных, буроинъекционных свай и методов их расчета, компьютерное обеспечение научных и проектных работ в строительстве. Автор, соавтор 5 научно-практических и учебно-методических пособий, 1 монографии, 25 научных статей и 4 патентов РФ на изобретения. (Россия, 350044, г. Краснодар, ул. Калинина, 13, E-mail: amigos_siv@mail.ru).